Ph.D. Thesis

Université de Limoges

University of Limoges

ED 653 - Sciences et Ingénierie (SI)

Institut de recherche XLIM, CNRS UMR 7252

A thesis submitted to University of Limoges
in partial fulfillment of the requirements of the degree of

Doctor of Philosophy

Électronique des Hautes Fréquences, Photonique et Systèmes / Télécommunication

Presented and defensed by

DANIEL RIBEIRO DOS SANTOS

On March 26, 2025

Printable photovoltaic photoreceptors for the factory of the future and the Internet of Things: toward energy harvesting and wireless optical communications

Thesis supervisor: **Johann BOUCLÉ** and **Anne JULIEN-VERGONJANNE**

JURY:

President of jury
M. Luiz POFFO, Professor, XLIM, Université de Limoges

Reporters
M. Bruno FRACASSO, Professor, LabSTICC, IMT Atlantique
M. David DUCHÉ, Associate Professor, IM2NP, Aix Marseille Université

Examiners
M. Bastien BÉCHADERGUE, Associate Professor, LISV, Université de Versailles Saint-Quentin-en-Yvelines
M. Johann BOUCLÉ, Associate Professor, XLIM, Université de Limoges
Mme. Anne JULIEN-VERGONJANNE, Professor, XLIM, Université de Limoges

Em memória do meu pai
À minha amada mãe
Aos meus dois queridos irmãos

Os homens valentes têm uma estrela em lugar do coração.
Jorge Amado

Acknowledgements

Between the lines on this particular page, I step away from my “PhD candidate” position, momentarily putting aside the required formality and impersonality of a work of this caliber, to write as a deeply personal human being, where emotions and rationality cannot be entirely separated. Here, I am expressing my thankfulness for those who lifted me up and helped through these last three years.

Nobody can go through a long journey alone, without any map to be guided by or a person to count on. Naturally, this leads to acknowledging the first two people that helped me in this long journey: my supervisors. **Johann Bouclé** and **Anne Julien-Vergonjanne** provided me all the time they could spare for my questions and my (long) discussions, nourishing my wisdom while igniting my motivation, for which they deserve the biggest thank you I can provide. But their support extended beyond their responsibilities, as each “ça va?” created a safe space to express myself, where in trade they provided me life advices and a heartwarming talk. From the bottom of my heart, I offer my deepest gratitude: *muito obrigado!*

I would also like to thank the all members of the jury, without whom my work could not be scientifically evaluated. The reporters **M. Bruno Fracasso** and **M. David Duché** for accepting to correct this long and detailed manuscript, and the examiners **M. Luiz Poffo** and **M. Bastien Béchadergue** for evaluating my defense and posing exciting questions.

A team would not be complete without each valuable member fulfilling their duties. So, I sincerely thank all members of the ELITE, SYCOMOR and PLATINOM teams who contributed to the development of this work: **Bernard Ratier**, **Sylvain Vedraine**, **Marie-Laure Guillat**, **Stéphanie Sahuguede**, **Pierre Combeau**, **Lilian Aveneau**, **Nicolas Parou** and **Lionel Rechignat**. Additionally, I extend my gratitude for others who played key roles in the success of this work, including **M. Sébastien Reynaud**, head of hyper frequency systems at CISTEME, **M. Sadok Ben Dkhil**, chief technology officer at Dracula Technologies and **Mme. Marie Parmentier**, process engineer at Dracula Technologies.

Beyond the pivotal human contributors, I also express my gratitude to the French Ministry of Higher Education and Research, the Nouvelle Aquitaine region and the University of Limoges, for providing the necessary funds for the work described in this thesis. I am equally thankful to the CASI board at XLIM for their financial support.

More than the necessary funding and scientific support, a social and emotional basis is not just important, but essential, for any human being in the workplace. Through these words, I expose my heartfelt appreciation for my lab mates and friends, who held my pieces together during this journey: **Baptiste Moeglen-Paget**, my French best friend and greatest connection in XLIM; **Clara Abbouab**, one of the kindest people I know; **Quang-Huy Do**, my Vietnamese brother; the always cheerful **Eva (Ruoxue He);** the brave-heart, **Ceren Yildrim**, and the science enthusiast, **Issoufou Ibrahim**. Additionally, I am glad that I crossed ways with **Eduard-Nicolae Sirjita**, **Heinich Porro** and **Cristian Jiménez**. Also, it is impossible to forget the people I worked with in the beginning, even though we parted ways long ago. Their influence remains with me to this day: **Amel Chehbani**, **Steve Joumessi, Alassane Kaba** and **Amina Boussebt**.

Beyond the everyday lab tasks, there are people who indirectly support us in ways we never expected. A huge shout-out to **Mahdieh Joharifar**, my Iranian friend who, even though we did not see each other often, already means so much to me; and to **Karina Rojas**, one of the sweetest people I have ever met.

Finally, I would like to express my gratitude to both my families: my biological family and the one I found in France. A huge “thank you”, from the deepest part of my soul, to my late father and my mother, **Luiz Fernando** and **Ana Cristina**, for raising me to become the person I am today, and to my brothers, **Vitor Ribeiro** and **Leonardo Ribeiro**, for shaping and supporting me throughout my life. Although we are not blood-related, my Brazilian family in France means more to me than I could have ever imagined, including: **Kariny Maia**, **Mateus Viana**, **Elmo Sette**, **Bruno Chaves**, **Lucila Teixeira**, **Dina Araujo**, **Cecília Rocha**, **Thaisa Nascimento**, **Rafael Nascimento**, **Carolina Pedrosa**, **Bruno Amorim**, **Lucas Fernandes**, **Gabriela Barbosa**, **Sara Pereira**, **Joyce Amorim** and **Guto Guido**. As the famous Brazilian writer Mário Quintana says, “A amizade é um amor que nunca morre”, which translates to “Friendship is a love that never dies”. With this sentiment, I immortalize you all in the lines of this work, carrying your names towards eternity.

Lastly, I would like to acknowledge the assistance of artificial intelligence tools (ChatGPT) for helping enhance the writing quality of this manuscript. Their use was strictly limited to providing suggestions for grammar and vocabulary improvements

Table of Contents

List of Abbreviations

AC	Alternating Current
ACO-OFDM	Asymmetrically Clipped Optical OFDM
ADC	Analog-to-Digital Converter
APD	Avalanche Photodiode
AWGN	Additive White Gaussian Noise
a-Si	Amorphous Silicon
BER	Bit Error Rate
BHJ	Bulk Heterojunction
BPSK	Binary Phase Shift Keying
BRDF	Bidirectional Reflectance Distribution Function
CDD	Charge-Coupled Device
CFL	Compact Fluorescent Lamp
CIGS	Copper Indium Gallium Selenide
CMOS	Complementary Metal-Oxide-Semiconductor
CS	Charge-Separated
c-Si	Crystalline Silicon
CSK	Color Shift Keying
CT	Charge-Transfer
DAC	Digital-to-Analog Converter
DC	Direct Current
DCO-OFDM	Direct Current Biased Optical OFDM
DD	Direct Detection
DSSC	Dye-Sensitized Solar Cell
EFMF	Error-Free Maximum Frequency
EH	Energy Harvesting
EIS	Electrochemical Impedance Spectroscopy
EMI	Electromagnetic Interference
EPBT	Energy Payback Time
EQE	External Quantum Efficiency
ETL	Electron Transport Layer
FF	Fill Factor
FFT	Fast Fourier Transform

FL	Fluorescent Lamp
FOV	Field-of-View
FSO	Free-Space Optics
GaAs	Gallium Arsenide
GaAsP	Gallium Arsenide Phosphide
HMI	Human-Machine Interface
HOMO	Highest Occupied Molecular Orbital
HPF	High-Pass Filter
HTL	Hole Transport Layer
IEC	International Electrotechnical Commission
IFFT	Inverse Fast Fourier Transform
IM	Intensity Modulation
IoT	Internet of Things
IQE	Internal Quantum Efficiency
ISI	Inter-Symbol Interference
ITO	Tin Oxide
JEITA	Japan Electronics and Information Technology Industries Association
LD	Laser Diode
LED	Light-Emitting Diode
LiFi	Light Fidelity
LOS	Line of Sight
LPF	Low-Pass Filter
LUMO	Lowest Unoccupied Molecular Orbital
MCM	Multi-Carrier Modulation
MCRT	Monte Carlo Ray Tracing
MIMO	Multiple-Input Multiple Output
MPP	Maximum Power Point
MPPT	Maximum Power Point Tracking
NLOS	Non-Line of Sight
NRZ	Non-Return-to-Zero
OCC	Optical Camera Communication
OFDM	Orthogonal Frequency Division Multiplexing
OLED	Organic LED
OOK	On-Off Keying

OP-AMP	Operational Amplifier
OPV	Organic Photovoltaic
OWC	Optical Wireless Communication
PAM-DMT	Pulse Amplitude Modulation Discrete Multitone
PCE	Power Conversion Efficiency
pc-LED	Phosphor-Converted LED
PD	Photodiode
PIN	Positive-Intrinsic-Negative
PPM	Pulse Position Modulation
PSC	Perovskite Solar Cell
PSD	Power Spectral Density
PV	Photovoltaic
QAM	Quadrature Amplitude Modulation
QDPV	Quantum-Dot Photovoltaics
QE	Quantum Efficiency
QoS	Quality of Service
RaPSor	Ray Propagation Simulator
RF	Radio Frequency
RFID	Radio Frequency Identification
RMS	Root Mean Square
RZ	Return-to-Zero
SDR	Software Defined Radio
Si	Silicon
SISO	Single-Input Single-Output
SLIPT	Simultaneous Lightwave Information and Power Transfer
SNR	Signal-to-Noise Ratio
STC	Standard Test Condition
TIA	Transimpedance Amplifier
USRP	Universal Software Radio Peripheral
UWOC	Underwater Wireless Optical Communication
VCSEL	Vertical-Cavity Surface-Emitting Laser
VLC	Visible Light Communication

Introduction

The convergence of modern communication demands and sustainable energy solutions has induced the exploration of exciting and innovative technologies for indoor IoT applications. Among these, Visible Light Communication (VLC) and Organic Photovoltaics (OPVs) have emerged as transformative approaches to address the dual challenges of efficient data transmission and renewable energy harvesting through optical waves. VLC takes advantage of the vast visible light spectrum, offering benefits such as spectrum availability, improved physical layer security, and compatibility with environments sensitive to electromagnetic interference. Simultaneously, OPVs stand out as promising candidates for indoor energy harvesting due to their high efficiency under low illumination, flexibility, and the reduced energetic footprint of their production methods. Recent advancements have demonstrated the potential of OPVs not only for energy harvesting but also as VLC receivers, enabling the simultaneous reception of energy and data.

This thesis is part of the regional project "IoT-PV", funded by the Nouvelle Aquitaine region and by the French "*Ministère de l'Enseignement Supérieur et de la Recherche*", which aims the promotion of innovative solutions for sustainable communication and energy systems. By supporting local resources and expertise, the project seeks to address the increasing energy demands of IoT networks while integrating cutting-edge technologies such as VLC and OPVs.

Finally, this thesis explores the integration of VLC and OPVs within the context of Simultaneous Lightwave Information and Power Transfer (SLIPT). The SLIPT concept, which combines energy harvesting and optical data reception into a single system, represents an innovative approach to address the increasing energy demands of modern low power IoT applications while promoting sustainability. By employing the dual functionality of OPVs as both energy harvesters and communication receivers, SLIPT has the potential to create self-powered systems that minimize reliance on batteries, thereby reducing maintenance requirements and improving operational efficiency.

This work explores multiple challenges and opportunities associated with SLIPT, from understanding the fundamental principles of VLC and OPVs to characterizing their performance under multiple indoor conditions. It examines the connection between energy harvesting and communication performance, highlighting key trade-offs and proposing innovative solutions to optimize system functionality. The work presented also includes the development of simulation tools and experimental setups that provide a deeper understanding of the dynamic behaviour of OPVs within SLIPT systems.

By addressing both theoretical and practical aspects, this research contributes to advancing the state-of-the-art in SLIPT technologies, creating a foundation on their integration into next-generation IoT ecosystems. The thesis is structured as follows:

Chapter I establishes the basis of the thesis by exploring VLC technology and the motivations for its adoption, including its advantages over traditional radio-frequency-based communication systems. It also introduces OPVs as a suitable solution for indoor energy harvesting and highlights their dual role as energy harvesters and optical receivers in SLIPT applications. This chapter concludes with the thesis objectives and contributions to the field.

Chapter II explores the technical characteristics of VLC systems, providing a comprehensive discussion of the key components of VLC systems, such as optical sources, channels, and receivers. The chapter also introduces OPVs, discussing their working principles, unique properties, and suitability for indoor energy harvesting. Additionally, it explores the SLIPT context, presenting key studies and lessons learned about integrating energy harvesting and communication within a unified system.

Chapter III focuses on the characterization of the OPV device used in this research. Static characterizations evaluate its energy harvesting performance through metrics such as spectral and angular responsivity, I-V behaviour, and flexibility. Dynamic characterizations evaluate its communication performance, including bandwidth and signal amplitude under various operating conditions. These analyses provide a foundation for understanding the trade-offs between energy harvesting and communication.

Chapter IV presents an indoor simulation framework for OPVs, including the validation of a flat OPV model and its extension to curved devices. The simulations, performed using a ray-tracing-based software, investigate the performance of OPVs in indoor environments. This chapter highlights the complex connection between environmental factors and OPV performance in SLIPT applications.

Chapter V describes the experimental bench developed for simultaneous energy and data transfer analysis. It provides details on the hardware setup, including the configuration of OPV-based receivers. Experiments conducted with the bench validate key findings, such as the trade-off between energy harvesting and communication, and demonstrate the feasibility of using OPVs in SLIPT systems.

Finally, the conclusion provides a comprehensive summary of the work presented in this thesis, emphasizing the significant contributions made to the field of SLIPT and the integration of VLC and OPVs. In addition to summarizing the major outcomes, the conclusion outlines important short-term and long-term perspectives for advancing this research area.

Chapter I

Establishing the Context

Summary

Chapter I. Establishing the Context

I.1. A comprehensive introduction to Visible Light Communication

I.1.1. Brief history

Light has played a crucial role in various aspects of human civilization, from enabling vision and growth in plants to facilitating advanced technologies in medicine and renewable energy. In recent years, the VLC has emerged as a groundbreaking technology and is gradually taking space in the telecommunication field for its particular aspects.

In fact, the transmission of information through light is not recent. In ancient times, smoke and light signals were the fastest ways to send emergency messages, for instance lighting beacon towers when the great wall of China was under attack, which could transmit the invasion information over 7000 kilometres [1]. Smoke signals were also constantly used by Australians aboriginals to signalling when entering foreign lands [2]. Optical communication is also commonly seen in boats with the use of signal lamps to exchange location information, a technology that is still found in the current society, when the radio communication must be silenced [3].

It was only in 1880 that Alexander Graham Bell invented the first apparatus capable of modulating sunlight with human voice, using a system composed by mirrors at the transmission and selenium at the reception [4]. The newly-discovered device, known as photophone, could modulate light reflections with a mirror, which vibrates according to the sound oscillation, and transmit it over a distance of 200 meters. By concentrating the light beam onto the selenium receiver, an electrical signal was generated, which was further reconverted into sound once again.

However, Bell's discovery did not attract great attention as the world was living an outstanding expansion of Radio-Frequency (RF) technologies provided by several other great scientists [5]. In 1888, Heinrich Hertz experimentally confirmed James Clerk Maxwell equations, proving the existence of electromagnetic waves radiations, an essential milestone for radio wireless communications [6]. Not much later, the first wireless communication systems using RF waves were proposed by leading figures, such as Father Roberto Landell de Moura [7], Guglielmo Marconi [8] and Ferdinand Braun [9]. The higher distance reach of RF systems (few kilometers) and the exciting and innovative behavior of electromagnetic waves significantly diminished the interest in optical communication, and the photophone project was put aside.

Nonetheless, the intrinsic physical layer security was still a great advantage of Optical Wireless Communications (OWC) over RF wireless systems, an important feature especially for military purposes. It drew attention of the German Army in 1935, which created an Infrared (IR) photophone using a tungsten filament lamp and an optical filter [10]. From the development of IR Light Emitting Diodes (LEDs) and Laser Diodes (LDs) in the 1960s, the interest in optical communications surged once again, leading to pioneering experiments and demonstrations. In 1962, the M.I.T Lincoln Labs achieved an image and audio transmission over 84 m with a LED [11], followed by the same transmission over 50 km [12] with a LD. However, the massive expansion of RF technologies made it difficult for the less developed optical communication systems to grow [13].

In 1962, Nick Holonyak created the first visible LED by replacing the mostly used Gallium Arsenide (GaAs) by Gallium Arsenide Phosphide (GaAsP), granting him the title of "father of the lighting-emitting diode" [14]. This innovation marked the initial step towards the development of VLC systems, as the fast switching capabilities of LEDs allow data transfer at rates imperceptible to the human eye [15]. In 1993, Dr. Shuji Nakamura created the first blue LED, enabling the development of white diodes, which granted him a Nobel prize in 2014 [16], [17]. The recognition is justified by the outstanding luminous efficiency of white LEDs compared to old technologies, with a current record of 310 lumen/watt, equivalent to 16 light bulbs or 70 fluorescent lamps [18]. From this point and beyond, the implementation of VLC systems for indoor illumination and communication was possible.

The first ever VLC system using fast switching LEDs was proposed in 1999 with green, red and yellow devices [19]. In 2000, the first communication system using white LEDs was proposed by Nakagawa Laboratory associated to Keio University, in Japan [20], and the VLC term was labelled in 2003 by the same institute [21], which created the Visible Light Communication Consortium (VLCC), now called Visible Light Communication Association (VLCA) [22]. Four years was required for the first two standards propositions to the Japan Electronics and Information Technology Industries Association (JEITA) [23]. In 2011, the IEEE 802.15.7 standard was proposed to address different challenges that were not discussed in the first two standards, such as flickering and dimming mitigation [24]. Subsequently, different OWC standards were and are being developed to address different modern society challenges, such as the IEEE 802.15.7-2018, focusing in short-range OWC for metropolitan area networks [25], and the IEEE 802.15.13, focusing on OWC in Industry 4.0 [26].

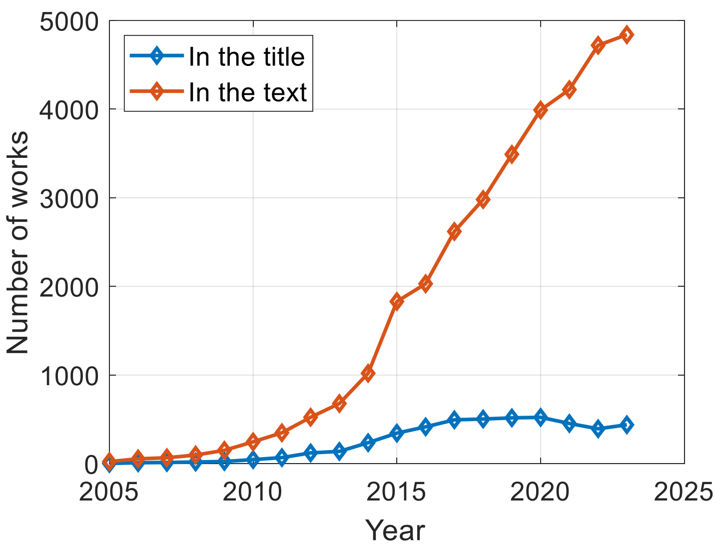

Figure 1: Number of publications containing the term "Visible Light Communication" over the years. Source: Data obtained from the Google Scholar search engine in June 2024.

In 2011, Harald Haas and his team introduced the term LiFi (Light Fidelity) during a TED talk, where he demonstrated the transmission of a high-definition video using a light bulb, which reached millions of viewers on streaming platforms [27]. Contrary to WiFi, its light counterpart takes advantage of OWC to develop a full wireless network system [28]. Recently, a standard defining communication protocols for LiFi was released [29]. VLC was already facing a notable expansion, which intensified considerably around 2010, evidenced by the growing number of published works in the field. Figure 1 shows the number of articles containing “Visible Light Communication” in the title (in blue) and within the body (in red), obtained through Google Scholar search engine, which demonstrates the rising interest in the subject. Today, optical communications are taking more space in the telecommunications field due to their complementary nature to RF systems. This growth is heavily supported by major companies and prestigious universities, including NASA [30], Siemens, University of Edinburgh and Oxford University [31].

I.1.2. Motivations

Although optical communication systems were proposed prior to RF ones, they were significantly less developed at the beginning of the 20th century. Due to the superior performance and range of wireless RF systems, the majority of research focused on them. Before the 1960s, optical components were not sufficiently developed to ensure a reliable communication, and only with the maturation of such systems that the field began to grow once again [13]. Indoor lighting was mainly established with incandescent and fluorescent light bulbs, which do not allow high-speed switching or precise modulation [32]. The creation of LEDs attracted the attention of communication scientists for their mostly linear behavior and high commutation speed. Recent works have demonstrated high data rate potential of diffuse VLC systems [33], [34], achieving a record-setting 46 Gbit/s in 2023 [35].

Light possesses numerous distinct attributes over radio waves, offering unique specifications for VLC compared to RF. In modern society, these specifications are employed to overcome current wireless communications challenges, from which we highlight some of the most impactful (non-exhaustive list) ones, with the corresponding benefits brought by the optical wireless communication.

I.1.2.1. Congestion of RF networks

In 2023, 5.4 billion people had access to the internet, representing 66% of total global population, a significant increase compared to 3.9 billion users in 2018, 51% of total global population [36]. An even greater expansion was observed in the number of devices connected to IP networks, surpassing three times the global population in 2023. In the Internet-of-Things (IoT) sector, 15.9 billion devices were deployed in 2023, with projections indicating a massive increase to 39.6 billion by 2033, as shown in Figure 2 [37].

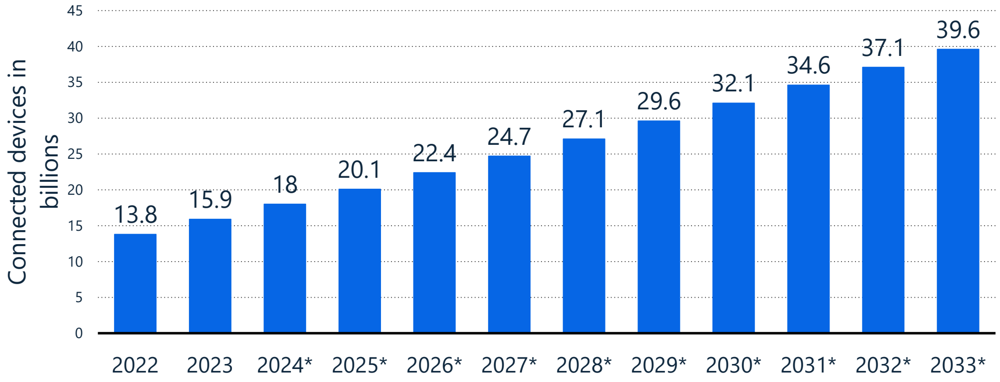

Figure 2: Number of IoT connections worldwide from 2022 to 2023, with forecasts from 2024 to 2033 (in billions).

Source: Transforma Insights [37].

Given that 80% of traffic data occurs in indoor scenario, the development of robust indoor networks seems necessary [38]. Due to this technological expansion, a reliable and low-latency network capable of delivering high data rates is required [39], [40]. However, existing systems rely on RF spectrum, which is fated to saturate [41].

The radio spectrum covers from 3 kHz up to 300 GHz, from which frequencies inferior to 6 GHz are licensed and restricted according to each country [32]. As reported by the IEEE 802.11 standard, the Wi-Fi technology can operate in two frequency regions, 2.4 GHz and 5 GHz, with a bandwidth of 22 MHz [42], [43]. In contrast, the visible light spectrum spans from 380 nm to 780 nm (380 THz – 790 THz), representing a total of 405 THz available spectrum, over one thousand times larger than the RF, as shown in Figure 3. Because optical waves do not interfere with common electronic devices, VLC operates in an unlicensed spectrum, enabling the entire bandwidth to be used for data transfer. Employing multiple channel multiplexing strategies, for example Wavelength Division Multiplexing (WDM), allows the optimal exploitation of the whole visible spectrum [44]. Moreover, light waves stay confined in a given space, allowing full spectrum recycling for different access points. This confinement minimizes interference and allows for multiple, simultaneous transmissions within the same environment, thereby improving the overall efficiency and capacity of the communication system.

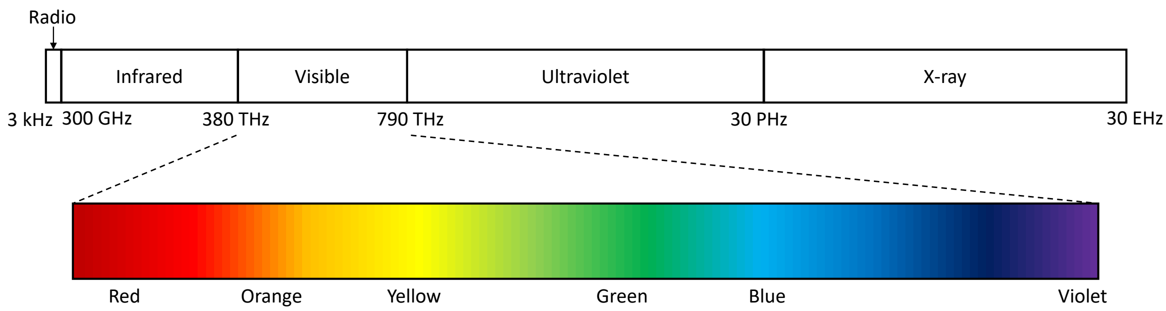

Figure 3: Electromagnetic Spectrum. The visible spectrum goes from 380 THz up to 790 THz, representing 1200 times more available spectrum than radio one.

These unique features represent a highly adaptive behavior of this technology, making it widely applicable in indoor environments to meet various data rate requirements, ranging from low data rate applications, like medical monitoring [45], to high-speed data transmission, such as virtual reality [46]. Similarly, IoT-connected devices require different data rates depending on their use cases. Figure 4 illustrates the range of data rates provided by different IoT communication protocols, from low data rate technologies like Sigfox (100 bit/s) and LoRaWAN (5 kbit/s), to medium-rate options such as Narrow-Band IoT (250 kbit/s), and high data rate protocols including Bluetooth (1 Mbit/s) and Wi-Fi (16 Mbit/s) [47], [48]. This wide range accommodates diverse IoT applications, spanning simple tasks like sensor data collection to high-bandwidth needs like video streaming.

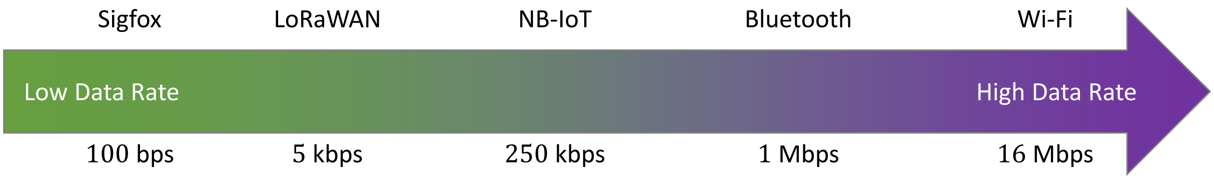

Figure 4: Data rate ranges for common IoT communication technologies. Data obtained from references [47], [48].

I.1.2.2. Eavesdropping and piracy

Among the various physical properties of RF waves, their ability to pass through objects presents both advantages and disadvantages. On one hand, RF waves have better reach and coverage compared to optical waves, ideal for long-range communication and Non-Line-of-Sight (NLOS) transmission. However, it intrinsically weakens physical layer security, making it more susceptible to interception, piracy and eavesdropping [49], [50], posing risks to sensitive data.

This vulnerability becomes especially concerning in scenarios where privacy and confidentiality are required. For instance, in healthcare, Radio Frequency Identification (RFID) are used to manage patient data and track medical equipment, but unsecured RF transmissions can expose private health information to unauthorized access [51]. Similarly, corporate espionage is a growing threat, where RF interception can compromise proprietary business communications and trade secrets. Furthermore, military and government operations are prime targets for eavesdropping, as intercepted RF communications could lead to intelligence leaks, compromising national security [52].

In such compromising environments, VLC (or infrared communications) presents a viable solution by offering a more secure alternative, as optical waves do not propagate beyond their intended area, reducing the risk of interception [53].

I.1.2.3. RF sensitive area

The strong Electromagnetic Interference (EMI) from RF waves is a well-known challenge that can disrupt the operation of sensitive equipment, particularly concerning in environments where precision and uninterrupted functioning are crucial. Hospitals, aircraft and industrial facilities, for instance, are filled with critical electronic systems that must function reliably to ensure safety and efficiency. In healthcare, devices like implantable cardioverter-defibrillators and pacemakers are particularly vulnerable to EMI [54]. Similarly, in aircraft and industrial environments, RF-based EMI can compromise the operation of navigation systems, control equipment and essential monitoring tools.

Since VLC operates within the visible, it effectively mitigates the issue of EMI that can disturb RF-based systems. This non-interference nature makes VLC a promising technology to replace or complement RF communication devices in EMI-sensitive areas, offering enhanced reliability, safety and efficiency [55], [56].

VLC offers other interesting and important features, including energy efficiency due to its dual functionality (illumination and communication). The same LED infrastructure used for lighting can also be employed for data transmission, reducing the need for additional power consumption. Additionally, VLC is easy to deploy, as LEDs are already widely present in most indoor environments. Finally, the simplicity of VLC systems, compared to the complexity of RF-based systems, makes implementation more straightforward and cost-effective.

Recent studies have highlighted interesting capabilities of Photovoltaic (PV) devices when used as VLC receivers, including their potential to simultaneously harvest optical energy. Consequently, we shall introduce the use of PV receivers for indoor energy harvesting applications.

I.2. Photovoltaics for indoor energy harvesting

While RF systems continue to face challenges in delivering the required communication performances (due to the reasons listed above), the exponential growth of connected devices is also introducing energetic concerns for modern society. As detailed before, the IoT sector is projected to compass 39.6 billion nodes by 2033 (see Figure 2), placing a wide range of power demands on IoT infrastructures. Therefore, the massive expansion will intensify the need for batteries, leading to an increase in global waste production and maintenance efforts to ensure uninterrupted operation. Consequently, energy efficiency and sustainability will become critical concerns [57], [58], especially considering the rising challenge of sustainable development and the requirement for technologies with very low energetic and environmental impacts.

In order to counterbalance this non environment-friendly problem, one main strategy is to harvest ambient energy to extend power cells lifetime (or completely eliminate them), from which different techniques can be employed, such as Photovoltaic (PV) Energy Harvesting (EH) [59] and thermal EH [60]. Under indoor scenarios, and due to their high specific power, obtaining electrical power through artificial illumination stands out compared to other techniques to supply autonomous IoT nodes [61]. In fact, this emerging area of research has garnered considerable attention over the past few years, attracting interest from diverse fields such as chemistry, electronics and beyond [62], [63], [64], [65]. Recent studies report interesting output power densities exceeding $100\ \mu W/cm^2$, sufficient to support a wide range of indoor IoT applications [66].

In this scenario, a range of PV technologies can be explored, starting with the 1st generation of solar cells, which includes devices with thick layers of Silicon (Si). This is followed by the 2nd generation (thin-film technologies), i.e. cells based on materials like Copper-Indium-Gallium-Selenide (CIGS), Amorphous Silicon (a-Si) and Gallium-Arsenide (GaAs). Finally, there is the 3rd generation, often referred as emerging solar cells, encompassing OPVs, Quantum-Dot Photovoltaics (QDPVs), Dye-Sensitized Solar Cells (DSSCs) and Perovskite Solar Cells (PSCs).

Although 1st generation Si cells still govern the market of power generation in both off-grid and grid-connected applications, their low specific power and efficiency under indoor conditions makes them less suitable for indoor EH. Thin-film technologies, being lighter and more flexible than their Si counterparts, are gaining attention in the IoT sector for diverse applications. However, they still fall short in Power Conversion Efficiency (PCE) when compared to emerging PV cells under indoor lighting [67]. Indeed, 3rd generation of solar cells is a great candidate for indoor IoT compared to conventional inorganic ones for their low production cost and energy payback time (EPBT) [68], [69]. Table 1 resumes the obtained record PCE of each technology for indoor scenarios with associated illumination conditions, reiterating the impact of emerging devices for IoT indoor applications.

Table 1: Reported record PCE for different PV technology under indoor illumination. The illumination level and technology are indicated: light-emitting diode (LED) or fluorescent lamp (FL) (data obtained November 2024).

PV Technology	Indoor Efficiency (%)	Illumination	Reference
Monocrystalline Si	9.7	890 lux (LED)	[70]
Polycrystalline Si	4.0	1000 lux (LED)	[71]
CIGS	12.5	1000 lux (LED)	[72]
a-Si	29.9	1000 lux (LED)	[73]
GaAs	22.9	1000 lux (LED)	[74]
OPV	36.5	1000 lux (LED)	[75]
QDPV	19.5	2000 lux (FL)	[76]
DSSC	35.6	1000 lux (FL)	[77]
PSC	45.5	1000 lux (LED)	[78]

I.2.1. OPV for indoor energy harvesting

Among the available options for indoor EH, DSSCs, OPVs and PSCs outperform other technologies. Nonetheless, dye-sensitized devices face commercialization challenges due to their reliance on platinum as counter electrodes, an expensive material [79]. Despite this limitation, DSSCs remain a promising solution for indoor applications. While high performance perovskite devices share some of the great advantages of OPVs (with better performance under dim illumination), they rely on toxic lead in their fabrication process, which poses significant environmental and regulatory problems, making commercialization difficult [81]. PSC are also very sensitive to processing conditions, which drastically impact their stability and reproducibility, even when controlled environments are involved during their processing. These considerations underscore the significance and potential of OPVs for indoor IoT applications. Some key advantages of this technology are outlined below (non-exhaustive list):

- **High efficiency under indoor conditions:** Organic devices demonstrate better performance under low illumination levels, such as those found indoor, compared to most technologies (see Table 1). The absorption of OPVs can be tuned to match the emission spectra of artificial light sources, such as LEDs and Compact Fluorescent Lamps (CFLs), achieving better efficiency with reduced energy losses. Figure 5 illustrates a comparison of normalized spectra for three different light sources: AM 1.5G (which simulates solar illumination at the Earth's surface) in blue, CFL in red, and white LED in purple. Larger bandgaps, compared to outdoor (1 sun) scenario, are expected for indoor conditions, and OPVs offer the flexibility of bandgap tuning through soft chemistry, representing an important advantage over Si-based technologies [82].

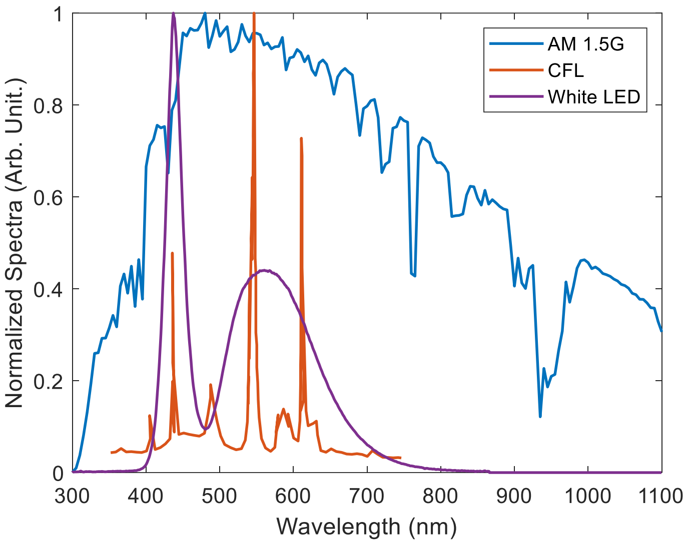

Figure 5: Normalized spectra of different light sources: AM1.5G solar spectrum (in blue), CFL (in red) and white LED (in purple).

- **Manufacturing cost, EPBT and scalability:** OPVs are produced using solution-processing techniques at low temperatures, representing a great advantage over Si-based devices, which requires extremely high temperatures and expensive purification processes. This contributes to a shorter EPBT for organic devices (around 0.3 years) compared to traditional Si solar cells (1.3 – 2.4 years) [83]. Furthermore, the production technique supports roll-to-roll manufacturing, allowing scalable and continuous production at relatively low cost [84].
- **Flexibility and high power density:** Due to their solution-based processing methods, OPVs can be printed onto various flexible substrates, including plastics (such as PET or parylene), textile (parylene-coated) and even paper. The flexibility enables easy integration into a wide range of IoT devices, including wearable and flexible electronics, as well as being suitable for deployment in various unconventional surfaces [85], [86]. Recent researches also demonstrate the significant power density of these devices under indoor lighting conditions, achieving up to 156 $\mu W/cm^2$ at 1000 lux when illuminated by a white LED [66]. This level of power is particularly suited for supplying various indoor IoT devices, as shown in Figure 6. With just a one-centimeter square device exposed to constant 1000 lux illumination, enough energy is produced to power autonomous sensors or actuators.

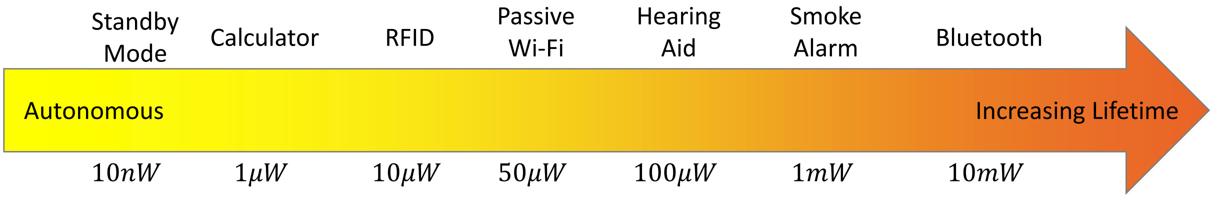

Figure 6: Average power consumption of different IoT devices and communication protocols. Data obtained from references [61], [87], [88], [89], [90].

As the demand for self-sustaining, energy-efficient technologies grows, OPVs will likely play an important role in reducing the environmental footprint of IoT systems while contributing to a more sustainable energy landscape. Moving forward, continued research and development in OPV materials and device architectures will be key to unlocking their full potential and driving further commercialization.

I.3. PV devices as OWC receivers

In optical communications systems, the signal or data to be transmitted is directly converted into optical power using a technique called Intensity Modulation (IM), typically implemented through optoelectronic devices such as LEDs or Laser Diodes (LD). In fact, the signal is superimposed onto a constant DC illumination level to avoid any potential dimming effects. As the light propagates, the optical data is detected and converted back into electrical signal by photosensitive devices known as photodetectors, which operate based on the photoelectric effect, as described in Einstein's theory [91]. Classical approaches employ Photodiodes (PD) as photodetectors, known for their high responsivity, fast response times, low dark-current noise and good linearity. For optimal performance, PDs function either in photovoltaic mode (short-circuit condition) or photoconductive mode (reverse-biased). After charge generation, a Transimpedance Amplifier (TIA) is usually employed to convert the provided photocurrent into readable voltage for further signal processing, as photodiodes alone do not provide sufficient voltage levels under these conditions [92]. In this process, the constant component of the electrical signal, derived from the DC illumination level, is filtered out, allowing only the variations of the optical power to be recovered. More detailed properties and functionalities of PDs and TIAs will be elaborated in subsequent chapters.

Although widely used in optical communications, this approach presents some minor inconveniences, including the requirement of an external power for the TIA [93], the introduction of additional noise sources [94], bandwidth constraints linked to the amplifier front-end [95] and potential instability due to the feedback network [96]. These drawbacks, though manageable in many systems, bring significant challenges in IoT embedded applications. In particular, the added complexity and power requirements can be problematic in low-power IoT systems where energy efficiency is a critical factor. The instability issues associated with the TIA feedback impedance can further complicate design and deployment. As IoT devices often prioritize low power consumption and reliability, addressing these concerns is crucial to ensuring smooth operation in embedded systems.

In light of this scenario, recent works have explored the dual functionality of PV devices as OWC receivers. These devices can simultaneously perform two key roles. First, the DC component of the electrical signal, which is typically filtered out for communication purposes, can instead be converted into electrical energy, which can thus be stored or dispatched thanks to an energy management unit to power various indoor IoT nodes. Second, the AC component, which represents fluctuations in optical power, is extracted and converted into a readable voltage for data decoding and communication. This emerging field, often called simultaneous lightwave information and power transfer, not only maximizes energy efficiency by utilizing ambient light but also enables self-powered communication systems, particularly well-suited for IoT applications in energy-constrained environments. Figure 7 shows a simple illustration of the SLIPT concept. In fact, even before the SLIPT term was defined, the concept itself was already studied.

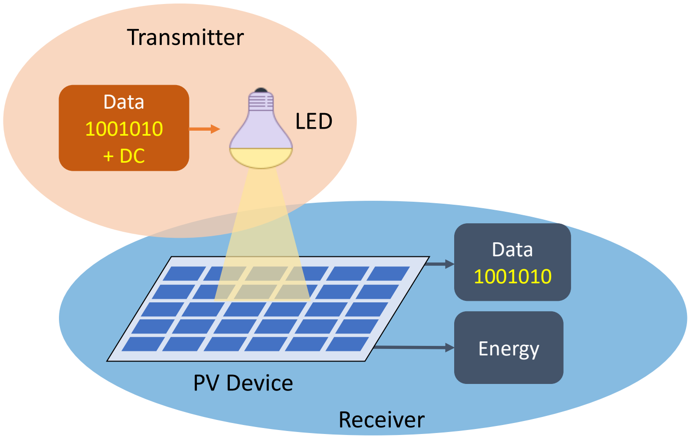

Figure 7: SLIPT concept using a PV device as OWC receiver for data reception and energy harvesting.

Source: Modified with permission from reference [97].

An in-depth analysis of the SLIPT context is proposed in Chapter II, reviewing key works and summarizing contributions across various topics, including reception circuits designed for PV devices, the impact of illumination on system performance, and the best EH and communication outcomes under different conditions. Given the emerging nature of the field, it lacks contributing papers specifically addressing SLIPT with VLC and OPVs. As a result, the analysis in Chapter II covers experiments involving any PV technology within an OWC scenario, extending beyond indoor or IoT-specific applications.

I.4. Thesis context

This thesis was proposed as part of the French regional project “IoT-PV”, formally entitled “*Photorécepteurs photovoltaïques imprimables pour l’usine du futur et l’Internet des Objets: vers la récupération d’énergie et les communications optiques sans fils*”, funded by the Nouvelle Aquitaine region (grant number AAPR2021A-2020-12033410) and the French “*Ministère de l’Enseignement Supérieur et de la Recherche*”. The research is conducted by two groups from the XLIM (UMR 7252) research institute: “*Electronique Imprimée pour Télécom et Énergie*” (ELITE) and “*Systèmes et Réseaux de Communications Optiques et Radio*” (SYCOMOR).

The project is further supported by CISTEME (*Centre d'Ingénierie des Systèmes en Télécommunications en Electromagnétisme et Electronique*), a multisite French Technologic Resources Centre (CRT) that enhances innovative research and facilitates the industrial deployment of such developments. In recent years, CISTEME has increased its involvement in OWC works, developing new competencies and raising the overall quality of projects like this one, as demonstrated by recent studies [55], [56]. The current thesis is also funded by *Université de Limoges*, with financial support attributed from the from CASI (*Comité d'Animation Scientifique Interdisciplinaire*) board at XLIM. The experimental work was mainly performed within the PLATINOM platform (www.unilim.fr\platinom), supported by the European Regional development foundation and the French government with the Nouvelle Aquitaine region (FEDER-PILIM 2015-2020).

This thesis also marked the beginning of a collaboration between the XLIM laboratory and the French company Dracula Technologies (www.dracula-technologies.com). Specializing in printed OPV technologies for low-power IoT devices, Dracula Technologies is rapidly establishing itself within the European PV ecosystem. All experiments required the use of encapsulated OPVs to ensure long-term stability, an area of expertise for Dracula Technologies. Their devices, printed on flexible substrates, offer new possibilities for exploring OPVs within the SLIPT framework. Although the ELITE team is proficient in fabricating and characterizing 3rd generation of PV devices, printing flexible and stabilized devices is a complex and labor-intensive process. This challenge led to the decision to collaborate with Dracula Technologies.

I.5. Thesis objectives

The thesis aims to analyse the SLIPT framework in the IoT context. Therefore, we have chosen to employ a flexible OPV for our studies, given the reasons provided above. Finally, we aim to characterize and evaluate this particular flexible OPV, developed by Dracula Technologies, for simultaneous energy harvesting and data reception. This primary objective is broken down into three specific tasks that demand focused attention, including:

- Characterization of the OPV device for both energy harvesting through static measurements and communication performance through dynamic analysis, described in Chapter III.
- Development of a new OPV model employed for indoor scenarios, simulating the optical channel properties when the OPV is used as a receiver, described in Chapter IV.
- Design and adaptation of a VLC test bench specifically suited for PV devices as receivers, with a focus on the SLIPT context, described in Chapter V.

I.5.1. Our contribution to the current state-of-the-art

In Chapter II, an in-depth analysis of the state-of-the-art is realized, highlighting some of the most significant works while also identifying gaps in the current literature. The primary contributions of this thesis to the scientific community are as follows:

- Our characterization methods, particularly the dynamic analysis, follow a logical and systematic approach, assessing multiple parameters in IoT scenarios that could influence OPV performance in both EH and data reception. These parameters include the solar cell operating point, illumination conditions, and device flexibility.

- For the first time, we conduct an indoor simulation using a Monte-Carlo Ray Tracing (MCRT) software with an OPV as an optical receiver, supported by experimental validation. This allows us to assess various EH and communication parameters while considering elements in IoT scenarios that may impact system performance, such as device curvature. The indoor simulation tool is particularly valuable for multiple applications, as previously demonstrated in SYCOMOR studies [98].
- A VLC experimental bench, already established within the SYCOMOR team and based on Universal Software Radio Peripherals (USRPs), has been enhanced and adapted for OPV receivers. In this setup, we conduct communication and energy harvesting experiments accounting for various SLIPT parameters, such as the solar cell operating point and illumination conditions.

I.6. Chapter conclusion

Chapter I provided a concise introduction to the context of this thesis, establishing the foundations for the in-depth analysis given in the following sections. It has examined the key motivations for VLC as a transformative technology, highlighting its benefits, such as spectrum availability, security, and applicability in environments sensitive to radio-frequency interference. The discussion also addressed the growing demands of the IoT, which necessitate innovative and sustainable solutions for energy harvesting and communication.

A detailed overview of OPVs as potential candidates for indoor energy harvesting further complemented this context. By exploring their unique material properties, such as tunability and high absorption efficiency under low illumination, the chapter established their relevance in addressing the challenges of IoT-powered environments. Additionally, the dual functionality of PV devices as OWC receivers was introduced, preparing the ground for SLIPT applications.

This introductory discussion naturally leads into Chapter II, which explores the integration of VLC, OPVs, and SLIPT in greater detail. While the first chapter provided the broader context and motivation, the next chapter focuses on the technical characteristics, operational principles, and interconnections of these technologies. It extends the contextual basis described here to examine how these components can work together to meet the demands of modern communication and energy systems, particularly in IoT and indoor applications.

Chapter II

VLC and OPVs: A Unified Approach to Energy Harvesting and Data Reception

Summary

Chapter II. VLC and OPVs: A Unified Approach to Data Reception and Energy Harvesting

This chapter explores the essential aspects of the key technologies involved in this research. First, it provides a thorough explanation of indoor VLC, covering necessary equations and foundational concepts to understand how visible light can be used for data transmission, with a special attention to indoor environments. Next, we shift focus to OPVs, particularly their role in indoor energy harvesting, explaining their underlying principles, unique properties, and methods for evaluating their performance. Finally, the chapter explores the SLIPT concept, examining its application not only in VLC and OPVs but also in a broader context, addressing the limited research currently available on SLIPT within the specific domains of VLC and OPVs. This approach offers a well-rounded view of the SLIPT potential in optical communication without confining it to a single technology. In the current chapter, all necessary equations and foundations required for subsequent chapters are clearly exposed.

II.1. Indoor Visible Light Communication technical characteristics

An optical communication system relies on two essential components: an optical source for electric-to-optical conversion and an optical receiver for optical-to-electric conversion. The optical source produces a transmitted optical power that is directly proportional to the current flowing through it (intensity modulation). The optical receiver, in turn, generates free charges in response to the absorbed optical power (direct detection). Unlike traditional RF communication systems, which can modulate amplitude, frequency, or phase, OWC depends solely on the intensity of the instantaneous optical power. Consequently, the optical signal must remain positive, and all modulation schemes are designed around this requirement.

The baseband electrical signal $X(t)$ is directly converted into an optical signal $X_i(t)$ via an optical source. Different sources emit light with different properties, which will be described in later sections. Here, $X_i(t)$ represents the instantaneous transmitted optical power and must be non-negative. In some scenarios, the average transmitted optical power P_{avg} follows indoor lighting standards or safety requirements, particularly in infrared communication. Therefore, the peak allowed optical power P_{max} is related to P_{avg} as shown in Equation II-1.

$$P_{avg} = \lim_{T\to\infty} \frac{1}{T} \int_{-T/2}^{T/2} X_i(t)dt \leq P_{max} \qquad \text{II-1}$$

Following optical generation, light may pass through various conditioning systems such as filters, lenses, or diffusers, each serving to adjust its spectral properties, intensity, or directionality to suit specific communication needs. Filters, for instance, can narrow or modify the spectral range of the light, improving signal selectivity and helping to reduce interference from ambient light sources. Lenses or collimators, on the other hand, control the beam divergence, which can either focus the signal for direct Line-of-Sight (LOS) communication or spread it for diffuse, NLOS applications. Although these components optimize various aspects of the transmission, they will not be considered in the scope of our analysis.

After conditioning, the transmitted optical signal $X_i(t)$ propagates through the channel, where it undergoes transformations (represented mathematically as a convolution) according to the channel impulse response $h(t)$. The channel characteristics depend on factors such as the link type (LOS or NLOS), ambient light conditions, and environmental factors like air composition, dust, and humidity. Absorption, scattering, and transmittance within the medium are influenced by these factors and play critical roles in determining how much signal loss or delay occurs.

In conventional setups using a photodiode as the receiver, the incident optical power is directly converted into a current, which acts as the electrical signal for further processing. The ratio of incident optical power to output current is defined by the receiver responsivity R, a key parameter that will be thoroughly discussed in the following sections.

Finally, the signal experiences noise modelled as an Additive White Gaussian Noise (AWGN), represented as $n(t)$, which introduces random fluctuations in the baseband signal. The noise is primarily due to photodetector noise and other electronic components, as well as ambient light shot-noise, further discussed in subsequent sections. The final recovered electrical signal $Y(t)$ is then obtained. Figure 8 shows the block diagram of a complete VLC system, illustrating the stages from baseband electrical signal generation to optical transmission, channel propagation, and final optical-to-electrical conversion at the receiver.

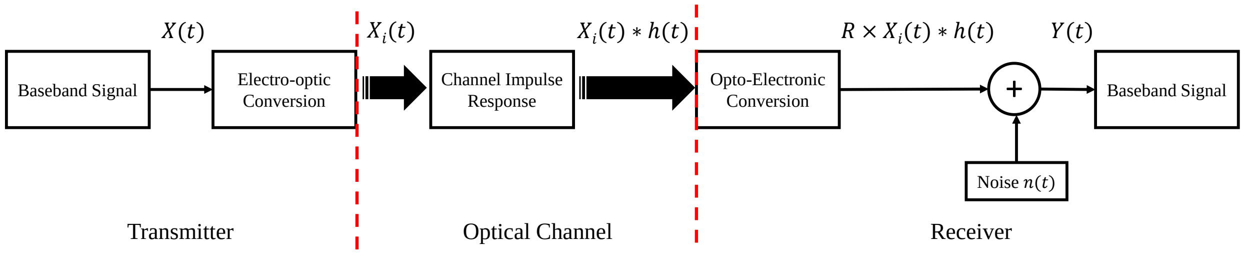

Figure 8: Block diagram of a VLC system.

At last, the output current $Y(t)$ is obtained as shown in Equation II-2.

$$Y(t) = RX_i(t) * h(t) + n(t) \quad \text{II-2}$$

In this section, we will examine the three main components of a VLC system: the transmitter, the optical channel, and the receiver. Thus, different noise sources and optical modulation schemes will also be analysed.

II.1.1. Photometry and radiometry

Before dwelling deeper into the VLC components, we should recall the reader about the basis of photometry and radiometry, highlighting their differences and connection. Radiometry and photometry are two distinct fields of optical measurement, each focused on different aspects of light.

Radiometry measures the physical properties of electromagnetic radiation. It involves parameters such as radiant flux (measured in watts, W), which represents the total energy emitted or received per unit time; irradiance (W/m²), describing the power received per unit area; and radiant intensity (W/sr), which combines the direction and spatial distribution of power.

Photometry, on the other hand, is concerned with the perception of light by the human eye, and it measures light based on the human visual response, particularly under photopic conditions where the eye is most sensitive to green light around 555 nm. Photometric units, therefore, account for the varying sensitivity of the human eye to different wavelengths. Key photometric parameters include luminous flux (measured in lumens, lm), which represents the perceived power of light, and illuminance (lm/m² or lux), which describes the perceived light power on a surface.

While radiometric units are objective and apply across the electromagnetic spectrum, photometric measurements are subjective and limited to visible light, adjusted through a luminosity function that mimics human vision (refer to Figure 9). Understanding these differences is essential in VLC and other optical communication systems, where photometric units often influence regulatory standards, while radiometric measures are used to design and evaluate the efficiency of the system and its performance.

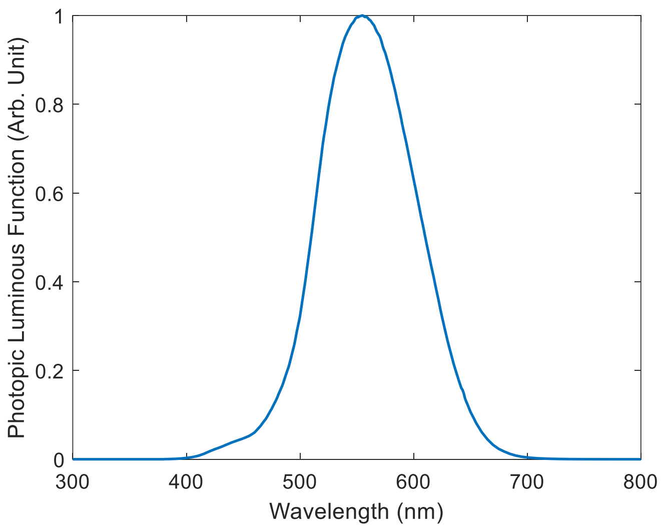

Figure 9: Photopic luminous function illustrating human eye sensitivity to different wavelengths.

The eye sensibility, described by the photopic luminous function $V(\lambda)$, can be approximated by a gaussian function, as shown in Equation II-3 [99]. Please note that, for $\lambda = 555\ nm$ (green spectral range), $V(555nm) = 1$.

$$V(\lambda) = 1.019e^{-285.4\left(\lambda\times10^{6}-0.559\right)^{2}} \quad \text{II-3}$$

Table 2 presents a summary of key radiometric and photometric quantities, including their names, symbols, mathematical definitions, and units.

Table 2: Comparison of radiometric and photometric quantities, including their symbols, definitions, and units.

	Quantity	Symbol	Definition	Unit
Radiometry	Radiant Energy	Q	$\int \Phi dt$	Joule (J)
	Radiant Flux / Radiant power	Φ, P	dQ/dt	Watt (W)
	Irradiance	E	$d\Phi/dA$	Watt per meter square (W/m^2)
	Radiant Intensity	I	$d\Phi/d\Omega$	Watt per steradian (W/sr)
Photometry	Luminous Energy	Q_V	$\int \Phi_V dt$	Lumen second ($lm.s$)
	Luminous Flux / Luminous Power	Φ_V, P_V	dQ_V/dt	Lumen (lm)
	Illuminance	E_V	$d\Phi_\mathrm{V}/dA$	Lux (lumen per meter square) (lx or lm/m^2)
	Luminous Intensity	I_V	$d\Phi_\mathrm{V}/d\Omega$	Candela (lumen per steradian) (cd or lm/sr)

The relation between a photometric unity and its corresponding photometric one is obtained with Equation II-4 [45].

$$\text{Photometric unit } (\lambda) = \text{radiometric unit } (\lambda) \times 683 \times V(\lambda) \qquad \text{II-4}$$

In this context, it becomes evident that 1 W of monochromatic green light produces 683 lumens, while 1 W of light at other wavelengths generates less luminous flux. It is crucial for the reader to understand this distinction between the light spectrum and its corresponding radiant flux value. For instance, stating an illumination level of 1000 lux without specifying the optical spectrum provides no insight into the actual radiant power.

For white light scenarios, the optical power depends on each wavelength, and the total transmitted optical power P_t is defined as shown in Equation II-5, where λ is the wavelength,

$\Phi_t(\lambda)$ is the source Power Spectral Density (PSD) and the integral limits define the minimum and maximum wavelength of visible light.

$$P_t = \int_{380}^{780} \Phi_t(\lambda) d\lambda \qquad \text{II-5}$$

Note that, under VLC scenarios, P_t is equivalent to P_{avg} in Equation II-1, which must be limited due to safety requirements. Furthermore, the transmitted luminous flux P_{tV} can be obtained from the source luminous power spectral density $\Phi_{tV}(\lambda)$, as shown in Equation II-6.

$$P_{tV} = \int_{380}^{780} \Phi_{tV}(\lambda) d\lambda \qquad \text{II-6}$$

It is essential to understand that, with knowledge of the optical signal PSD, converting from radiometric to photometric units becomes straightforward, which involves multiplying the spectrum by the photopic luminous function, as shown in Equation II-4. To obtain the actual value of the quantity (such as P_t or P_{tV}), one should integrate across the entire visible spectrum.

II.1.2. Indoor lighting standards

Indoor VLC can serve a wide range of applications, from office spaces and medical facilities to industrial settings. In these environments, lighting conditions adhere to established standards, which specify ideal illuminance levels and colour temperature of white light for various uses. According to the European EN 12464-1 standard [100] typical indoor lighting setups maintain around 500 lux for general activities, while areas like reception desks can operate with lower levels, around 300 lux. However, tasks requiring high precision, such as medical examinations, demand higher illuminance, reaching up to 1000 lux. Furthermore, according to the International Organization for Standardization, the ideal illumination for workplaces lies between 300 and 1500 lux [101].

II.1.3. Optical sources

The most commonly used optical sources in VLC are LEDs and LDs, each with distinct properties that impact communication performance. LEDs are prevalent in indoor lighting due to their energy efficiency, long lifespan, and ability to emit visible light without excessive heat. Meanwhile, LDs, with their highly directional light and narrow spectral bandwidth, are often used in scenarios that demand high data rates and long-distance communication. The choice of optical source significantly influences key VLC parameters such as bandwidth and overall system efficiency.

LEDs are the preferred choice for many VLC applications, especially in indoor lighting and low-cost IoT systems, due to their widespread availability, low power consumption, and ability to serve dual purposes as both lighting and communication sources. LEDs are driven with IM, where the data is superimposed onto a constant DC component to avoid flicker, which could disrupt the lighting quality. However, one limitation of LEDs is their relatively low bandwidth, usually limited to a few MHz, which restricts the achievable data rates in VLC.

LDs, on the other hand, offer significantly higher bandwidths, often exceeding several GHz, making them suitable for high-speed data transmission applications. LDs emit highly coherent light with a narrow beam divergence, which allows for greater focus and higher Signal-to-Noise Ratio (SNR) over long distances compared to LEDs. This characteristic makes LDs particularly useful in point-to-point VLC applications where high data rates are essential, such as in Free-Space Optics (FSO) communication systems. However, the narrow beam also means LDs are less suited for general illumination purposes and may require precise alignment between the transmitter and receiver. Additionally, LDs can pose eye safety concerns, especially at higher power levels, which limits their applicability in environments where human exposure is a factor. Therefore, in this thesis, the focus is solely on standard inorganic white LEDs.

II.1.3.1. White LED

White LEDs function similarly to standard diodes, with a structure based on a p-n junction formed from doped semiconductor materials. In the linear operating region, the emitted optical power is directly proportional to the driving current flowing through the device. However, outside this linear region, LEDs exhibit non-linear behaviour, which can lead to distortions and undesirable effects when driven improperly [102]. As an example, Figure 10 shows the non-linear behaviour of a commercial white LED (LE CW E2B from OSRAM). To prevent these distortions, the transmitter should operate within the linear region and maintain a low signal amplitude to avoid flickering effects.

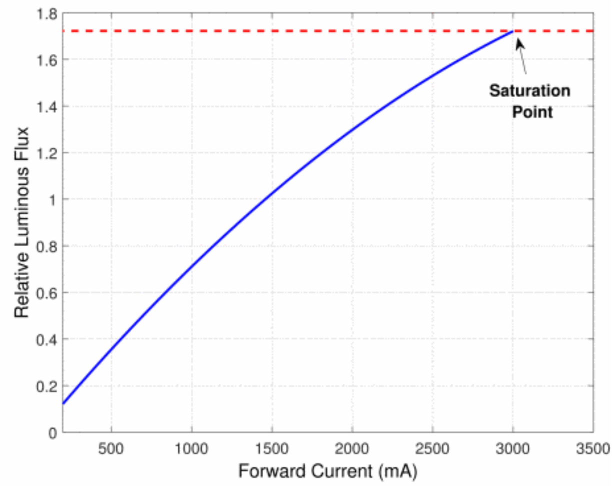

Figure 10: Relationship between forward current and relative luminous flux of a commercial white LED (LE CW E2B).

Source: Reproduced with permission from reference [102].

Similar to a standard inorganic diode, the p-n junction in a white LED creates an internal junction capacitance, which limits the response time and decrease the device bandwidth. This response also depends on the charge carrier lifetime, resulting in a 1st order low-pass filter behaviour characterized by a RC time constant τ. The -3 dB cutoff frequency f_c can then be computed as shown Equation II-7 [45].

$$f_c = \frac{1}{2\pi RC} = \frac{1}{2\pi\tau} \quad \text{II-7}$$

The low-pass filter effect results in a slower response time for the LED. Therefore, the cutoff frequency, or bandwidth B, can be computed based on the rise and fall times, denoted as τ_r and τ_f, respectively. These variables determine the time required to go from 10% to 90% of the maximum signal value (90% to 10% for τ_f). In first-order systems, these times can be derived from the time constant τ, since $\tau_r = 2.2\tau$ [103]. Thus:

$$f_c = B = \frac{\ln(9)}{2\pi\tau_r} \approx \frac{0.35}{\tau_r} \quad \text{II-8}$$

Similar to photovoltaic devices, optical sources based on semiconductors can be fabricated with different emissive materials, such as Organic LEDs (OLEDs) [104], or perovskite LEDs [105]. The choice of active layer material influences the emission spectrum, according to the considered optical bandgap; for instance, GaAs is used for infrared LEDs, while GaN is commonly used for blue LEDs. This thesis will focus exclusively on traditional inorganic LEDs, as non-inorganic materials are outside of its scope.

Currently, inorganic LEDs cannot directly generate white light, so alternative methods are used to achieve a broad emission spectrum. Two primary approaches are highlighted here. The first, known as Phosphor-Converted LED (pc-LED), involves a blue LED—typically made from GaN—combined with a layer of phosphor coating either on or around the LED chip. The phosphor absorbs part of the blue light and re-emits it at a longer wavelength, usually in the yellow range. The combination of blue and yellow light produces white light, with the colour temperature adjustable by varying the amount of phosphor. Additionally, pc-LEDs experience an intrinsic response time called phosphor decay—the time it takes for the phosphor layer to absorb and re-emit light—limiting their response speed. Figure 11.a provides a schematic of a pc-LED.

The second approach uses separate and distinct Red, Green, and Blue LEDs (RGB LEDs), which together generate white light (see Figure 11.b). In fact, these primary colours can be mixed to create any desired colour, including white, allowing more precise control over the emission spectrum compared to pc-LEDs. RGB LEDs can be individually tuned, offering a broader colour range with higher bandwidths than pc-LED [106].

Finally, Figure 11.c and Figure 11.d show the emission spectra of pc-LEDs and RGB LEDs, respectively. This factor is crucial, as all components in a VLC setup—including the optical channel and receiver—are influenced by the emission wavelength, with variations in spectra potentially affecting overall performance. Consequently, different white LED colour temperatures can also affect performance.

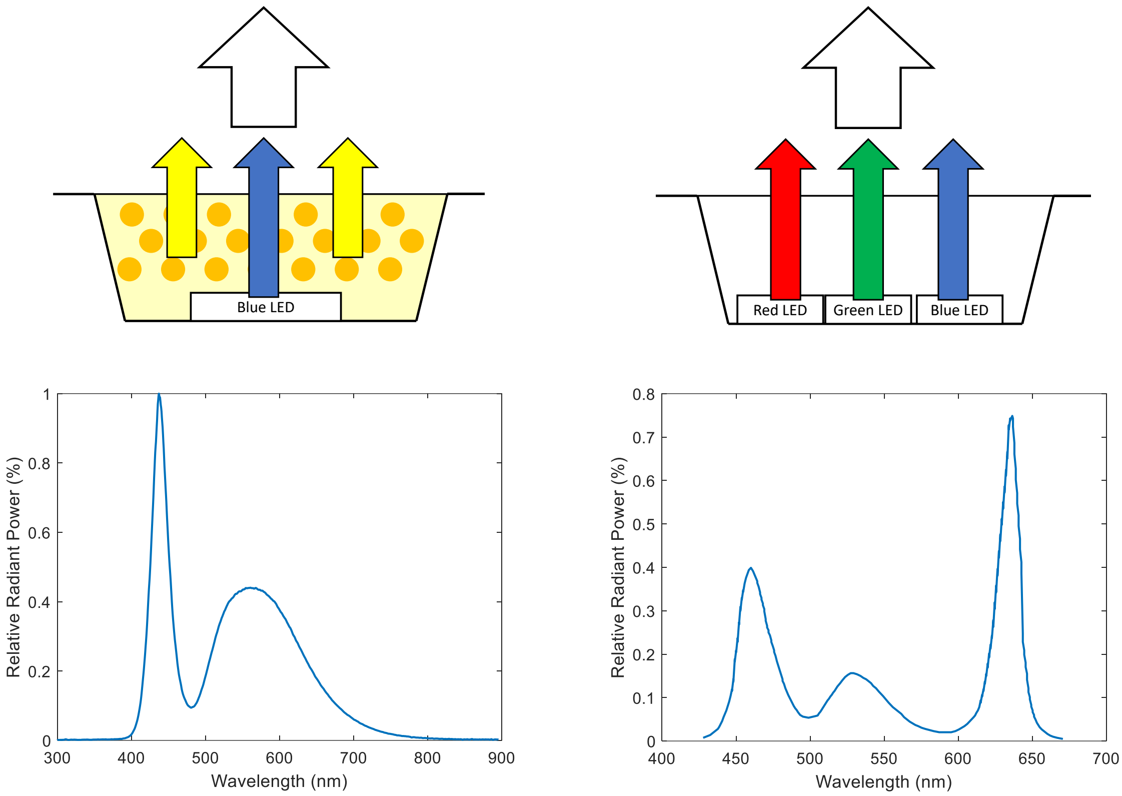

Figure 11: Comparison of white light generation methods in LEDs. (a) pc-LED structure. (b) RGB LED structure. (c) Emission spectrum $\Phi_t(\lambda)$ of pc-LEDs. (d) Emission spectrum $\Phi_t(\lambda)$ of RGB LEDs.

II.1.3.2. Radiation pattern, radiant intensity and optical power

In this section, we will examine key parameters of LEDs, focusing specifically on the spatial distribution of the optical power P_t. This analysis will use only certain radiometric quantities, disregarding spectral behaviour and photometric quantities without any loss of generality. This approach remains broad and applies to all wavelengths, without being limited to a specific one.

In the current analysis, we consider LEDs with a Lambertian emission pattern This pattern features azimuthal symmetry, where the radiant intensity I depends solely on the polar angle θ, such that $I = f(\theta)$. The maximum intensity, denoted I_0 is obtained at $\theta = 0°$. Figure 12 provides a schematic representation of LED emission, highlighting the maximum intensity I_0 and the spherical variables (r, θ, φ), which are essential for various analyses in this thesis.

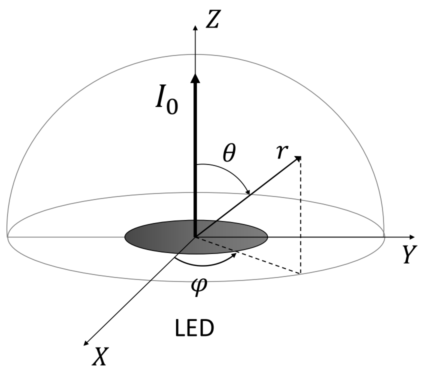

Figure 12: Spatial distribution of LED light emission.

The radiant intensity of Lambertian LEDs is described by Equation II-9, where m_1 represents the source directivity. m_1 is described by Equation II-10, where $\theta_{1/2}$ is the half-power angle of the LED, indicating the polar angle at which the intensity reaches $I_0/2$ [107].

$$I(\theta) = I_0 \cos^{m_1}(\theta) \tag{II-9}$$

$$m_1 = -\frac{\ln(2)}{\ln(\cos\theta_{1/2})} \tag{II-10}$$

Note that smaller values of $\theta_{1/2}$ increases the directivity of the device. These parameters indicate the capability of the LED to concentrate the transmitted optical power P_t in a given spatial orientation. The relationship between radiant intensity and optical power is described in Table 2. Consequently, P_t can be obtained as described in Equation II-11, where Ω represents the solid angle, with the integral limits covering the full solid angle over which the LED emits light, denoted as Ω_{max}.

$$P_t = \int_{\Omega} I(\Omega) d\Omega = \int_0^{\Omega_{max}} I(\Omega) d\Omega \tag{II-11}$$

In spherical coordinates, the differential solid angle $d\Omega$ can be expressed in terms of the azimuth and polar angles differentials, as shown in Equation II-12 (its demonstration is out of the scope of this thesis) [108].

$$d\Omega = \sin(\theta)\, d\theta d\varphi \tag{II-12}$$

Thus, the transmitted optical power can be written as:

$$P_t = \int_{\theta}\int_{\varphi} I(\theta,\varphi) \sin\theta \, d\varphi \, d\theta$$

$$P_t = \int_{\theta}\int_{\varphi} I_0 \cos^{m_1}(\theta) \sin\theta \, d\varphi \, d\theta$$

The LED emits light across all values of the azimuth angle φ, but only covers solid angles for polar angles θ inferior to $\pi/2$, as it does not emit optical power in the backward direction. So, by solving the integral, P_t is determined as a function of I_0, as shown in Equation II-13.

$$P_t = \int_0^{\pi/2}\int_0^{2\pi} I_0 \cos^{m_1}(\theta) \sin\theta \, d\varphi \, d\theta$$

$$P_t = \frac{2\pi}{m_1 + 1} I_0 \tag{II-13}$$

Finally, the radiant intensity is expressed in terms of transmitted optical power P_t, as shown in Equation II-14.

$$I(\theta) = P_t \frac{m_1 + 1}{2\pi} \cos^{m_1}(\theta) \qquad \text{II-14}$$

Equation II-14 is important for future analysis on different VLC link scenarios. Figure 13 illustrates how the radiant intensity $I(\theta)$ of a LED varies with the polar angle for different directivities m_1 (in this scenario, the transmitted power is normalized). Please note that higher m_1 results in greater I_0 values, indicating that, the LED emits light more narrowly around the 0° polar angle, concentrating the optical power in a forward direction. These characteristics are important for VLC applications, as the directivity factor influences the coverage area and intensity distribution, allowing tailored light propagation for specific scenarios or environments.

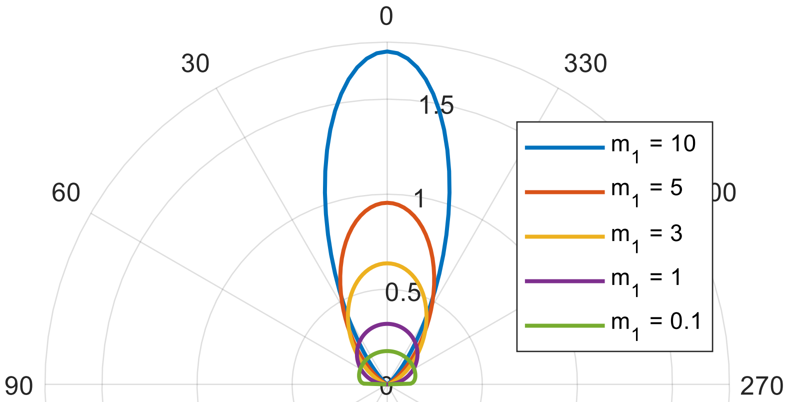

Figure 13: Radiant intensity of an LED as a function of the polar angle for various m_1 values.

II.1.4. Optical receivers

VLC receivers play a crucial role in converting transmitted optical signals back into electrical signals that can be processed to retrieve information. Classical approaches typically employ photodiodes as receivers, operating in either photovoltaic (zero bias) or photoconductive (reverse bias) modes for fast and linear responses. In these modes, the generated charge carriers are directly proportional to the received optical power and are extracted as short-circuit current, which is also proportional to the optical signal strength. However, as we will explore in the following sections, this relationship does not always hold under different operating conditions or with other types of PV devices.

Different photodetectors operate uniquely depending on the application context, and each receiver type can be made from various materials, each altering the underlying physics of the device. Nevertheless, we will focus on the fundamental principles of each receiver type, independent of the specific material technology. For example, material choice affects characteristics such as charge carrier diffusion time and response efficiency. Figure 14 illustrates the relative response of photodetectors made from various inorganic materials, excluding other technologies without affecting the general understanding. These differences are essential when selecting device materials for specific applications; for instance, VLC applications typically utilize Si or GaAs-based devices.

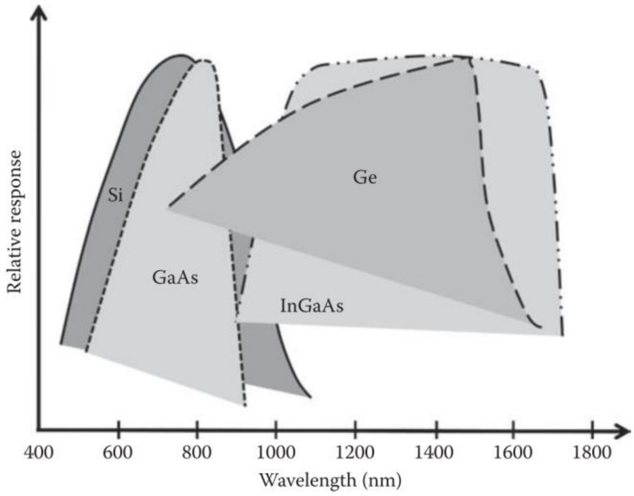

Figure 14: Relative response of photodetectors for different materials.

Source: Reproduced with permission from reference [91].

In OWC systems, multipath distortion occurs when the transmitted light signal reflects off surfaces in the environment, such as walls, ceilings, and objects, before reaching the receiver. This can cause multiple copies of the signal to arrive at slightly different times, creating interference patterns that can degrade the received signal quality. However, in OWC, multipath fading behaves differently compared to traditional radio RF systems, primarily due to the very short wavelength of visible or infrared light and the larger photodetector area typically used in optical receivers. Consequently, it captures multiple incoming paths simultaneously and averages out the variation caused by them. This reduces the impact of multipath fading on the received signal and simplifies the design of optical receivers [45].

Before proceeding, it is important to define the *Field-of-View* (FOV) of photoreceivers, which represents the maximum incident angle at which the device can effectively detect light. For standard non-encapsulated surfaces, the FOV is typically set to $90°$, meaning the device cannot detect light arriving from behind. Various receiver designs utilize optical structures, such as non-imaging concentrators, to modify this parameter. However, for the purpose of further analysis, we will assume that such structures are not used.

The ratio between the number of electrons leaving the device and the number of input photons is called External Quantum Efficiency (EQE), denoted as η_{qe}. It is defined as shown in Equation II-15 [91], where R_{ref} is the reflection coefficient at the air-semiconductor interface, ξ is the part of the generated charge carriers that actually contributes to the output current, α is the absorption coefficient and d is the inner distance where the optical power is absorbed.

$$\eta_{qe} = \frac{Electrons\ out}{Photons\ input}$$

$$\eta_{qe} = (1 - R_{ref})\xi(1 - e^{-\alpha d}) \qquad \text{II-15}$$

Several factors impact the EQE of photosensitive devices, such as internal current losses (affecting ξ), active layer thickness (affecting d), and the angle of incidence of incoming optical power (affecting R_{ref}). Indeed, increasing the angle of incidence can enhance the reflection coefficient between the device layers.

Thus, the output electrical current I provided by the photodetector, when an average monochromatic optical power P_r arrives on its surface, is described by Equation II-16, where q represents the electronic charge, λ the wavelength of the optical signal, h the Planck constant and c is the speed of light in a vacuum [109]. The term R, known as the receiver *responsivity* (in A/W) plays a crucial role and defining this relationship will be essential for discussions in subsequent chapters. Notably, the responsivity R varies with the angle of incidence Ψ of the optical power P_r; hence, we express it as $R(\Psi)$, to highlight this dependence. Figure 15 shows an example of a receiving optical power P_r arriving with an incident angle Ψ, generating an output current I.

$$I = \frac{\eta_{eq} q \lambda}{hc} P_r = R(\Psi) P_r \tag{II-16}$$

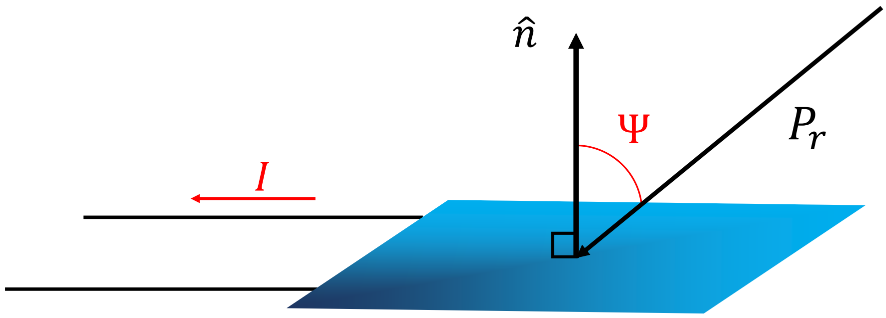

Figure 15: Incident optical power P_r forming an incident angle Ψ with the photodetector normal $\hat{n}$, generating an output current I.

This relationship holds for any wavelength λ. In a broad-spectrum scenario, such as white light (illustrated in Figure 11.c), the optical power is spread across multiple wavelengths. Consequently, each λ contributes to a small portion to the total current $I(\lambda)$, which depends on both spectral responsivity $R(\lambda, \Psi)$ and received power spectral density $\Phi_r(\lambda)$, as shown in Equation II-17.

$$I(\lambda) = R(\lambda, \Psi) \Phi_r(\lambda) \tag{II-17}$$

The total output current I generated by a photodetector is then obtained by integrating $I(\lambda)$ over all contributing wavelengths (for VLC, the visible spectrum – 380 nm up to 780 nm), as shown in Equation II-18.

$$I = \int_{\lambda} I(\lambda) d\lambda \tag{II-18}$$

In fact, the responsivity $R(\lambda, \Psi)$ is influenced by both the incident angle Ψ and the wavelength λ meaning that variations in incident angle can lead to changes in spectral responsivity [110], [111]. However, for cases where spectrum distortion due to incident angle is minimal, these variables can be treated as independent [112]. This assumption will be confirmed in the frame of this work, as discussed it in the next sections. Consequently, the overall responsivity is expressed in terms of the spectral responsivity R_λ and angular responsivity R_Ψ, as shown Equation II-19, with the indices λ and Ψ indicating a dependency solely on the wavelength and incident angle, respectively. Here, the function R_Ψ is relative and normalized, with maximum value equals 1.

$$R(\lambda, \Psi) = R_\lambda(\lambda) R_\Psi(\Psi) \qquad \text{II-19}$$

In widely used Si-based photodiodes, the peak spectral responsivity is typically achieved at normal incidence ($\Psi = 0°$). Similarly, $R_\lambda(\lambda)$ values are usually measured under this condition and are commonly provided in datasheets. Additionally, these measurements are usually conducted under short-circuit conditions, so the output current is in fact the short-circuit current. Therefore, we shall note it as I_{sc}. Furthermore, the short-circuit current varies based on the angle of incidence of the optical power, as shown in Equation II-20.

$$I_{sc} = R_\Psi(\Psi) \int_\lambda R_\lambda(\lambda) \Phi_r(\lambda) d\lambda \qquad \text{II-20}$$

For receivers that exhibit no specific response to the incident angle, meaning $R_\Psi(\Psi) = 1$, Equation II-20 simplifies to focus solely on spectral analysis. A clear example of the $R_\Psi(\Psi)$ function is provided in the datasheet of the BPV10NF photodiode, fabricated by Vishay Semiconductors, as shown in Figure 16.

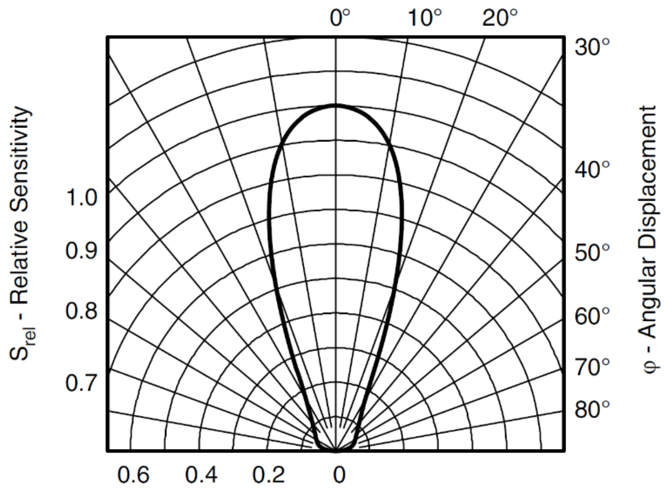

Figure 16: Relative responsivity $R_\Psi(\Psi)$ in function of the incident angle Ψ of the BPV10NF photodiode.

Source: BPV10NF datasheet.

II.1.4.1. Photodiodes

Unlike PV devices, which are primarily optimized for energy conversion, photodiodes are designed for rapid response and sensitivity to low-intensity optical signals. The key distinction lies in their fabrication: photodiodes generally use lower doping concentrations to enhance speed and maintain linearity under varying light intensities [113]. Conversely, PV devices are engineered with thicker active layers and higher doping levels to maximize light absorption and energy conversion efficiency [114].

PIN photodiode

Positive-Intrinsic-Negative (PIN) photodiodes are the most classically used photodetector for OWC. In typical inorganic structures, it typically consists of a p-n junction, where an intrinsic (i-type) layer may also be present, forming a p-i-n structure for enhanced sensitivity and faster response. When photons from an external light source strike the photodiode, they create electron-hole pairs within the junction. These carriers are separated by the electric field at the junction, leading to a flow of current proportional to the incident light intensity. As passive devices, their responsivity $R_{\lambda}(\lambda)$ remains inferior to 1.

These photodiodes are projected to explore fast responses while maintaining a good quantum efficiency and responsivity within the desired spectrum. They are designed to operate under significant reverse bias, which enhances linearity and quickens their response time. Figure 17 shows an example of I(V) curves of a traditional Si-based photodiode under varying illumination. Here, the device operates under reverse bias, and the linearity can be seen at this region. Like LEDs, photodiodes exhibit inherent geometric capacitance due to their depletion region, introducing a low-pass filter effect with an RC time constant. However, their small active area minimizes junction capacitance, further supporting high-speed operation.

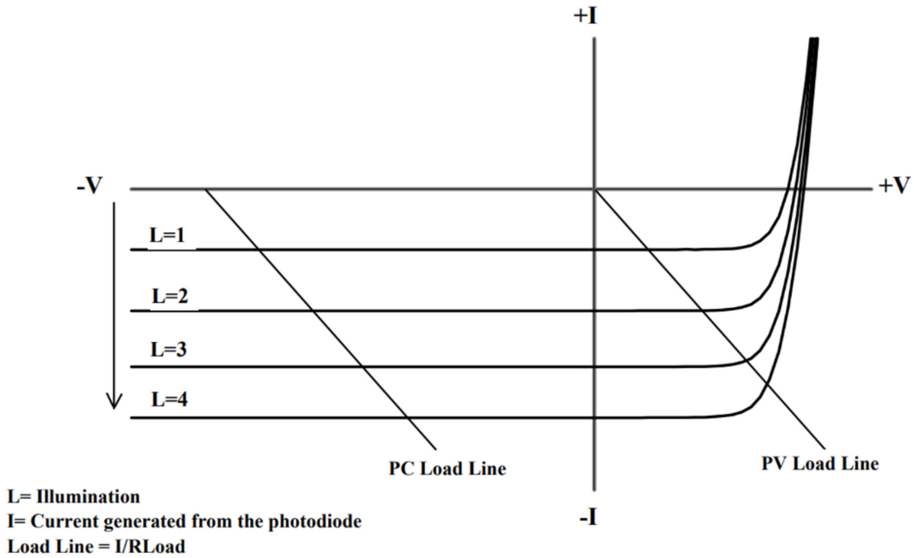

Figure 17: Example of I(V) curves for a traditional photodiode under varying illumination levels.

Source: Reproduced with permission from reference [115].

APD

Avalanche Photodiodes (APDs) are advanced photodetectors designed to achieve current gain through repeated electron ionization. By applying a high electric field across the depletion region, APDs amplify the signal as incoming photons generate electron-hole pairs, which are then accelerated, leading to impact ionization. This cascading effect multiplies the carriers, significantly boosting the signal and enhancing the device responsivity, often reaching gain values between 50 and 300 [116]. However, this gain process also amplifies photogenerated noise and introduces a slightly slower response time due to the avalanche multiplication mechanism.

In classical approaches, the small-signal model of a PD (either PIN or APD) is described as a current source, representing the photogenerated current I_{ph} - proportional to the incident optical power - in parallel with a shunt capacitance C_{sh} (accounting for the device diffuse and junction capacitances) and a shunt resistance R_{sh} (modelling recombination losses and the dynamic resistance of the device). Additionally, a series resistance R_s represents the voltage loss due to internal material resistance the layers interfaces. However, the series resistance is often ignored in classical scenarios [117], [118]. The model is shown in Figure 18.

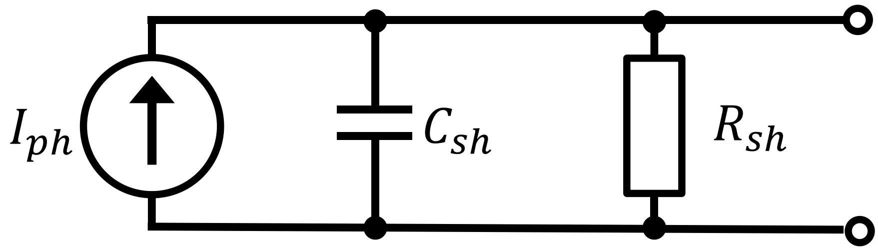

Figure 18: Small signal model of a PD.

II.1.4.2. PV devices

Compared to photodiodes, PV devices were not primarily intended for detecting low fluctuations of optical signals. Instead, they were developed to obtain high PCE and output power under various lighting scenarios, such as indoor and outdoor. Nonetheless, as described previously, recent researches have demonstrated the interesting communication performance of PV cells, paving the way for newer and exciting application possibilities.

These devices are mostly designed to operate in forward bias mode, normally at the Maximum Power Point (MPP), providing an output power to the external circuit, described by the product of the output voltage by the output current ($V \times I$). In this operating mode, different constraints are seen for communication performances, behavior that will be described later in the current chapter. Finally, the equivalent electrical model of PV devices is similar to the PD model, but they operate mostly at the 4th quadrant, providing power to an external circuit (as it can be seen in Figure 17).

Compared to conventional PDs, PV devices (which are mostly modules based on series-connected PV cells) generate a higher output voltage under the same illumination conditions. This feature enables alternative receiver topologies that do not require active circuits for current-to-voltage conversion (such as TIAs) or additional amplification. Consequently, with an appropriate receiver design, it is possible to recover energy from the DC component of the optical signal. Although PDs can also be used for this purpose, their communication and EH performances would be significantly lower in forward bias conditions. Further sections will explore in details some interesting properties of PV devices.

II.1.4.3. Optical Cameras

Optical data can also be received using a Charge-Coupled Device (CDD) or Complementary Metal-Oxide Semiconductor (CMOS) sensor, a technique known as Optical Camera Communication (OCC) [119]. In this process, each photodiode within the sensor converts incoming photons into electrical charges corresponding to the light intensity. The sensor samples these variations spatially across its pixel array and temporally at a rate determined by the camera frame rate. The electrical signals generated by the pixels are then read, amplified, and digitized to create images that reflect the modulated light intensities. By analysing the sequences of captured images, variations in light intensity are extracted and decoded into digital information. The achievable data rate is primarily constrained by the camera frame rate, typically ranging from a few b/s to several kb/s for standard cameras operating at 30–60 frames per second.

II.1.4.4. Front end circuit of classical schemes: the TIA

For optimal operation in OWC, conventional photodiodes require an external active circuit known as a TIA. This circuit serves two critical functions at the receiver: it converts the photodiode output current into a readable voltage signal while maintaining the necessary bias voltage for the photodetector. The TIA consists of an Operational Amplifier (OP-AMP) with a feedback network comprising a resistor R_f and a capacitor C_f in parallel, as illustrated in Figure 19. The PD bias is provided by the voltage source V_{cc}; if $V_{cc} > 0$, the device is reversely polarized.

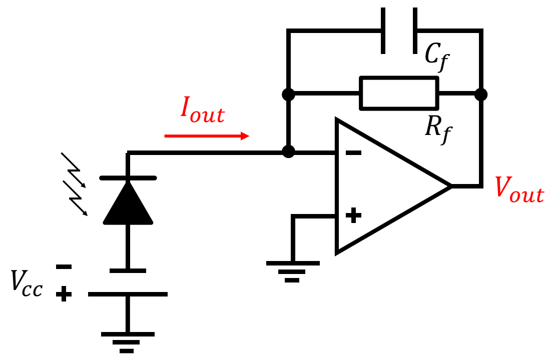

Figure 19: Schematic of a TIA circuit associated to a photodiode.

The DC component of the optical power $I_{out_{DC}}$ passes through the feedback network and is amplified by the resistor R_f, resulting in a DC voltage $V_{out_{DC}} = -I_{out_{DC}} \times R_f$. In fact, the TIA introduces different effects on the system, such as instability, which is mitigated by using the feedback capacitor C_f [96]. For the AC analysis, the small signal model is employed, as shown in Figure 18. For simplicity, the series resistance is ignored and V_{cc} is set to $0\,V$. Considering the OP-AMP internal capacitances, including the common-mode input capacitance C_{cm} and differential-mode capacitance C_{diff} [120], the total system capacitance C_{in} at the TIA input is described by Equation II-21.

$$C_{in} = C_{sh} + C_{diff} + C_{cm} \qquad \text{II-21}$$

Note that I_{out} is not the actual generated photocurrent I_{ph}, as shown in Figure 18, since it accounts for internal losses. Taking into account both diagrams and the capacitance C_{in}, the transfer function can be obtained with $V_{out}(s)$ as output and $I_{ph}(s)$ as input, as shown in Equation II-22. In this equation, f_0 and A_0 are the open loop cut-off frequency and gain of the

OP-AMP respectively, and s is the Laplace variable, used for system performance analysis [121].

$$\frac{V_{out}(s)}{I_{ph}(s)} = -\left[\frac{C_{in}+C_f}{2\pi f_0 A_0}s^2 + \left(C_f + \frac{C_f + C_{in}}{A_0} + \frac{1}{2\pi f_0 A_0 R_f}\right)s + \frac{A_0+1}{R_f A_0}\right]^{-1} \qquad \text{II-22}$$

A more detailed analysis of this equation could reveal how each component influences system performance; however, this is beyond the scope of the current work. The feedback capacitor C_f is designed to counteract the capacitances of both the photodiode and the amplifier, restoring system stability. The feedback resistor R_f, while increasing signal amplification, also reduces the system -3 dB bandwidth [122]. For weaker optical signals, higher R_f values are required, which further limits the system frequency response. Different methods can be employed to increase the receiver bandwidth without compromising its stability [123], [124].

As discussed in later chapters, TIAs can also be applied to PV devices, enabling similar operating principles.

II.1.5. Optical channel modelling

As mathematically described in Equation II-2, the channel impulse response $h(t)$ is essential to obtain the output signal $Y(t)$ (typically the short-circuit current) in OWC systems. The characteristics of this response are influenced by various factors, particularly the type of link between the transmitter and receiver, which can be categorized as LOS, NLOS, or hybrid, each offering unique properties and suited to different applications.

In LOS communication, the transmitter and receiver are positioned so that they have a direct, unobstructed path between them. This setup allows the optical signal to travel in a straight line, leading to minimal signal loss and low latency. LOS is highly desirable for applications that require high-speed data transmission and low error rates, as it maximizes the received signal strength and reduces multipath interference. Nonetheless, LOS is highly sensitive to obstacles, even that minor obstruction can completely block the signal. This mode is mostly employed in non-dynamic indoor scenarios, as well as in FSO links in outdoor environments [125].

In NLOS communication, the transmitter and receiver do not have a direct path, and the signal reaches the receiver after reflecting off surfaces like walls, ceilings, or objects. NLOS mode allows for greater flexibility in receiver positioning and can be useful in scenarios where a direct path is not feasible or practical. However, NLOS propagation introduces signal attenuation and multipath distortion, which can degrade the signal quality and reduce maximum achievable data rates. NLOS is commonly used in applications requiring wider coverage, like indoor navigation [126].

Many OWC systems operate in a hybrid mode where both LOS and NLOS paths are present. In this case, the LOS path provides a strong, primary signal, while the NLOS components provide additional robustness against blockages. The mixed mode can enhance system reliability and coverage but requires careful management of multipath interference to avoid degradation in signal quality [127]. Figure 20 illustrates the three main propagation modes in OWC: (a) LOS mode, where the transmitter and receiver are directly aligned; (b)

NLOS mode, where the link relies solely on reflections as the transmitter and receiver are not aligned; and (c) Hybrid mode, where aligned transducers receive additional contributions from reflected optical power.

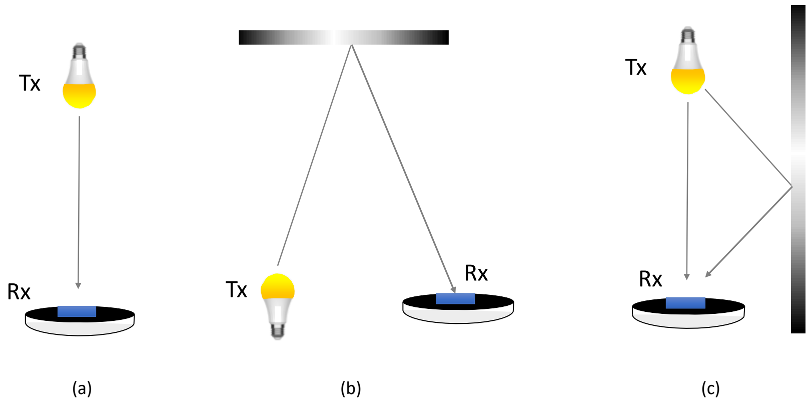

Figure 20: Different propagation modes in OWC: (a) LOS; (b) NLOS; (c) Hybrid.

In a first approach, for simplicity, let us analyse the channel characteristics assuming a single wavelength scenario, without loss of generality. Following this, we will expand the analysis to a broad-spectrum VLC application, applying the equations to each wavelength individually and considering the LED PSD. In our analysis, no optical filter or concentrator are employed.

II.1.5.1. Monochromatic link

In the most general scenario, where there is both a LOS and NLOS link between N transmitters and a single receiver, the channel impulse $h(t)$ consists of independent LOS and NLOS components. Additionally, each individual optical source n contributes to the overall impulse response independently [128], as shown in Equation II-23. Here, k represents the number of light reflections before arriving at the receiver. It is important to note that light may reflect multiple times before reaching the receiver; however, after a certain number of reflections, its optical power becomes sufficiently low and can be neglected. Thus, $h_n^{(0)}$ corresponds to the LOS component of the n-th optical source.

$$h(t) = \sum_{n=1}^{N} \left(h_n^{(0)}(t) + \sum_{k=1}^{\infty} h_n^{(k)}(t) \right) \qquad \text{II-23}$$

For simplicity in further analysis, only a single optical source (Simple-Input Simple-Output – SISO - scenario) will be examined, without loss of generality. Ultimately, each source contribution is independent of the others, so the overall effect can be determined by summing the contributions from each source. When the emitter transmits an instantaneous optical power $X_i(t)$, containing the desired signal with an average optical power P_t, this signal undergoes attenuation and distortion due to the channel $h(t)$. The received instantaneous optical signal becomes $X_i(t) * h(t)$, with an average optical power P_r (refer to Figure 8 for illustration). In fact, the average value of a time-domain variable corresponds to its zero-frequency component in the frequency domain. Utilizing the Fourier transform and convolution properties, the average received optical power P_r can be expressed as the product of the transmitted optical power P_t and the zero-frequency value of the channel frequency response $H(0)$, also called channel DC gain, as described in Equation II-24. Thus, $H(0)$ can be obtained as shown in Equation II-25.

$$P_r = P_t H(0) \tag{II-24}$$

$$H(0) = \int_{-\infty}^{\infty} h(t)dt = \int_{-\infty}^{\infty} h^{(0)}(t)dt + \int_{-\infty}^{\infty} \sum_{k=1}^{\infty} h^{(k)}(t)dt \tag{II-25}$$

Therefore, the channel DC gain can be obtained from both LOS and NLOS components, as shown in Equation II-26.

$$H(0) = H_{LOS} + H_{NLOS} \tag{II-26}$$

Finally, each component will be analysed independently.

II.1.5.1.1. LOS link

In LOS links, the channel impulse response $h^{(0)}(t)$ is described by a time-shifted impulse with amplitude H_{LOS} [91], which accounts for channel attenuation due to light dispersion. $h^{(0)}(t)$ is described by Equation II-27, where d denotes the distance between transmitter and receiver, Ψ the optical link incent angle, c is the speed of light in a vacuum and $\delta(.)$ is the Dirac function.

$$h^{(0)}(t) = \begin{cases} H_{LOS}\delta\left(t - \frac{d}{c}\right), & 0 \leq \Psi \leq \mathrm{FOV} \\ 0, & \text{Otherwise} \end{cases} \tag{II-27}$$

To determine the channel LOS attenuation, it is essential to revisit fundamental concepts in spherical geometry. Figure 21 illustrates the concept of a solid angle Ω, containing a flat surface A, with its normal vector $\hat{n}$ parallel to the distance vector $\hat{d}$, which connects the origin of the spherical coordinates to the centre of area A.

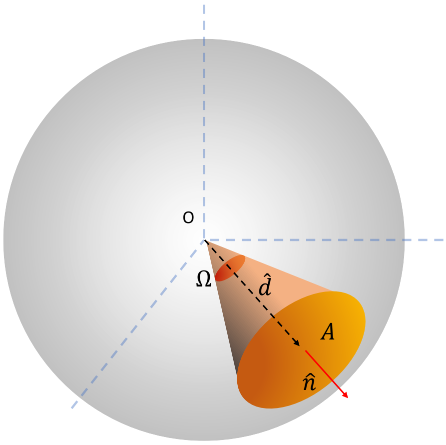

Figure 21: Illustration of a solid angle Ω subtended by an area A at a distance d from the origin in a spherical coordinate system.

As the surface normal is parallel to the distance vector, the area A is mostly known as *effective area* in the OWC community, and is denoted as A_{eff}. In this scenario, if the solid angle Ω is sufficiently small, A_{eff} can be approximated to the sphere curved surface. Therefore, the solid angle Ω can be described by Equation II-28.

$$\Omega = \frac{A_{eff}}{d^2} \qquad \text{II-28}$$

Now, let us assume an area A_r where the normal vector $\hat{n}$ is not aligned to the distance vector $\hat{d}$, resulting in an incident angle Ψ between them, as shown in Figure 22.

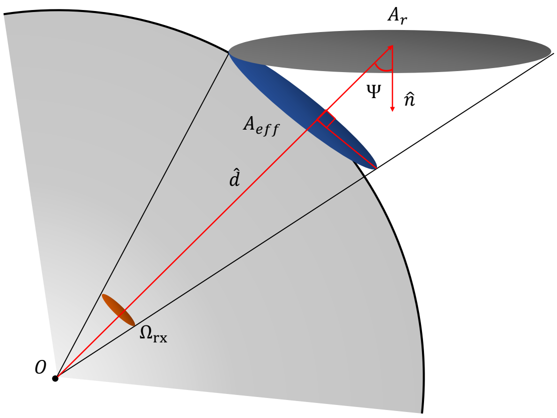

Figure 22: Illustration of an area A_r with an incident angle Ψ between the normal vector $\hat{n}$ and the distance vector $\hat{d}$, showing the effective area A_{eff} and solid angle Ω_{rx} subtended from the origin.

In this scenario, the surface value of the area A_{eff} depends on the area of A_r and on the incident angle Ψ, described by the Lambert Cosine Law [129], and is shown in Equation II-29.

$$A_{eff} = A_r \cos(\Psi) \qquad \text{II-29}$$

Finally, for sufficiently small solid angles (which is normally the case for indoor OWC applications, where $A_r \ll d^2$), the solid angle Ω_{rx} subtended by a real area A_r with incident angle Ψ subtended by its normal $\hat{n}$ and the distance vector $\hat{d}$ to a given point in space, is described by Equation II-30.

$$\Omega_{\mathrm{rx}} = \frac{A_r}{d^2}\cos(\Psi) \qquad \text{II-30}$$

Consider now a LOS configuration between the transmitter and a receiver with an active area A_r, and an irradiance angle θ, a separation distance d and an incidence angle Ψ, as shown in Figure 23. For all analyses, we assume a punctual optical source and a small solid angle Ω_{rx} subtended by A_r and the LED. The full analysis considering a non-small solid angle is provided in Appendix 1.

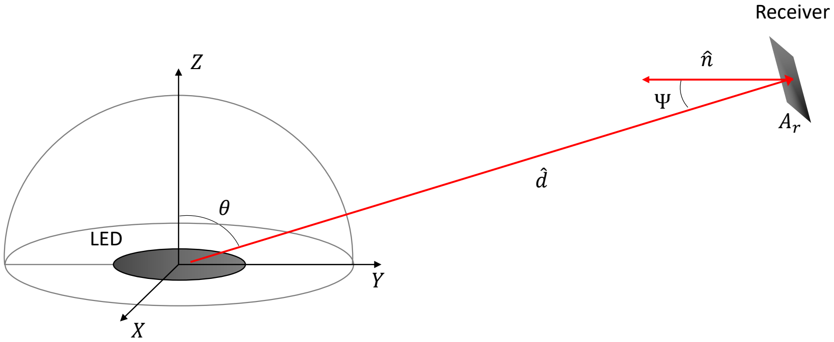

Figure 23: Schematic representation of light propagation from an LED with emission angle θ towards a receiver with an area A_r and incidence angle Ψ.

The received optical power P_r is calculated by integrating the LED radiant intensity $I(\Omega)$ over the entire solid angle Ω_{rx} subtended by the receiver surface A_r, as described in Equation II-31.

$$P_r = \int_0^{\Omega_{\mathrm{rx}}} I(\Omega)\, d\Omega \qquad \text{II-31}$$

For simplicity, we assume that the solid angle Ω_{rx} is small enough for the radiant intensity to remain constant within this region, depending only on the radiant angle θ. Therefore, the received optical power is described by Equation II-32.

$$P_r = I(\theta)\int_0^{\Omega_{\mathrm{rx}}} d\Omega = P_t \frac{m_1 + 1}{2\pi}\cos^{m_1}(\theta)\, \Omega_{rx}$$

$$P_r = P_t A_r \frac{m_1 + 1}{2\pi d^2}\cos^{m_1}(\theta)\cos(\Psi) \qquad \text{II-32}$$

Finally, the channel DC gain of the LOS component is described by Equation II-33.

$$H_{LOS} = A_r \frac{m_1 + 1}{2\pi d^2} \cos^{m_1}(\theta) \cos(\Psi) \tag{II-33}$$

Again, this is only valid for incident angles smaller than the receiver FOV. Ultimately, for a multiple source scenario, the received optical power P_r is the sum of the contribution of each source n separately, as shown in Equation II-34.

$$P_r = A_r \sum_{n=1}^{N} P_{t_n} \frac{m_{1_n} + 1}{2\pi d^2} \cos^{m_1}(\theta_n) \cos(\Psi_n) \tag{II-34}$$

II.1.5.1.2. NLOS link

Unlike LOS links, where the optical path between the source and detector is unobstructed, NLOS communication relies on the reflection, scattering, or diffraction of light off surfaces like walls, ceilings, and other objects within the environment. In NLOS links, multiple reflections are taken into account to accurately estimate the channel impulse response and understand the channel behaviour.

The nature of reflections in NLOS links depends on the physical properties of the surface and is characterized by its Bidirectional Reflectance Distribution Function (BRDF) [130]. Various mathematical models effectively represent the reflective properties of real-world materials, including the Lambertian BRDF for diffuse reflection, dielectric BRDF for specular reflection, and the Blinn-Phong BRDF, which combines both diffuse and specular components [131]. The type of reflection produced by a surface can be determined by the Rayleigh criterion [132]. However, it has been shown that most indoor surfaces exhibit Lambertian properties within the optical spectrum [133].

Diffuse reflectors, also known as Lambertian or matte materials), scatter light uniformly in all directions according to Lambert's cosine law, as illustrated in Figure 24. In this model, the surface acts both as a receiver with a FOV of $\pi/2$ and as an optical source with unit directivity m_1. The received optical power P_r is reflected and scaled by the reflection coefficient ρ, which depends on the surface geometric irregularities and the optical wavelength. This implies that the same material can reflect different wavelengths to varying intensities. For instance, a blue surface reflects blue light more effectively while absorbing red light, resulting in its distinctive colour.

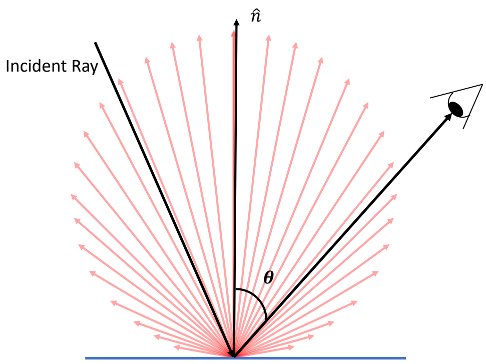

Figure 24: Lambertian scattering model.

Modelling the impulse response for NLOS links involves simulating or measuring the contributions from multiple reflections. In fact, this problem is recursive, since later reflections depend on previous ones. As an example, we can compute the NLOS impulse response for the first order reflection $h_{NLOS}^{(1)}(t)$ of N_R reflecting elements of the environment, as shown in Equation II-35.

$$h_{NLOS}^{(1)}(t) = \frac{A_r(m_1+1)}{2\pi^2} \sum_{j=1}^{N_R} \rho_j \cos^{m_1}(\theta_{1j}) \cos(\theta_{2j}) \frac{\cos(\Psi_{1j})\cos(\Psi_{2j})}{d_{1j}^2 d_{2j}^2} \Delta\text{A}.\,\delta\left(\text{t} - \frac{d_{1j}+d_{2j}}{c}\right) \qquad \text{II-35}$$

Here, the index j denotes the j-th reflecting element within the environment, and any variable containing this term relates specifically to that element. Thus, θ_{1j} is the source irradiance angle, Ψ_{2j} is the incidence angle at the receiver surface, θ_{2j} and Ψ_{1j} are the irradiance and incidence angles of the element j respectively, associated to a reflection coefficient ρ_j and an area ΔA. Hence, d_{1j} and d_{2j} represent the distance between source and the element j and between element j and the receiver, respectively. Figure 25 illustrates the described configuration.

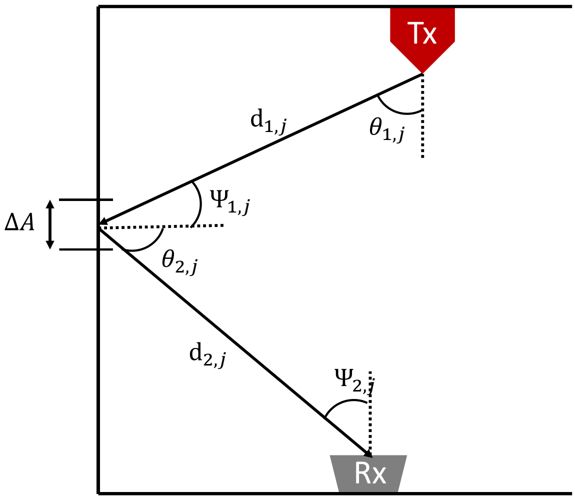

Figure 25: Example of a NLOS link considering one reflection only.

For further reflections, a recursive method is realized, at which each reflector element j_1 is in a LOS configuration according to another reflector element j_2. Finally, due to the complexity of obtaining the impulse response of NLOS scenarios, numerical techniques are employed to approximate it with high accuracy. The most commonly used methods include the Monte Carlo ray-tracing techniques, image-based methods, and iterative approaches [45].

In diffuse links (NLOS), multiple optical signals may reach the receiver at different times due to the reflections from various surfaces within the environment. This multipath channel can introduce time-dispersive issues, such as Inter-Symbol Interference (ISI), which can be qualified by the channel root mean square delay spread D_{rms}, defined as shown in Equation II-36. Here, μ represents the mean delay spread, as defined in Equation II-37.

$$D_{rms} = \left[\frac{\int (t-\mu)^2 h^2(t)dt}{\int h^2(t)dt}\right]^{1/2} \qquad \text{II-36}$$

$$\mu = \frac{\int t h^2(t)dt}{\int h^2(t)dt} \qquad \text{II-37}$$

To prevent ISI, the communication bit rate R_b should be kept significantly lower than D_{rms}, typically by a factor of ten or more [127]:

$$R_b < 1/(10D_{rms}) \qquad \text{II-38}$$

II.1.5.2. Wide spectrum

The analysis of the optical channel was conducted under the assumption of a monochromatic link. In wide-spectrum scenarios, each wavelength may perform differently due to the wavelength-dependent reflection coefficients of surfaces and the attenuation characteristics of the optical channel. For example, infrared communication is preferred over other wavelengths in FSO for its reduced atmospheric absorption and scattering [125]. However, in typical indoor environments, we assume that the medium is clear and exhibits no wavelength dependency. As a result, the primary factor affecting wide-spectrum scenarios is the reflection coefficient of the surfaces within the environment.

For a wide-spectrum transmission, the channel impulse response depends on each wavelength independently, therefore, it is denoted as $h(t;\lambda)$ [134], as shown in Equation II-39.

$$h(t;\lambda) = \sum_{n=1}^{N}\left(h_n^{(0)}(t) + \sum_{k=1}^{\infty} h_n^{(k)}(t;\lambda)\right) \qquad \text{II-39}$$

Again, the LOS contribution lies unchanged for wide-spectrum indoor links because the atmospheric absorption and scattering lies negligible under these conditions. In this scenario, and similarly to a monochromatic situation, the average received PSD $\Phi_r(\lambda)$ is related to the transmitted PSD $\Phi_t(\lambda)$ by the channel impulse response as described in Equation II-40. Consequently, the received optical power P_r is described by Equation II-41. In this context, the integration over wavelengths should include the entire spectrum containing significant optical power. For VLC applications, this typically ranges from 380 nm to 780 nm. To simplify notation, however, we have opted not to specify these limits explicitly.

$$\Phi_r(\lambda) = \Phi_t(\lambda)\int_{-\infty}^{\infty} h(t;\lambda)dt \qquad \text{II-40}$$

$$P_r = \int_{-\infty}^{\infty}\int_{\lambda} \Phi_t(\lambda)h(t;\lambda)d\lambda\, dt \qquad \text{II-41}$$

Here, we define the normalized transmitted power of the optical source $S(\lambda)$, as defined in Equation II-42. This parameter is crucial for spectral analysis in cases where the actual optical source power is unknown. It also emphasizes the key wavelengths relevant to the communication or energy harvesting scenario. Additionally, note that $\int S(\lambda) = 1$. For scenarios where the optical spectrum is not deformed (such as close-range LOS links), Equation II-42 is also valid when analysing the received PSD $\Phi_r(\lambda)$ and the received optical power P_r.

$$S(\lambda) = \frac{\Phi_t(\lambda)}{P_t} \tag{II-42}$$

Consequently, the received optical power P_r is written as shown in Equation II-43.

$$P_r = P_t \int_{-\infty}^{\infty} \int_{\lambda} S(\lambda) h(t;\lambda) d\lambda \, dt \tag{II-43}$$

In Equation II-44, we define $h_\lambda(t)$ as the *channel impulse response pondered by the normalized PSD of the source* $S(\lambda)$ [134]. As described before, this normalization allows us to emphasize the wavelengths most relevant to the scenario under analysis. For instance, in a given indoor environment, infrared optical waves will exhibit a distinct impulse response compared to ultraviolet waves, meaning that using the UV impulse response would not accurately reflect the performance of an IR link.

$$h_\lambda(t) = \int_{\lambda} S(\lambda) h(t;\lambda) d\lambda \tag{II-44}$$

Finally, for wide spectrum links, the received power P_r and the channel DC gain $H(0)$ are described in Equations II-45 and II-46 respectively.

$$P_r = P_t \int_{-\infty}^{\infty} h_\lambda(t) dt \tag{II-45}$$

$$H(0) = \int_{-\infty}^{\infty} h_\lambda(t) dt \tag{II-46}$$

Ultimately, with the channel impulse response pondered by the source normalized PSD $h_\lambda(t)$, other important parameters can also be obtained, such as the mean delay spread μ_λ and the mean square delay spread D_{rms_λ}, as described in Equations II-47 and II-48 respectively. Here, the index λ indicates that the wavelength influence is considered in calculating these parameters, unlike those presented in Equations II-36 and II-37.

$$\mu_\lambda = \frac{\int t h_\lambda^2(t) dt}{\int h_\lambda^2(t) dt} \tag{II-47}$$

$$D_{rms_\lambda} = \left[\frac{\int (t - \mu_\lambda)^2 h_\lambda^2(t) dt}{\int h_\lambda^2(t) dt} \right]^{1/2} \tag{II-48}$$

In a scenario with N sources, the received optical power P_r is calculated by summing the individual contributions from each transmitter n, as shown in Equation II-49. It is important to note that $h_{\lambda_n}(t)$ depends on the specific link between each source n and the receiver, as well as the normalized PSD $S_n(\lambda)$ of each source.

$$P_r = \sum_{n=1}^{N} P_{t_n} \int_{-\infty}^{\infty} h_{\lambda_n}(t)\, dt \qquad \text{II-49}$$

II.1.5.3. Optical channel simulation

Calculating the channel impulse response involves solving integrals derived from the light transport equation, which models how optical energy is distributed within the environment. To achieve this, several numerical approaches have been developed. One widely used method is ray tracing, where rays are tracked from the source to the receiver (or vice-versa), accounting for multiple reflections along the way. While ray tracing provides an accurate estimation of the NLOS channel impulse response, it becomes computationally extensive with increasing number of reflections, especially in highly reflective settings. To improve efficiency, simplified models sometimes consider only first-order reflections (single-bounce paths), but these can fall short in capturing the full multipath effects in more complex environments [135].

Barry *et al*. pioneered a multi-reflection approach to incorporate a range of multipath effects that can emerge in such environments [107], [136]. Although effective, this technique demands substantial computational resources and time, limiting its practicality. Subsequently, a ray tracing method was developed specifically for shading rendering, which significantly reduced processing time [137], and was later adapted for radio channel simulation [138]. This adaptation demonstrated that ray tracing could be an efficient tool for modelling optical and radio channels with reduced computational requirements.

Recent studies have shown the outstanding performance of a software based on Monte Carlo (MC) simulation, associated to ray-tracing algorithm, developed at the XLIM laboratory, called Ray Propagation Simulator (*RaPSor*) [139], [140]. This tool has supported numerous researches, some validated experimentally and others exploring various aspects of OWC [53], [98], [134], [141], [142]. RaPSor allows for the evaluation of the channel impulse response across multiple independent wavelengths $h(t;\lambda)$, in any optical link scenario that can be effectively modelled while accounting for a large number of reflections. This versatility enables its application across a range of setups, from simple SISO configurations to more complex mobile Multiple-Input Multiple-Output (MIMO) systems, with the capability to generate distinct impulse responses for each transmitter-receiver link.

Now considering an indoor scenario with N identical sources, each with transmitted optical power P_t and with a normalized PSD $S(\lambda)$, the received optical power P_r at a photodetector can be evaluated from the simulated results $h_n(t;\lambda)$, as extended from Equation II-49 and described in Equation II-50. We have opted not to explicitly state the channel impulse response weighted by the source normalized PSD, $h_{\lambda_n}(t)$, since $h_n(t;\lambda)$ is directly provided by the simulator.

$$P_r = P_t \int_{-\infty}^{\infty} \int_{\lambda} S(\lambda) \sum_{n=1}^{N} h_n(t;\lambda)\, d\lambda\, dt \qquad \text{II-50}$$

Finally, the received PSD $\Phi_r(\lambda)$ is obtained as shown in Equation II-51. This expression highlights how reflections from environmental elements can introduce various spectral effects, including distortion and wavelength shifting.

$$\Phi_r(\lambda) = P_t \int_{-\infty}^{\infty} S(\lambda) \sum_{n=1}^{N} h_n(t;\lambda)\, dt \qquad \text{II-51}$$

Using Equations II-4 and II-51 allow the spectral luminous flux to be derived from MCRT simulations. By integrating this over all relevant wavelengths and normalizing by the receiver active surface area A_r, the illuminance E_v is calculated, as shown in Equation II-52. As noted, illuminance is a key factor in adhering to lighting standards and characterizing energy harvesting performance.

$$E_v = \frac{683}{A_r} \int \Phi_r(\lambda) V(\lambda) d\lambda \qquad \text{II-52}$$

For a wide spectrum simulation, the results can be fully extended to cover the short-circuit current I_{sc} of photosensitive devices. Using both Equations II-20 and II-51, I_{sc} can be obtained as described in Equation II-53.

$$I_{sc} = P_t \int_{\lambda} R_{\lambda}(\lambda) \int_{-\infty}^{\infty} S(\lambda) \sum_{n=1}^{N} h_n(t;\lambda) R_{\Psi}(\Psi)\, dt\, d\lambda \qquad \text{II-53}$$

Here, each ray can reach the receiver surface with a specific incident angle Ψ, generating a current influenced by the factor $R_{\Psi}(\Psi)$. As different incident angles yield varying results, the angular responsivity term must be included in the simulation. To account for this effect, we have kept this term alongside $h_n(t;\lambda)$ in our analysis. We define then the channel impulse response pondered by the receiver angular properties as $h_{\Psi}(t;\lambda)$, indicated by the index Ψ, as shown in Equation II-54. This term has been incorporated into our simulator to extend our results to the short-circuit current I_{sc}.

$$h_{\Psi}(t;\lambda) = h(t;\lambda) R_{\Psi}(\Psi) \qquad \text{II-54}$$

Note that if the receiver does not exhibit any specific response to angular changes in responsivity, i.e. $R_{\Psi} = 1$, extending the simulator for this purpose is unnecessary. Finally, Equation II-55 shows how to obtain the short-circuit current of a photosensitive device from a MCRT simulation result that provides $h(t;\lambda)$.

$$I_{sc} = P_t \int_{\lambda} R_{\lambda}(\lambda) \int_{-\infty}^{\infty} S(\lambda) \sum_{n=1}^{N} h_{\Psi \mathrm{n}}(t;\lambda)\, dt\, d\lambda \qquad \text{II-55}$$

II.1.6. Sources of noises

Similar to RF communications, the electrical signal at the optical receiver output is often weak and hidden by noise. In VLC systems, multiple noise sources can affect the system performance and SNR, each with different properties and distributions. Nonetheless, and according to the central limit theorem, the high number of random variables approximates each noise to a zero-mean Gaussian distribution with variance σ_{total}^2 [143]. This is expressed in Equation II-56, where σ_{shot}^2 and $\sigma_{thermal}^2$ represents the shot noise and thermal noise variances respectively [45]. The characteristics and origins of these noise components are further discussed.

$$\sigma_{total}^2 = \sigma_{shot}^2 + \sigma_{thermal}^2 \qquad \text{II-56}$$

The current analysis is conducted for a conventional setup, where the photodetector short-circuit current is extracted using a TIA.

II.1.6.1. Shot noise

Arising from the discrete nature of light and the quantum behaviour of photodetection, shot noise is associated with the statistical fluctuations in the arrival of photons. It becomes more pronounced at low light levels and can limit the minimum detectable signal. In fact, the shot noise follows a Poisson distribution, and as it is independent of the electrical signal, it is classified as an AWGN. As stated before, the high number of random variables (photon count) approximates the shot noise as a Gaussian distribution with variance σ_{shot}^2.

Shot noise originates from three primary sources: ambient illumination, the optical signal, and the photodetector dark current. Among these, ambient noise is typically the most significant limitation in VLC systems, as it introduces unwanted optical interference from environmental light sources unrelated to the transmitter, significantly degrading system performance. Dark noise, on the other hand, is a result of the dark current—a small current that flows through the photodetector even in the absence of any optical signal. This dark current is caused by the thermal generation of charge carriers within the photodetector material. Finally, the total shot noise variance σ_{shot}^2 is described by Equation II-57, where q is the elementary charge, B is the photodetector bandwidth and I_s, I_b and I_d represent the short-circuit circuit currents generated by the optical signal, the ambient light and dark current, respectively.

$$\sigma_{shot}^2 = 2q(I_s + I_b + I_d)B \qquad \text{II-57}$$

Furthermore, the ambient noise is typically greater than the other noise sources, simplifying the shot noise variance, as described in Equation II-58 [45]. Here, the term $2qI_b$ is the noise spectral density, represented as N_0.

$$\sigma_{shot}^2 = 2qI_bB = N_0B \qquad \text{II-58}$$

Finally, classical values of the generated current I_b for different ambient sources in the visible and with photodiodes are exposed in Table 3 [144].

Table 3: Generated current I_b for various ambient optical sources.

Optical source	$\boldsymbol{I_b}$
Direct sunlight	$1000\ \mu A$
Indirect sunlight	$190\ \mu A$
Incandescent light	$56\ \mu A$
Fluorescent light	$2\ \mu A$

Reproduced with permission from reference [45].

II.1.6.2. Thermal noise

The thermal noise, also known as Johnson-Nyquist noise, is a fundamental source of electronic noise arising from the random motion of charge carriers (electrons) within conductors and electronic components. This noise is inherent in all electronic devices and is present regardless of any external optical signals. The random thermal motion of electrons within a conductor generates fluctuations in voltage, leading to thermal noise. The magnitude of this noise is directly proportional to the temperature of the conductor and the bandwidth over which the system operates. The thermal noise has a flat spectral density, independent of the system frequency. Also, it is the Gaussian distribution with zero mean. Its variance $\sigma_{thermal}^2$ is described by Equation II-59.

$$\sigma_{thermal}^2 = \frac{4KTB}{R_L} \qquad \text{II-59}$$

Here, K is the Boltzman constant, T is the system absolute temperature in Kelvin, R_L the equivalent resistance of the circuit and B the receiver bandwidth. In VLC systems, thermal noise is generally much lower than ambient noise.

II.1.7. Modulation schemes

The transmission of data in VLC systems is achieved by encoding information into the optical signal through various modulation techniques. Due to the unique characteristics and limitations of VLC, traditional RF modulation schemes must be adapted to meet the specific requirements of optical signals. In RF communications, data can be encoded into the amplitude, frequency, or phase of the carrier signal. Coherent optical sources, such as LDs, allows the use of advanced and complex modulation techniques, including phase modulation schemes like Binary Phase Shift Keying (BPSK) with the help of electro-optic modulators. However, LEDs are incoherent optical sources, which makes phase modulation impossible. Instead, information is primarily encoded in the amplitude of the optical signal using IM or through spectral modulation techniques such as Color Shift Keying (CSK).

This work focuses primarily on amplitude modulation schemes. The requirement for a strictly positive optical signal in VLC systems does not allow the use of bipolar modulation schemes common in RF systems. However, slight modifications to these schemes make them suitable for optical communications. As discussed earlier, indoor VLC can address a wide range of communication needs, supporting various data rates. Depending on the application and environmental conditions, different modulation methods can be applied to meet the desired quality of service.

These methods include both single-carrier and multi-carrier approaches, each offering distinct advantages. Simpler approaches typically operate in baseband, avoiding the use of high-frequency carriers and reducing system complexity. On the other hand, external optical circuits can be incorporated to modulate data onto higher-frequency carriers, enabling improved performance but at the cost of increased system complexity. In this context, we will explore and highlight some of the most significant modulation techniques used in the literature.

- **Single-carrier baseband**

Baseband modulations are named as such because the modulated data remains near the zero-frequency range. Different modulation schemes were proposed in the IEEE 802.15.7 standard, from which we highlight the On-Off Keying (OOK) and the Pulse Position Modulation (PPM).

OOK is the simplest and most widely used modulation scheme in OWC due to its ease of implementation and compatibility with IM/DD systems It operates using two logical levels: “1” represents the presence of an optical signal, while “0” signifies its absence. Each level is transmitted over a bit period T_b, as shown in Figure 26. OOK can be implemented with either Return-to-Zero (RZ) or Non-Return-to-Zero (NRZ) formats, depending on the system duty cycle.

However, it has notable limitations, including inefficient use of available bandwidth compared to more advanced modulation schemes (low spectral efficiency), high susceptibility to noise, poor power efficiency. Additionally, extended sequences of “0” can result in prolonged absence of optical power, leading to flickering effects and potential synchronization loss at the receiver.

The PPM is a time-based modulation scheme where the position of an optical pulse within a symbol duration determines the transmitted symbol. This scheme is a multi-level strategy, where a symbol containing M bits results in $L = 2^M$ possible time positions, referred to as L-PPM. Notably, the 2-PPM modulation is effectively the Manchester coding applied to OOK (or OOK-RZ). In this scheme, bits are defined by level transitions: a low-to-high transition within the symbol period represents a "1," while a high-to-low transition represents a "0" (see Figure 26).

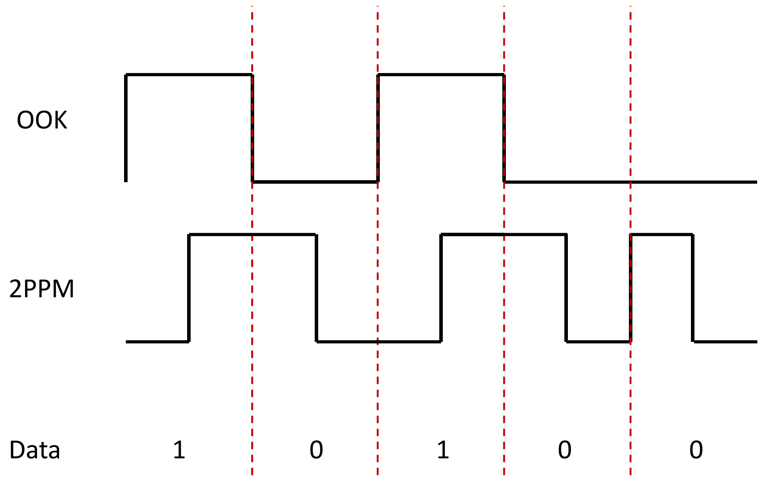

Figure 26: Comparison of OOK and 2PPM modulation.

L-PPM offers several advantages over OOK, such as maintaining a consistent average optical power per bit that is independent of the transmitted message. It also provides better power efficiency by concentrating energy into shorter pulse durations within each symbol, reducing susceptibility to flickering effects, and demonstrating greater resilience to noise (such as shot noise) when soft decoding methods are applied. However, L-PPM does have notable drawbacks, including requiring more bandwidth for the same data rate (poor bandwidth efficiency), increased system complexity, and the need for precise synchronization between the transmitter and receiver. Despite these limitations, in scenarios where bandwidth is not a limiting factor, or high data rates are not required, and where low power consumption is a priority, L-PPM emerges as an attractive modulation scheme due to its simplicity, energy efficiency, and reliable performance.

- **Multi-carrier**

Multi-Carrier Modulation (MCM) refers to the technique of dividing the transmitted data stream into multiple parallel sub-streams, each modulated onto a different carrier frequency within the available bandwidth. This approach is typically employed to improve the spectral efficiency, mitigate ISI and support higher data rates at the cost of reduced power efficiency [145].

Orthogonal Frequency Division Multiplexing (OFDM) is the most common MCM applied on modern optical communication systems [146]. In OFDM-based VLC, the data stream is divided into multiple orthogonal sub-carriers, and each sub-carrier is modulated in the electrical domain. The modulated electrical signal is then used to drive the LED for intensity modulation. At the receiver end, the photodetector demodulates the sub-carriers and reconstructs the original data. OFDM is a highly efficient modulation scheme that efficiently uses the available bandwidth. However, it demands higher computational complexity due to the use of Fast Fourier Transform (FFT) and Inverse FFT (IFFT).

While OFDM is extensively applied in RF systems requiring high data rates, directly using this strategy in optical communications presents challenges due to the bipolar nature of the electrical signal generated by the IFFT process. LEDs, being intensity-modulation devices, require unipolar and positive-only signals. To address this, adaptations such as adding a DC bias to the final signal have been introduced, leading to Direct Current Biased Optical OFDM

(DCO-OFDM). Although this approach ensures signal compatibility with LEDs, it increases the system energy requirements [147]. Another adaptation involves carefully selecting the carrier frequencies to produce a unipolar signal directly through IFFT processing, resulting in Asymmetrically Clipped Optical OFDM (ACO-OFDM), which eliminates the need for a DC bias [148].

In this thesis, where the primary focus is on utilizing PV devices for SLIPT applications, we have chosen L-PPM as the preferred modulation scheme over alternatives like OOK and OFDM. This choice aligns with the dual objectives of our work: optimizing energy harvesting alongside communication performance. Unlike OFDM, which is highly spectral-efficient but requires complex signal processing and high power consumption, L-PPM offers better power efficiency and reduced system complexity. Compared to OOK, L-PPM minimizes flickering effects and ensures consistent average optical power regardless of the data being transmitted, making it ideal for systems where energy harvesting plays a crucial role. In this work, we will analyse key communication parameters of L-PPM.

II.1.7.1. L-PPM

L-PPM encodes information by varying the position of a single optical pulse within a time slot, with period T_s, of a fixed symbol period T_{sym}. In this scheme, each symbol period is divided into L ($= 2^M$, where M is the number of bits per symbol, or bit resolution) equal time slots, where only one time slot contains the optical pulse, and the position of this pulse corresponds to a specific data symbol. For example, in 4-PPM, each symbol represents M=2 bits of data and the pulse can occupy one of four possible time slots (refer to Figure 27). The pulse position represents the decimal value of the input bit sequence. The absence of pulses in the other slots ensures that the average transmitted optical power remains constant, regardless of the data sequence. At the receiver side, the position of the detected pulse is interpreted to recover the transmitted data.

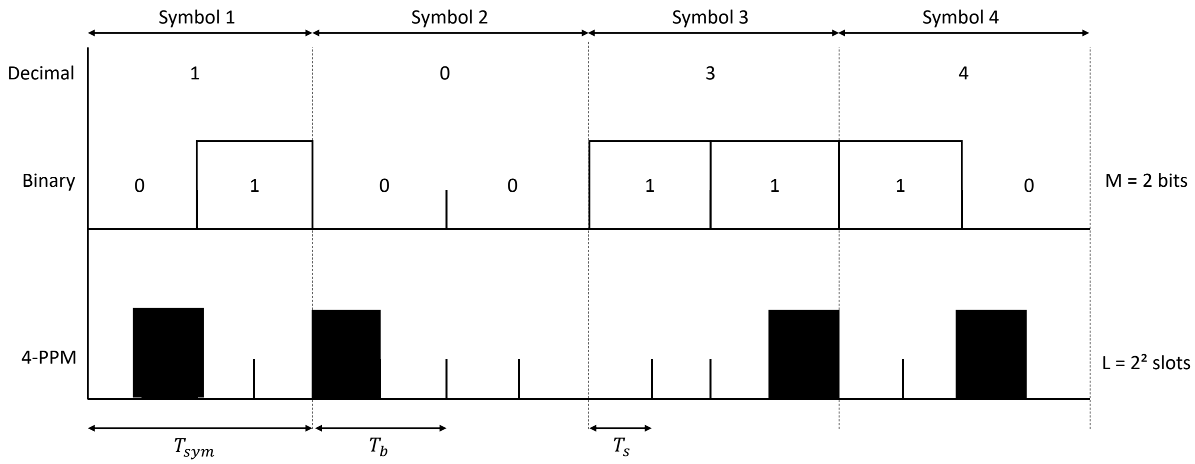

Figure 27: Scheme of 4-PPM.

Source: Modified with permission from reference [91].

In L-PPM, the slot duration T_s is related to the symbol duration T_{sym} and to the bit duration T_b as shown in Equations II-60 and II-61 [91].

$$T_s = \frac{T_{sym}}{L} \quad \text{II-60}$$

$$T_s = \frac{T_b M}{L} \quad \text{II-61}$$

Here, the bit rate R_b is defined as:

$$R_b = 1/T_b \quad \text{II-62}$$

Considering an average optical power P_t, the transmitted optical signal representing the binary symbol can be described by Equation II-63, where LP_t is the peak optical power and $m \in \{1,2,\ldots,L\}$ identifies the slot that contains the pulse. Note that, in this scenario, the average symbol optical power remains constant and is equals to P_t.

$$x(t) = \begin{cases} LP_t, & t \in [(m-1)T_s, mT_s] \\ 0, & \text{elsewhere} \end{cases} \quad \text{II-63}$$

To understand the bandwidth of digital signals, one must obtain the PSD of the signal and analyse the positions of the first spectral nulls. However, obtaining the spectral behaviour of L-PPM signals is out of the scope of the current work. Figure 28 shows the PSD of the L-PPM for $L = 4, 8$ and 16, obtained from reference [91]. Here, all modulations employed the same average transmitted optical power P_t. The frequency axis is normalized to the bit-rate R_b.

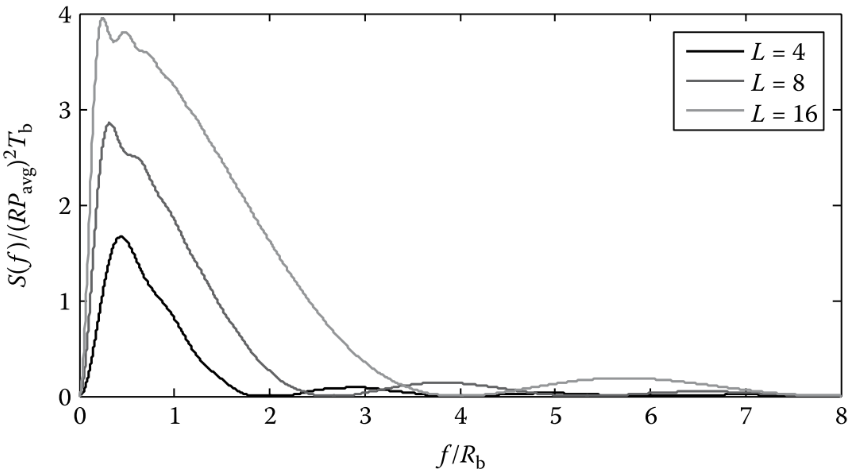

Figure 28: PSD of PPM for L=4,8 and 16.

Source: Reproduced with permission from reference [91].

It is important to highlight that the required signal bandwidth B increases as the modulation order L increases. The bandwidth B can be obtained as shown in Equation II-64.

$$B = R_b \frac{L}{M} \quad \text{II-64}$$

Compared to traditional OOK-NRZ modulation, where the bandwidth B equals the bit rate R_b and the spectral efficiency is unitary, the required bandwidth for L-PPM systems is L/M times superior, demonstrating an important drawback of this strategy.

II.1.7.1.1. Error probability on Gaussian channel

A Gaussian channel is a communication channel model that introduces AWGN into the transmitted optical signal. It is one of the most studied and fundamental models in communication theory due to its simplicity and close approximation of many real-world scenarios. The addition of AWGN can cause detection errors at the receiver, impacting system performance. In PPM, assuming constant synchronization, detection errors are confined to the symbol itself, potentially resulting in a maximum of M incorrect bits per symbol. Here, we shall assume a monochromatic link without loss of generality. Also, we shall ignore any particular angular behaviour of the receiver, meaning that $R_{\Psi}(\Psi) = 1$ (see Equation II-20). Other simplifications include:

1- The transceivers are in a LOS link configuration without multipath dispersion;

2- The dominant noise is the background light shot noise;

3- There is no electronic bandwidth limitation.

After optical propagation, the photodetector generates a short-circuit current $i_{sc}(t)$ proportional to the incident optical power P_r. This output signal is then processed through a unit energy filter, matched to the transmitter pulse filter, with a rectangular impulse response $r(t)$. Following the convolution with the matched filter, the resulting signal undergoes decoding, which can be performed using either hard or soft decoding techniques. Figure 29 shows the block diagram of the L-PPM transmission and reception system, highlighting essential components such as the matched filter and decoding stages.

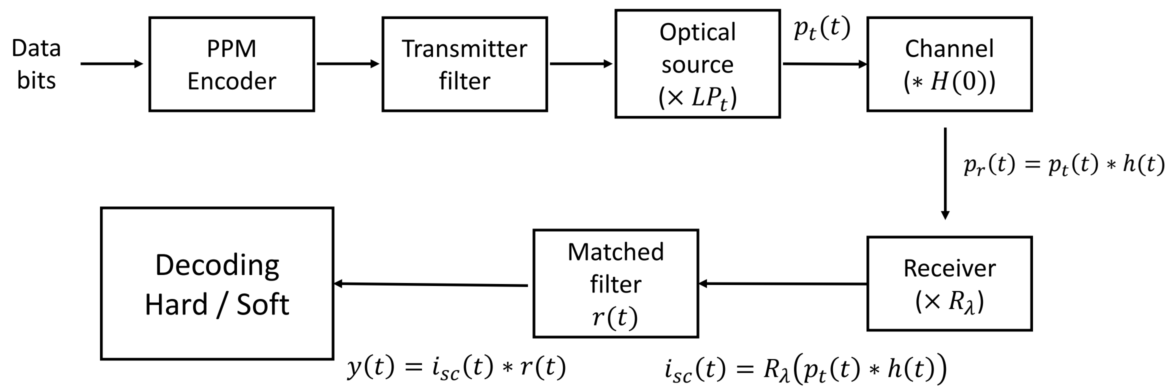

Figure 29: Block diagram of the L-PPM transmission and reception system.

The expected electrical symbol for L-PPM is provided in Figure 30 (the specific slot position is irrelevant for this analysis), with AWGN effects excluded from consideration.

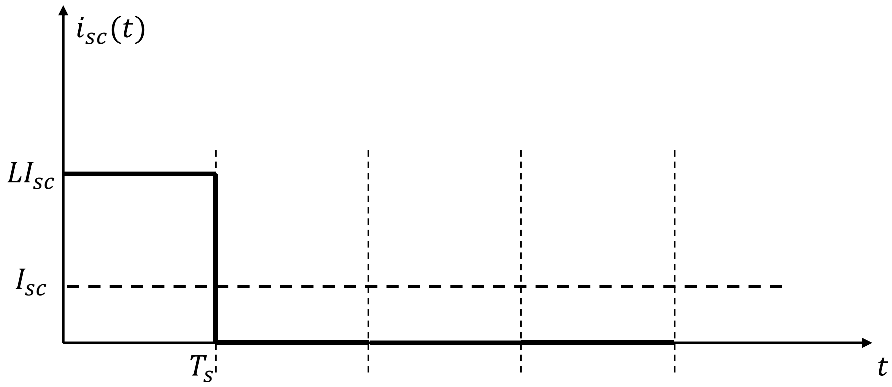

Figure 30: Expected electrical symbol generated by the photodetector when no noise is considered.

Knowing that the symbol duration is LT_s, the average short-circuit, denoted as I_{sc} (shown in the schematic above), can be determined. Thus, it is proportional to the average received optical power P_r scaled by the responsivity R_λ. Here, the total symbol energy E_{sym} is equivalent to the energy of a single pulse E_s, defined by Equation II-65. It is important to emphasize that the specific position of the pulse within the symbol does not alter its energy or behaviour.

$$E_s = \int_0^{T_s} (LI_{sc})^2 dt = L^2 I_{sc}^2 T_s \qquad \text{II-65}$$

For a monochromatic scenario and using Equations II-16, II-24 and II-61, the average short-circuit current I_{sc} and the slot energy E_s are described by Equations II-66 and II-67 respectively.

$$I_{sc} = R_\lambda P_t H(0) \qquad \text{II-66}$$

$$E_s = \frac{LM\big(R_\lambda P_t H(0)\big)^2}{R_b} \qquad \text{II-67}$$

Here, the average energy per bit is the total symbol energy $E_{sym}(= E_s)$ divided by the number of bits per symbol (M), as described below:

$$E_b = \frac{E_s}{M} = \frac{L\big(R_\lambda P_t H(0)\big)^2}{R_b} \qquad \text{II-68}$$

Before continuing obtaining the error probability of a L-PPM communication on a Gaussian channel, let us obtain the SNR of this scheme. This parameter is a measure used in communication systems, electronics, and signal processing to quantify the strength of a desired signal relative to the level of background noise. It is a key metric for evaluating the performance of a system, as it determines how well the system can distinguish the signal from the noise. The SNR is mathematically expressed as the ratio of the signal power P_{signal} to the noise power P_{noise}:

$$SNR = \frac{P_{signal}}{P_{noise}} \quad \text{II-69}$$

Coming back to the short-circuit current generated by the photodiode, and knowing that each symbol contains the same electrical power, we can extend the symbol power (i.e. the energy contained in a symbol divided by the symbol duration) to the signal power P_{signal} of a full digital message. Therefore, P_{signal} is computed as shown below.

$$P_{signal} = \frac{1}{T_{sym}} \int_0^{T_{sym}} (LI_{sc})^2 dt$$

The integral represents the energy contained in a symbol, which is described by Equation II-67. Therefore, the signal power is:

$$P_{signal} = L\big(R_\lambda P_t H(0)\big)^2 \quad \text{II-70}$$

The shot noise $n(t)$ is modelled as an AWGN with double-sided PSD $N_0/2$. Here, the noise power P_{noise} (which also represents its variance σ_{noise}^2) is described by Equation II-71, where B is the signal bandwidth.

$$P_{noise} = N_0 B \quad \text{II-71}$$

Using Equations II-64 and II-71, the SNR for the L-PPM scheme is defined by Equation II-72.

$$SNR_{PPM} = \frac{M\big(R_\lambda P_t H(0)\big)^2}{N_0 R_b} \quad \text{II-72}$$

Equation II-73 shows the SNR per bit E_b/N_0, a critical metric in communications that provides a standardized measure of communication system performance, enabling comparisons across different systems, modulation schemes, or channel conditions.

$$\frac{E_b}{N_0} = \frac{L\big(R_\lambda P_t H(0)\big)^2}{N_0 R_b} \quad \text{II-73}$$

Finally, the SNR in terms of E_b/N_0 is shown below:

$$SNR_{PPM} = \frac{M}{L}\frac{E_b}{N_0} \quad \text{II-74}$$

Contrary the OOK modulation, where $SNR_{OOK} = E_b/N_0$, the SNR in L-PPM depends heavily on the modulation order L. To achieve the same SNR, OOK modulation requires a higher energy per bit to meet the desired Quality of Service (QoS), making L-PPM more energy-efficient for certain applications.

Returning to the analysis, the short-circuit current $i_{sc}(t)$, shown in Figure 30, passes through the matched filter $r(t)$. In this scenario, the noise variance at the filter output depends on the noise PSD and on the energy of the filter impulse response. Therefore, to ensure optimal performance, a unit-energy filter is employed, characterized by a rectangular response with an amplitude of $1/\sqrt{T_s}$ and duration T_s, as shown in Figure 31. Additionally, Figure 31 illustrates the detected symbol and the corresponding output of the matched filter.

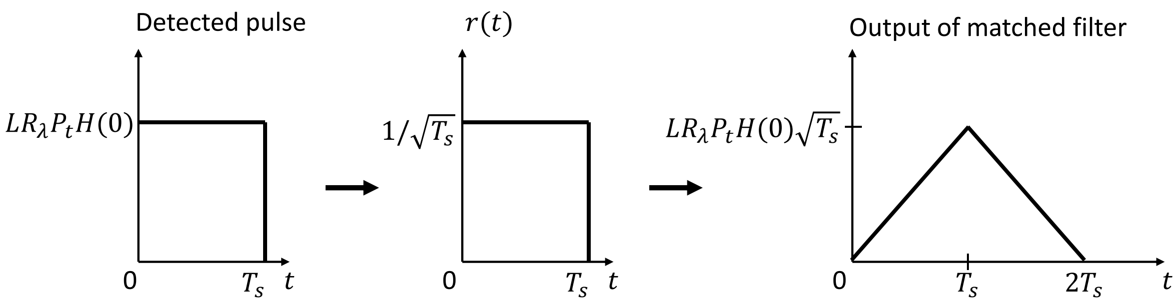

Figure 31: Detected pulse at the photodetector output, unit-energy matched filter $r(t)$ and output of the matched filter.

Source: Modified with permission from reference [91].

After the convolution process, the output of matched filter reaches a peak value of $LR_\lambda P_t H(0)\sqrt{T_s}$, equivalent to $\sqrt{E_s}$ (refer to Equations II-65 and II-66), as illustrated in Figure 31. The matched filter output is then decoded, which can be achieved using two distinct methods, described as follow:

- **Hard decision decoding**

The hard decision decoding employs a threshold detector to decide each slot of the matched filter electrical output. If the value is superior to the threshold at the sampling instant, a "1" is considered, and "0" otherwise. To obtain the error probability for the hard decoding, one must analyse the slot error probability $P_{se-PPM-H}$ (the index represents Slot Error, PPM modulation and Hard decoding), extend it to the symbol error probability $P_{syme-PPM-H}$, to finally obtain the bit error probability $P_{be-PPM-H}$.

In digital communications, the error probability refers to the likelihood of incorrectly detecting a transmitted bit, such as interpreting a "1" as a "0" or a "0" as a "1". This is calculated using conditional probabilities to account for such errors [149]. For Gaussian channels affected by AWGN, the error probability can be estimated by the Marcum Q-function $Q(.)$ or the complementary error function $erfc(.)$. Both functions are mathematically related, as described in Equation II-75. In this work, we have opted to employ the Marcum function for further analysis.

$$Q(x) = \frac{1}{2} erfc\left(\frac{x}{\sqrt{2}}\right) \qquad \text{II-75}$$

Considering the presence of an AWGN with double-sided PSD $N_0/2$ and an optimum threshold α_{T-opt}, the slot error probability $P_{se-PPM-H}$ is obtained as described in Equation II-76, where $P(0)$ and $P(1)$ are the probability of receiving an empty slot and a pulse, respectively [91].

$$P_{se-PPM-H} = P(0)Q\left(\frac{\alpha_{T-opt}}{\sqrt{N_0/2}}\right) + P(1)Q\left(\frac{\sqrt{E_s} - \alpha_{T-opt}}{\sqrt{N_0/2}}\right) \quad \text{II-76}$$

Considering a completely aleatory signal, the pulse has an equiprobability of being in any slot, meaning that all possible symbols are equiprobable. Therefore, $P(0)$ and $P(1)$ can be obtained as shown below.

$$P(0) = \frac{L-1}{L}$$

$$P(1) = \frac{1}{L}$$

Finally:

$$P_{se-PPM-H} = \frac{L-1}{L}Q\left(\frac{\alpha_{T-opt}}{\sqrt{N_0/2}}\right) + \frac{1}{L}Q\left(\frac{\sqrt{E_s} - \alpha_{T-opt}}{\sqrt{N_0/2}}\right) \quad \text{II-77}$$

Equation II-77 describes the slot error probability given the optimal threshold α_{T-opt}, with $\sqrt{E_s}$ derived from Equation II-67. Unlike OOK, where the threshold is typically set at half the peak of the matched filter output, the optimal threshold for L-PPM is more complex. This is because the probabilities of receiving an empty slot and receiving a pulse are unequal. The optimal threshold depends on the modulation order as well as the signal and noise powers [91]. Nonetheless, for scenarios with low error probabilities, $\alpha_T = \sqrt{E_s}/2$ offers good performance, especially for lower modulation order. Therefore, the slot error probability for the L-PPM hard decoding is written as:

$$P_{se-PPM-H} = Q\left(\sqrt{\frac{E_s}{2N_0}}\right) \quad \text{II-78}$$

In terms of SNR_{PPM} or E_b/N_0, the slot error probability is (refer to Equation II-68):

$$P_{se-PPM-H} = Q\left(\sqrt{\frac{L}{2}SNR_{PPM}}\right) \quad \text{II-79}$$

$$P_{se-PPM-H} = Q\left(\sqrt{\frac{ME_b}{2N_0}}\right) \quad \text{II-80}$$

The slot error probability can be easily extended to the symbol error probability $P_{syme-PPM-H}$ using basic probability theory. The probability of an incorrect symbol is simply the complement of the probability of receiving a correct symbol. The probability of a correct symbol, in turn, is the likelihood that all L slot are correctly received, expressed as $(1 - P_{se-PPM-H})^L$. Finally, $P_{syme-PPM-H}$ is written as:

$$P_{syme-PPM-H} = 1 - (1 - P_{se-PPM-H})^L \qquad \text{II-81}$$

Here, we shall assume that each symbol is Independently and Identically Distributed (IID). As an approximation, the bit error probability $P_{be-PPM-H}$ is calculated by dividing the average number of incorrect bits per symbol by the number of bits per symbol M. The average number of incorrect bits per symbol is determined through a combinatorial analysis, which considers all possible combinations where at least one bit within a symbol is incorrect [53]. Finally, the bit error probability of a hard decoding in a L-PPM communication is described by Equation II-82.

$$P_{be-PPM-H} = \frac{L/2}{L-1} P_{syme-PPM-H} \qquad \text{II-82}$$

In practical communication systems, data transmission does not always succeed, and bit errors often occur. To quantify this, we define the Bit-Error-Rate (BER), a critical metric in digital communication systems, representing the ratio of the number of erroneous bits received to the total number of bits transmitted over a communication channel. It is mathematically expressed as:

$$BER = \frac{Number\ of\ wrong\ bits}{Total\ number\ of\ transmitted\ bits} \qquad \text{II-83}$$

When a sufficiently large number of bits is transmitted, the BER shall converge to the bit error probability, which is determined by the modulation scheme and the corresponding E_b/N_0 ratio. BER is used to quantify the reliability and performance of a communication system. A lower BER indicates better system performance, as it implies fewer errors in the received data.

Therefore, we have performed a simple Matlab® simulation to analyse the convergence of the BER into the error probability. The simulation considers 300 symbols sent from the transmitter to the receiver, while an AWGN is added into the received signal, with variable PSD (resulting in variable SNR). A decoding process following each task described in the current section is performed, for each SNR. Finally, we have obtained a simulated BER and slot error rate. The results were then compared to the error probabilities described above. Figure 32 shows the obtained slot error rate, BER, $P_{be-PPM-H}$ and $P_{se-PPM-H}$ for multiple SNRs (in dB).

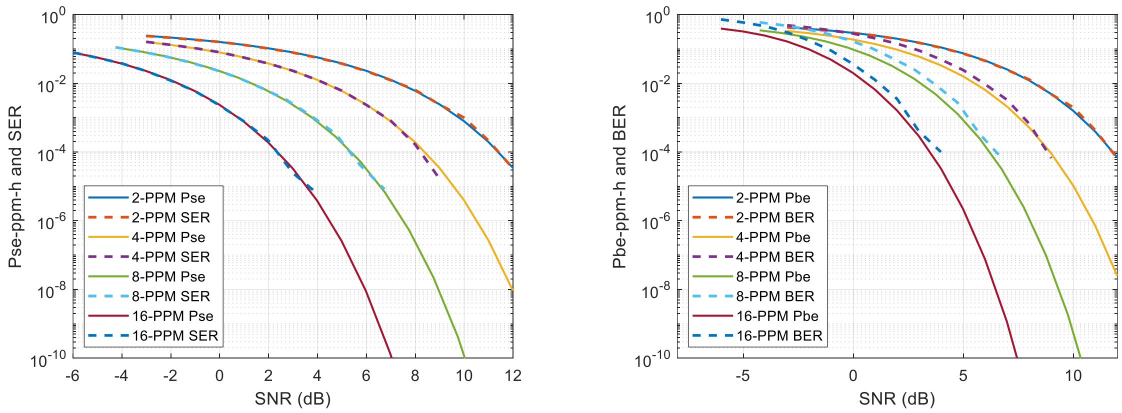

Figure 32: Comparison of error probabilities and simulated error rates as a function of the SNR for 2-PPM, 4-PPM, 8-PPM, and 16-PPM modulation schemes. (a) Slot error rate; (b) BER.

Figure 32.a shows the obtained SER alongside the theoretical $P_{se-PPM-H}$, computed with Equation II-79 for multiple SNR values. Indeed, these results validate the chosen optimum threshold value. As we convert the slot error probability into bit error probability, different approximations were realized. For higher modulation orders, these approximations are more evident, as illustrated in Figure 32.b, where a slight discrepancy between the obtained BER and $P_{be-PPM-H}$ can be observed.

For a specified QoS, represented by the expected BER, modulation schemes with higher orders L require less signal power to meet the performance requirements. However, this requires more complex systems designs and precise synchronization. As detailed before, the required system bandwidth is proportional to the desired data rate R_b by a factor L/M. Consequently, higher modulation orders demand more advanced and sophisticated transceiver designs.

Soft decision decoding

Soft decoding in L-PPM involves leveraging the received signal amplitude information and probability distribution to improve the detection of transmitted symbols. Unlike hard decoding, which strictly assigns a received signal to the most likely symbol based on a simple threshold, soft decoding considers the likelihood of each possible symbol. Supposing constant synchronization, the soft detector will assign a high level “1” to the slot that contains most energy.

In fact, the actual symbol energy level is out of important for the soft decoding, as the information itself is contained in the relative energy between slots. This approach, while more computationally complex than the hard decoding, demonstrates greater robustness against noise, particularly in scenarios where shot noise is the dominant factor affecting the system performance. Additionally, it is more robust to temporal dispersion effects, such as the multipath distortion in diffuse scenarios.

For soft decoding in L-PPM, the slot error probability $P_{se-PPM-S}$ depends on the relative energy between slots and is less straightforward than the hard decoding case. The slot with the highest detected energy is chosen as the one containing the pulse, making the slot error probability dependent on the cumulative distribution function of the noise across all slots. However, John R. Barry demonstrated that we can relate the performances of different modulations schemes with the OOK error probabilities through the analysis of the required average transmitted optical power P_t, valid for high SNR values [150]. Here, the soft decoding requires $-5\log_{10}(\frac{LM}{4})$ average optical power, resulting in a bit error probability described as:

$$P_{be-PPM-S} \approx Q\left(\sqrt{SNR_{PPM}L}\right) \qquad \text{II-84}$$

Similarly, a 300-symbol transmission simulation was performed to compare the obtained BER and $P_{be-PPM-S}$ for the soft decoding scenario using Matlatb®. The results are illustrated in Figure 33 for multiple modulation orders L.

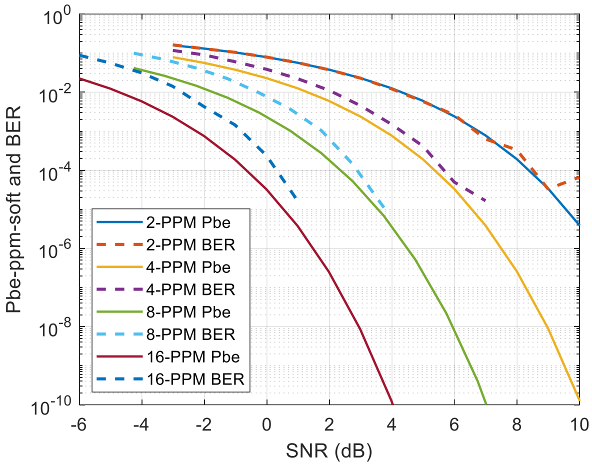

Figure 33: BER and bit error probability (Pbe) of soft-decoded L-PPM across different modulation orders (2-PPM, 4-PPM, 8-PPM, 16-PPM) as a function of SNR.

Similarly, we have illustrated the equations and evaluated the precision of the approximations. Here, for higher modulation orders and lower SNR values, the observed BER tends to exceed the predicted $P_{be-PPM-S}$, highlighting the impact of the approximations made during the calculations. Nonetheless, for a fixed QoS, higher modulation orders demonstrate the ability to achieve the required performance at lower SNR levels, emphasizing their resilience against noise.

Ultimately, to compare the performance obtained with hard and soft decoding methods, the 2-PPM error probabilities and simulated BERs are plotted in the same graph (see Figure 34).

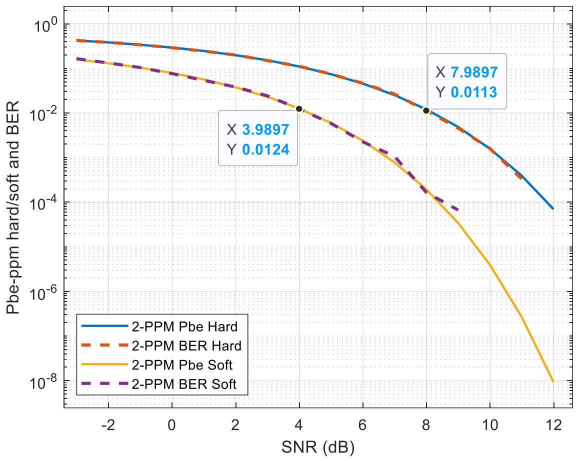

Figure 34: Comparison of error probabilities and simulated BERs for 2-PPM modulation using hard and soft decoding methods.

The figure demonstrates the superior performance of soft decoding over hard decoding in a 2-PPM modulation scheme, particularly at lower error probabilities. For the same SNR, the error probability achieved with soft decoding (yellow and purple curves) is consistently lower than that of hard decoding (blue and red curves). For instance, to reach a BER of approximately 1.15×10^{-2}, soft decoding requires around 4 dB less SNR compared to the hard one. Despite the increased computational complexity, this robustness makes soft decoding an attractive choice for applications requiring enhanced performance in challenging environments.

This completes the discussion of all essential equations and foundational concepts related to VLC, which are necessary for the subsequent analyses presented in this thesis.

II.2. Organic photovoltaic cells

OPVs devices have emerged as a promising solution for energy harvesting due to their lightweight nature, flexibility, and the ability to tune their optical and electronic properties through molecular engineering. Unlike traditional inorganic photovoltaics, OPVs are fabricated using solution-based processes, enabling low-cost and scalable manufacturing methods such as roll-to-roll or sheet-to-sheet printing. These features make OPVs particularly attractive for applications in environments where space, weight, and adaptability are critical, such as indoor IoT systems [151].

Furthermore, the potential of OPVs extends beyond energy harvesting. Their inherent flexibility and compatibility with transparent and semi-transparent substrates make them well-suited for integration into building surfaces, furniture, and IoT devices themselves [152]. This integration allows for seamless energy harvesting without compromising aesthetics or functionality, further supporting the deployment of pervasive IoT networks in smart buildings and indoor environments [153].

In the current section, we will explore the key aspects and important equations of OPVs that are critical for subsequent analyses.

II.2.1. Working principle

The fundamental operation of OPVs is governed by the electronic properties of the materials, particularly by the energy of their Highest Occupied Molecular Orbital (HOMO) and Lowest Unoccupied Molecular Orbital (LUMO). The HOMO represents the energy level where the highest energy electrons reside in their ground state, while the LUMO corresponds to the lowest energy level available for excited electrons. The difference between these levels, referred to as the bandgap, determines the range of photon energies the material can absorb. In a classical vision, the HOMO and LUMO frontier orbitals act as the classical valence and conduction bands in a crystalline semiconductor.

When a photon with sufficient energy is absorbed in the donor or acceptor materials, an electron is excited from the HOMO to the LUMO, leaving behind a positively charged hole in the HOMO. This photoexcitation forms a tightly bound electron-hole pair, or exciton, held together by Coulombic forces due to the low dielectric constant of organic materials. Excitons in OPVs have a short lifetime, typically in the range of nanoseconds, and can only travel a limited distance, known as the exciton diffusion length, before recombining. This diffusion length is typically 5-20 nm in organic materials, requiring a careful design of the active layer to ensure that excitons reach the donor-acceptor interface before recombining [154]. In planar laminate structures, thick active layers have efficiency penalty due to charge recombination processes. However, thin active layers devices demonstrate poor absorption properties.

At the donor-acceptor interface, the difference in energy levels between the LUMO of the donor and the LUMO of the acceptor provides the driving force for exciton dissociation. The electron transfers from the donor LUMO to the acceptor LUMO, while the hole remains in the donor HOMO (refer to Figure 35). Recent advancements in acceptor absorbance also allow the reverse process: photons absorbed by the acceptor generate tightly bound excitons, with holes transferring from the acceptor HOMO to the donor HOMO, while electrons remain in the acceptor LUMO. This process separates the exciton into “quasi” free charge carriers in the interface: an electron in the acceptor and a hole in the donor, called Charge-Transfer (CT) state, at which both charges are still bound by the Coulombic force. Finally, if external forces overcome the Coulombic attraction, the CT state transitions into a Charge-Separated (CS) state, where the charges are fully free. The dissociation efficiency depends on the strength of the energy offset and the ability of the materials to facilitate rapid charge transfer. If the energy offset is insufficient, exciton separation may be incomplete, leading to losses due to recombination.

Following exciton dissociation, the separated charges must be transported to their respective electrodes, or charge transport layer in more developed systems. The acceptor material facilitates electron transport to the cathode, while the donor material facilitates hole transport to the anode. Figure 35 provides a simplified schematic illustrating the key processes underlying the working principle of OPVs, represented in terms of layer energy. In the figure, filled circles denote electrons, while empty circles represent holes.

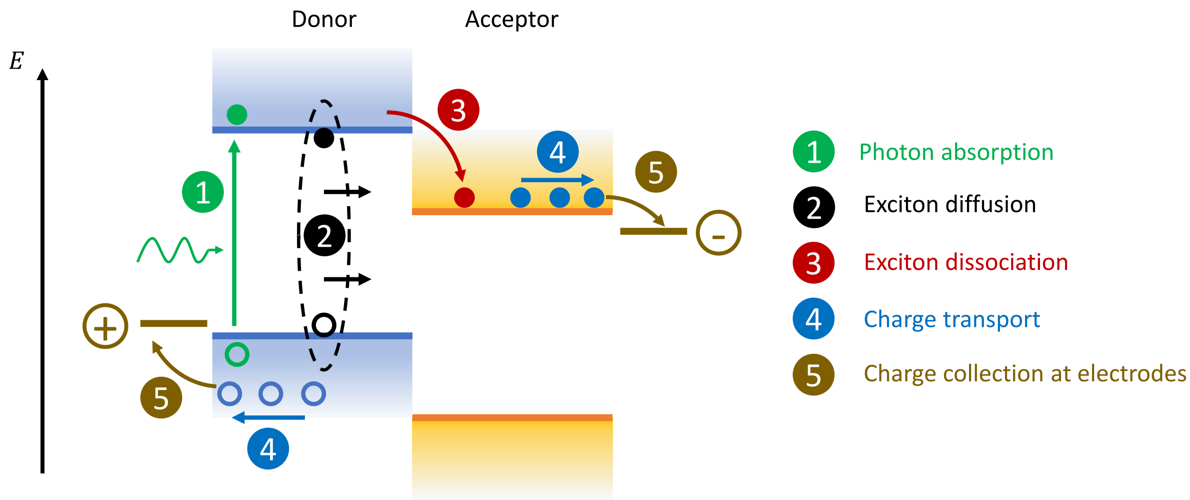

Figure 35: Key processes in the working principle of OPVs in terms of layer energy.

To maximize performance, the morphology of the donor-acceptor blend is carefully engineered to create a nanoscale interpenetrating network, as seen in BHJs. This structure ensures that every exciton formed within the active layer has a high probability of reaching the interface, while also providing continuous pathways for the transport of free charges to the electrodes, minimizing recombination and maximizing device efficiency.

II.2.2. OPV Structure

Similar to other PV technologies, OPVs are fabricated with stacks of different layers, each responsible for a particular role. The most common used layers are briefly described as follows [154]:

- **Active layer**

The active layer is the core of OPV functionality, where photons are absorbed, and excitons are generated. This layer comes in various structural configurations:

1. **Planar configuration (stacked layers):** Two complementary semiconductors are stacked in distinct layers.
2. **Bulk Heterojunction:** The most advanced and efficient structure, where donor and acceptor semiconductors are blended into a single solution, creating a highly interfacial and intricate network for exciton dissociation.

- **Charge transport layers**

Even after exciton generation, diffusion and separation at the donor-acceptor interface, the resulting free charges (electrons and holes) still face the risk of recombination. To prevent this and ensure efficient charge extraction, transport layers are employed in OPVs:

- **Hole Transport Layer (HTL):** The HTL aids in transporting holes (positive charges) from the active layer to the anode, which collects them. Additionally, it blocks electrons, ensuring unidirectional charge flow. Common layers that are employed as HTLs include PEDOT:PSS and Molybdenum trioxide (MoO_3), as well as many polymeric or molecular organic materials.
- **Electron Transport Layer (ETL):** The ETL facilitates the transport of electrons to the cathode while blocking holes. This layer ensures efficient electron extraction and minimizes recombination. Common ETL layers include metal oxides such as Zinc Oxide (ZnO), Tin Oxide (SnO_2) or Titanium Oxide (TiO_2), as well as a broad variety of organic compounds, such as the high performant polyethylenimine ethoxylated (PEIE) [155].

Transparent electrode

This electrode typically consists of a transparent conductive material, such as Indium Tin Oxide (ITO), which permits light to reach the active layer while efficiently collecting charges. Alternative methods involve the use of materials like ZnO associated to silver nanowires, which maintain transparency and conductivity without significantly affecting the light absorption properties of the device [84].

Top electrode

The top electrode in laboratory-scaled OPVs is typically made of metals such as Aluminium (Al), Silver (Ag), or Gold (Au), which are responsible for collecting charges and enabling their transfer to the external circuit. The choice of metal depends on the targeted device architecture (direct or inverted), as collecting holes or electrons require high or low work function materials, respectively.

Other layers, while not directly involved in charge generation and extraction, play crucial roles in device development. The substrate, typically glass or flexible plastics like PET or PEN, provides mechanical support, while encapsulation—whether rigid or flexible—protects the OPV from environmental degradation due to oxygen, moisture, UV radiation, and temperature fluctuations.

Two different structures are normally employed for OPVs: the conventional (or direct) and the reverse structures. The difference lies on the disposition of the electrodes. In conventional topologies, the transparent electrode is employed as the anode, collecting holes (positive charges), while the electrons are collected at the metal electrode. In reverse structures, the opposite is observed [156]. In fact, it has been demonstrates that inverted structures provide improved stability due to the employment of a more stable high work function metal as the top electrode, such as silver of gold [157]. Figure 36 shows the layered structure of OPVs in a (a) conventional and (b) inverted structures.

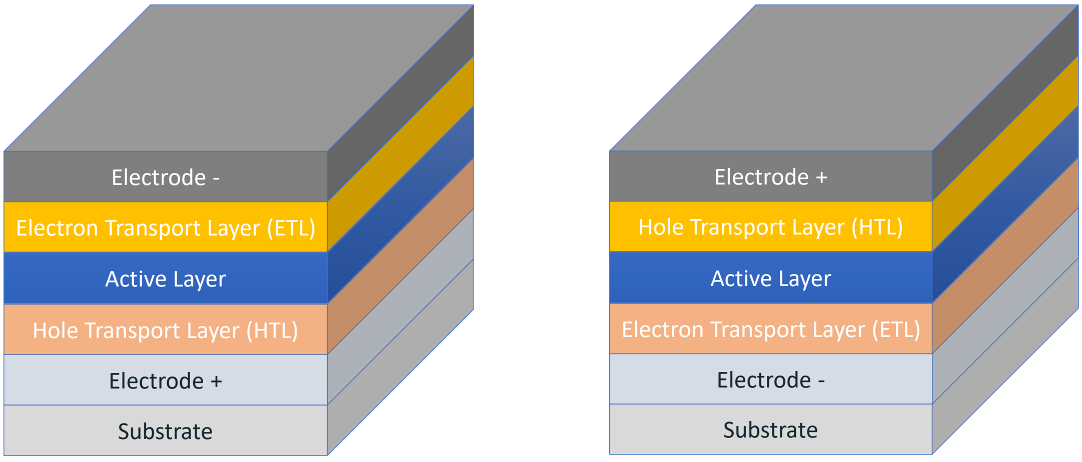

(a) (b)

Figure 36: Layered structure of OPVs. (a) Conventional structure; (b) Inverted structure.

II.2.3. Brief history and evolution of OPVs

Solar cell operates by harvesting optical energy through the photovoltaic effect, firstly seen by the French physicist Alexandre E. Becquerel in 1839 [158]. Decades later, Albert Einstein's groundbreaking theoretical explanation of the photovoltaic effect earned him the Nobel Prize in Physics in 1921 [159]. This effect is the process by which light energy, in the form of photons, is directly converted into free charge carriers within a semiconductor material. When photons strike the material, their energy can excite electrons, allowing them to escape their atomic bonds to get delocalized in the material, and generate an electric current under the influence of an internal electric field. The first step for the development of OPVs had place in 1970 by Alan J. Heeger, Alan G. MacDiarmid and Hideki Shirakawa, which discovered semiconductor properties in polyacetylene, granting them the Nobel Prize in Chemistry in 2000 [160].

Shortly after the initial discovery, the first two-layer OPV device was introduced in 1986 [161]. Although groundbreaking, this device struggled to achieve satisfactory performance due to the limited donor-acceptor interface area which did not enable the efficient separation of excitons (electron-hole pairs) in organic semiconductors. Indeed, due to a quite low dielectric permittivity associated with organic materials, these excitons are strongly bound at room temperature. Consequently, the exciton diffusion lengths in organic materials are very short (5-20 nm), justifying the need for an energetically favourable interface between an electron donor and an electron acceptor material to efficiently dissociate them. In 1995, Yu et al. introduced the Bulk Heterojunction (BHJ) configuration, which marked a significant advancement by blending organic semiconductors to create a nanoscaled networked interface within the device [162]. This pioneering structure, using MEH-PPV as the donor and C_{60} as the acceptor, laid the foundation for subsequent OPV innovations and substantial improvements in their performance enabled by an efficient exciton dissociation and subsequent free charge generation.

Advancements in OPV technology initially focused on material and molecular research and optimization. In the early 2000s, a highly successful BHJ structure was introduced, pairing $PC_{61}BM$ (commonly known as PCBM) as a fullerene acceptor with P3HT as the donor polymer. This configuration gained significant traction, with over a thousand studies published between

2002 and 2010 [163], and achieved a record PCE of 6.5% under standard conditions in 2009 [164] (average efficiency around 5% however). Despite its groundbreaking results, the wide bandgap of P3HT limited solar spectrum absorption, constraining performance. As a result, the OPV research community shifted focus towards developing alternative organic materials with narrower bandgaps for donors, aiming to reduce internal losses and enhance efficiency. As a result, various new polymers and small molecules were explored as alternatives to P3HT as donor materials, often paired with PCBM or its derivatives, such as $PC_{71}BM$ and bisPCBM, as acceptors. Notable polymer donors include PTB7, PTB7-Th, and PBDB-T, achieving PCEs of 7.4%, 10.31%, and 7.45%, respectively [165], [166], [167].

To further improve OPV performance, researchers more recently developed innovative acceptor structures, with Non-Fullerene Acceptors (NFAs) standing out for their significant advancements. Among these, ITIC and Y6 have shown exceptional potential in enhancing efficiency across various studies [168], [169], [170]. Within a short span, ITIC-based NFAs boosted OPV performance to achieve PCEs of up to 14% [171], while Y6-based devices reached even higher efficiencies of 15.7% [172].

In 2020, a new wideband polymer known as D18 was introduced, demonstrating exceptional compatibility with the Y6 NFA and achieving an impressive performance of 18.22% [173]. To further enhance OPV efficiency, modern approaches such as ternary blending have been adopted. This method involves incorporating three distinct materials into a single BHJ (e.g., two donors and one acceptor, or one donor and two acceptors). By leveraging the unique properties of each material, ternary blends enhance device performance through improved light absorption, energy transfer, charge separation, and optimized layer morphology [174]. This innovative strategy has driven advancements in OPV technology, resulting in an impressive PCE of 19.2%, achieved using the D18 donor combined with the PM6:L8-BO active layer [175]. Finally, the current OPV PCE record is 20.82%, obtained in 2024 by Chen *et al.* [176].

The demonstrated performance of OPVs positions them as promising alternatives to conventional inorganic systems for specific outdoor applications. However, their true potential appears to be in indoor environments, where favourable ambient conditions contribute to greater stability and durability. Additionally, their superior efficiency under indoor lighting compared to traditional inorganic technologies underscores their suitability as sustainable energy-harvesting solutions for indoor applications.

II.2.4. Towards indoor energy harvesting

OPVs are particularly well-suited for indoor energy harvesting, especially under LED lighting, due to their ability to match the specific characteristics of indoor light sources. One of the main advantages of OPVs over other photovoltaic technologies, such as Si-based devices, is their tunable absorption spectrum. The energy bandgaps of OPV materials can be engineered to around 1.9 eV, which is optimal for efficiently absorbing light in the range of 400–750 nm, the typical spectrum of indoor LEDs [79]. This alignment enables OPVs to achieve a maximum theoretical PCE nearing 60% under such conditions and allows OPVs to effectively harvest energy from light sources that are narrower in spectrum compared to natural sunlight, unlike Si solar cells, which are optimized for broader sunlight absorption and show lower efficiency under artificial lighting conditions [79]. As an example, Figure 37 shows the absorption spectra of an OPV with PM6:Y6 acting as active layer. The normalized emission spectra of the AM 1.5G and an example white LED are also illustrated in Figure 37.

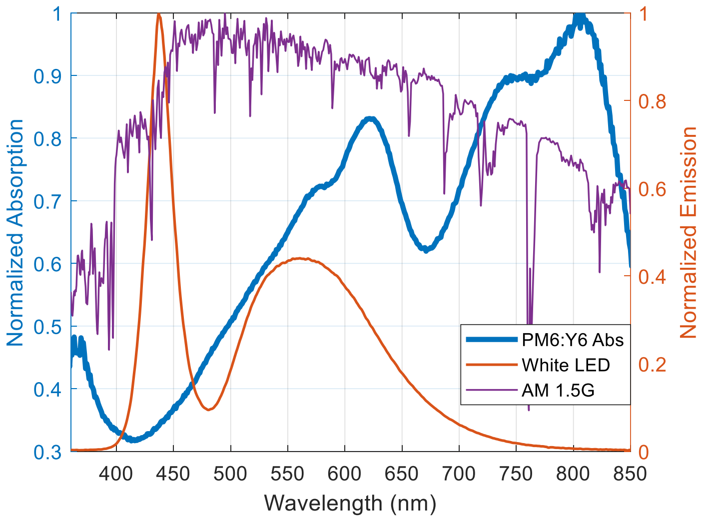

Figure 37: Normalized absorption spectrum of example OPV compared with the emission spectrum of a white LED and the AM1.5G solar spectrum.

Here, a clear mismatch is observed between the absorption spectrum of the active layer and the emission spectrum of the LED. The majority of the absorption occurs in the near-infrared region, whereas most of the emitted power from the LED is concentrated in the green (550 nm) and blue (450 nm) regions. However, compared to silicon-based solar cells, OPVs offer greater flexibility in tailoring their absorption spectrum to align with specific wavelengths, making them more adaptable to different light sources.

In addition to their spectral advantages, OPVs benefit from low energy losses under indoor lighting, as their energy levels can be adjusted to align well with the light source. This efficient energy alignment reduces recombination losses and improves the open-circuit voltage V_{oc} of the device, further enhancing performance. By contrast, Si-based devices, with a fixed bandgap of 1.1 eV, are less suited to the narrow light spectra from LEDs, resulting in a mismatch that limits their efficiency under such conditions.

Moreover, OPVs exhibit high absorption coefficients, which enables them to operate efficiently even with thin active layers. This characteristic is particularly beneficial in low-light environments, as it allows OPVs to generate significant photocurrents despite the limited intensity of indoor light sources. The tailored bandgap of OPVs minimizes thermalization losses, ensuring that absorbed photons are more effectively converted into electricity, resulting in higher PCEs than other technologies like Si, especially under low-intensity illumination [89], [177].

Additionally, OPVs have emerged as an ideal solution for indoor energy harvesting in IoT applications due to their unique material and functional properties. One key advantage is their flexibility and adaptability to various device shapes and surfaces. This makes them suitable for integration into a wide range of IoT devices, such as wearables, smart sensors, and environmental monitors. The ability to fabricate OPVs on lightweight and flexible substrates using low-cost manufacturing techniques like roll-to-roll printing further enhances their applicability. The spectral compatibility of OPVs allows them to achieve exceptional

PCEs, including a record-breaking 36.5% under 1000 lux LED illumination using a PM6:Y6 active layer [75]. Their ability to operate effectively under low-intensity light makes them a reliable choice for continuous energy harvesting.

Finally, the semi permeability and design flexibility of OPVs open up innovative applications in indoor IoT systems. For example, they can be seamlessly integrated into transparent or semi-transparent devices, such as smart windows and decorative lighting systems. Notably, flexible OPVs fabricated on PET substrates have demonstrated efficiencies reaching 19% under 400 lux LED illumination [178]. This multifunctionality aligns with the requirements of modern IoT ecosystems, which demand sustainable and functional power sources.

II.2.5. Indoor performance evaluation standard

As the indoor photovoltaics is a relatively recent concept that gained significant attention in the early 21st century, the metrology to evaluate device performance initially lacked standardization, making comparison across different studies challenging. Outdoor photovoltaic measurements, however, have long adhered to the Standard Test Condition (STC), established in the 1980s by the International Electrotechnical Commission (IEC) under IEC 60904-1. STC defines standardized testing conditions as an irradiance of 1000 W/m² at 25°C, using the AM1.5G solar spectrum.

It was only recently, in 2023, the that IEC introduced standardized characterization methods for indoor energy harvesting with the publication of IEC TS 62607-7-2 [179], titled “Nano-enabled photovoltaics - Device evaluation method for indoor light”. This technical specification recommends assessing photovoltaic performance under illumination levels of 50, 200, and 1000 lux to reflect different indoor lighting conditions. Furthermore, it emphasizes the importance of precisely detailing the optical source characteristics, measurement instruments, and calibration processes to facilitate more consistent performance comparisons in the literature.

II.2.6. Electrical characteristics

The performance of OPVs is evaluated through a set of key parameters that provide insights into their efficiency and functionality. These parameters, including the open-circuit voltage (V_{oc}), short-circuit current density (J_{sc}), Fill Factor (FF), and PCE, are critical for understanding and optimizing device performance. Each parameter reflects a specific aspect of the device operation, from the energy extracted per photon to the maximum power output achievable under standard conditions. These parameters can be obtained from measurements of J-V curves, detailed below.

When light reaches the surface of an OPV, an exciton is generated and subsequently separated into free charges, which are then collected at their respective electrodes. For instance, under short-circuit conditions (low impedance), most of the generated charge carriers contribute to the current. Conversely, under open-circuit conditions (high impedance), charge extraction is prevented, resulting in the maximum voltage observable at the OPV terminals. The relationship between output current density J and the output voltage V of PV devices is mathematically described by the Shockley equation, described below, and which can also be described by the equivalent electrical circuit used to model the device. We describe this equivalent circuit in subsequent sections. Here, J_0 is the saturation current, q is the elementary charge, n is the ideality factor of the device, k is the Boltzmann constant, T is the absolute temperature in kelvins and J_{ph} the generated current density.

$$J(V) = J_0\left[e^{(qV/nkT)} - 1\right] - J_{ph} \qquad \text{II-85}$$

An example of a J-V characteristic of a PV device under illumination is shown in Figure 38, regardless of the used technology. Here, we highlight the short-circuit current density J_{sc} device and the open-circuit voltage V_{oc}. The electric power P_{out} generated by the PV device is calculated as the product of the output current and the output voltage. Consequently, the power density, in W/m² or more commonly mW/cm², is the current density times the output voltage. Please note that, under short-circuit and open-voltage conditions, the PV device does not provide any output power to the external system. We have then highlighted the MPP of the curve, which is described by the voltage V_{max} and current density J_{max} at which the maximum output power density $Power\ density_{max}$ is generated.

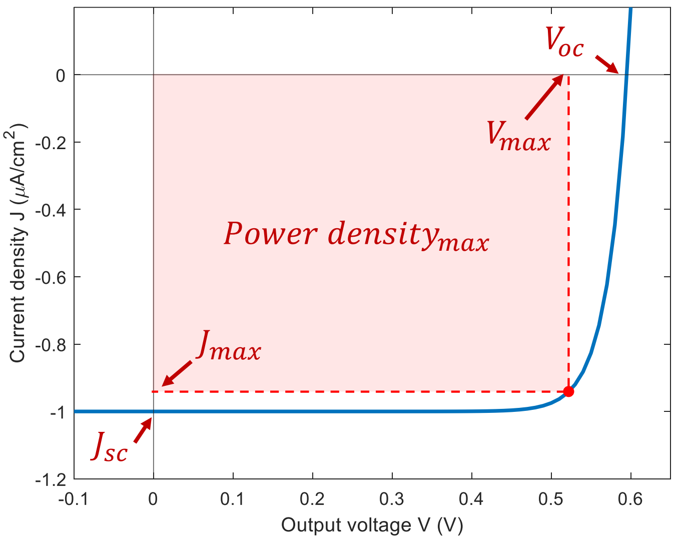

Figure 38: J-V curve characteristic of a PV device.

Following the J-V characteristic of PV devices, the output power P_{out} as a function of the operating voltage V can also be determined. By normalizing to a unit active area, the $P_{out}(V)$ function is obtained, as shown in Figure 39. By knowing that the solar cell provides power only when its bias stays in the IV quadrant of the J-V curve (shown in Figure 38), we have chosen to account only for the operating points that stay in this region.

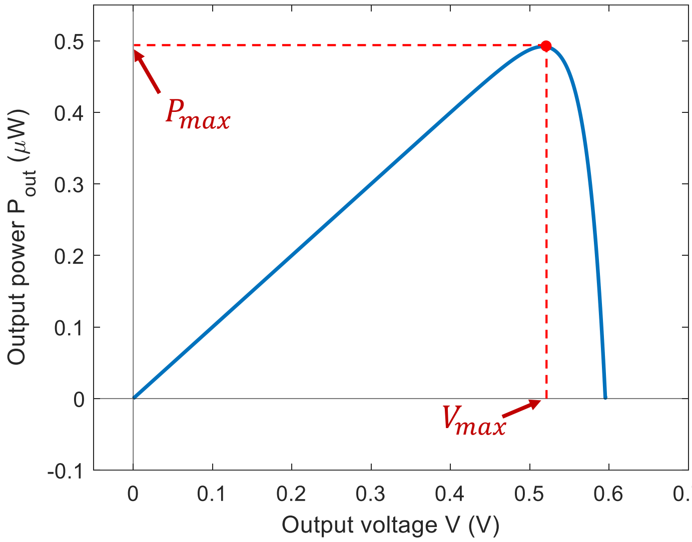

Figure 39: P-V curve characteristic of a PV device.

Similar to photodiodes, the short-circuit current provided by conventional PV devices is described by Equation II-20, while the EQE is described by Equation II-15. The open-circuit voltage can be obtained by Equation II-86, derived from the Shockley equation [180].

$$V_{oc} = \frac{nkT}{q} \ln\left(\frac{J_{ph}}{J_0} - 1\right) \quad \text{II-86}$$

In fact, the open-circuit voltage depends heavily on the energy difference between the LUMO of the acceptor and the HOMO of the donor. This dependence arises from the relationship between the energy offsets at the donor-acceptor interface and the efficiency of charge separation and recombination processes. In theory the maximum obtainable $V_{oc_{max}}$ depends only on the difference between both energy levels. However, in real devices, the V_{oc} is lower than the theoretical maximum due to different energy losses, such as non-radiative recombination and voltage losses at the donor-acceptor interface [154]. Consequently, the V_{oc} can be obtained from Equation II-87, where ΔE_{loss} represents the energy losses.

$$V_{oc} = \frac{1}{q}\left[E_{LUMO}^{acceptor} - E_{HOMO}^{donor}\right] - \Delta E_{loss} \quad \text{II-87}$$

An ideal OPV device, without any internal losses, would generate maximum theoretical output power equals to V_{oc} times I_{sc}. However, due to different electrical losses, the MPP does not occur at V_{oc} and I_{sc}. To account for this, we define the FF as the ratio of the maximum power density output of the device to the product of the open-circuit voltage and the short-circuit current density, as described in Equation II-88. It is a key performance parameter in PV devices that quantifies the quality of the device J-V characteristic. It is a measure of how "square" the curve is, reflecting the ability of the device to deliver maximum power.

$$FF = \frac{Power\ density_{max}}{V_{oc} \times J_{sc}} = \frac{V_{max} \times J_{max}}{V_{oc} \times J_{sc}} \quad \text{II-88}$$

The fill factor is a positive value inferior to 1, 1 being an ideal OPV. Finally, the PV device PCE is the output power P_{out} (or power density) divided by the incident optical power P_r (or irradiance E), as shown below:

$$PCE = \frac{P_{out}}{P_r} = \frac{V_{oc} \times I_{sc} \times FF}{P_r} = \frac{V_{oc} \times J_{sc} \times FF}{E} \qquad \text{II-89}$$

II.2.6.1. Static electrical model

All PV devices can be modelled as an electrical equivalent circuit, which tries do described all phenomena that occurs within the device. One of the simplest yet effective models is the single-diode equivalent circuit, which uses a single diode to describe the non-linear (logarithmic) behaviour of the solar cell (refer to Figure 40).

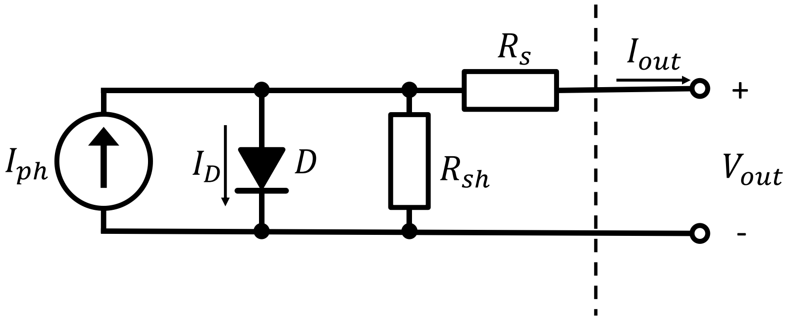

Figure 40: Single diode model of PV devices (static operation).

Here, I_{ph} represents the actual generated current of the device. In fact, this current cannot be directly determined from the responsivity $R(\lambda, \Psi)$, since this parameter is obtained under short circuit conditions, and inherently accounts for different internal losses within the device. Therefore, to obtain I_{ph}, knowledge of the Internal Quantum Efficiency (IQE) is required. IQE quantifies the ratio of photogenerated charge carriers per absorbed photons.

The shunt resistance R_{sh} models current losses within the device, being normally caused by recombination and leakage pathways. Higher R_{sh} values represent reduced current losses. The series resistance R_s accounts for voltage losses due to the intrinsic resistances of the device materials and the interfacial resistances between layers. Lower R_s values correspond to reduced voltage losses. Please note that, if $R_{sh} \to \infty$ and $R_s \to 0$, the device approaches an ideal lossless behaviour, leading to $FF \to 1$.

In this scenario, the Shockley ideal equation can be adapted to account for different losses, modelled as both R_{sh} and R_s. Here, the output current I_{out} as a function of the output voltage V_{out} can be obtained as shown in Equation II-90.

$$I_{out} = I_{ph} - I_D - I_{sh}$$

$$I_{out} = I_{ph} - I_0 \left[\exp\left(\frac{V_{out} + I_{out}R_s}{n\frac{kT}{q}} \right) - 1 \right] - \frac{V_{out} + I_{out}R_s}{R_{sh}} \qquad \text{II-90}$$

This transcendental equation describes the I-V characteristics of any PV device while accounting for its internal losses. In fact, the impact of both series and shunt resistances can be observed in the I-V (or J-V) characteristics of an OPV. An increase in R_{sh} causes a steeper initial slope near the short-circuit condition, reflecting greater voltage losses. Conversely, a decrease in R_s, indicative of higher leakage losses, results in a steeper final slope near the open-circuit voltage condition. This behaviour is illustrated in Figure 41.

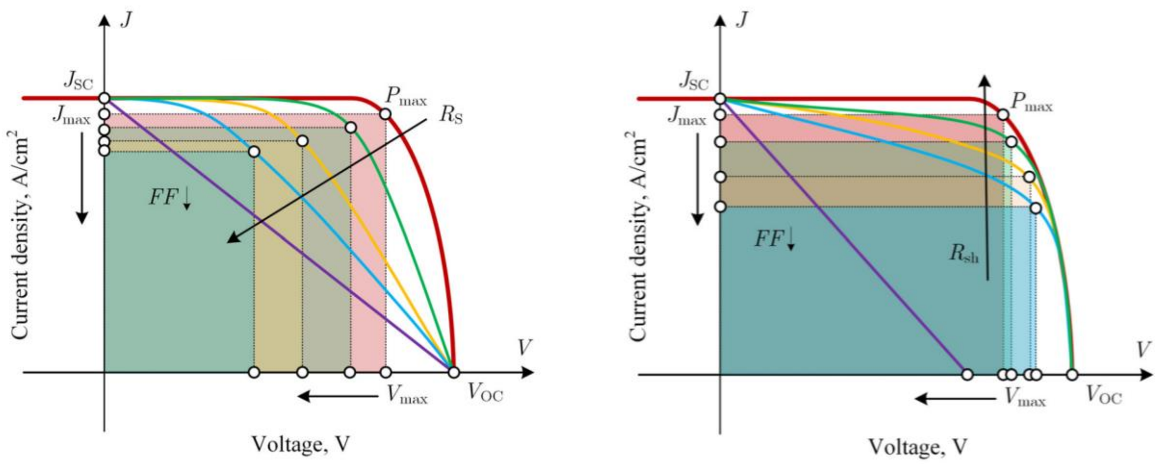

Figure 41: Effect of internal resistances on the J-V characteristic of a PV device: (a) increasing R_s; (b) increasing R_{sh}.

Source: Reproduced with permission from reference [181].

More refined models can be used to describe the electrical behaviour of PV devices in greater detail. For instance, the double-diode model provides improved accuracy compared to the single-diode model by incorporating additional recombination mechanisms within the solar cell [182]. This model incorporates two diodes to represent different recombination processes. Even more complex models are discussed in the literature, including the triple-diode model [183], models that separately analyse the unique properties of each layer and their impact on performance under varying light intensities [184], [185] and models that consider the interconnection of multiple OPV cells in large-area modules [186]. However, such models fall beyond the scope of this thesis.

Powerful characterization techniques like impedance spectroscopy (also known as Electrochemical Impedance Spectroscopy, or EIS) offer precise insights into the internal workings of PV devices. By analysing the Nyquist diagram obtained under various illumination conditions, EIS reveals valuable information about internal processes and losses. [187], [188]. This technique is particularly useful for studying charge transport, recombination dynamics, and extracting internal capacitance values, which are linked to the dielectric properties and thicknesses of the device layers. Nonetheless, this characterization method is also out of the scope of this thesis.

II.2.7. Dynamic behaviour

The dynamic behaviour of OPVs refers to the time-dependent processes and mechanisms that govern their performance, particularly under varying illumination. This behaviour includes charge generation, transport, recombination, and extraction dynamics, which are influenced by material properties like charge carrier mobilities, exciton diffusion, and interfacial effects. Indeed, in a varying illumination scenario, excitons and free charge carrier require a certain amount of time to go from one state to another.

Compared to crystalline Si-based devices, OPVs demonstrate inferior charge carrier mobility, typically below $10\ cm^2/Vs$, and often ranging between 10^{-3} to $10^{-1}\ cm^2/Vs$ in many cases [189]. This reduced mobility is attributed to several factors. OPVs often feature a disordered or semi-crystalline structure in the active layer, which introduces traps and energetic barriers to disturb charge movement. Charge transport is also mostly described through polarons, which accounts for the significant local polarization effects of free charges in the organic structure. Multiple trapping-detrapping processes are also governing the global charge transport in organic semiconductors. Additionally, organic materials have a lower dielectric constant (~3) compared to silicon (~11.7), leading to weaker screening of Coulombic interactions [190]. Altogether, this makes charge carriers in OPVs more prone to recombination [191].

The low mobility of free charge carriers results in higher recombination rates within the device. Consequently, it limits the active layer thickness between 100 and 200 nm, ensuring charge extraction before recombination. As OPVs are considered for use in communication scenarios, understanding the parameters of charge mobility and exciton diffusion length is critical for further comprehension.

Two primary factors influence the time response of an OPV: the low drift mobility of organic materials and the discharge time through a hypothetical load resistance. The first factor, discussed previously, is governed by Equation II-91, where W is the thickness of the active layer, μ is the hole mobility and E is the electrical field inside the OPV [192].

$$\tau = \frac{W}{\mu E} \quad \text{II-91}$$

The time required to discharge the OPV through a hypothetical load resistance is determined by the RC time constant, which arises from the device geometrical capacitance. As previously discussed, OPVs consist of a stack of multiple layers sandwiched between two electrodes. This structure naturally creates capacitances, as the device operates similarly to a capacitor, with two conductive electrodes separated by a dielectric material with permittivity ε. Consequently, the device acts as a low-pass filter, characterized by a time constant $\tau_{RC} = RC$, where R represents the combined internal and load resistances, and C is the geometrical capacitance of the OPV [193]. Finally, the RC time constant is described by Equation II-92, where A_r is the active area of the OPV [192].

$$\tau_{RC} = R\varepsilon\frac{A_r}{W} \quad \text{II-92}$$

Both time responses can limit the OPV response, and in fact, the slower process will govern the dynamics of the device. As the device size increases, the geometric capacitance increases and dominates this behaviour. Although it is essential to account for all factors influencing the dynamic behaviour of OPVs, comprehensively modelling every aspect on a large scale is impractical. Instead, high-level characterizations can be used to model the overall dynamic behaviour of the device.

Global characterization of PV devices can be achieved through various methods. Normally, for communication systems, a common approach is to determine the receiver bandwidth B, or cutoff frequency f_c. One approach involves direct frequency measurement, where the frequency response of the solar cell is evaluated by applying a sinusoidal signal of varying frequency to a light emitter, such as an LED. The amplitude and phase of the output signal from the receiver are then measured, enabling the generation of a Bode plot that illustrates the frequency-dependent behaviour of the device, therefore obtaining the bandwidth B. Figure 42.a shows an example of a Bode measurement (magnitude only).

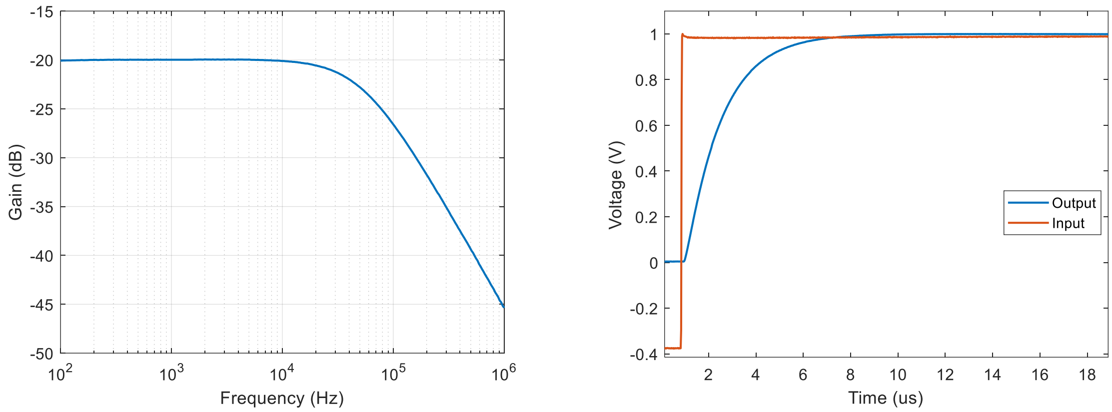

(a) (b)

Figure 42: Different dynamic characterization methods: (a) frequential method, through direct Bode measurement; (b) temporal method, through the rise time τ_r measurement.

Alternatively, and considering that the geometric capacitance dominates de system, the bandwidth can be estimated by measuring the time response τ_{RC} of the receiver. In this approach, a square wave input is applied to the emitter (e.g., an LED), and the resulting response of the solar cell, modelled as a low-pass filter with an RC time constant, is observed. The overdamped response is characterized by the rise time τ_r, which is the time taken for the output to increase from 10% to 90% of its maximum value. In such systems, the time response τ_{RC} relates to the rise time τ_r by Equation II-93, while the system bandwidth is directly obtained through the RC constant, as described by Equation II-94 [103].

$$\tau_r = 2.2\tau_{RC} \tag{II-93}$$

$$B = \frac{1}{2\pi\tau_{RC}} = \frac{1}{2\pi RC} \tag{II-94}$$

Finally, the bandwidth B can then be calculated through the rise time τ_r using Equation II-95 [103]. If the fall time τ_f is superior than the rise time, it should be used instead of τ_r, as the equation applies for both rise and fall times. Figure 42.b shows an example of the transient behaviour of OPVs.

$$B = \frac{0.35}{\tau_r} \tag{II-95}$$

II.2.7.1. Dynamic equivalent model

From the static equivalent circuit shown in Figure 40, a dynamic equivalent model can also be obtained, i.e. a model that takes into account different internal characteristics that affects the charge kinetics of the device. In fact, the characteristics of organic photovoltaic cells can be modelled exactly as inorganic ones [194]. The single (or double) diode models can be converted into small-signal equivalent circuits to understand their AC (or dynamic) performance (valid only for small signal amplitudes compared to the DC value). In these models, the diodes are replaced by a dynamic resistor r_d (which models the local resistance of a diode for a given operating current) in parallel with two capacitors, the junction C_j and the diffusion C_{diff} capacitances, as shown in Figure 43. The angular frequency ω symbol illustrates the AC variables, such as the generated AC current $i_{ph}(\omega)$, the output current $i_{out}(\omega)$ and voltage $v_{out}(\omega)$.

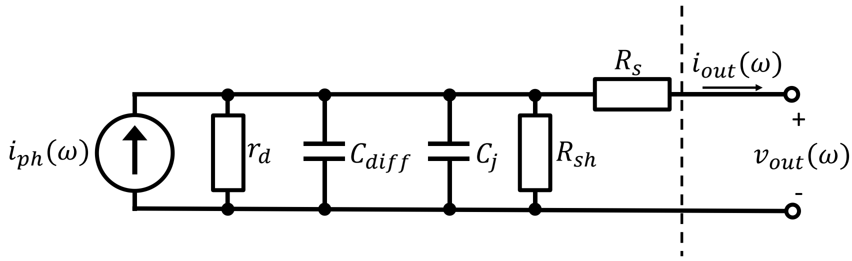

Figure 43: Equivalent circuit model of a PV device for communication purposes.

Unlike conventional silicon-based devices, OPVs do not rely on two doped semiconductors forming a PN junction with a depletion region, which typically gives rise to a junction capacitance C_j. In bilayer OPVs, however, localized space charges, arising from impurities or broken bonds, accumulate at the donor-acceptor interface, where band bending occurs [195]. In such configurations, the junction capacitance at the interface can be measured using AC perturbation techniques.

This approach is also applicable to BHJ OPVs, but the relationship between capacitance and the donor-acceptor interface remains a topic of discussion [196]. Two main models attempt to explain this: the first suggests a weak band bending at the interface [197], while the second, more contemporary model approximates the active layer blend as a single polymer sandwiched between two electrodes. In this case, a space charge forms near the cathode, resembling a Schottky junction [198], [199].

In OPVs, diffusion capacitance C_{diff} arises from the movement of charge carriers (electrons and holes) within the device active layer. This capacitance is particularly significant when the device operates under forward bias, where increased injection and recombination of charge carriers occur. The diffusion capacitance reflects the dynamic response of the carrier population to changes in voltage, influencing the overall frequency-dependent behaviour of the OPV [200].

Under single-diode model, the dynamic resistance r_d is described by Equation II-96, where n is the diode ideality factor, V_T is the thermal resistance, V_{out} is the DC output voltage, I_{out} is the DC output current and I_0 is the reverse saturation current [201].

$$r_d = \frac{nV_T}{I_0(e^{\frac{V_{out}+I_{out}R_S}{nV_T}})} \qquad \text{II-96}$$

The diffusion capacitance C_{diff} is defined as shown in Equation II-97 [194]. Here, τ represents the charge carrier lifetime. For BHJ OPVs, the junction capacitance C_j cannot be mathematically determined, as previously discussed.

$$C_{diff} = \frac{\tau}{nV_T} I_0 e^{\frac{V+IR_S}{V_T}} \qquad \text{II-97}$$

This concludes the discussion of the key principles, material properties, and performance characteristics of OPVs for indoor energy harvesting, providing a solid foundation for the analyses and applications explored in the subsequent sections of this thesis.

II.3. The SLIPT context

Due to the limited research available on SLIPT, this thesis extends the analysis to the broader application of OWC with PV devices, without being restricted to VLC or OPVs. Nevertheless, the presented analysis remains general and provides valuable insights that can be applied to SLIPT scenarios using VLC and OPVs. Furthermore, while the works reviewed are not limited to indoor IoT scenarios, the findings are highly relevant and adaptable for such applications.

In this section, we will synthesize the significant contributions that have shaped the current understanding of SLIPT, beginning with the initial proof-of-concept studies, progressing through key advancements, and concluding with an analysis of the critical aspects of the works discussed.

II.3.1. Preliminary demonstration

Although the first white LED based VLC system was demonstrated in 2000, it was not until 2013 that a PV panel was successfully used for both simultaneous energy harvesting and data reception. Kim et Won's pioneering work employed a 729 mm² commercial Si PV panel, which harvested solar energy while simultaneously receiving a VLC signal [202]. Their research also examined the effect of solar irradiance on the received optical amplitude, establishing that despite using different optical sources (sunlight and white LEDs), the concept of SLIPT was validated. In fact, the key feature of SLIPT lies in the separation of the DC component (energy) and the AC component (communication) at the receiver.

Shortly after, in 2014, Professor Haas's research group demonstrated the first use of a single optical source for both illumination and data transmission in a SLIPT context, employing a commercial silicon PV panel with an active area of 432 cm². In their initial proof of concept, they connected the photosensitive device to a variable load and an analog signal processing circuit composed of a Low-Pass Filter (LPF) and an amplifier [203]. This approach, while simple, showed the potential of PV-based SLIPT systems for both energy harvesting and data detection. The variable load was primordial in determining the operating point of the solar panel, thus impacting both communication (BER) and energy harvesting (harvested power) performances. The research progressed in 2015 with the development of the first integrated SLIPT front-end receiver circuit, further advancing this dual-functionality approach, as shown in Figure 44 [204].

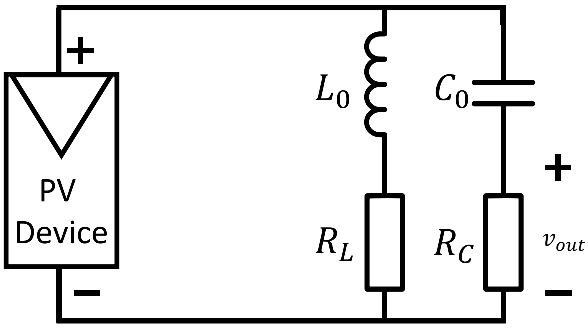

Figure 44: First proposed SLIPT front-end receiver circuit.

Source: Modified with permission from reference [204].

The proposed system is based on a LPF to extract the DC component for energy harvesting, and on a High-Pass Filter (HPF) to recover the AC signal for data decoding. Thus, the front-end circuit is entirely passive, using components such as resistors, inductors and capacitors. The generated electric signal, containing both DC and AC components, is filtered so that low frequencies are blocked by the capacitor C_0, while higher frequencies are attenuated by the inductor L_0. The recovered signal v_{out} is then read across the resistor R_c in the HPF branch. This circuit topology is particularly advantageous because it eliminates the need for external power sources.

In this pioneer work, the solar panel is modeled using the well-established single-diode electrical model, which accurately reflects the behavior of the solar panel in terms of energy harvesting. Additionally, the study conducts rigorous analyses, exploring the influence of external parameters (such as R_L, L_0, R_c, C_0) on both EH and communication performances. It also examines the frequency response of the solar panel for various load-based operating points. Finally, it introduces a novel noise analysis by coupling the single-diode model with the proposed front-end circuit. Furthermore, using complex modulation schemes such as OFDM associated to M-ary Quadrature Amplitude Modulation (M-QAM), they achieved 11.84 Mbit/s (associated to a 1.6×10^{-3} BER) while simultaneously harvesting 30 mW, for an irradiance of $3.65 \times 10^{-3} W/cm^2$.

These pioneering studies raised several important questions regarding the performance of PV devices in SLIPT scenarios. Key concerns include the impact of the solar panel operating point and illumination levels on both communication and EH performance. Indeed, in traditional static operations of PV systems, optimal energy output is achieved by operating at the MPP, which is tracked through various methods to ensure maximum efficiency. However, in SLIPT applications, operating at the MPP does not necessarily lead to the best communication performance, an important aspect that will be elaborated on in the following chapters, where the trade-offs between EH and data transmission are analyzed in depth. Furthermore, these pioneer works brought up different questions concerning PV performances in SLIPT scenarios, such as (but not limited to) the effect of partial shading on device efficiency, the challenges of simulating indoor environments with solar cells and how the flexibility of the solar cell material influences overall system performance.

In fact, it wasn't until 2017 that the telecommunications community officially conceived the term SLIPT to describe the combined processes of energy harvesting and data reception [205], [206]. Though SLIPT is a newer concept compared to VLC, it has shown significant increase in recent years. As illustrated in Figure 45, the number of research papers containing the term "Simultaneous Lightwave Information and Power Transfer" in their titles (in blue) and within their texts (in red) has steadily grown (data obtained through Google Scholar search engine).

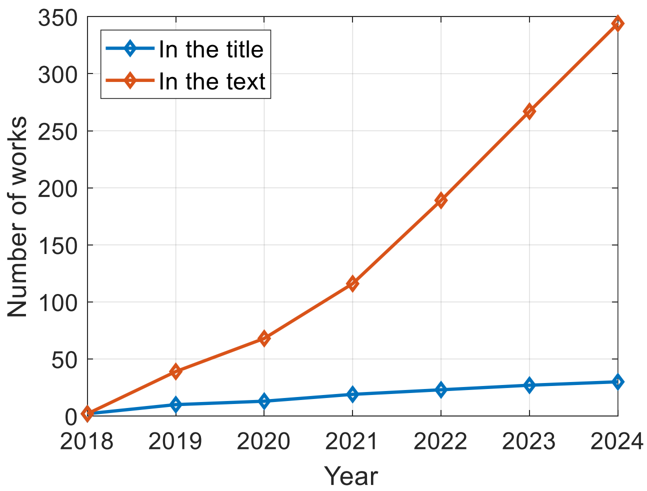

Figure 45: Number of publications containing the term "Simultaneous Lightwave Information and Power Transfer" over the years.

Source: Data obtained from the Google Scholar search engine in October 2024.

Even before the first SLIPT proof of concept, the impressive PCE of OPVs under indoor illumination naturally raised questions about their dynamic performance in VLC applications [207], [208]. Although the devices were referred to as photodetectors, they were fabricated with PV architectures. However, by applying a negative bias, their energy-harvesting functionality was denied, focusing instead on their potential for data reception, marking an early step in exploring OPVs beyond their EH capabilities.

Still in 2015, a state-of-the-art OPV device was tested, for the first time ever, in the SLIPT context, using the same front-end circuit developed in [204] (refer to Figure 44). This OPV, with a small active area of 8 mm², demonstrated remarkable results, achieving a data rate of 34.2 Mbit/s with a BER of 4.08×10^{-4} over a 1-meter direct link while simultaneously generating $430\ \mu W$ of electrical power from a red laser at its MPP [165], [192]. At the time, this represented the highest data rate achieved by VLC systems based on PV receivers.

II.3.2. Key studies and current state-of-the-art

Given its novelty, the SLIPT concept has opened up numerous avenues for exploration. However, it lacks standardized testing protocols, unlike PV technologies used in outdoor scenarios. Most current research focuses on uncovering unique behaviors and characteristics of PV devices in SLIPT applications, which makes comparation difficult. Nonetheless, some key studies are summarized in the current section. Although some works unveil different aspects of 1st and 2nd generation of solar cells, some studies are general and can be extended to any photovoltaic device technology (such as the front-end circuit provided in [204]). Additionally, the current development is not restricted to IoT or indoor scenarios, as it lacks sufficient references to fully support such a narrow scope, without loss of generality.

II.3.2.1. On the dedicated front-end circuit

The key distinction between traditional VLC systems and the SLIPT ones is the use of PV devices instead of photodiodes, coupled with a specialized front-end circuit designed to separate energy and data. Therefore, we highlight some of the main findings related to the design and operation of this system.

In 2016, a research team from Yonsei University in South Korea developed the first active front-end circuit powered directly by the PV receiver [209]. Using a 42.35 cm² monocrystalline Si solar panel, the system harvested energy from 250 lux over a distance of 10 cm, charging an embedded battery to power a DC-DC (boost) converter. The converter could apply a 30 V reverse bias to the PV panel, improving the carrier drift velocity and enhancing the device bandwidth. Finally, the system achieved 17 Mbit/s data rate with a BER of 10^{-3} over a 10 cm link. Indeed, PV devices under energy harvesting constraints operate between short-circuit and open-circuit conditions, normally at the MPP, introducing non-linearity effects, such as the ones observed in [210]. By operating the PV panel in reverse bias condition (photoconductive mode), the device benefits from reduced junction capacitance, improving linearity, response time and responsivity. The same strategy was later adapted for Underwater Wireless Optical Communication (UWOC) by Lei *et al.*, where multiple solar panels were used to detect signals while simultaneously powering all the electronics involved in the receiver [211].

Soon after, two major studies proposed a more advanced circuit design to enhance both EH and data reception. In [212], a novel circuit, derived from [204], was theoretically developed. It optimized the operating point and bandwidth by replacing the original load (R_L) and communication branch (R_C) with more suitable circuits, as shown in Figure 46.

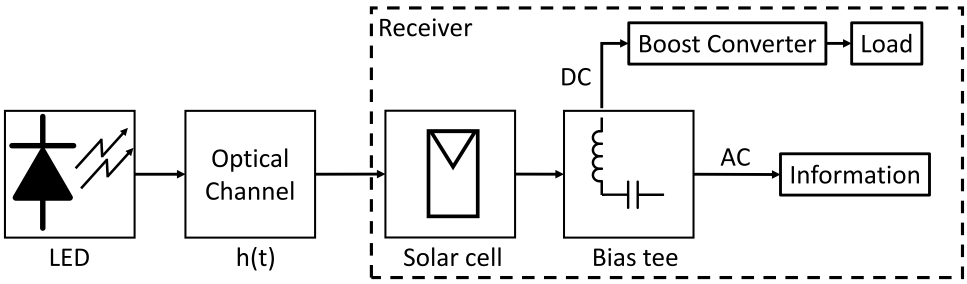

Figure 46: Front-end circuit proposed by Sepehrvand *et al.*

Source: Reproduced with permission from reference [212].

The communication branch was replaced by a TIA-based circuit, powered by the EH branch. The load R_L was substituted by a DC-DC converter with a controllable switch, allowing dynamic adjustment of the solar cell operating point. By employing the single-diode model, the analysis explored output power and capacity bound based on operating voltage, determined by the DC branch. As the operating voltage increases, the system maximum capacity bound decreases while output power rises until it reaches the MPP. Beyond this point, the receiver experiences a drop in performance, as higher voltages surpassing the MPP do not yield significant gains in output power nor capacity bound. The study further introduces an optimization procedure based on the receiver battery condition, emphasizing the inherent trade-offs in SLIPT scenarios between energy harvesting and communication performance. This approach helps balance power output and data reception efficiency, depending on real-time system demands.

The self-reverse-biased PV configuration, first introduced in [209], was further improved by Kadirvelu *et al.*, who implemented the first experimental front-end circuit using a DC-DC converter capable of dynamically adjusting the PV device operating point based on energy requirements [213]. Unlike previous designs, the communication branch still used a resistance R_C to signal detection, further processed by using a band-pass filter and a comparator. Using a 9 cm² GaAs cell, the system generated $347\ \mu W$ from a red LED placed 32.5 cm away, while simultaneously decoding data at 2.5 kbit/s. In fact, this power level was sufficient to supply all electronics on the receiver side.

Other approaches involve automatically switching the solar cell operational mode based on the desired scenario, such as the technique proposed by De Oliveira Filho *et al.* [214]. This method, known as time-switching SLIPT, features an EH branch with a Maximum Power Point Tracker (MPPT) and a supercapacitor. The EH branch can be fully disconnected from the solar cell via a controllable switch. When disconnected, the solar cell is reverse-biased using a TIA, improving data reception capabilities.

Although various architectures have been introduced, they all share a common principle: extracting the DC component of the electrical signal from other frequency components. The main differences between these approaches lie in optimizing the solar cell operating point and employing different signal processing techniques. Some advanced methods, such as equalization in the signal decoding branch, have also been proposed to enhance performance [215].

II.3.2.2. On the illumination influence

Photodiodes are primarily designed to operate in photovoltaic or photoconductive modes, where the output current responds linearly to the incident optical power under moderate illumination. Photovoltaic devices, however, are optimized to deliver maximum power under specific lighting conditions. As a result, varying illumination can significantly affect their performance, influencing both EH and data reception capabilities. While current increases linearly, the output voltage saturates near the open-circuit voltage (a concept explained in subsequent sections and chapters). Finally, key studies have examined how different illumination impacts PV based systems performance, offering deeper insights into this behaviour.

Bialic *et al.* explored how illumination affects the communication performance of two types of PV panels — CIGS and a-Si — outside the SLIPT context [216]. Both devices were directly connected to an oscilloscope modelled as a load R_L, without the use of active circuits. In a first experiment, increasing the signal (without any external constant lighting) by reducing the distance between emitter and receiver initially improved the SNR, but led to saturation and a subsequent drop. In a second analysis, the authors verified the influence of an external DC lighting on the performance. The SNR measured for the CIGS panel declined with higher illumination, while the a-Si panel showed an unexpected improvement. Figure 47.a and Figure 47.b illustrates these contrasting behaviours.

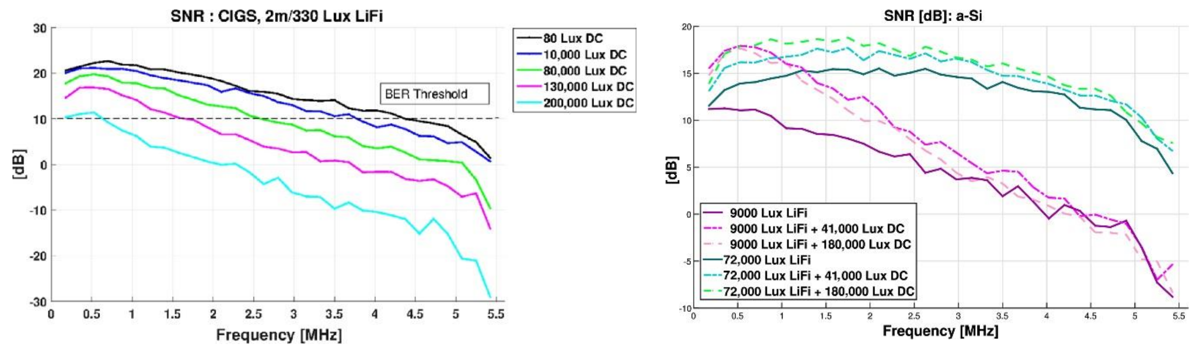

(a) (b)

Figure 47: SNR experimentally obtained with two PV panels in function of the illumination: (a) results obtained with a CIGS panel and constant signal intensity (330 lux), but variable lighting condition (from 80 lux up to 200k lux); (b) results obtained with an a-SI panel and two signal intensities (9000 and 72k lux), with variable lighting condition (from 0 lux up to 180k lux).

Source: Reproduced with permission from reference [216].

The exact reason behind the improved performance of the a-Si device with background illumination remains unclear. Although the experiments were conducted under illumination levels unrealistic for typical indoor environments, the findings suggest potential suitability for outdoor applications.

A French research team conducted an in-depth analysis of how illumination affects the frequency response of various photosensitive devices, leading to several publications. In [217], Lorrière *et al.* characterized an APD and a CIGS module in a VLC experimental setup. They adjusted the distance between the emitter and receiver, varying both the DC and peak-to-peak illumination. Under low light conditions, the photodiode outperforms the PV device due to its higher sensitivity. However, as the distance decreases, the optical signal increases and the APD saturates at around 16k lux, while the solar cell continued to improve, emphasizing the strength of PV devices in high-illumination environments. Since the optical signal itself increases when decreasing the distance, both devices benefit from better SNR before reaching saturation (which does not happen with the CIGS module).

The same devices were tested outdoors under varying solar irradiation while maintaining a constant distance between emitter and receiver, ensuring consistent signal intensity [218]. Similar behaviour to that observed in the CIGS device in [216] was seen in both receivers: as ambient light increased, they approached saturation, causing a reduction in signal magnitude. Nonetheless, the solar cell demonstrated better performance than the APD under these conditions. Finally, the authors defined Error-Free Maximum Frequency (EFMF) as the highest operational frequency where communication remains error-free, with a BER below 10^{-3} when using error correction codes. Figure 48 shows the obtained EFMF for different solar intensity for both receivers. The PV module demonstrates greater robustness than the APD under intense illumination, allowing the system to support higher data rates in such conditions.

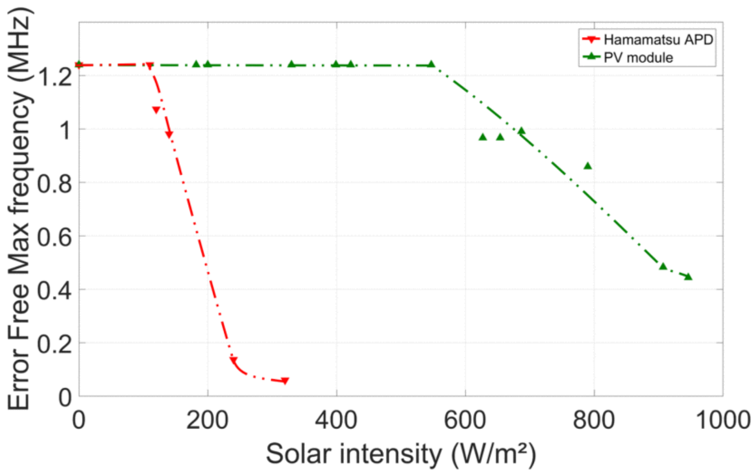

Figure 48: Error free maximum frequency in function of the incident solar intensity for VLC receiver based on APD (in red) and on PV module (in green).

Source: Reproduced with permission from reference [218].

The same French research team adopted an innovative approach by examining various aspects that can affect an OPV module, including partial shading, illumination, and operating modes [194]. Lorrière *et al.* compared the device behaviour in short-circuit mode (using a TIA) and open-circuit mode (connected to high impedance). As detailed before, the short-circuit current changes linearly with light intensity, while the open-circuit voltage follows a logarithmic behaviour, saturating under strong illumination. Under open-circuit conditions, the device exhibits reduced signal amplitude as ambient DC lighting increases, a pattern observed in several previous cases. In contrast, under short-circuit conditions, external constant lighting has no direct effect on the frequency response of the OPV module. Studies indicate that the device achieves a higher bandwidth when operating in short-circuit mode.

This analysis was followed by a partial shading experiment where all nine cells of the OPV module were progressively shaded, from 0% to 99%, in 11% increments. Under short-circuit conditions, shading effectively reduced the module active area, diminishing the signal amplitude. However, under open-circuit conditions, partial shading mitigated the saturation effect, resulting in increased signal amplitude but reduced bandwidth (refer to Figure 49.a).

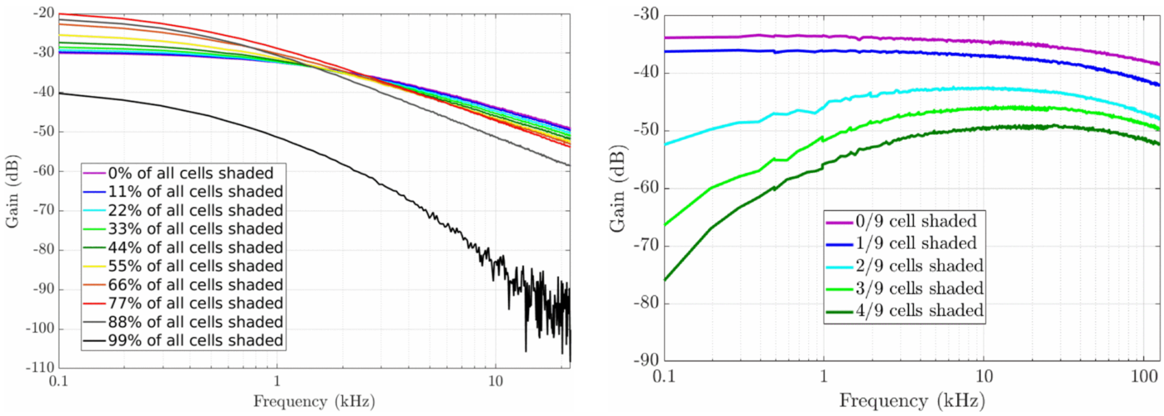

(a) (b)

Figure 49: Frequency response of OPV, analysed in [194], for different conditions: (a) in open-circuit mode with partial shading; (b) in short-circuit mode with varying numbers of shaded cells.

Source: Reproduced with permission from reference [194].

An additional analysis examined the effect of shading specific cells. Under open-circuit conditions, shading more cells led to a reduction in overall signal magnitude with a slight decrease in bandwidth. In contrast, under short-circuit conditions, shading one or more cells introduced a bandpass filter effect, as seen in Figure 49.b. This behaviour arises because shaded cells act as high-impedance elements at low frequencies, modifying the frequency response of the device.

Das *et al.* were the first to investigate the effects of solar radiation intensity on both communication and energy harvesting performances with a SLIPT system using a solar simulator and operating at the MPP [215]. They employed the more precise double-diode model to estimate device performance under varying irradiation levels. As intensity increased, harvested power rose, while the maximum achievable data rate declined proportionally. This behaviour was in fact observed in previous experiments under open-voltage condition, but in the current scenario, the communication branch uses a TIA, and the irradiance variation does not saturate it, but decreases the SNR due to higher noise.

Chen *et al.* effectively highlighted the non-linearity of a PV device output voltage in function of the incident optical power in their innovative work [219]. They successfully demonstrated the non-linear effect under low illumination using eye diagrams (refer to Figure 50). To mitigate this non-linearity, they proposed two techniques: (1) localized distortion compensation lighting, which adds extra DC lighting to move the PV cell out of the non-linear region; and (2) post-distortion compensation, where distortion is estimated at a specific illumination level and corrected after signal reception.

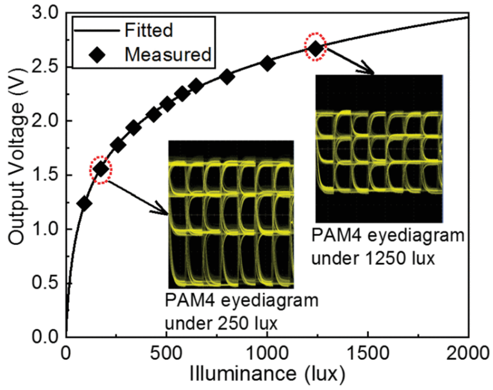

Figure 50: Measured eye diagram for multiple illumination levels, originated from the experiment described in [219]. Evaluated at open-circuit condition.

Source: Reproduced with permission from reference [219].

Recently, Morales *et al.* investigated the bandwidth and gain of a commercial Si panel under varying illumination levels, ranging from 42 lux to 5530 lux [220]. Through the analysis of the open-circuit voltage, they performed impedance spectroscopy measurements to obtain the equivalent electrical model for each illumination. Their findings showed that higher illumination levels lead to increased cutoff frequencies but decreased gain, highlighting the need to balance SNR (determined by the electrical signal amplitude) and bandwidth.

A recent innovative work by Zhou *et al.* investigated interesting aspects affecting the communication performance of crystalline Si (c-Si) PV-based receivers [221]. The authors employed seven different c-Si PV cell architectures under three different LED colours (blue, green and red) to evaluate the impact of light wavelength on the communication performance. The study tested the cells at varying operating voltages and light intensities (100 W/m^2, 300 W/m^2 and 500 W/m^2). The findings reveal that the operating voltage plays a significant role on the communication performance, with higher operating voltages leading to reduced bandwidth. Moreover, the LED colour had a minimal impact on the performance. Interestingly, at lower voltages, higher intensity obtained better bandwidth, whereas at higher voltages, intensity had little effect.

In conclusion, the influence of illumination on PV device performance is an important factor in optimizing both energy harvesting and communication. Ambient lighting, while beneficial for boosting harvested energy, can adversely affect communication by saturating the system and reducing signal integrity. By operating in short-circuit mode, non-linearity and saturation can be minimized, although this compromises energy harvesting capabilities.

II.3.2.3. On the best performances

Despite the absence of standardized testing conditions, several published works demonstrate the remarkable performance of PV devices in both communication and energy harvesting applications.

Shortly after the initial proof of concept, a high-performance system was developed by a research group from the University of Edinburgh using a 1 mm diameter GaAs solar cell [222]. A variable resistor was connected to the receiver terminals to independently optimize the operating points for communication and EH. With an infrared Vertical-Cavity

Surface-Emitting Laser (VCSEL) with 3.62 mW optical power, the system achieved 42% PCE under MPP and at 1 mm distance, equivalent to 458 mW/cm². At 2 m distance with optical lenses and low load (7.1 Ω), it reached 522 Mbit/s while maintaining 1.3×10^{-3} BER.

The small surface area of the device inherently results in low geometric capacitance, which leads to an impressive 24.5 MHz bandwidth. Furthermore, by utilizing advanced modulation techniques like OFDM combined with QAM, the system effectively exploits the available SNR, ensuring high data rates without being restricted by the receiver bandwidth limitations.

Soon afterward, the same research group expanded their work by using the front-end circuit described in [204] (refer to Figure 44), coupled with the same small surface GaAs solar cell [223]. At a distance of 40 cm, the device received 2.35 mW of infrared optical power, generating 0.98 mW of electrical power at its MPP, corresponding to a PCE of 41.7%. Under these conditions, the system achieved a data rate of 783 Mbit/s with a BER of 2.8×10^{-3} BER. By switching to short-circuit operation, the system pushed the performance to 1041 Mbit/s with a BER of 2.2×10^{-3}, though this eliminates the EH capability.

The authors also analysed the interesting impact of signal amplitude on communication performance, while maintaining constant average optical power. As expected, increasing the signal amplitude did not affect the generated power, which depends solely on the DC component. However, higher signal amplitudes led to better communication performance, as illustrated in Figure 51, where larger amplitudes (u_g in the graph) allow higher maximum data rate with an acceptable BER. Although this improvement is beneficial for data transmission, the increased signal amplitude can also have other effects on the system, such as introducing flickering in the optical source, which may need to be addressed in certain applications.

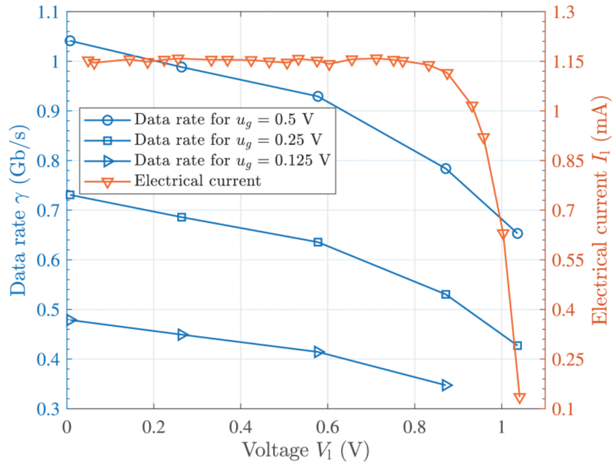

Figure 51: Data rate (in blue) and electrical current (in orange) as a function of voltage (V_i) for three modulation depths (u_g = 0.5 V, 0.25 V, and 0.125 V). Achieved data rates are associated to BER values between 1.2×10^{-3} and 1.9×10^{-2}. Data based on experiments from reference [223].

Source: Reproduced with permission from reference [223].

Although obtained under ideal laboratory conditions with a direct LOS link, these results represent the current record performance for an OWC system with a PV receiver, achieving 783 Mbit/s at MPP and 1041 Mbit/s in short-circuit mode, with an impressive PCE of 41.7%. This achievement is likely tied to the use of GaAs technology and the small surface area of the PV device, which enhances bandwidth by reducing geometric capacitance.

Coming back to 1st generation devices, Das *et al.* introduced a significant development in the field of OWC using a low cost commercial polycrystalline Si solar panel [224]. Although the authors did not use a SLIPT based system, they analysed the communication performance of a 667 cm² Si panel over a 2 m infrared link with a VCSEL, achieving data rates of up to 74 Mbit/s with a BER of 3.3×10^{-3} using OFDM and Pulse Amplitude Modulation Discrete Multitone (PAM-DMT). The work highlights the use of analog equalization and adaptative bit and power loading to overcome the solar panel low bandwidth, which was measured to be 270 kHz.

The same research team presents the world first OWC system deployed under real-world conditions using the exact same polycrystalline Si panel [225]. This pioneering project aimed to provide high-speed internet access by creating a 30 m Free-Space Optical (FSO) link between a lighthouse and two residential properties on the Orkney Islands of Scotland. The system achieved a bidirectional communication link capable of harvesting energy from ambient sunlight and from the infrared VCSEL optical source while transmitting data simultaneously.

The PV panel, with a power generation capacity of up to 5 W under optimal sunlight conditions, was able to reach a data rate of 8 Mb/s. In contrast to the high-performance results of GaAs-based systems in laboratory settings, as described in [223], this study demonstrates the practicality and feasibility of Si PV receivers in real-world applications. While the Si PV receiver data rate of 8 Mb/s is much lower than the 1 Gb/s achieved in the GaAs laboratory experiments, the Si panels offer broader applicability due to their low cost, large surface area, and ability to operate effectively in natural outdoor environments

Now turning to the emerging generation of solar cells, the work proposed by Mica *et al.* introduces an important advancement in the use of perovskite materials in the SLIPT context [193]. In this pioneering study, the researchers employed a triple-cation perovskite material as the active layer, using an n-i-p architecture for the device. By fine-tuning the layer thickness (between 60 and 965 nm), they aimed to independently optimize both the PCE and communication performance. The device, based on cesium-containing perovskite — first reported for photovoltaic applications [226] — was selected for its high PCE and bandwidth. The energy harvesting parameters were measured using a white LED with an incident optical power of $0.9\ mW/cm^2$, while communication performance was evaluated using a red LD.

As the thickness of the active layer increased, the measured PCE improved proportionally, peaking at 21.4% at 640 nm, before declining with further thickness increases. Meanwhile, the bandwidth also increased with thicker active layers, reaching a maximum of 586 kHz at 965 nm (refer to Figure 52.a), measured under short-circuit conditions. Although thicker layers achieved higher bandwidths, the overall data rate for OFDM schemes depends more on individual subcarrier performance than on total device bandwidth. As a result, the 250 nm layer performed the best, achieving a data rate of 56 Mbit/s with a BER of 3×10^{-3} over a 40 cm LOS link (see Figure 52.b), representing the highest reported value for perovskite devices.

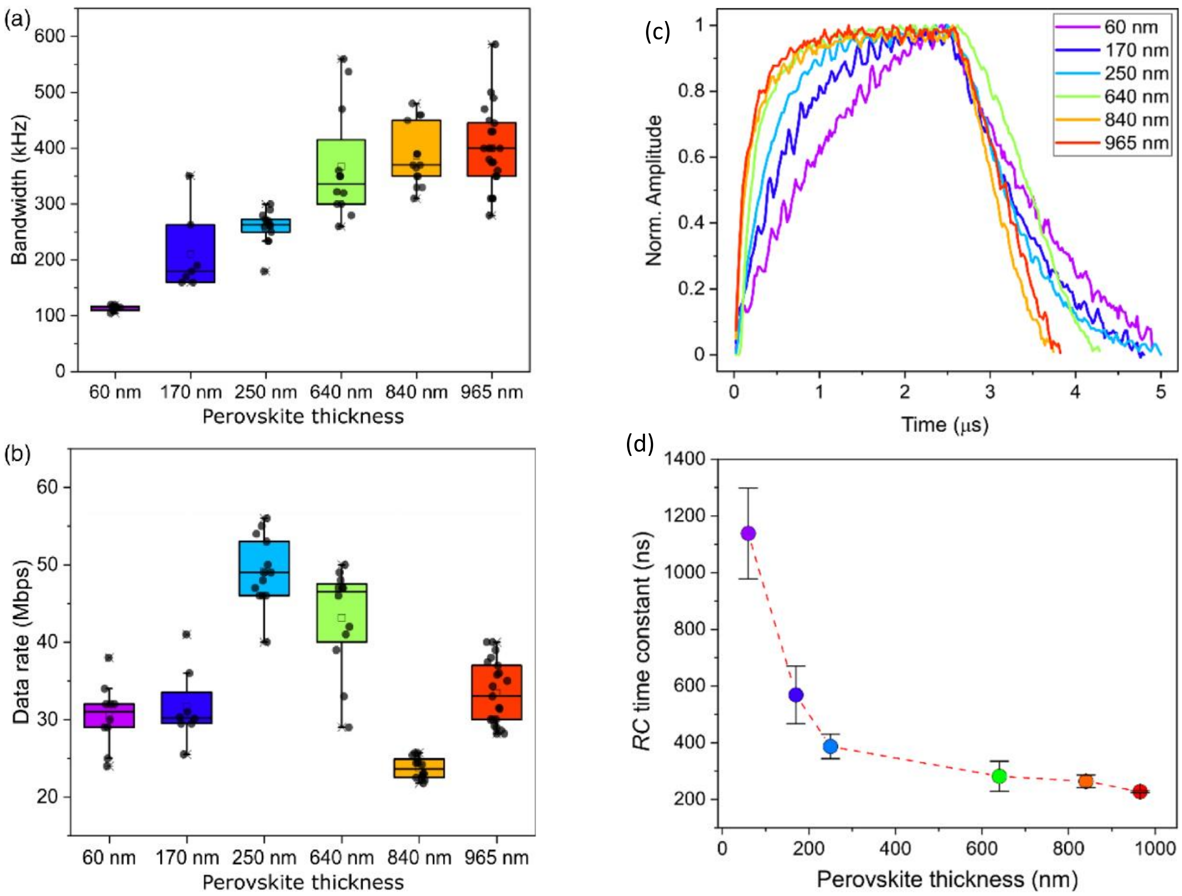

Figure 52: Different parameters of triple-cation perovskite solar cells in function of active layer thicknesses: a) Bandwidth; b) Data rate; c) Normalized amplitude; d) RC time constant. Data from reference [193].

Source: Adapted with permission from reference [193].

Mica *et al.* found that the increase in bandwidth is directly related to the reduction in geometric capacitance (C) as the active layer thickness increases, while maintaining an acceptable internal resistance (R), thereby reducing the RC constant of the system (refer to Figure 52.d). Transient voltage measurements further confirmed that thicker active layers decrease the device rise time, which behaves as a first-order low-pass filter, as shown in Figure 52.c.

This study by Mica *et al.* represents the first, and so far, the only work that thoroughly investigates the influence of the physical structure of photovoltaic devices on communication performance within the SLIPT context. While many previous studies have focused on the energy harvesting or data transmission capabilities of PV cells independently, this research uniquely addresses how key parameters such as active layer thickness directly affect both communication performance and energy harvesting efficiencies.

In [227], Tavakkolnia *et al.* explored the potential of OPVs in the SLIPT context, using a MIMO system to enhance performance, while adapting the first proposed front-end circuit (refer to Figure 44). The researchers compared the efficiencies obtained from three different devices, each with a unique donor/acceptor combination, while using the inverted architecture for enhanced stability. Interestingly, the best energy conversion and communication performances were obtained by the same device, consisting of a polymer donor (PTB7-Th) and an NFA (EH-IDTBR). Indeed, the absorption spectra of non-fullerene acceptors is better adapted for indoor lighting, which likely contributed to its superior EH performance in these conditions [228]. However, this alone does not fully explain its improved communication performance. Under indoor condition (white LED – 5.9 mW/cm²), the OPV achieved a PCE of 14.1%.

For the communication tests, the 10 mm² OPVs were placed 40 cm away from a red laser. The authors highlight that the OPV, in a SISO configuration, achieved a data rate of 147.5 Mb/s while harvesting 3.7 mW of electrical power, setting a new record for OPV-based OWC systems (surpassing the previous record of 42.3 Mbit/s obtained in [192]). By scaling the setup to a 2-by-2 MIMO configuration, the system was able to reach 221 Mb/s with 6.8 mW of harvested power. Finally, in the 4-by-4 MIMO setup, the system achieved an impressive data rate of 363 Mb/s while harvesting 10.9 mW of power. The bandwidth of the OPVs was measured at 2.77 MHz for the best-performing configuration, and adaptive bit and power loading techniques were used to maximize the data rate despite the bandwidth constraints.

This work highlights that OPVs show significant promise for high-speed data communication while simultaneously harvesting energy, making them ideal candidates for future IoT and smart device applications. The amazing indoor performance of these devices, combined with their flexibility and low-cost fabrication, positions them as key components in the development of energy efficient indoor communication systems.

In conclusion, the reviewed studies illustrate the rapid development and promising potential of PV devices as OWC receivers, particularly in the SLIPT context. These key works highlight the diverse applications and advantages of different PV technologies, from the high data rates achieved with GaAs-based systems to the flexibility and cost-efficiency of organic and perovskite devices. Each technology presents unique strengths: GaAs excels in bandwidth and communication performance, while OPVs and perovskites offer greater adaptability for indoor IoT applications and energy harvesting under low-light conditions.

Despite these advances, challenges remain, particularly in optimizing the trade-offs between energy harvesting and communication performance, as well as addressing technical limitations such as bandwidth constraints. Additionally, most studies are conducted under ideal laboratory conditions with LOS links and optical concentrators, while record-breaking efficiencies are often achieved with small-surface devices, such as almost all employed OPVs. These conditions do not accurately represent the practical use of PV devices for indoor energy harvesting. For a more in-depth analysis of the literature, we recommend the following reference, which is derived from the work presented in this thesis [229].

II.3.3. Lessons learned

From the reviewed works, several key lessons can be drawn, each contributing to our understanding of different aspects of PV devices in SLIPT systems. These insights will be discussed in the current section, with particular emphasis on important considerations when using PV devices as SLIPT receivers. We highlight critical factors such as the trade-off between energy harvesting and communication performance, the operation point dependence and the impact of illumination conditions. Understanding these elements is essential for optimizing SLIPT performance in future applications.

II.3.3.1. Output variable and PV operating voltage

As stated before, using a PV device for VLC can eliminate the need for active circuits typically used with traditional photodiodes for data reception. Consequently, most studies analysed the performance of PV cells under open-circuit mode, directly connecting them to an oscilloscope with a high-impedance input (~$1\ M\Omega$) to measure the output voltage. However, some works employed a TIA to extract the current from the receiver, normally operating in short-circuit (zeros bias) mode.

Here, there are two key aspects to consider: the output variable and the operating point. While these are related, they are distinct. The output variable refers to how we read the photogenerated charges from the device, either as a current or a voltage. On the other hand, the operating point refers to the DC (constant) voltage across the device terminals, which determines how the device functions in the system. Both factors play a critical role in optimizing performance but serve different purposes.

- **Output variable**

In short-circuit condition, the voltage across the device is 0 V, which can be achieved either by using a TIA under zero bias or by connecting the device to a low-value resistor (refer to Figure 53 for reference). In the first scenario (TIA), the output current flows through the active circuit and is converted into readable voltage via a feedback resistor. In the second case (low resistor), while the device remains near 0 V, fluctuations in the optical signal are converted to a small output voltage (which is almost zero for low signal conditions), which can be directly read by an oscilloscope.

In open-circuit conditions, the operating voltage depends on the PV characteristics (as detailed in Equation II-87 for OPVs) and is high enough to prevent current flow. This can be obtained through a TIA with forward bias or by connecting a high-impedance load, such as a $1\ M\Omega$ oscilloscope. In the first case (TIA), the operating point is set by the bias voltage, and a minimal output current is converted into voltage via a feedback resistor. In the second scenario (high-impedance), the device operates at the open-circuit condition, and optical signal fluctuations are observed directly as voltage readings on the oscilloscope.

This is evident in circuits that employs two branches for SLIPT applications. In the classical setup (Figure 44), the operating point is defined by the load resistor R_L, while the output signal is measured as voltage across the resistor R_C. Alternatively, the communication branch can be replaced with a circuit that reads the AC output current, as seen in more complex front-ends, such as the one proposed in [212] (Figure 46). In this topology, a TIA is used to extract the current as the output variable, while the operating point remains fixed. Note that, regardless of the operating point, from short-circuit to open-circuit modes, the output current will always be measured accordingly.

The influence of the output variable is clearly demonstrated in the study performed by Lorrière *et al.* [194]. The authors employed two analysis methods: using a TIA under short-circuit condition (current reading), and employing a high-impedance load to place the OPV module in open-circuit mode (voltage reading). When analysing shading effects on the OPV module, they found that each method produced different results. Blocking entire cells creates high impedance for the current reading method, while partial shading of all cells moved the device out of saturation in the voltage reading scenario. The output variable concept will be experimentally explored in Chapter III and Chapter V. Figure 53 shows two basic methods for voltage reading (left) and current reading (right). It is important to note that the operating voltage in the TIA setup determined by the voltage source V_{cc}.

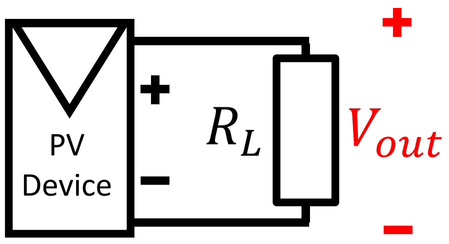

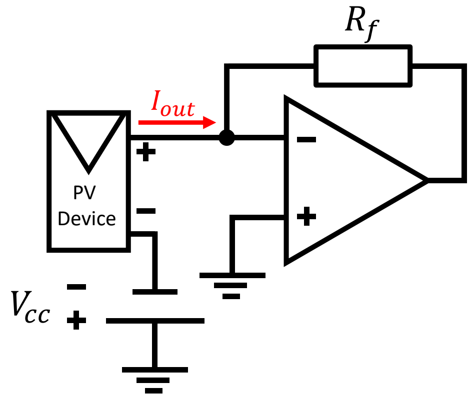

Figure 53: Simple circuits for: a) voltage reading; b) current reading.

Operating voltage

From the analysis of the reception circuit to the achievement of the best performances, each study outlined the working point of the solar cell. In dual-function scenarios, the device operates between short-circuit and open-circuit modes, typically at the MPP. Under static conditions, the clear dependence of the maximum output power on the voltage is seen, as shown in Figure 39. The non-linear behaviour of the PV device, modelled as a diode, leads to a non-linear relationship between output power and voltage. Beyond the MPP, power and output current drop significantly, while output voltage slightly increases until reaching the open-circuit level.

In communication analysis, different works have shown that higher operating points result in reduced communication performance, both theoretically and experimentally. Multiple works analyse the single-diode model under AC excitation, as shown in Figure 43.

The clear dependence of the voltage on the internal parameters of the PV device demonstrate that the bandwidth is also influenced by these factors. In their work, Sephrvand *et al.* simulated the single diode model at different operating points while reading the output voltage, theoretically demonstrating that the lower bound on Shannon capacity [230] decreases with increasing DC voltage [212], as illustrated in Figure 54.

The same trend is noticed in the recent work published by Zhou *et al.*, where higher operating points lead to a decrease on the receiver bandwidth [221]. The authors identified that, under low DC voltage mode, the junction capacitance C_j has major impact on the system dynamic performance, while at higher operating voltages, the diffusion capacitance C_{diff} dominates the bandwidth variation.

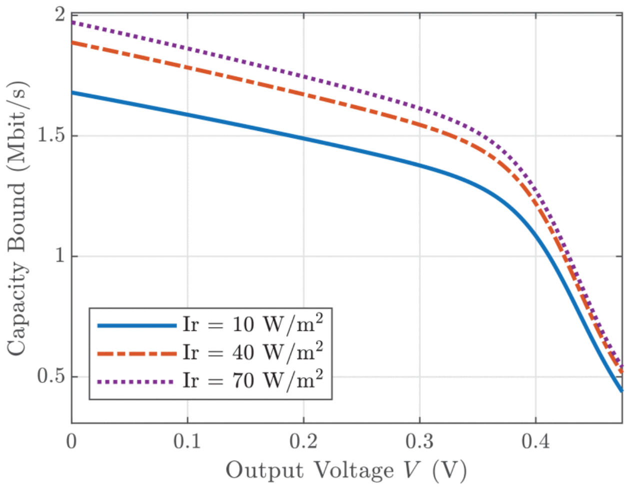

Figure 54: Simulated lower bound on Shannon capacity in function of operating voltage for different irradiance levels, described in [212].

Source: Reproduced with permission from reference [212].

The high-performance GaAs cell employed by Haas's research team exhibited a similar trend. In their initial study, they measured the frequency response of the small-surface device under various load conditions, with the device directly connected to an oscilloscope for voltage readings. The results, illustrated in Figure 55 confirmed that higher operating voltages lead to reduced communication performance, as indicated by a decrease in bandwidth in this case.

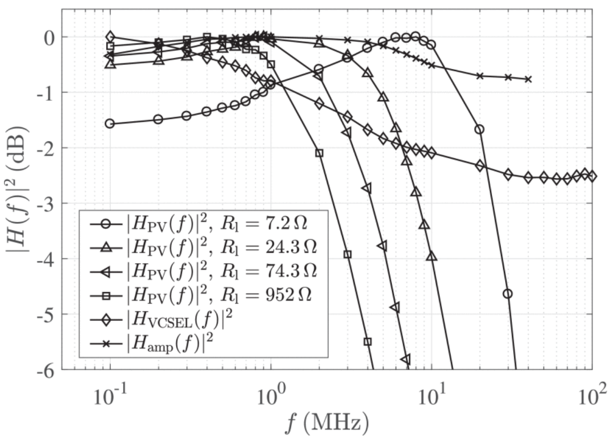

Figure 55: Frequency response for different load resistances at the GaAs PV receiver terminals, compared with the VCSEL and amplifier transfer functions, described in [222].

Source: Reproduced with permission from reference [222].

The same trend was observed in their last study, as already shown in Figure 51. In this scenario, the maximum achieved data rate had an increase of 32.95% when switched from the MPP to the short-circuit mode.

In conclusion, all studies suggest that PV devices demonstrate better performance under short-circuit conditions, whether the output is measured as current or voltage. Some researches have investigated output voltage readings under open circuit conditions by connecting the receiver to a high-impedance oscilloscope. However, no study has yet explored PV performance in open circuit-mode with current output readings using a TIA.

All research suggests that operating at a lower voltage improves bandwidth. However, the choice of output reading method significantly affects the resulting SNR. Under short-circuit conditions, current readings provide high responsivity and strong signal amplitude, whereas voltage readings in the same mode yield low signal amplitude, but good linearity. As the operating point shifts towards open-circuit conditions, the output voltage can easily saturate with increasing illumination, which further reduces the signal amplitude. In this case, the output current becomes less responsive to the incident optical power, leading to a decline in SNR.

II.3.3.2. Illumination influence

Light can influence a solar cell in various ways, depending on factors such as its frequency (AC or DC) and instantaneous optical power. Many studies have examined the impact of optical power intensity on communication and EH performance, but not all have considered the nature of the light itself. To clarify these findings, we will now present the gathered information in a more structured and logical manner.

- **Optical signal intensity**

Not all studies have specifically analysed the effect of optical signal amplitude on receiver communication performance (noting that amplitude has no impact on EH performance). Among those that did, references [216], [223] and [217] stand out for precisely focusing on the optical signal intensity, which in its own way also contains a DC component.

Bialic *et al.* connected the PV devices directly to a $50\,\Omega$ oscilloscope, approximating short-circuit conditions with voltage reading method. Under this mode, PV devices require higher optical power to reach saturation, explaining why the CIGS module saturates around 140k lux — an extremely high illumination level. Under lower illumination levels, increasing the light intensity leads to a better signal amplitude, resulting in a better SNR. No information about the bandwidth performance was given.

Lorrière *et al.* conducted a similar study but placed the PV modules in open-circuit mode (voltage reading). Despite this mode typically leading to saturation under low light conditions, the device showed increased SNR with higher optical signal intensity. However, no information regarding the effect of signal amplitude on bandwidth was provided.

In fact, Fakidis *et al.* were the only researchers to isolate the effect of signal amplitude on communication performance (refer to Figure 51), using a voltage reading method at various operating points. By varying the signal amplitude while keeping the total irradiance on the receiver constant, they achieved an improved SNR and a higher maximum data rate at an acceptable BER. However, they did not provide information on how signal amplitude affects bandwidth. Thus, as mentioned earlier, excessively increasing the amplitude can cause undesirable effects, such as flickering.

In conclusion, these studies did not clarify the impact of signal amplitude on the physical properties of the PV device, as no information on receiver bandwidth was provided. However, decreasing the distance between the transmitter and receiver increases the optical signal amplitude, thereby improving SNR and enhancing communication performance. Additionally, due to the inherent DC component in VLC signals, reducing the distance may saturate the device, ultimately lowering SNR and degrading communication performance, fact that is further explored in Chapter V. It is also important to note that no experiments using current reading via a TIA were conducted in this scenario. All the gathered information is summarized in Table 4, where the impact of increasing optical signal power is considered, with or without the inclusion of the DC component of the VLC signal.

Table 4: Impact of increasing optical signal power (with or without considering the DC component of the VLC signal) on PV-based receiver performance in terms of SNR and bandwidth improvements. Voltage reading scenario.

Rising optical signal power ↑ **Voltage reading**	**SNR/ Electrical Signal Amplitude**	**Bandwidth**
Short-Circuit	↑ (until saturation)	?
Open-Circuit	↑ (until saturation)	?

DC lighting intensity

Most studies examining the impact of light intensity on system performance focus on ambient lighting or the optical signal DC component (though similar, they originate from different sources). In fact, this component can affect both the solar cell DC gain (through saturation) and its bandwidth. Although it is intuitive that the signal amplitude decreases under saturation conditions, the behaviour of the receiver cutoff frequency under varying background lighting is less straightforward.

Most research has employed PV devices in open-circuit mode with voltage readings to analyse background irradiation. Under these conditions all devices experienced a drop in static gain at higher light intensities, indicating voltage saturation. However, most works indicate that the cell bandwidth increases with increasing light intensity. Thus, a clear trade-off between SNR (signal amplitude) and bandwidth is observed in open-circuit scenarios, as carefully detailed in [220].

At lower operating voltages, near the MPP, Das *et al.* investigated the frequency response and SNR of a Si panel connected to a specialized front-end circuit, including an equalizer and a TIA. In this study, the output current was used as the reading variable, which is less prone to saturation effects compared to output voltage. Although the PV panel was not analysed independently, the results demonstrate significant and promising developments in the field. As ambient lighting increases, the receiver generates more optical power, but both SNR and bandwidth decrease accordingly. Similarly, the data rate diminishes with higher light intensity.

At short-circuit condition, both output variables were analysed for their dependence on the light intensity. In the output current analysis (using a TIA), conducted by Lorrière *et al.* [194], a linear behaviour was observed, explaining why varying ambient lighting levels had no impact on the signal amplitude. However, no information concerning the bandwidth was provided in this study. Nonetheless, increasing background irradiation raises the shot noise, which in turn reduces the system SNR. Consequently, the maximum achievable data rates for an acceptable BER are expected to decline as irradiation levels rise. For output voltage readings, Bialic *et al.*'s work can be approximated to short circuit conditions due to the low resistive load of $50\ \Omega$. The two PV modules, CIGS and a-Si, showed contrasting behaviours: the CIGS module exhibited a decline in both SNR and bandwidth at higher illumination levels, while the a-Si module showed improvements in both. However, further increases in DC lighting led to a drop in both parameters, likely due to saturation effects. The underlying reason for this difference remains unclear.

In conclusion, we have compiled the gathered information in Table 5 (voltage reading) and Table 6 (current reading), illustrating the effect of increasing ambient lighting (or the VLC DC component) on the communication performance of PV-based receivers. As ambient lighting increases, the electrical SNR decreases, either due to reduced signal amplitude (caused by saturation in voltage reading) or increased noise power (in current reading). The bandwidth, however, does not follow a consistent pattern. In open-circuit conditions, it increases with higher illumination levels, whereas, in short-circuit conditions, it decreases for voltage readings and increases for current readings.

Table 5 : Impact of increasing ambient lighting or VLC DC component on PV-based receiver performance in terms of SNR and bandwidth improvements. Voltage reading scenario.

Rising illumination ↑ **Voltage Reading**	**SNR/Electrical Signal Amplitude**	**Bandwidth**
Short-Circuit	↓*	↓*
Open-Circuit	↓	↑

*Results considering the CIGS cell in [216] and the a-Si module after saturation.

Table 6 : Impact of increasing ambient lighting or VLC DC component on PV-based receiver performance in terms of SNR and bandwidth improvements. Current reading scenario.

Rising illumination ↑ **Current Reading**	**SNR/ Electrical Signal Amplitude**	**Bandwidth**
Short-Circuit	↓	↑
MPP	↓**	↓**
Open-Circuit	?	?

**Results considering full receiver, including equalizer and TIA, explored in [215].

Non-linear distortion

Concerning the non-linear behaviour of PV devices, Chen *et al.* were the only researches to experimentally analyse the non-linearity of the solar cell output voltage (in open-circuit mode) as a function of the light intensity level (refer to Figure 50). Their analysis was based on the single-diode model, where the open-circuit voltage V_{oc} can be approximated by Equation II-86.

As J_{ph} is directly proportional to the incident optical power, Equation II-86 implies that the output voltage varies logarithmically according to the light intensity. This behaviour leads to a non-linear distortion at lower illumination levels, which can be critical in multilevel modulation scenarios. Chen *et al.*'s work demonstrates this effect in the open-circuit mode with voltage reading.

Shading

Lorrière *et al.* conducted the only shading analysis available in the literature. In fact, the impact of shading varies depending on different factors, including the type of device (module or cell), output variable, operating point, and how the device is shaded.

In PV cells, shading reduces the total active surface exposed to ambient light and the optical signal, leading to a decrease in the output current regardless of the operating point. For the output voltage, shading lowers the illumination level, potentially allowing the device to move out of saturation, but decreasing the bandwidth.

In series-connected PV modules, the type of shading is primordial for fully understanding the receiver behaviour. When a uniform percentage of all cells in the module is shaded, the response is similar to that of a single cell. However, if specific cells are shaded, the behaviour varies depending on the output variable. For output voltage, an increase in shaded cells leads to a reduction in both static gain and bandwidth. For output current, the shaded cells act as impedances, creating complex bandpass effects, as previously discussed and illustrated in Figure 49.b.

Conclusion

In conclusion, the current analysis emphasizes how illumination conditions influence receiver performance. A clear trade-off is evident: increasing illumination levels may reduce the optical system SNR, but can simultaneously improve the receiver bandwidth. The effect varies depending on the modulation scheme employed; for example, OFDM relies heavily on SNR, which explains the lower data rates observed in [215].

Illumination effects also vary based on the front-end circuit and operating mode. In SLIPT scenarios, higher ambient lighting increases the maximum output power but negatively impacts communication performance. On the other hand, increasing the signal amplitude enhances communication capabilities without compromising energy harvesting.

Another trade-off emerges in open-circuit voltage reading mode: low illumination levels introduce non-linearity issues, while high illumination levels push the PV device towards saturation, leading to reduced SNR. Balancing these factors is essential for optimizing overall system performance.

II.3.3.3. PV technology

The development and variety of PV technologies have significantly influenced their application in SLIPT and communication systems. From first-generation c-Si solar cells to the more recent organic and perovskite solar cells, each generation exhibits unique characteristics that affect both energy harvesting and communication performances. Despite the advancements, there remains a lack of comprehensive studies directly comparing these technologies. As a result, more focused research is required to better understand the trade-offs and advantages inherent in each PV technology within the SLIPT framework.

When comparing various PV technologies, such as c-Si, GaAs, OPV, CIGS, and Perovskite, it is important to assess several key parameters that define their overall performance, including PCE, bandwidth and material properties. Below is a detailed comparison of these technologies based on current research and literature:

- **C-Si**

C-Si is the most widely used PV technology due to its long-established role in traditional photovoltaic applications. In communication, its primary advantage lies in its well-understood material properties and high PCE under standard illumination conditions. However, it suffers from relatively low bandwidth, such as the one measured by Das *et al.*, at around 270 kHz, which is significantly lower compared to other inorganic technologies.

Key Advantage: Low cost and established reliability.

Limitation: Low bandwidth and slower response times.

- **GaAs**

GaAs-based PV devices offer the highest communication performance among the reviewed technologies. GaAs cells feature superior carrier mobility and a much smaller geometric capacitance due to their smaller surface area, which leads to much higher bandwidth, often exceeding 24 MHz, as demonstrated by Fakidis *et al.* GaAs also outperforms other materials in both energy harvesting and data rate performance, as seen with systems achieving up to 1.04 Gbit/s. This is due to its high responsivity to infrared light, making it suitable for high-speed applications. However, GaAs is relatively expensive and not suitable for widespread or large-area deployment, especially in IoT applications requiring cost efficiency.

Key Advantage: Extremely high bandwidth and data rates, excellent performance in energy harvesting.

Limitation: High cost and smaller surface area limit large-scale applications.

- **OPV**

OPVs are emerging as strong contenders due to their flexibility, low production costs, and high adaptability to indoor lighting conditions, making them particularly promising for IoT devices. While OPVs generally have lower PCE compared to inorganic counterparts like c-Si and GaAs, they perform exceptionally well under low-light indoor conditions where other technologies might struggle. In a SISO configuration, OPVs have demonstrated good communication performance. For instance, in the study by Tavakkolnia *et al.*, a 10 mm^2 OPV device achieved a data rate of 147.5 Mb/s while simultaneously harvesting 3.7 mW of power from a red laser.

However, OPVs still lag behind GaAs and Perovskite cells in terms of raw communication bandwidth, which is typically lower due to intrinsic material limitations like lower carrier mobility. Despite this, the combination of flexibility, low cost, and excellent performance under low-light conditions makes OPVs highly attractive for specific use cases, especially for wearable or indoor IoT devices where flexibility and energy efficiency are critical.

Key Advantage: Flexibility, low cost, tuneable properties, and excellent performance under low-light conditions.

Limitation: Lower overall efficiency and bandwidth compared to GaAs.

- **CIGS**

CIGS technology is highly effective for indoor energy harvesting, particularly in low-light environments, due to its high absorption coefficient and stable performance under artificial lighting. While its carrier mobility is lower than GaAs and OPV, it supports steady energy harvesting and moderate communication performance, making it an option for low-power IoT applications. CIGS cells perform best when energy generation is prioritized over high-speed data transmission.

Key Advantage: High absorption coefficient, reliable EH performance under indoor lighting, and long-term stability.

Limitation: Lower carrier mobility and bandwidth compared to GaAs and OPV, making it less suited for high-speed communication.

- **Perovskite Solar Cells**

Perovskite solar cells are an emerging technology that combines the best of both worlds: high PCE and relatively high bandwidths. Their tuneable material properties enable optimization for both energy harvesting and communication, offering a maximum bandwidth of 586 kHz and data rates of up to 56 Mb/s under certain conditions, as observed by Mica *et al.* Perovskites superior performance under low-light conditions and potential for further optimization make them a promising alternative for indoor SLIPT applications. However, their stability and long-term reliability remain an issue, especially in harsh environmental conditions.

Furthermore, one significant concern with perovskite technology is the presence of lead in the active layer, which poses environmental and health risks. While research is ongoing to develop lead-free perovskites, current high-performance devices still rely on lead-based materials, limiting their scalability and commercialization due to regulatory and sustainability issues.

Key Advantage: High PCE, tuneable properties, and good performance under low-light conditions.

Limitation: Stability and degradation concerns limit their current viability for widespread deployment, and contains lead.

In summary, GaAs technology clearly stands out in terms of raw communication performance due to its high bandwidth and data rates, while OPV and Perovskite technologies offer the most promise for IoT and indoor energy-harvesting applications due to their flexibility, adaptability to low-light conditions, and potential for further improvements. C-Si remains an attractive, low-cost option, although it is hampered by its limited bandwidth. CIGS, while efficient for energy harvesting, struggles in communication applications and is less competitive compared to the other technologies in the SLIPT context.

Nonetheless, we emphasize that this analysis offers a broad perspective on the impact of PV technology on SLIPT performance. While GaAs technology demonstrated both high PCE and data rates, it remains unclear whether these results are primarily due to the small active area (0.78 mm^2) or the inherent properties of the technology.

II.3.3.4. Active area and modules

The size of the active area in PV receivers plays a crucial role in determining the overall communication and energy harvesting performances. As seen in several studies, a trade-off exists between the active area and the bandwidth of the receiver. Larger PV receivers offer distinct advantages over smaller surface devices, such as higher electrical power generation and a larger detection area, which improves the receiver SNR and reduces issues related to alignment and blocking during communication. However, this benefit comes at the expense of reduced bandwidth, primarily due to the increased geometric capacitance of larger devices, which slows their response time, explicitly described in Equation II-92.

For example, Fakidis *et al.* demonstrated that smaller GaAs solar cells (with active areas as small as 0.78 mm^2) can achieve significantly higher bandwidths—up to 24.5 MHz—compared to larger Si or CIGS modules, whose bandwidths typically remain below 1 MHz. The reduced capacitance in smaller devices allows for faster response times, which enhances communication performance, particularly in high-speed data transmission scenarios.

This balance between active area and bandwidth is further complicated when considering the type of PV receiver, whether it is a single cell or a series-connected module. Series-connected modules can exhibit unique behaviours under partial shading, where some cells may continue to contribute to energy generation while others act as impedances. This adds another layer of complexity in optimizing PV receiver performance for communication and energy harvesting. In fact, no study has yet explored how a PV module responds when the optical signal is directed at only one cell, while the remaining cells are exposed solely to ambient lighting.

Figure 56 demonstrates the correlation between maximum measured bandwidth and data rates with respect to the active area of PV devices, based on an extensive literature review. It is important to note that bandwidth is affected by variables such as the applied bias on the PV cell and the ambient illumination conditions. Additionally, data rates are significantly influenced by the modulation technique, with multicarrier schemes like OFDM generally providing higher rates compared to simpler methods like OOK. Nonetheless, a clear trend is observed: smaller active areas typically result in faster response times due to reduced geometric capacitance. However, for more accurate conclusions, these communication parameters should be measured under consistent testing conditions.

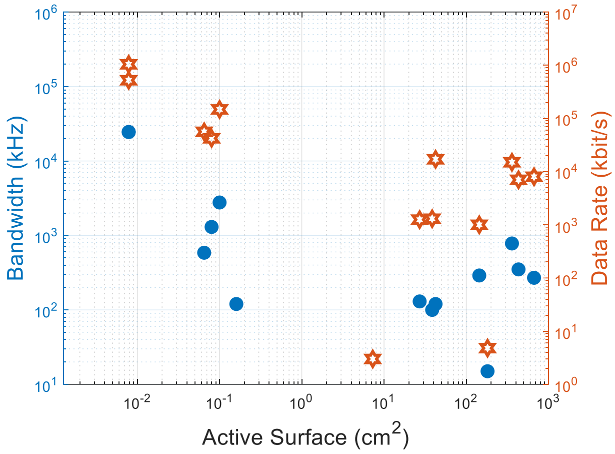

Figure 56: Reported bandwidth and data-rate for PV-based receivers with varying active surface areas. Data obtained from references [192], [193], [202], [203], [209], [214], [222], [223], [225], [227], [231], [232], [233], [234].

Source: Reproduced with permission from reference [229].

II.3.3.5. Lessons learned - conclusion

In conclusion, the current section highlights the multifaceted factors that impact the performance of PV receivers in communication and SLIPT systems. The operating point plays a crucial role, as both short-circuit and open-circuit conditions offer distinct advantages and drawbacks, depending on the output variable (voltage or current).

Illumination conditions significantly affect the system performance, with higher ambient lighting often leading to saturation, non-linear behavior, or reductions in SNR. While increased signal amplitude enhances communication performance, careful consideration must be given to potential drawbacks, such as flickering or excessive power input.

Different PV technologies, from c-Si and GaAs to emerging OPVs and Perovskites, each exhibit unique strengths and limitations in communication efficiency, energy harvesting capabilities, and adaptability to indoor and outdoor environments.

The active area and receiver type present another trade-off: smaller active areas yield better bandwidth due to reduced geometric capacitance, whereas larger areas enhance SNR and energy harvesting, though they suffer from reduced bandwidth. Overall, these lessons emphasize that optimizing SLIPT and communication systems requires a comprehensive understanding of how each parameter influences the balance between energy harvesting and data transmission.

II.3.4. SLIPT conclusion

The use of PV devices as receivers in OWC systems presents promising advantages, but also introduces a range of complexities. As outlined, the role of PV technology in OWC involves a delicate balance between energy harvesting and communication performance, with a variety of factors influencing each. Understanding how these devices perform under different conditions—whether related to illumination levels, operating points, or the physical characteristics of the PV technology—is crucial for optimizing their use in next-generation communication systems. The ability of PV devices to serve dual functions (data reception and energy harvesting) makes them particularly attractive for IoT applications, but their operational nuances require careful consideration.

Thus, this thesis centers on the implementation of a specific OPV within the SLIPT context, particularly with indoor white LED VLC. While various studies employ different methodologies, such as exploring distinct PV receivers or diverse OWC scenarios (e.g., FSO, infrared communication), the core principles and findings from these researches are broadly applicable. The insights gained can be extended to other types of optical communication systems without compromising generality.

II.4. Chapter conclusion

This chapter has provided a detailed examination of the key concepts, technologies, and advancements that compose the basis of this thesis, focusing on VLC, OPVs, and SLIPT. This emerging field is continuously taking space within both communication and physics communities. However, there remain several areas that are underexplored, such as the impact of different VLC links (e.g., NLOS and hybrid) on the SLIPT system performance, the influence of the PV cell flexibility on the receiver physical properties, and on the overall system performance.

Beginning with an exploration of VLC, the chapter outlined its fundamental principles, technical characteristics and relevance. We highlighted its ability to simultaneously provide lighting and data transmission, making it an attractive solution for indoor environments. The discussion also addressed the critical equations and parameters governing VLC links, providing a theoretical basis necessary for the works performed in subsequent chapters.

The analysis then shifted to OPVs, highlighting their unique material properties, such as tuneable bandgaps, high absorption coefficients and flexibility, which make them particularly suitable for indoor EH. OPVs were discussed not only in the context of their performance under LED lighting but also as promising candidates for integration into IoT devices. This adaptability to varying light sources and their capability to function efficiently in low-light conditions demonstrate their potential for indoor IoT applications.

The final section addressed SLIPT, an emerging strategy that integrates communication and energy harvesting into a single system. Given the limited research specifically on VLC-based SLIPT with OPVs, the chapter extended its scope to analyse works involving different PV technologies within OWC scenarios. This broader perspective allowed the identification of key challenges, such as the influence of illumination on system performance and the optimization of receiver circuits. These findings were also discussed in the context of their applicability to indoor IoT applications.

Extending from the current analysis, the next chapter shifts from the theoretical discussions to a closer look at the real characteristics of an OPV. Chapter III focuses on the detailed characterization of OPVs, including their static and dynamic electrical behaviours. This step connects the theoretical concepts covered here with practical strategies for using OPVs in energy and communication applications.

Chapter III

Diving into the Characterization of OPVs

Summary

Chapter III. Diving into the Characterization of OPVs

In the preceding chapter, the theoretical and operational basis using OPVs in indoor energy harvesting and communication systems were established. From this foundation, Chapter III explores the static and dynamic characterizations of a particular OPV, which are essential for understanding its performance, limitations and potential applications in various scenarios. For example, in real IoT scenarios, numerous factors can affect the performance of OPVs for both energy harvesting and communication performances, highlighting the importance of such characterizations.

The static characterization focuses on the energy harvesting performance, analysing parameters such as PCE, short-circuit current and open-circuit voltage under specific lighting scenarios. These measurements are crucial for determining their compatibility for indoor IoT applications, where EH methods have already proven their value. Meanwhile, the dynamic characterization examines the OPV response to time-varying optical signals, emphasizing their potential as VLC receivers in SLIPT systems.

Here, we will evaluate different variables that can affect OPV performance in both EH and communication, such as illumination conditions, operating point, output variable and flexible OPV curvatures. Therefore, this analysis will quantify the effects of different IoT parameters on the overall system performance. The characterizations are deeply detailed and conducted independently, without compromising the conclusions drawn for the broader SLIPT scenario.

III.1. Employed OPV

For all experimental approaches, including the ones provided in this chapter and on subsequent ones, a flexible OPV developed by Dracula Technologies was used [235], as shown in Figure 57.

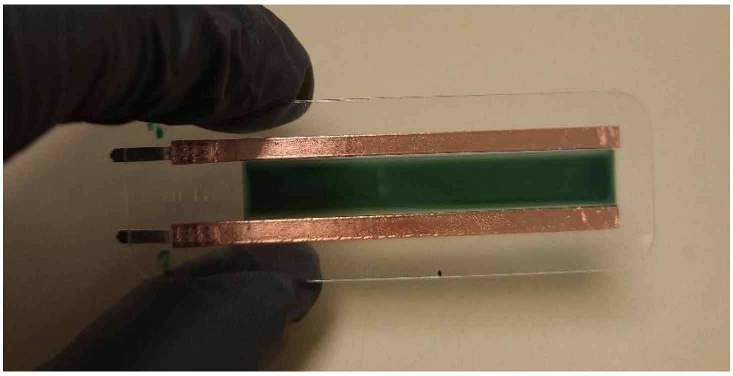

Figure 57: Flexible OPV cell fabricated by Dracula Technologies, which was used in all experimental analyses.

The device measures 4.7 cm in length and 0.66 in width, resulting in an active area A_r of 3.102 cm². It was inkjet printed on a flexible substrate and fully encapsulated to protect it from environmental factors that could degrade the active layer. Additionally, the specific device architecture and the materials comprising each layer are not disclosed, as this product involves the specific know-how of Dracula Technologies regarding the optimisation of active layer materials, interfaces and device architectures, as well as regarding their printability on flexible substrates and over large area. In any case, the device is exploiting a single-junction OPV architecture based on the bulk-heterojunction concept. It also uses commercial active layer materials known for their excellent electronic properties for indoor applications. The charge extraction is realized through two metallic (copper) electrodes, as demonstrated in the figure above.

III.2. Optical source

Unless otherwise stated, a broadband white LED was used for most characterizations to approach the conditions of real-life scenarios. The experiments employed an OSRAM LE CW E3B high-power LED, featuring a 2.1 mm × 3.2 mm light emitting surface and a Lambertian radiation pattern with half power angle $\theta_{1/2}$ of 65°, representing a directivity m_1 of 0.8048 (refer to Equation II-14). Under nominal operation, it requires a forward current of $700\,mA$ and a forward voltage of approximately $21\,V$. Under these conditions, it can generate around 800 lumens.

For all experiments, temperature stabilization was required to maintain a constant transmitted optical power P_t. The device was mounted on a high-performance heat sink to ease heat dissipation. However, no information concerning the dynamic behavior (bandwidth or rise time) of this white LED was provided. Other source parameters are not relevant to this thesis and have therefore not been addressed.

As discussed in Chapter II, the normalized transmitted optical power $S(\lambda)$ is an essential parameter for different future analyses. Using a dedicated spectrometer, the received PSD $\Phi_r(\lambda)$ can be obtained, and dividing it by the received optical power P_r results in $S(\lambda)$. For this purpose, we have employed the BLACK-Comet spectrometer (model STE-BC-220/1100), developed by StellarNet Inc, to obtain $S(\lambda)$ across a wavelength range of 300 nm to 900 nm with a 0.5 nm resolution.

By multiplying $S(\lambda)$ with the photopic luminous function $V(\lambda)$, the normalized luminous power spectrum can also be obtained. Finally, $S(\lambda)$ is shown in Figure 58.a and the product $S(\lambda)V(\lambda)$ is shown in Figure 58.b

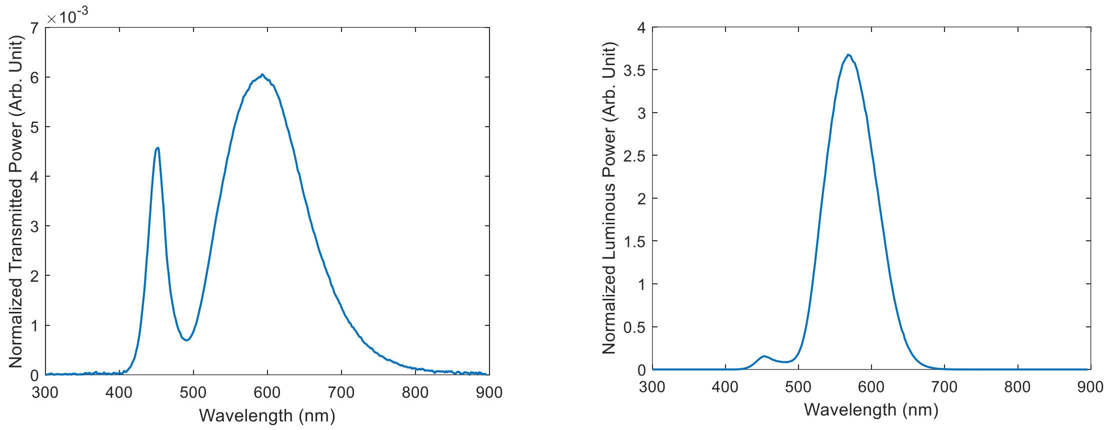

(a) (b)

Figure 58: Measured spectra of the employed optical source. (a) Normalized transmitted power $S(\lambda)$; (b) Normalized luminous power $S(\lambda)V(\lambda)$.

For this specific LED, the ratio of irradiance to illuminance remains constant at 314, indicating that an irradiance of 1 W/m² corresponds to 310 lux. Finally, changing the forward current that drives the LED alters its optical power P_t. In this analysis, it is assumed that the source spectrum does not depends on the optical power intensity. This assumption was verified in the considered range of operating conditions reported in this work.

III.3. Static characterizations – energy harvesting performance

In this section, we will perform multiple static characterizations, which were theoretically described in Chapter II. They will enable us to quantify the energy harvesting performance of the device. By employing these analyses on SLIPT systems, we can estimate different performances under indoor IoT scenarios, such as the PCE and maximum output power delivered by the OPV device.

The characterization begins with the measurement of the EQE $\eta_{qe}(\lambda)$, extended to the spectral responsivity $R_\lambda(\lambda)$, as described in Equation II-16. Following the spectral characterization, the angular responsivity $R_\Psi(\Psi)$ is obtained. Subsequently, multiple I-V curves are measured under different illuminance levels, providing insights into the light-dependent behaviour of multiple static parameters of the OPV. Finally, the influence of OPV curvature on the short-circuit current is analysed for a LOS scenario.

III.3.1. Spectral responsivity $R_\lambda(\lambda)$ and EQE $\eta_{qe}(\lambda)$

This characterization is performed by applying a known monochromatic optical power onto the photosensitive device and by measuring its output current I. Using a wide spectrum optical source coupled to a monochromator, each wavelength λ can be analysed separately, resulting in a current-per-wavelength function $I(\lambda)$. In most applications, the optical power is concentrated in a small spot with known area, without covering the whole device.

With an incident angle $\Psi = 0°$, we consider that $R_{\Psi}(0°) = 1$ (refer to Equations II-17 and II-19 for guidance). As the received PSD $\Phi_r(\lambda)$ is a known calibrated variable, the spectral responsivity $R_{\lambda}(\lambda)$ and EQE $\eta_{qe}(\lambda)$ are obtained as described by Equations III-1 and III-2.

$$R_{\lambda}(\lambda) = \frac{I(\lambda)}{\Phi_r(\lambda)} \tag{III-1}$$

$$\eta_{qe}(\lambda) = \frac{R_{\lambda}(\lambda)hc}{q\lambda} \tag{III-2}$$

Depending on the system, these spectral parameters can be obtained for different bias modes, meaning they are not limited to short-circuit conditions. As detailed in the last chapter and further demonstrated in subsequent sections, the sensitivity of the device depends on its operating point. However, for the purposes of this thesis, this characterization is performed exclusively under short-circuit conditions. Two different methods can be employed with this characterization:

- **DC mode**

  In DC mode, the light spot is constant and time invariant, resulting in a steady output current $I(\lambda)$. However, in this mode, the photodetector is not entirely illuminated, distancing from a real-life scenario, where the whole detector is active. In this mode, more complex optical phenomena, such as photon trapping, can occur.

- **AC mode**

  In AC mode, the light spot is modulated as a square signal with a user-defined frequency f, resulting in a time variant output current $I(\lambda)$. In this mode, an external constant light source can be applied to the device, while the system remains capable of isolating the current that is generated by the modulated light spot used for characterization. This setup better reflects real-life conditions where the device is entirely illuminated. However, it can pose challenges for devices with low charge carrier mobility, as higher modulation frequencies may hinder the device ability to transition between states, ultimately affecting the accuracy of the results.

In our scenario, the characterization procedure was performed using the Quantum Efficiency (QE) system developed by Enlitech, the QE-T, as shown in Figure 59. A provided Si-based reference photodetector, of known and certified spectral response, allows us to calibrate the received PSD $\Phi_r(\lambda)$ of the system under test.

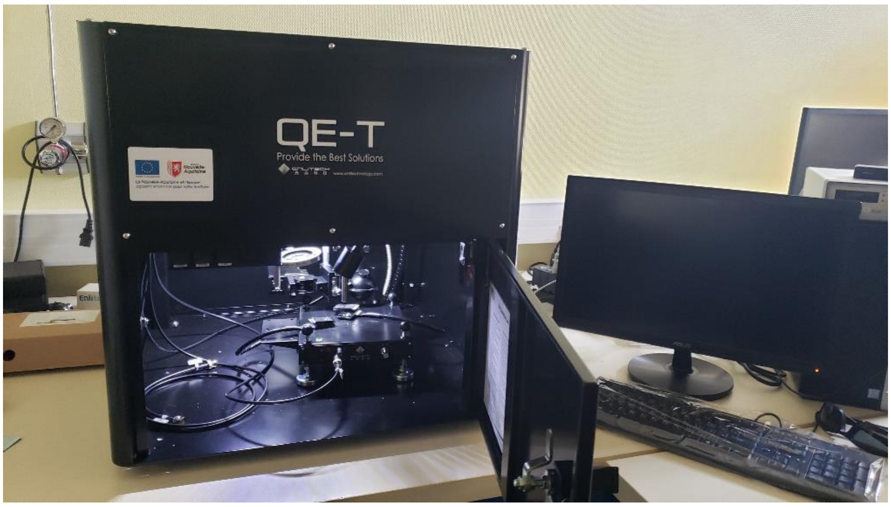

Figure 59: QE-T system developed by Enlitech and employed for $R_{\lambda}(\lambda)$ and $\eta_{qe}(\lambda)$ characterization.

For our study, we have employed both AC and DC methods for comparison. However, no significant differences were observed between the results. Both spectral parameters were obtained over a range from 300 nm to 900 nm, with a 0.5 nm step. Finally, the obtained $R_{\lambda}(\lambda)$ and $\eta_{qe}(\lambda)$ curves are shown in Figure 60.a and Figure 60.b respectively.

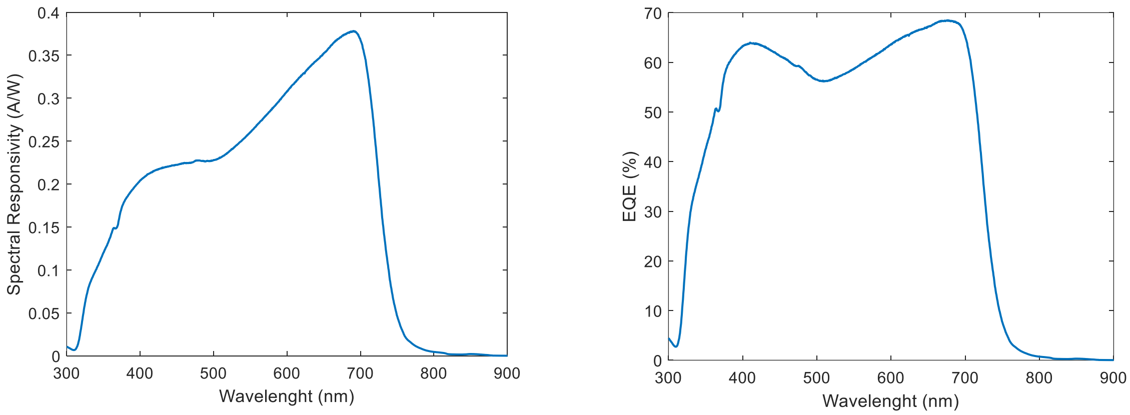

(a) (b)

Figure 60: Measured spectral parameters of OPV used in experiments: (a) spectral responsivity $R_{\lambda}(\lambda)$; (b) EQE $\eta_{qe}(\lambda)$.

The obtained results demonstrate a strong response up to approximately 750 nm, making it particularly suitable for indoor applications. This wavelength range aligns well with the typical spectrum of indoor lighting, in particular to the previously measured characteristics of the experimental LED. In contrast, outdoor OPV systems are often designed to extend their EQE beyond 900 nm to maximize current generation under sunlight. This focused spectral response shows an optimization to achieve ideal spectral matching between the artificial light source and the receiver, a key factor for enhancing indoor OPV performance.

For future analysis, we will specifically employ the spectral responsivity $R_{\lambda}(\lambda)$ for its importance in electrical evaluations, as detailed in equations provided in Chapter II.

III.3.2. Angular responsivity $R_{\Psi}(\Psi)$

In order to obtain the relative angular responsivity $R_{\Psi}(\Psi)$ of photosensitive devices, its short-circuit current shall be measured for different incident angles Ψ. In this scenario, measuring it under a diffuse link is not possible due to the complexity of the channel impulse response H_{NLOS}. As a result, the relative responsivity is obtained under a LOS link, and a specific experimental setup was designed accordingly.

As described in Equation II-33, the channel DC gain for a LOS link depends on the distance d between transmitter and receiver, on the radiant angle θ and on the incident angle Ψ. Therefore, by fixing d and θ, the OPV angular behaviour can be obtained by changing Ψ. Basing our analysis on Equations II-20, II-33 and II-44, and limiting our evaluation to a LOS link, the short-circuit current as a function of the incident angle Ψ is described by Equation III-3. Note that the term inside the bracket is constant for any incident angle.

$$I_{sc}(\Psi) = \left[A_r \left(\frac{m_1 + 1}{2\pi d^2}\right) \cos^{m_1}(\theta) \int R_{\lambda}(\lambda)\Phi_t(\lambda)d\lambda\right] \cos(\Psi)\, R_{\Psi}(\Psi) \qquad \text{III-3}$$

With Equation III-3 and by measuring the short-circuit current for different incident angles Ψ, the $\cos(\Psi)\, R_{\Psi}(\Psi)$ term can be obtained. However, as described in Chapter II, the relative angular responsivity function is normalized with maximum value equals 1. Therefore, receiver angular dependence can be simplified as described in Equation III-4, where $I_{sc_{max}}$ is the maximum measured current, normally obtained under normal incidence ($\Psi = 0°$).

$$R_{\Psi}(\Psi) \cos(\Psi) = \frac{I_{sc}(\Psi)}{I_{sc_{max}}} \qquad \text{III-4}$$

For the experimental approach, we employed the same optical source described in Section III.2. To ensure constant emitter-receiver distance and radiation angle $\theta = 0°$, we have meticulously developed an angular characterization bench. Its schematic and real-life picture are shown in Figure 61.a and Figure 61.b respectively. Here, the bench accounts for different incident angles from $-90°$ up to $90°$. Furthermore, the characterization can be performed for different horizontal orientation of the OPV, corresponding to the azimuth angle in spherical coordinates.

In the current scenario, given that the OPV dimensions are significantly larger than those of commonly employed photodiodes for signal detection, it is important for the solid angle subtended by the source and the OPV area to remain small for Equation III-3 to hold, as detailed in Equation II-30. Therefore, to satisfy this condition, we have chosen to employ a significant distance d of around 25 cm.

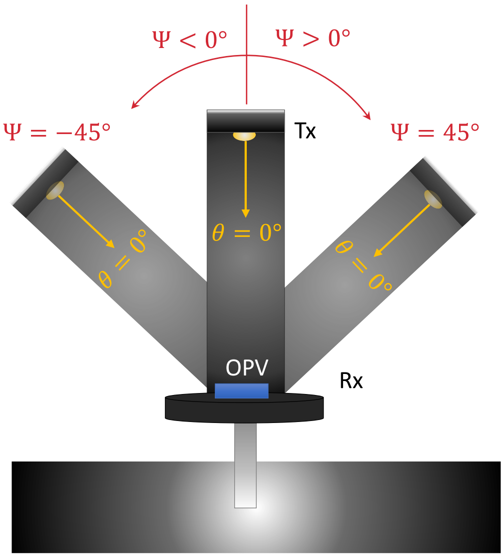

(a)

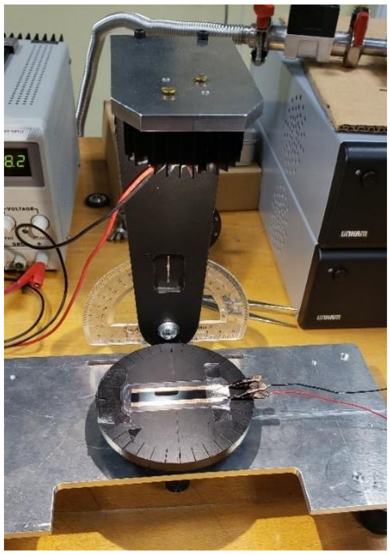

(b)

Figure 61: (a) Schematic of angular characterization bench representing three positions of the source arm; (b) Real-life photo of the angular characterization bench.

Source: Reproduced with permission from reference [134].

For the short-circuit current measurement, we have employed the 2621B source-measure unit, developed by Keithley. This device enables precise measurement of a circuit output current while applying a specified voltage, or alternatively, the measurement of the output voltage while applying a specified current. The measurements were performed in the room placed in dark conditions.

Our experimental results demonstrated that this particular OPV presents azimuthal symmetry, meaning that the short-circuit current I_{sc} depends only on the polar angle θ, while the horizontal alignment has no particular impact on it. The experimentally measured $\cos(\Psi)\, R_{\Psi}(\Psi)$ curve is shown in Figure 62 in red, alongside the theoretical $\cos(\Psi)$ curve, in blue. A comparison of both curves confirms that this OPV has no particular angular behaviour, as R_{Ψ} is constant and very close to 1.

In this context, we introduce the concept of Lambertian receiver, where the short-circuit current features azimuthal symmetry and follows a cosine power distribution, analogous to the radiant intensity of Lambertian LEDs, described in Equation II-9. Additionally, we define the concept of half-current angle $\Psi_{1/2}$, which corresponds to the angle at which the short-circuit current is reduced to half of its maximum value $I_{sc_{max}}$. Note that the term "half-power angle" is inaccurate here, since R_{Ψ} describes the optical-to-electrical conversion performance of the device [134]. Similar to optical sources, we can also extend this concept to a receiver directivity, analogously employing Equation II-10. For the OPV tested, the obtained half-current angle $\Psi_{1/2}$ equals 60°, with a corresponding directivity of 1. Both parameters are shown in Figure 62.

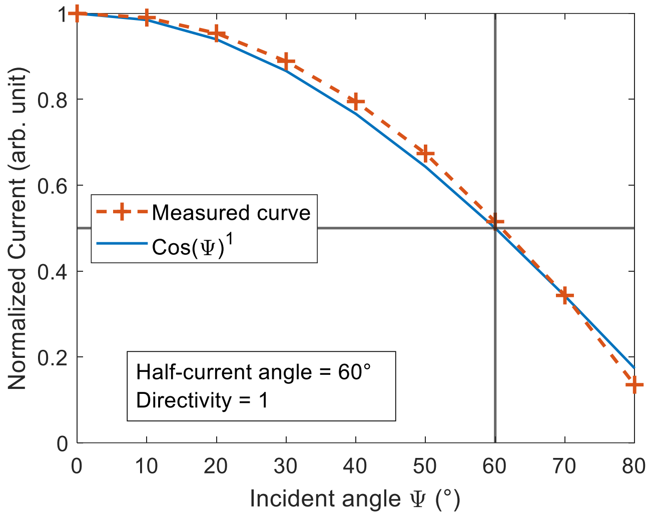

Figure 62: Measured $\cos(\Psi)\, R_\Psi(\Psi)$ function (in red) and $\cos(\Psi)$ function (in blue).

Source: Reproduced with permission from reference [134].

The reader might question if it is appropriate to describe $\Psi_{1/2}$ as half of the maximum value of the function $\cos(\Psi)\, R_\Psi(\Psi)$, instead of analysing only the relative angular behaviour. In fact, the cosine function will always be present in both LOS and NLOS links, since it defines the variation of the incident optical power on the device. Therefore, it is unnecessary to separate these functions, as their combined effect is essential to the device performance.

To extend the angular characterization performed with the wide-spectrum white LED, we investigated the influence of optical wavelength on the relative angular responsivity to determine whether the hypothesis described in Equation II-19 holds for this device. For this purpose, we conducted the same characterization using three different LEDs: red, blue, and one green. The resulting angular behaviours are presented in Figure 63.

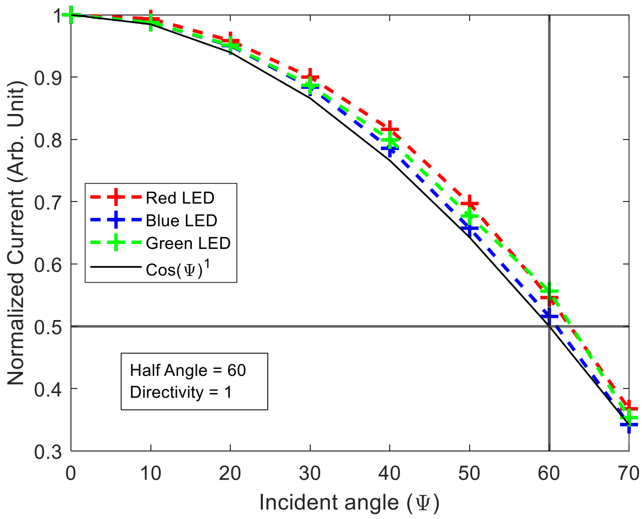

Figure 63: Measured $\cos(\Psi)\, R_\Psi(\Psi)$ functions for different LED colour and $\cos(\Psi)$ function.

From the obtained curves, minor variations are observed. The main reason behind this effect is still unknown and further research is required to comprehend it. Different physical factors can be used to try to explain this behaviour, such as interference effects, linked to the wavelength, and the dispersion of refractive index for different wavelengths, defined by Cauchy's equation. Nonetheless, these variations are small enough to approximate each curve to the $\cos(\Psi)$ function, similar to the wide spectrum behaviour.

The current characterization is essential to understand how the device will perform for optical waves that arrive with different incident angles Ψ. These results will be essential for implementing an OPV device model in optical propagation simulations, as described in Chapter IV.

III.3.3. I-V behaviour for multiple illumination levels

In this chapter, we perform I-V characterizations for varying illumination levels to evaluate the energy harvesting performance of the OPV in indoor scenarios, where lighting conditions can differ depending on the environment, as described in Section II.1.2.

For this experiment, we have employed the same wide-spectrum white LED described before. All characterizations were performed using the Keithley 2621B source-measure unit, which allows for automated voltage application while simultaneously reading the OPV output current through dedicated Matlab® interface software. The illumination level was set by changing the supply current of the optical source and ensuring temperature stabilization. Thus, the illumination level was measured using the BLACK-comet spectrometer at the exact same position as the OPV. Additionally, the measurements are realized in a perfect alignment scenario ($\theta = \Psi = 0°$). The characterization process is shown in Figure 64.

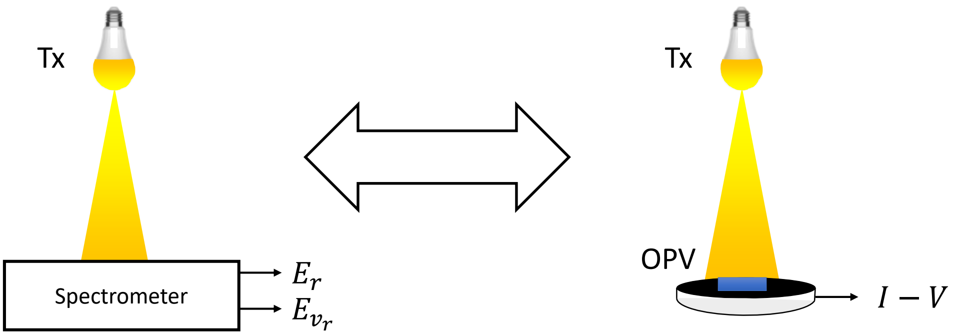

Figure 64: I-V curve characterization method. In left, the illuminance and irradiance measurement using a spectrometer. In right, the obtention of the I-V curve.

The illumination levels used in this characterization range from 703 lux to 1805 lux, covering a total of 29 distinct values, corresponding to radiometric values from 2.26 W/m² to 5.81 W/m². It is worth noting that for illumination levels outside this range, such as 300 lux or 500 lux, an approximation function can be derived from the parameters measured within the specified range. Finally, the obtained I-V curves are shown in Figure 65, with the indication of the illumination evolution.

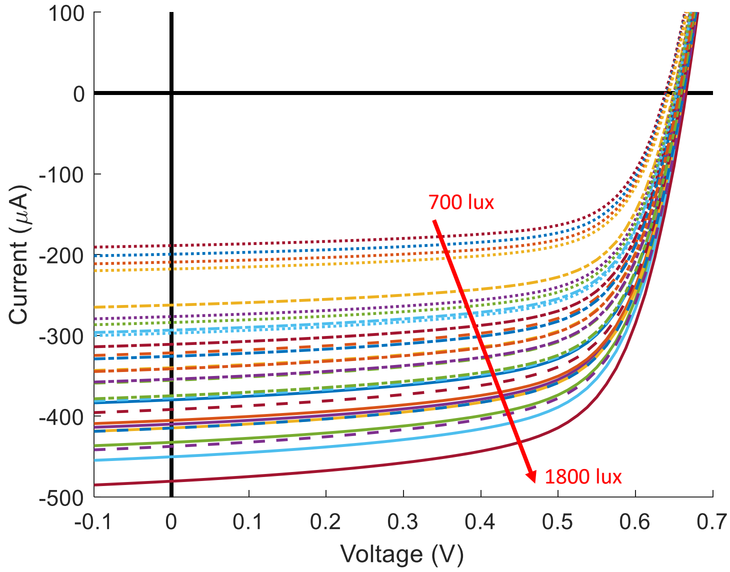

Figure 65: Measured I-V curves of the employed OPV for different illumination levels.

Source: Reproduced with permission from reference [134].

Analogously, the output power density per voltage P-V curves can also be extended from this characterization. With it, a sense of how much power the device can provide can be understood. This characterization is shown in Figure 66.

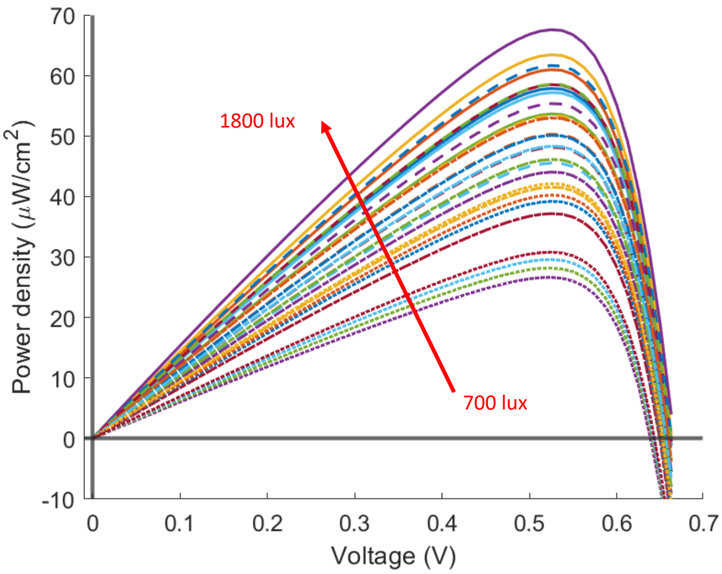

Figure 66: Measured P-V curves of the employed OPV for different illumination levels.

Source: Reproduced with permission from reference [134].

Analysing the I-V curves can provide us different parameters of the OPV, such as PCE, P_{max}, J_{sc}, V_{oc}, R_{shunt}, R_s and FF. In fact, the shunt and series resistances can be obtained thought the inverse of the slopes (derivative) at 0 V and at the open-circuit voltage respectively, as explained in Chapter II. Consequently, these measured parameters as a function of the illumination are shown in Figure 67.

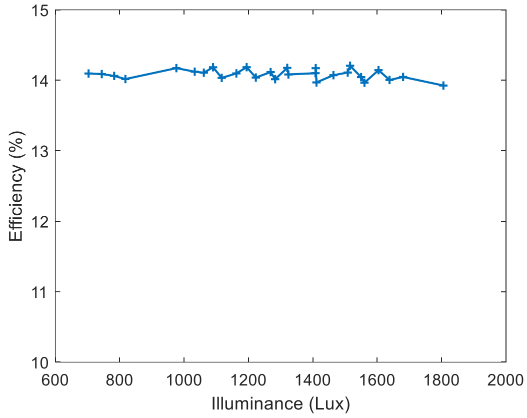
15
14
13
12
11
10
Efficiency (%)
600 800 1000 1200 1400 1600 1800 2000
Illuminance (Lux)

(a)

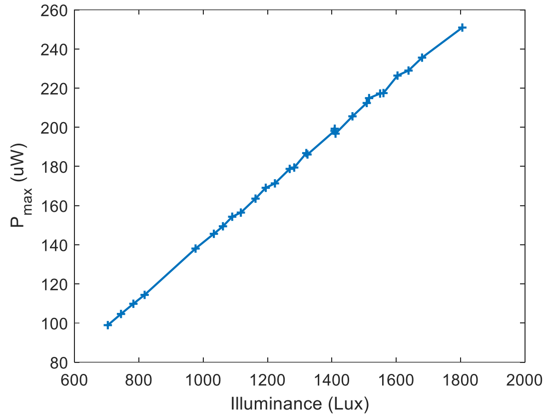
260
240
220
200
180
160
140
120
100
80
P_{max} (uW)
600 800 1000 1200 1400 1600 1800 2000
Illuminance (Lux)

(b)

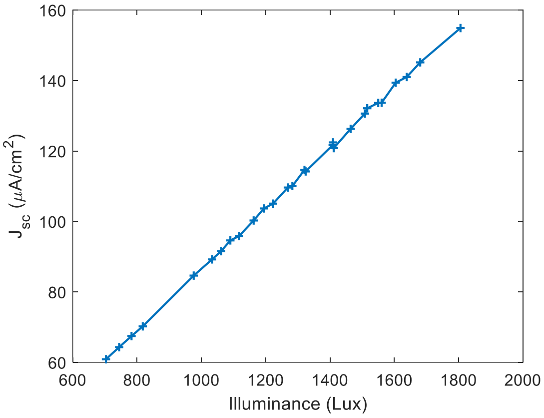
160
140
120
100
80
60
J_{sc} (μA/cm^2)
600 800 1000 1200 1400 1600 1800 2000
Illuminance (Lux)

(c)

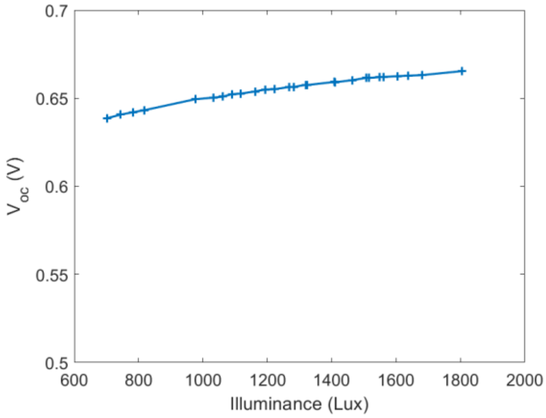
0.7
0.65
0.6
0.55
0.5
V_{oc} (V)
600 800 1000 1200 1400 1600 1800 2000
Illuminance (Lux)

(d)

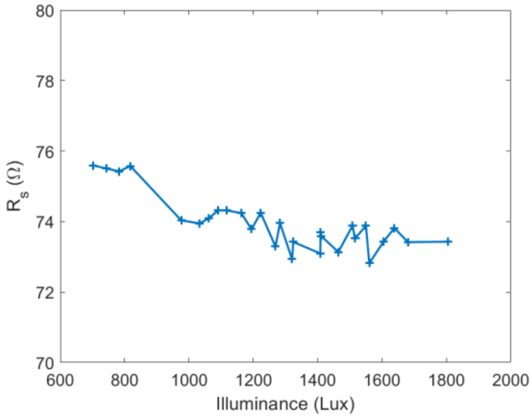
80
78
76
74
72
70
R_s (Ω)
600 800 1000 1200 1400 1600 1800 2000
Illuminance (Lux)

(e)

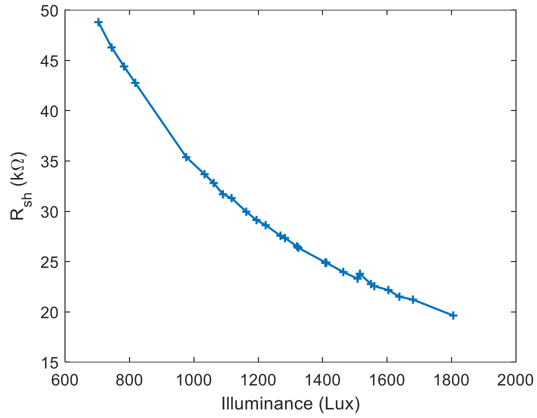
50
45
40
35
30
25
20
15
R_{sh} (kΩ)
600 800 1000 1200 1400 1600 1800 2000
Illuminance (Lux)

(f)

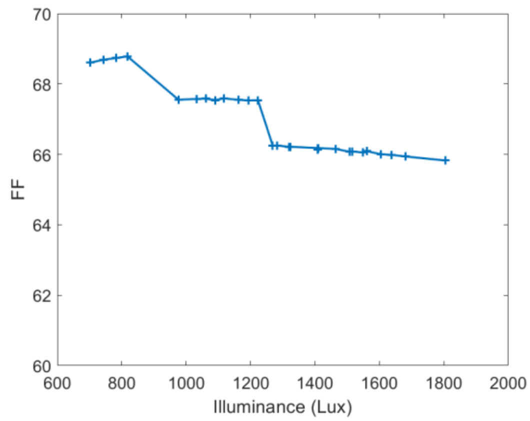

(g)

Figure 67: Measured OPV static parameters in function of the illuminance: (a) PCE; (b) P_{max}; (c) I_{sc}; (d) V_{oc}; (e) R_s; (f) R_{sh}; (g) FF.

The experimental results indicate that the efficiency of the OPV is minimally influenced by light intensity in the considered range, remaining around 14% with slight variations. This stability in efficiency suggests that the OPV operates consistently across the tested illumination range, a desirable characteristic for indoor energy harvesting applications where lighting conditions can vary. Thus, as the received optical power P_r increases, the maximum output power P_{max} of the OPV increases linearly. This behaviour is supported by the short-circuit current I_{sc}, which varies linearly. However, the open-circuit voltage V_{oc} follows a logarithmic trend, behaviour first described in Chapter II and mathematically explained by Equations II-20 and II-86. Nonetheless, its variation is still limited at lower values, as the OPV can reach the average V_{oc} (around 0.65 V) even at low illumination values.

Additionally, the series resistance R_s shows a slight decrease, with significant fluctuations, primarily attributed to measurement imprecisions. The shunt resistance R_{sh}, on the other hand, exhibits a clear decrease with higher illumination levels. This trend is explained by the higher recombination losses at elevated light intensities, as more charge carriers are generated, leading to an increased probability of recombination pathways, which result in a reduction of R_{sh}.

The interplay between these factors explains why an increase in I_{sc} and V_{oc} does not result in a proportional improvement in the OPV PCE. The gains in current and voltage are counterbalanced by the losses due to increased recombination, reflected in the reduced R_{sh}. This balance highlights the importance of optimizing OPV materials and device architecture to minimize recombination effects, ensuring that improvements in light absorption and charge generation translate more effectively into better EH performance.

Extending the analysis of the I-V curves, the influence of the OPV operating voltage on its output current vs. illumination can be studied. Here, we evaluate how the sensitivity of the OPV changes when an external circuit is used to set its operating point. In practical applications, this is typically achieved using a TIA. Additionally, this analysis can be extended to the photoconductive mode (reverse bias), where the photodetector sacrifices its energy harvesting capability to achieve improved communication performance. The resulting output currents are displayed in Figure 68.

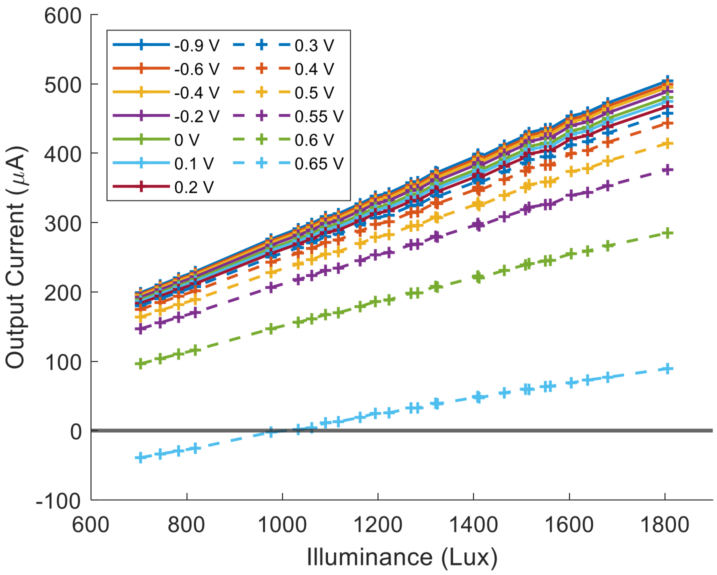

Figure 68: Output current as a function of the illuminance for different operating voltages.

The curves highlight that the output current is significantly influenced by the applied voltage, with higher reverse voltages resulting in higher current values due to enhanced carrier separation. Near the short-circuit condition, the output current remains nearly constant, exhibiting consistent sensitivity, as indicated by the uniform slope of the linear behaviour. However, as the operating voltage approaches the open-circuit condition, the device sensitivity decreases significantly, and the current drops substantially, reflecting a diminished driving force for charge collection. This behaviour underscores why traditional photodetectors, such as photodiodes, predominantly operate in photoconductive mode to maximize sensitivity and current output.

III.3.4. The V(R) relation

When a load is connected to the terminals of an OPV, the operating point, or output voltage, varies logarithmically with the load resistance for a given illumination level. Consequently, at a fixed load, the operating point is directly influenced by the illumination level. To better understand this behaviour, Figure 69 shows the output voltage V as a function of the parallel load resistance R for various illumination levels, derived from I-V characterization (where R is obtained by dividing the output voltage by the output current).

Notably, an increase in illumination shifts the curve toward lower resistance values, indicating that the OPV reaches its open-circuit condition at smaller resistances. For instance, at a fixed load such as $1\ k\Omega$, changes in illumination can shift the OPV out of its non-linear region, a phenomenon previously observed in the literature for communication scenarios [219]. Similarly, at higher resistances like $3\ k\Omega$, the OPV can enter saturation, therefore, a non-linear region, significantly impacting performance. Conversely, lower resistance values exhibit minimal sensitivity to changes in illumination, providing greater stability under varying conditions, but with lower voltage values.

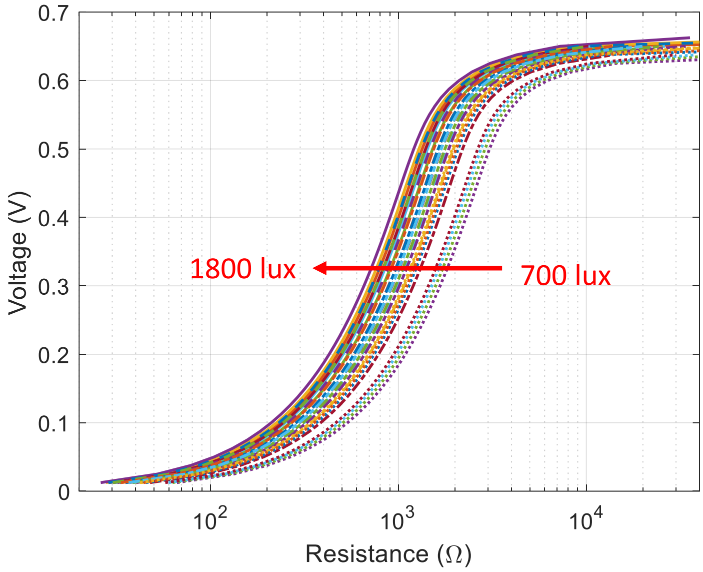

Figure 69: OPV voltage vs. resistance behaviour for different illumination levels.

These results highlight the device high sensitivity to illumination conditions when a load is connected, a behaviour further explored in subsequent sections and chapters. As a result, the resistance corresponding to the maximum output power P_{max} also varies with illumination levels. This resistance value can be determined from the I-V characterization, and is illustrated in Figure 70.

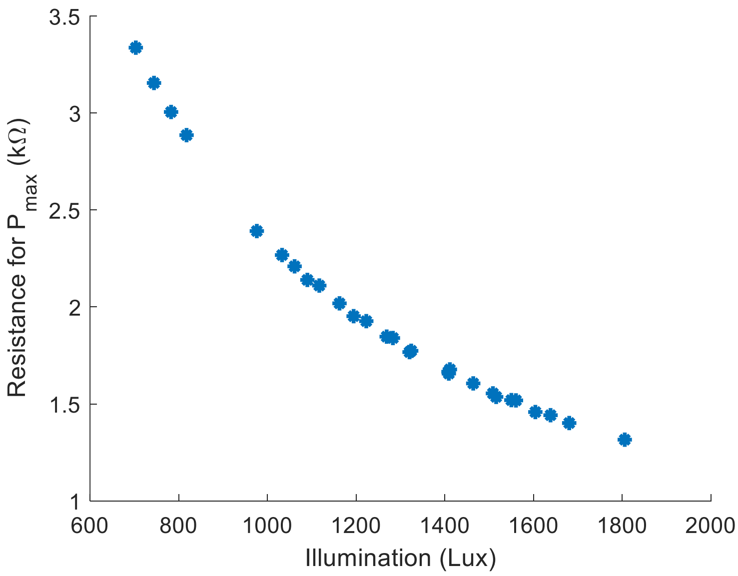

Figure 70: Required parallel resistance to obtain maximum output power for different illumination levels.

Finally, these results underscore the complex behaviour of OPV devices in energy harvesting applications, emphasizing the need for active circuits, such as MPPT systems, to ensure operation under optimal performance conditions.

III.3.5. OPV flexibility

In this section, the influence of the OPV curvature on the generated short-circuit current I_{sc} under LOS link is evaluated. The equations developed in Chapter II consider a flat receiver with an active area A_r and an incident angle Ψ, where all parameters that affect the channel DC gain H_{LOS} are known, and the provided short-circuit current I_{sc} can be estimated. However, for curved receivers, H_{LOS} cannot be described by Equation II-33, but a more complex analysis is required, which will be described in Chapter IV. The purpose of this experiment is to evaluate the angular behaviour of curved devices, as their flexibility and ability to adapt to curved surfaces are crucial features for IoT applications. Note that the OPV is curved along its length in this work.

In fact, the influence of flexible OPV curvatures extends beyond a high-level analysis of the short-circuit current and has become a key area of interest within the PV community. Depending on the type of bending, various internal material effects can arise. For instance, a common flexible structure consists of a PET or PEN substrate combined with an ITO layer. Depending on the curvature, the ITO may experience either compression or tension, each leading to distinct effects. Figure 71 illustrates examples of ITO under compression and tension, along with the substrate (PEN/PET) and other OPV layers, shown together for clarity. As demonstrated by Tran *et al.* [236], compression was found to have no impact on the OPV resistance, whereas tension could significantly increase it.

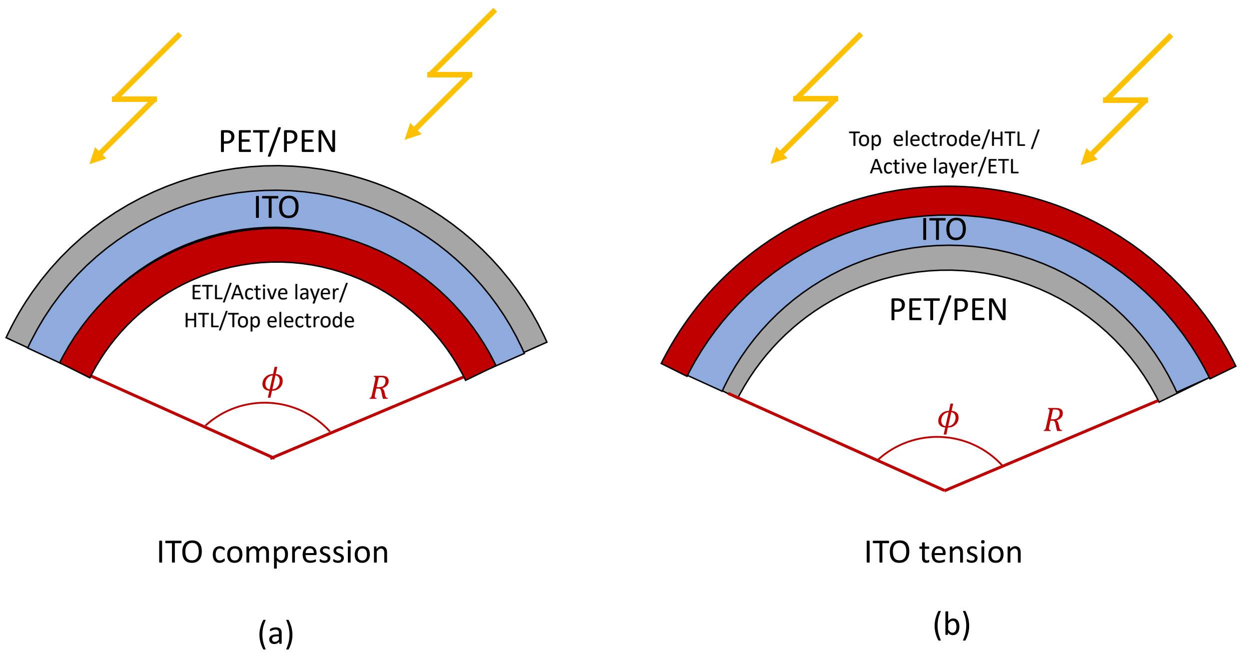

Figure 71: Illustrative schematic of OPV curvature with multiple layers demonstrating: (a) ITO under compression and (b) ITO under tension. The diagram explicitly shows the curvature radius R, the curvature angle ϕ, and the illuminated surface.

As the composition of each layer remains undisclosed, it is unclear whether the transparent electrode is made of ITO and whether it undergoes compression or tension. In this study, we focused solely on analysing convex curvatures, where the illuminated surface is bent as illustrated in Figure 71, leaving the study of concave curvatures for future research. For this purpose, three structures were developed to hold the OPV while maintaining specific curvatures, as shown in Figure 72. Each structure radius corresponds to the desired curvature, leading to their designations: “Big” (big radius, small curvature), “Medium” (medium radius, medium curvature), and “Small” (small radius, large curvature). Further curvature experiments shall use this notation.

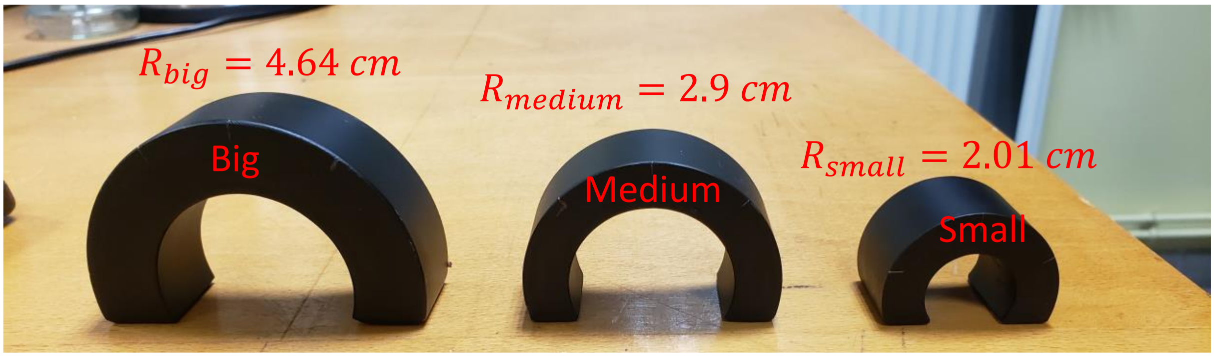

Figure 72: Developed structures to maintain OPV curvature.

Their corresponding radii for the structures are: $R_{Big} = 4.64\ cm$, $R_{Medium} = 2.9\ cm$ and $R_{Small} = 2.01\ cm$. Given the OPV length ($l = 4.7\ cm$), the curvature angles ϕ_x (refer to Figure 71) can also be calculated using Equation III-5, where the index x represents the used structure. Consequently, the obtained angles are: $\phi_{Big} = 58°$, $\phi_{Medium} = 93°$ and $\phi_{Small} = 133.8°$.

$$\phi_x = \frac{l}{R_x} \qquad \text{III-5}$$

In our analysis, we employed the same angular bench shown in Figure 61 and the white LED described before. As our main goal was to evaluate influence of the curvature on the performance, the actual transmitted optical power P_t was not a critical factor. Again, the Keithley 2621B source-measure unit was employed for the short-circuit current measurement. The obtained results are shown in Figure 73.

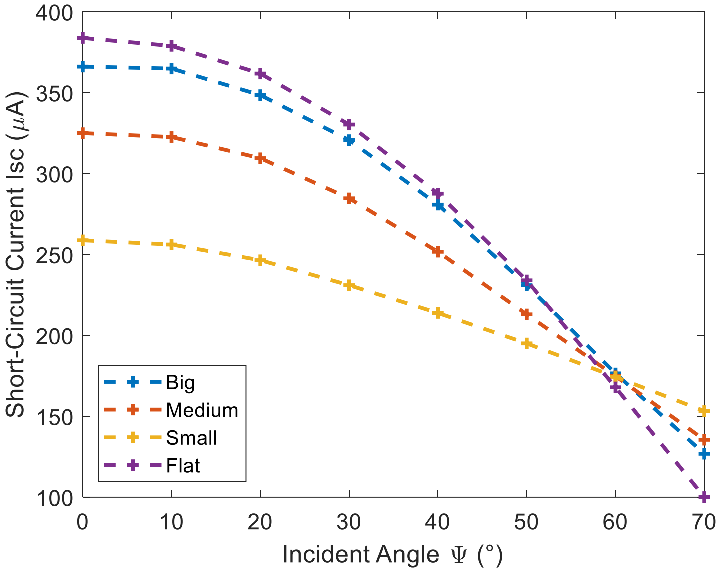

Figure 73: Measured I_{sc} in function of the incident angle Ψ for different curvatures.

The experimental results reveal several notable conclusions. For a flat OPV, the device outperforms curved ones when the incident angle is not a critical factor, such as in perfectly aligned scenario. In fact, curving the OPV significantly reduces the solid angle subtended by the source and the receiver under perfect alignment condition, fact that will be further explored in Chapter IV. However, curved devices are less affected by variations in the incident angle compared to flat devices. As a result, devices with greater curvature exhibit reduced dependency on the incident angle Ψ. This innovative behaviour is particularly valuable in high-mobility applications, such as wearable devices like connected bracelets, where the incident angle of LOS links can frequently vary.

Finally, we have concluded all static characterizations of this particular OPV, developing the energy harvesting foundation for subsequent chapters.

III.4. Dynamic characterizations – communication performance

In this section, the OPV dynamic characterization is carefully described. Here, we will evaluate the bandwidth B of the device under different conditions, along with an examination of signal intensity, which plays a crucial role in determining the overall SNR in communication applications. Two distinct methods are employed for this analysis: frequency response measurements using the Bode method and rise/fall time evaluations using the transient method, both of which were outlined in Chapter II. To enhance the readability of the main text, the transient method has been moved to Appendix 2, as the characterization results are of greater significance than the method itself. Nonetheless, a comparison of the precision and reliability of these methods will still be conducted.

The OPV bandwidth and signal amplitude were measured under various conditions, including illumination levels of 100 lux, 500 lux, and 1000 lux; operating points ranging from short-circuit to open-circuit; four OPV curvatures (as described in the previous section); and two output variables: current extracted using a TIA and voltage extracted with a parallel load (refer to Figure 53).

The experiments are conducted under a LOS link scenario with perfect alignment between the transmitter and receiver. Initially, the frequency method is used to evaluate the effect of illumination on the bandwidth and signal amplitude for both front-end circuits (TIA and parallel load), using a flat OPV. Next, the performance of curved OPVs is evaluated under 500 lux, again for both front-end configurations. Finally, the same steps are repeated using the transient method, resulting in a comparison of both techniques.

In this setup, the illumination levels (100 lux, 500 lux and 1000 lux) are determined by the DC component of the optical signal. The transmitter and receiver are placed 33 cm apart, and a converging lens is employed to concentrate the transmitted optical power onto the OPV surface. The illumination level is measured using the BLACK-comet spectrometer, which captures the average illumination value without accounting for variations in the optical signal. For the scenario, the TIA feedback resistance R_f (refer to Figure 19) was set to $1\ k\Omega$, providing good signal amplitude values. Stability analysis revealed that the absence of a feedback capacitor provided the fastest and most effective response. The TIA employed a LM358AN OP-AMP with symmetric supply source of $\pm 5\ V$. For the bias, an external source was employed. It is important to note that the output voltage of a TIA circuit is intrinsically negative, as shown in Equation II-22.

A direct comparison between the TIA and parallel load front-ends at the receiver side is not straightforward. With the TIA approach, the OPV operating point is directly determined by a voltage source. In contrast, for the parallel load configuration, the operating point is influenced by the illumination conditions as shown in Figure 69.

Again, the white LED described before was employed for the dynamic characterizations, while the DSOX1202G oscilloscope, by Keysight, was used, with $1\ M\Omega$ input impedance. The schematic of the proposed bench is shown in Figure 74. It is important to note that the resulting optical signal varies depending on the method used (frequency or transient).

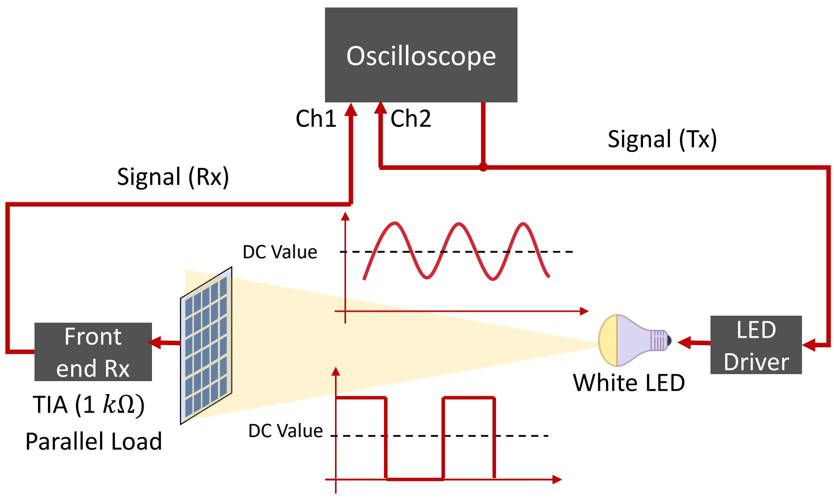

Figure 74: Schematic of the dynamic characterization bench. For the frequency method, the sinusoidal wave is used, while for the transient method, the square wave is used.

III.4.1. Optical source front-end circuit

As detailed in Section II.1.3, LEDs present a linear operating region where the transmitted optical power is proportional to the forward current. Additionally, the conversion of forward voltage to optical power is not linear and creates signal distortions. Consequently, a dedicated transmitter front-end circuit is required for two main purposes: first, the electrical signal, which is normally a voltage, must be linearly converted into a current to drive the optical source; and second, to combine the AC component of the signal with the DC component, a function commonly performed by a bias tee. Figure 75 shows the proposed circuit, which was based on the TSH512 Hi-fi stereo/mono infrared transmitter and stereo sub-carrier generator datasheet, developed by STMicroelectronics.

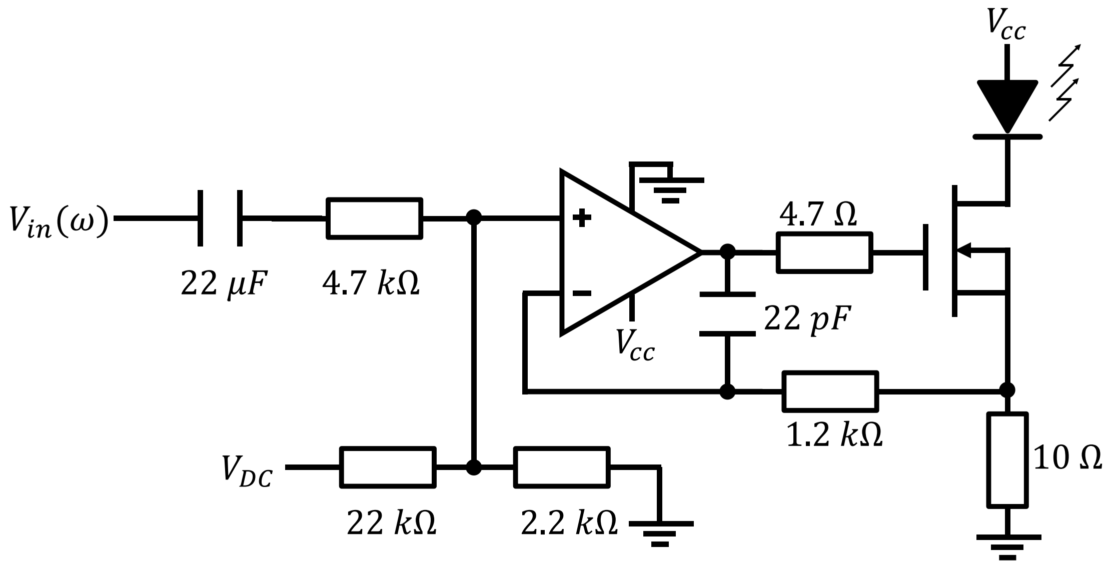

Figure 75: Proposed front-end circuit for LED driving.

The detailed operation of this circuit is out of the scope of this thesis. Here, the input signal will consist of either a sinusoidal wave (for the frequency method) or a square wave (for the transient method). The V_{DC} value determines the DC component of the optical signal, therefore setting the average illumination level on the OPV. Following a careful analysis and accounting for our specific LED source device, we concluded that the following V_{DC} values correspond to the desired illumination levels E_v:

Table 7: Required V_{DC} values for desired illumination levels E_v.

V_{DC} (V)	E_v (lux)
2.46	100
11.46	500
25.46	1000

For both methods, the peak-to-peak amplitude of the electrical signal was set to 660 mV, which provided good optical signal amplitude for the characterization process while avoiding flickering effects. To validate the performance of the proposed optical transmitter, a fast photodiode receiver, the DET025A(/M) by Thorlabs, was used to measure its frequency response. The photodiode was configured with low gain to achieve a high bandwidth of 2 GHz, enabling precise characterization. Using this reference detector, the transmitter exhibited a low-pass filter behaviour with a -3 dB bandwidth of approximately 150 kHz, as shown in Figure 76.

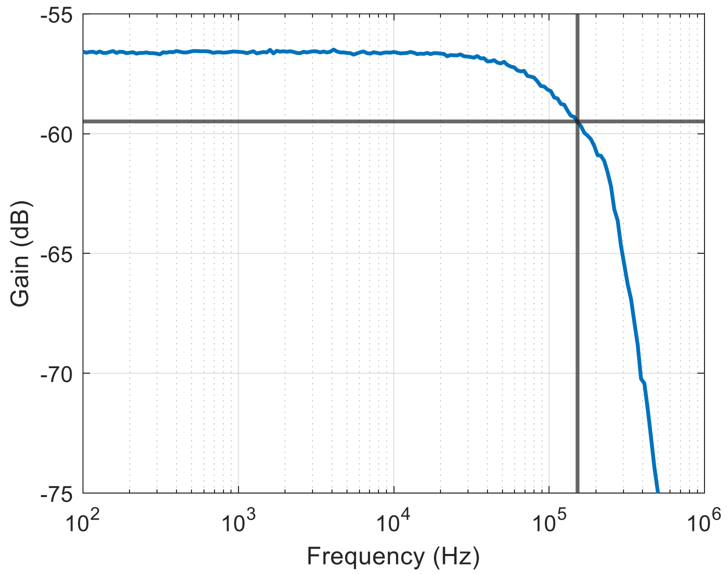

Figure 76: Measured frequency response of the optical transmitter using the reference fast photodetector.

In conclusion, if the OPV frequency characterization also results in a -3 dB bandwidth similar to that of the transmitter, it would indicate that the system performance is primarily limited by the transmitter. However, given the OPV relatively large active area compared to devices specifically optimized for communication, it is anticipated that the OPV bandwidth will be the primary limiting factor for the overall system.

III.4.2. Frequency method

For the frequency method, we used the frequency response measurement of the oscilloscope (Bode measurement), which automatically applies a sinusoidal wave with varying frequencies to the input and measures the corresponding output signal. The system calculates the gain by dividing the amplitude of the input signal by the amplitude of the output signal. Frequencies ranging from $100\ Hz$ to $100\ kHz$ were tested, resulting in a total of 200 measured values. To simplify the presentation only the bandwidth and signal magnitude analyses is discussed, while the detailed Bode curves are omitted.

III.4.2.1. Illumination influence

Initially, the impact of average illumination on OPV performance is examined. The analysis begins by evaluating the output current performance using the TIA configuration. Subsequently, this is compared to the output voltage performance achieved with the parallel load front-end.

- **TIA – Output current**

  For the output current, it is anticipated that the current value will decrease as the operating voltage increases, a behaviour consistent with the predictions from the I-V curve measurements. The results obtained for various illumination levels are summarized below.

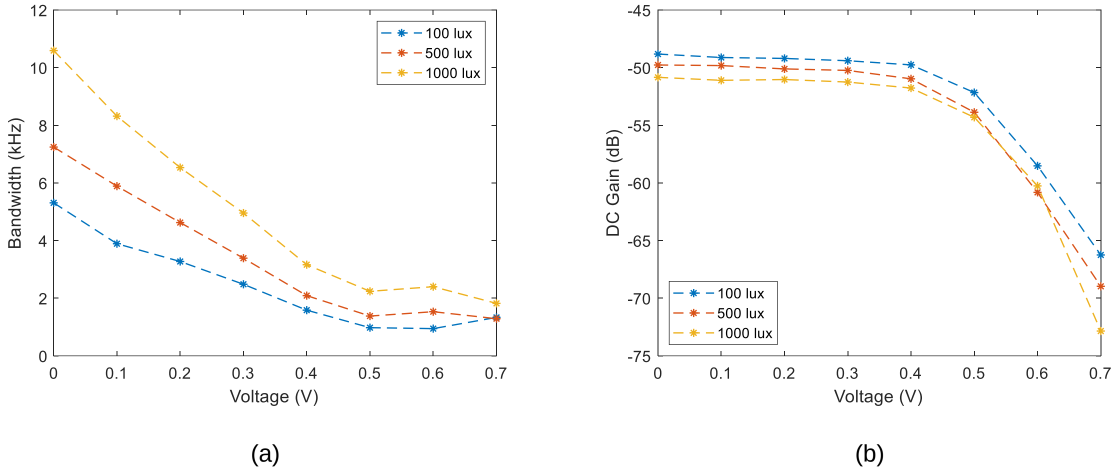

Figure 77: OPV measured dynamic parameters as a function of operating point for multiple illuminations, Bode method and output current: (a) Bandwidth; (b) DC Gain.

In Figure 77.a, the behaviour described in Chapter II is observed: higher operating voltages leads to lower bandwidths. Additionally, the OPV bandwidth increases with rising illumination for the output current measurement, fact that was previously noted in the literature, as detailed in Table 6. This effect is particularly evident when the device operates under short-circuit conditions, while higher operating points, the bandwidth converges to approximately $2\,kHz$ regardless of illumination level.

Furthermore, increasing the illumination slightly decreases the signal amplitude, as shown in Figure 77.b. This is due to higher noise level, which directly affect the frequency measurement process. Similarly, higher operating voltages result in lower signal amplitudes, further highlighting the trade-offs between operating conditions and the dynamic performance of the OPV.

Moreover, the measured bandwidth values are lower than those reported in the literature, as illustrated in Figure 56. This outcome is anticipated, given that OPVs printed on flexible substrates typically underperform compared to devices fabricated in controlled laboratory conditions on rigid, stable substrates. However, a direct comparison between the present measurements and those in the literature remains challenging due to the lack of standardized protocols for this type of characterization.

Under this scenario, the OPV tends to experience a decrease in communication performances at higher operating voltages. Therefore, in a SLIPT scenario, there is no actual interest in going beyond the MPP, as it will generate less power and will perform poorly. In the current setup, determining the precise MPP of the OPV is not possible, as no information is available regarding the DC values of either the current or the voltage. Additionally, these findings reaffirm the anticipated behaviour: the system limitations are primarily dictated by the OPV bandwidth rather than the optical source.

Parallel load – Output voltage

As described in Chapter II, the output voltage can be directly measured by connecting the device to a parallel load, as shown in Figure 53.a. As seen in previous reports, higher illumination values tend to saturate the output voltage. Again, important communication parameters can be extracted from the experiments, as shown below.

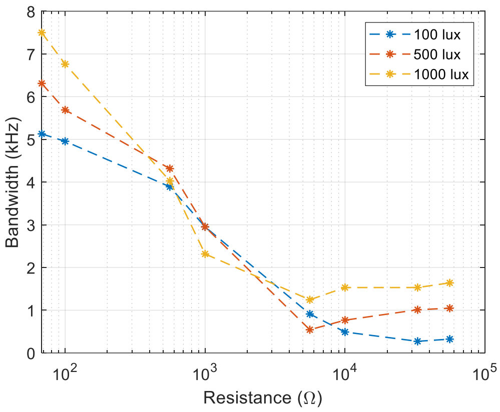

(a)

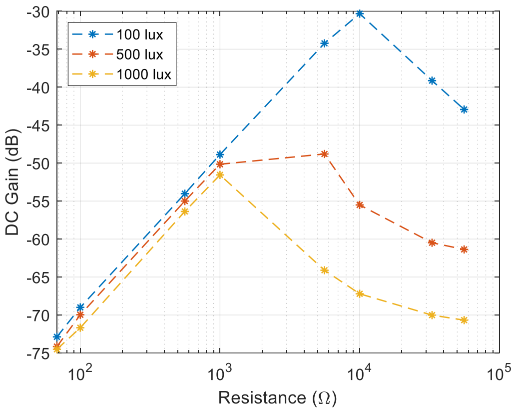

(b)

Figure 78: OPV measured dynamic parameters as a function of operating point for multiple illuminations, Bode method and output voltage: (a) Bandwidth; (b) DC Gain.

In Figure 78.a, it is evident that as the resistance increases, the bandwidth decreases for all illumination levels. In fact, this behaviour is expected, as higher resistances introduce larger RC time constant, slowing the response time of the global receiver system. However, in comparison to the output current (TIA) method, the differences in bandwidth between illumination levels are less significant, with the curves intersecting at medium resistance values. Furthermore, the voltage reading method exhibits bandwidths that are comparable in magnitude to those achieved with the output current approach.

In Figure 78.b, the conclusions are less straightforward compared to the output current method. Here, the signal amplitude initially increases with increasing resistance values, but a saturation effect occurs when the load resistance becomes too large, causing the signal amplitude to drop drastically. Higher illumination levels lead to saturation at lower resistance values. At low resistances, the illumination level has minimal impact on the signal amplitude, fact previously seen in the V-R curves, shown in Figure 69. However, at medium resistance values, the influence of illumination becomes more noticeable. This is due to the signal amplitude approaching saturation for higher illumination levels, while lower illumination levels continue to show a gradual increase in signal amplitude.

From the combined analysis of both curves, it becomes clear that there is a trade-off between bandwidth and DC gain, governed by the choice of resistive load. Low resistances favour bandwidth but compromise gain, while higher resistances can improve gain at the cost of reduced bandwidth. Finally, the results demonstrate a strong dependence of the OPV dynamic performance on the ambient illumination level when analysing the output voltage. At low load resistances, the device shows minimal sensitivity to variations in illumination, providing a stable output, but with weaker signal amplitude. Conversely, at high load resistances, the performance becomes highly dependent on illumination levels, with the output often reaching saturation even at lower intensities, such as 100 lux.

The proposed characterization has provided valuable insights into the OPV performance under various illumination scenarios. For both output variables, increasing the operating point (either by adjusting the bias voltage with the TIA or by increasing the parallel load value) leads to a reduction in the receiver bandwidth, while higher illumination levels result in slightly improved bandwidths with a TIA, but no further conclusions with the parallel load. In terms of signal amplitude, the output current offers a reliable method for signal detection with minimal interference from the optical DC component, such as ambient lighting conditions, but at the expense of requiring an active circuit. Conversely, the output voltage exhibits significant dependence on environmental illumination levels, yet it benefits from being part of a passive circuit design.

Complementary analysis of illumination effects is presented in Appendix 2 employing the transient method. For now, the focus shifts to examining the impact of curvature on dynamic performance.

III.4.2.2. Curvature influence

For the curvature analysis, the OPV was positioned in the same location as in previous experiments and shaped using the structures described in Section III.3.5. Each result is associated with its respective structure: “flat”, “big”, “medium” and “small”. This analysis aims to address various concerns related to flexible OPVs, particularly the impact of curvature on their internal properties and overall performance, as briefly described in Section III.3.5 and shown in Figure 71. Again, both receiver front-end topologies were employed, with a constant 500 lux illumination level.

- **TIA – Output current**

  It is worth noticing that the results previously obtained for the flat OPV at 500 lux can be compared to the ones obtained with various curvatures. For the output current method, the obtained dynamic parameters are shown in Figure 79.

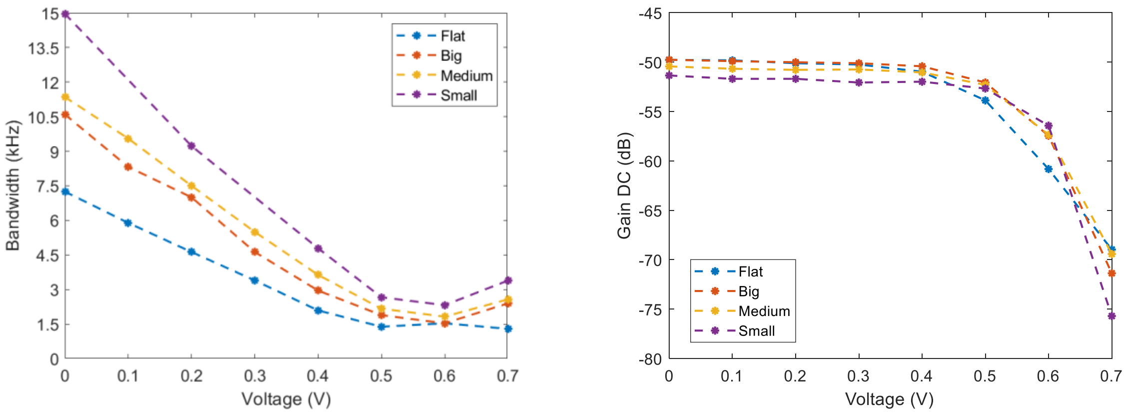

(a) (b)

Figure 79: OPV measured dynamic parameters as a function of operating point for multiple curvatures, Bode method and output current: (a) Bandwidth; (b) DC Gain.

From the obtained results, significant noise was observed at operating points of 0.1 V and 0.3 V for the “small” topology, heavily affecting the accuracy of the bandwidth measurements for these values. Repeated measurements were performed to ensure reproducibility, and the consistency of the results excludes errors in the measurement process. However, the source of this noise remains unidentified for these particular conditions. Consequently, these values were excluded from Figure 79.a.

Again, for any curvature, an increase on the operating point results in a decrease of the bandwidth. The results provided in Figure 79.a reveal that curvier devices exhibit slightly higher bandwidth as the curvature radius decreases. However, the reason of this behaviour remains unclear, though some hypotheses are discussed later. At higher operating voltages, the bandwidth values for all curvatures converge at around 3 kHz.

In Figure 79.b, the DC gain behaviour is relatively consistent across all curvatures, with only minor variations observed. The gain remains stable at lower voltages but begins to drop significantly as the operating voltage approaches the open-circuit condition, regardless of the curvature (trend observed in previous experiments). Notably, larger radii show slightly higher gain at very low voltages.

Here, the “medium” and “big” configurations show minimal differences in performance between them. However, it is clear that both outperform the flat device. Previous curvature experiments demonstrated that curvier devices detect less optical power under perfect alignment condition, as described in Section III.3.5. Similarly, in the current approach, curvier configurations detect less intensity of both AC and DC optical components, leading to a reduced output signal amplitude for smaller radii. This observation could explain why the DC gain of the curvier configurations is lower than that of less curved devices. However, this does not account for their superior bandwidth compared to flatter configurations. As shown in Figure 77.a, lower illumination levels typically result in reduced bandwidth, yet curvier devices, despite receiving less optical power, exhibit higher bandwidth. One possible explanation for this behaviour is that the curvature may alter the internal properties of the device. This hypothesis will be further investigated in subsequent sections through I-V curve measurements under dark conditions for different curvatures.

Parallel load – Output voltage

While the first two resistance values ($68\,\Omega$ and $100\,\Omega$) for each curvature exhibited significant noise, making them unsuitable for reliable conclusions regarding the bandwidth, they can still provide satisfactory results for the DC gain. The refined dynamic parameters are displayed in Figure 80.

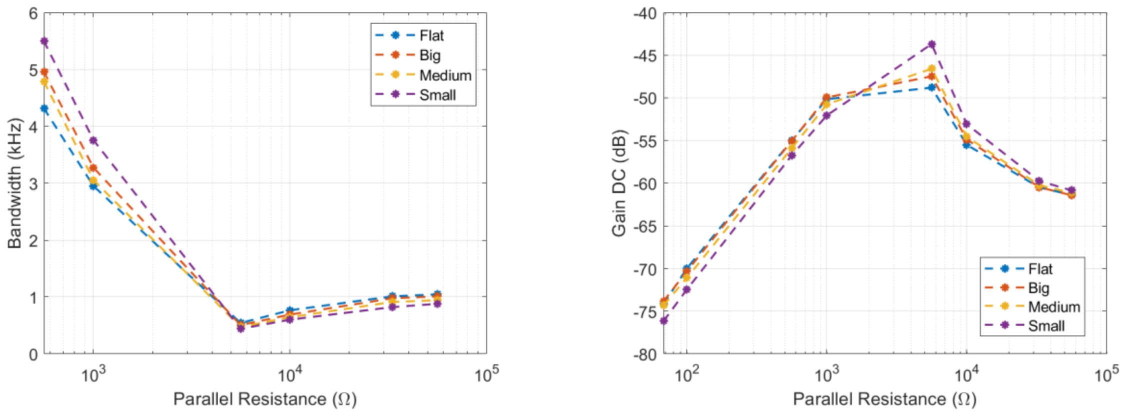

(a) (b)

Figure 80: OPV measured dynamic parameters as a function of operating point for multiple curvatures, Bode method and output voltage: (a) Bandwidth; (b) DC Gain.

Figure 80.a shows that, similar to the results obtained before, as the resistance increases, and consequently the operating point, the bandwidth decreases consistently across all curvature configurations. This behaviour aligns with the expected increase in the RC time constant at higher resistances, which slows the system response time.

Considering the resistances from $560\,\Omega$ and beyond, the bandwidth loss behaviour agrees with the one obtained with the TIA method (Figure 79) for increasing operating point. At higher operating points, all topologies converge to approximately $1\,kHz$. The differences in bandwidth among all configurations, including the flat topology, are relatively minor and not particularly significant.

Figure 80.b shows the DC gain behaviour as a function of parallel resistance for multiple curvatures. Similar to the observations made for the TIA configuration, curvier devices detect less optical signal amplitude, resulting in reduced DC gain at low resistance values. However, due to their lower detection of the DC component of the optical signal, they reach saturation at higher resistance values.

The conducted experiments offered valuable insights into the impact of curvature on the OPV frequency response. For both front-end configurations, the DC gain results indicate that the effect of curvature on signal amplitude is primarily due to reduced detection of AC optical power, as discussed in the static curvature characterization in Section III.3.5. However, the bandwidth analysis reveals that curvature has minimal influence on the output voltage bandwidth but leads to an increase in the output current bandwidth. Complementary information concerning this behaviour is further investigated using the transient method, described in Appendix 2, with a comparison of both methods presented in subsequent sections.

III.4.3. Dark I-V characterization

In a first approach, to investigate the internal variations of the OPV under different curvatures, a dark I-V characterization was conducted. This method is essential for understanding the intrinsic electrical properties of PV cells, as it isolates their behaviour from the influence of photo-generated carriers (refer to Figure 40). The measurements were performed using the same equipment detailed in the static characterization section. The resulting curves are presented in Figure 81.

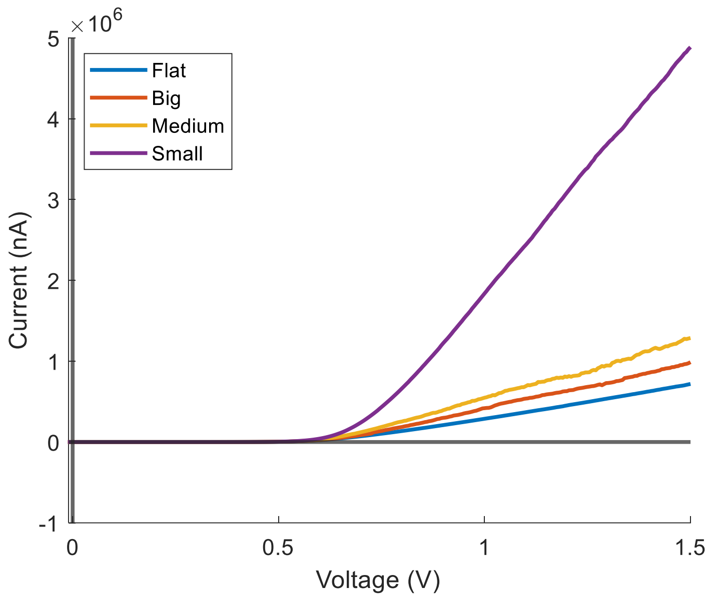

Figure 81: Measured OPV dark I-V curves for different curvatures.

At the same voltage values, it is noticeable that curvier devices tend to allow more current. Interestingly, this fact is supported by a decrease of the OPV series resistance R_s for higher curvatures, clearly seen as an increase of the slope, a trend previously noted in Figure 41. In fact, a decrease of the series resistance also validates some of the obtained results: considering a low pass filter with RC time constant, a decrease in R_s reduces the time constant, thereby increasing the device bandwidth. Interestingly, this trend contrasts with some reports in the literature, which suggest that the resistance of the device increases with larger curvatures [236], [237]. Various studies highlight that multiple factors influence the impact of curvature on device properties, including the curvature radius, whether it is convex or concave, and the specific materials used. For instance, some reports indicate that compression or stretching of ITO layers produces differing effects; however, no existing studies report an improvement in R_s with curvature.

Nonetheless, the dark I-V curve analysis serves as a preliminary step to explore the influence of curvature on the OPV internal parameters. These observations highlight the need for further analysis to correlate mechanical deformation with the device intrinsic properties and its impact on dynamic performance. However, this was not the primary scope of our work.

III.4.4. Method comparison

We performed dynamic characterizations employing two different methods: the first is based on a direct frequency response of the receiver trough Bode measurements; while the second is based on a transient temporal method, where the receiver is modelled as a first-order low pass filter with RC time constant, resulting in an overdamped response characterized by rise and fall times (Appendix 2). The validation of the transient method through comparisons with the frequency one validates the low-pass filter behaviour of the OPV.

Based on the analysis presented, it is evident that both methods capture the essential trends in the dynamic behaviour of our flexible OPV cell. For instance, the observed decrease in bandwidth with increasing operating point and the sensitivity to illumination levels are consistently reflected in both methods. However, discrepancies arise in measurements involving high curvatures or low resistances, where noise and imprecision affect the transient method more significantly than the frequency one. To ensure a straightforward comparison, we have chosen to plot the results from both methods exclusively for the flat OPV scenario, as illustrated in Figure 82.

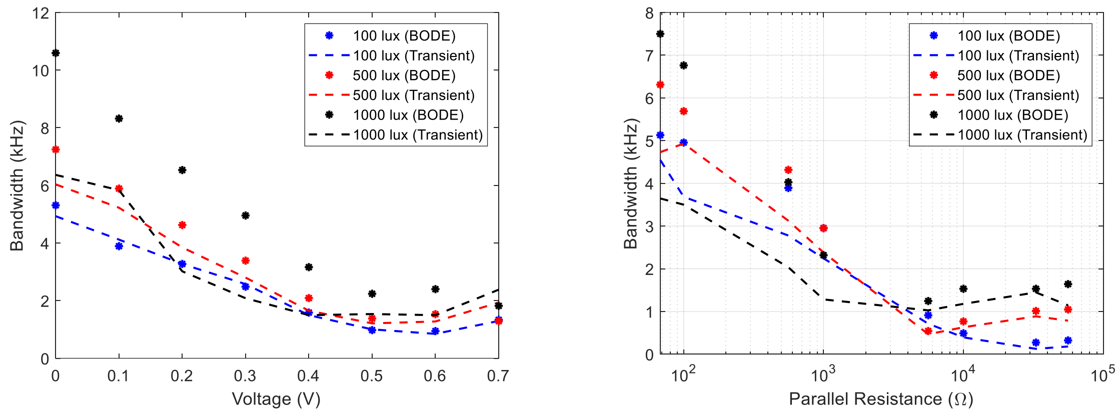

(a) (b)

Figure 82: Bandwidth comparison between the frequency (BODE) and transient methods under both front-ends: (a) TIA; (b) Parallel resistance.

Another critical difference lies in the ability to measure static parameters like V_{mean}. The transient method uniquely provides insights into the average voltage under varying conditions, an essential metric for understanding OPV performance in SLIPT scenarios. Meanwhile, the strength of the frequency method lies in its ability to characterize bandwidth more robustly, particularly when noise is a limiting factor.

Ultimately, the choice of method depends on the application. For precise dynamic characterization, especially in research settings where bandwidth is a priority, the frequency method is preferable. However, for rapid assessment and integration into practical systems, the transient method offers a more streamlined approach.

III.4.5. Dynamic characterization conclusion

The analysis of both frequency and transient methods revealed consistent trends, such as the reduction in bandwidth with increasing operating points and the performance dependence on illumination levels. Additionally, curvature experiments further highlighted the impact of mechanical deformation on OPV behaviour, suggesting potential modifications to intrinsic device properties.

The results from both methods confirm the hypothesis that curvier devices detect less optical power than flat ones under perfect alignment conditions. Consequently, their performance metrics resemble those of flat devices receiving reduced optical power. Regarding bandwidth, while some findings suggest that curvier devices exhibit slightly higher bandwidths, as seen in Figure 79.a and Figure 130.a, other results, such as Figure 80.a, show differing trends, where the "big" topology outperforms the "medium" one. Nonetheless, all curved configurations generally demonstrate marginally better bandwidths compared to flat devices.

Moreover, results showed that higher illumination levels slightly increase device bandwidth, especially at lower operating points. However, as the operating point increases, the bandwidth significantly decreases across all front-end configurations. For any illumination level, the bandwidth converges to values between $1\,kHz$ and $2\,kHz$ at the open circuit condition. At the short-circuit condition, the bandwidth ranges from $4\,kHz$ to $8\,kHz$, depending on the illumination level. Irregular results, such as a bandwidth of $12\,kHz$ observed during the Bode measurement at 1000 lux with the TIA, suggest the need for further investigation. Considering a flat OPV while accounting for both TIA and parallel load front-ends and both characterization methods, the expected bandwidth for different operating points are resumed in Table 8.

Table 8: Expected flat OPV bandwidth for different operating point, including short-circuit, intermediary points and open-circuit. Results obtained from both TIA and parallel load front-ends, with both methods.

	Short-Circuit	Intermediary	Open-Circuit
Expected bandwidth (kHz)	$4-8$	$3-5$	$1-2$

Measurements using the output current method exhibited more noise compared to the parallel load configuration. This is likely due to the complexity of the TIA front end, which incorporates multiple voltage sources that can introduce additional noise, amplified based on the feedback resistance R_f. However, we have meticulously demonstrated that the parallel load front-end has an important dependence on the illumination levels.

These measured bandwidth values align with the hypothesis that the geometric capacitance of the OPV primarily limits the receiver time response. To evaluate whether the order of magnitude of these bandwidths is accurate, we can estimate the RC time constant for an OPV of this size using Equation II-92. Assuming a typical OPV active layer thickness of approximately 200 nm and a relative permittivity ε_r of 4, which is consistent with values reported in the literature for organic materials [190], the absolute permittivity ε is calculated as 3.5417×10^{-11}. At an illumination level of 1000 lux, the estimated series resistance R_s is around $74\,\Omega$, as shown in Figure 67.e. Considering the $68\,\Omega$ parallel load, the flat OPV bandwidth measured using the frequency method is approximately $7.5\,kHz$. Using these values, the RC time constant τ_{RC} is estimated to be 7.80 μs, and based on Equation II-94, the expected bandwidth would be $20\,kHz$. While this calculated value does not perfectly match the measured bandwidth, it provides a reasonable and reliable estimation. As discussed in Chapter II, additional factors influence the dynamic behaviour of OPVs, such as charge carrier mobility, which was not included in this comparison. Furthermore, the resistance introduced by other electronic components and measurement instruments in the experimental setup, which were not accounted for in this analysis, may also contribute to the discrepancy

Finally, these results underscore the complex connection between OPV physical properties, operating conditions, and environmental factors, such as illumination and curvature. While the current analysis has established a first approach, further investigations into the internal properties of curved OPVs, particularly through more complex characterizations, are necessary to fully understand the mechanisms driving their dynamic behaviour. For clarity, the characterization results obtained using the frequency method are summarized in Table 9 and Table 10 for the TIA and parallel load configurations, respectively. The tables analyse the impact of increasing variables (illumination or curvature) on both signal amplitude (or SNR) and bandwidth across different operating points: short circuit (SC), intermediate, and open circuit (OC).

Table 9: Measure impact of increasing illumination condition on OPV-based receiver performance in terms of signal amplitude (or SNR) and bandwidth improvements. Current reading scenario.

TIA	**Increasing illumination ↑ (flat OPV)**			**Increasing curvature ↑ (500 lux)**		
Operating point	**SC**	**Intermediary**	**OC**	**SC**	**Intermediary**	**OC**
SNR / Signal Amplitude	↓	↓	↓	↓	↓	↓
Bandwidth	↑↑↑	↑↑	↑	↑↑↑	↑↑	↑

Table 10: Measure impact of increasing illumination condition on OPV-based receiver performance in terms of signal amplitude (or SNR) and bandwidth improvements. Voltage reading scenario.

Parallel load	**Increasing illumination ↑ (flat OPV)**	**Increasing curvature ↑ (500 lux)**

Operating point	SC	Intermediary	OC	SC	Intermediary	OC
SNR / Signal Amplitude	↓	↓↓*	↓↓↓*	↓	↑	--**
Bandwidth	↑	--**	↑	↑	--**	--**

*Values depend on the saturation condition of the OPV, therefore, the V-R relation.

** Inconclusive or equal results.

III.5. Chapter conclusion

The comprehensive analyses presented in Chapter III have provided a detailed characterization of flexible OPVs, emphasizing both their static and dynamic behaviours. Static measurements revealed crucial insights into energy harvesting performance under various illumination levels, angular orientations, and mechanical deformations.

Dynamic characterizations, using both frequency and transient methods, further demonstrated the influence of operating points, illumination intensity, and device curvature on OPV dynamic characteristics performance. Notably, while higher illumination levels slightly improved bandwidth, increasing the operating voltage consistently led to reduced dynamic response. The curvature experiments exposed intriguing shifts in device parameters, with curvier configurations displaying unexpected bandwidth trends, necessitating further investigation into their intrinsic properties.

From the perspective of front-end circuit design, the analysis demonstrated that working with the output voltage inherently leads to a high dependence on illumination levels. Based on the state-of-the-art analyses presented in Chapter II, a hybrid front-end circuit could be proposed to overcome this limitation. This circuit would combine the use of output current detection with a complex receiver, such as a TIA, for the communication branch while employing a parallel load to set the operating point for the energy harvesting branch.

These findings underline the dual challenges and opportunities in using OPVs for simultaneous energy harvesting and optical communication. While the achieved results provide a solid foundation, they also raise questions about the internal property changes induced by curvature and their implications for device performance.

Chapter IV transitions into a simulation-driven analysis, extending the characterization of OPVs to an indoor scenario. By incorporating flat and curved models, this next chapter aims to validate experimental results, explore optical propagation, and evaluate the performance under a simulated indoor condition, further bridging the gap between theory and application.

Chapter IV

On the Indoor Simulation of OPVs

Summary

Chapter IV. On the Indoor Simulation of OPVs

The characterizations described in Chapter III have provided a robust understanding of OPV performance under various conditions, such as static, dynamic, and curvature-dependent scenarios. While these experimental studies show important insights into the relations between curvature, operating points, and illumination, they highlight the complexity of the OPV behaviour, particularly for real-world applications involving communication and energy harvesting.

Chapter IV introduces the simulation of indoor optical channels as a complementary method to predict and evaluate OPV performance in communication and energy harvesting applications for indoor scenarios. The simulation-based approaches offer the advantage of rapidly exploring different environments, allowing for the study of complex systems where experiments are particularly challenging. As detailed in Chapter II, the RaPSor software, developed at the XLIM laboratory, is employed for all simulations.

Indoor optical simulations are particularly relevant for VLC and SLIPT applications, where the performance of OPV devices is influenced by factors such as illumination distribution, environmental reflections and mobility. These simulations help to optimize system design and predict its behaviour across multiple scenarios.

Chapter III demonstrated that OPV parameters, such as bandwidth, signal amplitude, V_{oc}, I_{sc} and output power P_{out}, are highly sensitive to environmental conditions. Consequently, these findings emphasize the need to understand how the channel will affect the OPV performance, for both curved and flat conditions. By extending the experimental characterizations to indoor simulation, we can evaluate its performance on broader scenarios, such as diffuse links with multi curvature systems.

Therefore, the main objective of the current chapter is to integrate two new models into the OWC channel simulator: one for flat OPVs and another for curved OPVs. These models enable the evaluation of their performance in indoor scenarios where diffuse links play a significant role. Chapter IV is structured into two main sections, focusing on flat and curved OPVs respectively. For each section, the implemented model is experimentally validated through measurements of the short-circuit current I_{sc} under both LOS and NLOS conditions. Additionally, the LOS link equation for a curved OPV in a perfectly aligned setup is analysed, emphasizing the impact of curvature on the solid angle subtended between the source and receiver. Finally, two extensive simulations are conducted to illustrate the device efficiency under indoor environments.

The current chapter meticulously describes the work realized through this thesis at XLIM, which resulted in two recent articles [134], [238].

IV.1. RaPSor

As detailed before, RaPSor, is an advanced optical channel simulation tool that integrates Monte Carlo techniques with a ray-tracing algorithm to model the propagation of light in complex environments. The simulation is designed to evaluate channel impulse responses $h(t;\lambda)$ across multiple independent wavelengths, making it a versatile tool for analysing various optical communication scenarios, including SISO and MIMO configurations. With the obtained channel impulse response, the received optical power can be evaluated for different conditions. By incorporating the angular and spectral characteristics of optical receivers, RaPSor extends its capabilities to model the short-circuit current generated under different conditions.

For a simulation execution, multiple parameters must be defined for different components, such as:

- **Simulation configuration**

  Type of link (SISO, SIMO, MISO or MIMO), simulation mode (ray shooting or ray gathering), number of considered reflections, time step, time window, number of rays and employed wavelengths [239].

- **Environment definition**

  Dimensions of each surface of the environment, employed BRDF, and corresponding BRDF parameters (reflectivity ρ for Lambertian surfaces, defined for each employed wavelength). Complex elements, such as multi-surface objects, can be created using 3D modelling software and seamlessly imported into RaPSor.

- **Optical source parameters**

  Type of source – including, but not limited to, punctual, surface and LED array – position, direction, area and $\theta_{1/2}$ for Lambertian sources.

- **Optical receiver parameters**

  Type of receiver – including, but not limited to, punctual, disc and rectangle – position, direction, area, FOV and $\Psi_{1/2}$ for Lambertian receivers.

The simulation can provide two different results: the impulse response for each employed wavelength $h(t;\lambda)$; and the impulse response pondered by the receiver angular properties $h_{\Psi}(t;\lambda)$, as described in Equation II-54. Again, if the receiver does not describe any particular angular behaviour, such as $R_{\Psi} = 1$, the two responses are identical $h(t;\lambda) = h_{\Psi}(t;\lambda)$. The simulator already accounts for a Lambertian receiver with half-current angle of $\Psi_{1/2}$ (see Figure 62 for reference). These results enable the extraction of valuable information, including, but not limited to, illumination levels, mean delay spread, and short-circuit current delivered by a particular photoreceiver (according to its dedicated receiver circuit) through a post-processing analysis.

Until the work described in this thesis, RaPSor was mostly employed with photodiodes as receivers for both OWC and VLC. Here, we demonstrate, for the first time, an OPV model for the ray-tracing software, based on experimental validation.

IV.2. Flat OPV model

As outlined in the previous section, implementing a new receiver model in the simulator requires a precise definition of all relevant OPV parameters. For this purpose, the receiver dimensions were set to match the specifications of the real device provided by Dracula Technologies, and specifically a rectangular dimension of 4.7 cm × 0.66 cm, with a $90°$ FOV, meaning it cannot detect light from behind (as a first approximation). Additionally, the half-current angle $\Psi_{1/2} = 60°$ for a Lambertian receiver, determined through the characterization detailed in Section III.3.2, was incorporated into the model. Again, this particular OPV do not demonstrate any particular angular behaviour, so $h(t;\lambda) = h_{\Psi}(t;\lambda)$. Finally, this new OPV model was validated through experimental measurements of I_{sc}. The same standard high-power white LED described in Chapter III was used for the experiments described in this chapter.

IV.2.1. Flat model validation

To align the model with real-world measurements, the simulated channel impulse response $h(t;\lambda)$ is converted to the expected short-circuit current I_{sc} trough Equation II-53. This process incorporates the source normalized PSD $S(\lambda)$ and the spectral responsivity of the OPV receiver $R_{\lambda}(\lambda)$, both shown in Figure 83.

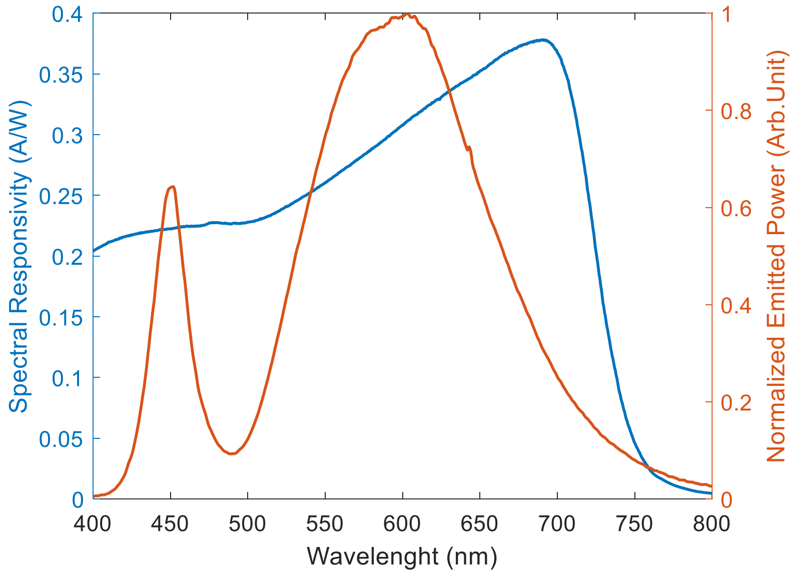

Figure 83: Source PSD $S(\lambda)$ (in red) and OPV spectral responsivity $R_{\lambda}(\lambda)$ (in blue).

The transmitted optical power P_t of the source is measured with the BLACK-comet spectrometer under perfect alignment condition. In this setup, the spectrometer measures a received optical power P_r, which is then extrapolated to P_t using the LOS DC gain H_{LOS}, as defined in Equation II-33. The short-circuit current measurement process is similar to the one described in Section III.3.2, employing the same equipment.

Finally, Figure 84 shows a flowchart outlining the methodology used to validate the OPV model. The validation process relies on measuring the short-circuit current I_{sc} for both LOS and combined LOS+NLOS links. The primary advantage of utilizing a ray-tracing simulator lies in its ability to assess the contribution of diffuse components in complex environments. As a result, validating the newly implemented model under NLOS conditions becomes an essential step in the process.

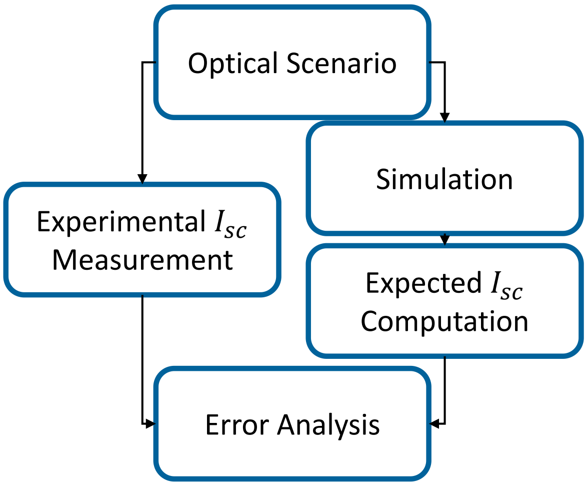

Figure 84: Flowchart of the OPV model validation methodology.

Source: Reproduced with permission from reference [134].

Among the potential sources of measurement errors, the calibration of the transmitted optical power P_t stands out as a significant factor. To account for this uncertainty, a pessimistic $\pm 5\%$ error margin has been applied to the experimental measurements for both link scenarios.

IV.2.1.1. LOS

To validate the LOS OPV model, the same experimental bench used for the angular characterization, shown in Figure 61, was employed, with the OPV length aligned along the bench rotation axis. To differentiate this setup from the original characterization scenario, the distance between the LED and the OPV was adjusted to $d = 15.4\ cm$. For accurate validation, simulations and experiments were conducted while varying the incident angle Ψ from 0° to 80°. Since LOS equations are wavelength-independent, the normalized spectrum at the emission remains identical to that at the reception, with no spectral distortion observed. Therefore, a single wavelength simulation is realized for each transmitter-receiver spatial configuration. In fact, for a LOS link, the channel DC gain H_{LOS} can be analytically obtained as described by Equation II-33. Therefore, the expected short-circuit current I_{sc} based on the theoretical LOS equations can also be obtained.

The results presented in Figure 85 demonstrate a strong agreement between the theoretical short-circuit current derived from the LOS equations, the experimental measurements, and the simulation results. The consistency across the three data sets validates the accuracy of the implemented simulation model for a flat OPV receiver. Minor deviations observed between the experimental and theoretical/simulated results are within the 5% error margin accounted for in the experimental setup, highlighting the reliability of the experimental and simulation methodologies. These discrepancies can be attributed to factors such as precision in the spatial alignment of the LED and OPV or inaccuracies in measuring the transmitted optical power P_t. This correlation underscores the robustness of the proposed model for predicting OPV performance under LOS conditions, supporting its use in further complex scenario analyses.

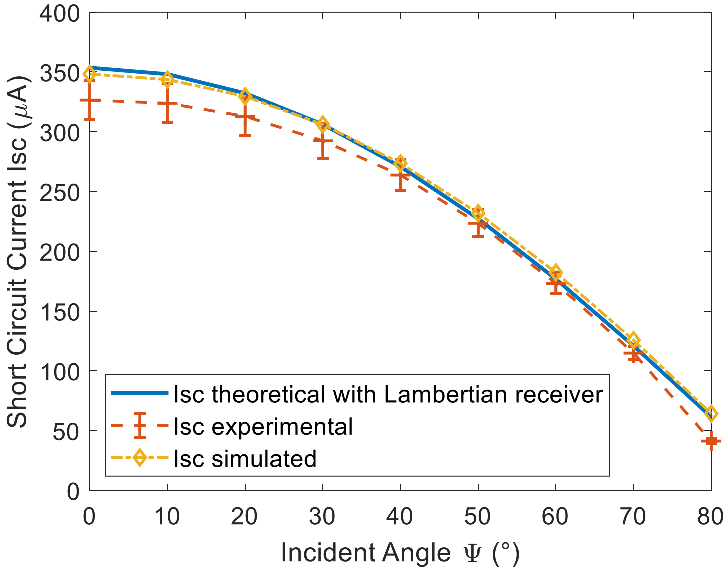

Figure 85: Expected short-circuit current I_{sc} using LOS link equation (in blue), obtained experimental short-circuit current I_{sc} with 5% error bar (in red) and expected short-circuit current I_{sc} obtained from simulation results (in yellow).

Source: Reproduced with permission from reference [134].

IV.2.1.2. LOS + NLOS

To be able to extend the simulation results to indoor scenarios, including IoT ones, the model validation under NLOS link is necessary. For increased reliability, the NLOS influence must be comparable to the LOS one, or surpass it, meaning that materials with high reflectivity must be considered. For simplicity, we have chosen to employ a Lambertian material with high reflection coefficient ρ, such as white paper sheets.

The angular characterization bench was adapted to account for diffuse links. For this purpose, two metal plates were placed 10 cm from the center of the structure, were the OPV is hold. To induce strong reflections from a Lambertian surface, both metal plates were then covered with white paper with spectral reflectance $\rho_{paper}(\lambda)$. For the simulations, this spectral reflectance needs to be measured. Therefore, we have employed the Cary 300 spectrophotometer from Agilent Technologies to perform a UV-Visible spectroscopy of the paper sheet under normal incidence.

Figure 86 shows the measured $\rho_{paper}(\lambda)$ for wavelengths ranging from 380 nm up to 800 nm, along with the source normalized PSD $S(\lambda)$. The spectral reflectance of the white paper demonstrates a nearly constant reflectance value of 0.8 across the wavelength range. Plotting both curves together illustrates how the source spectral power distribution interacts with the reflective properties of the material, crucial for accurately modelling light propagation in indoor optical scenarios.

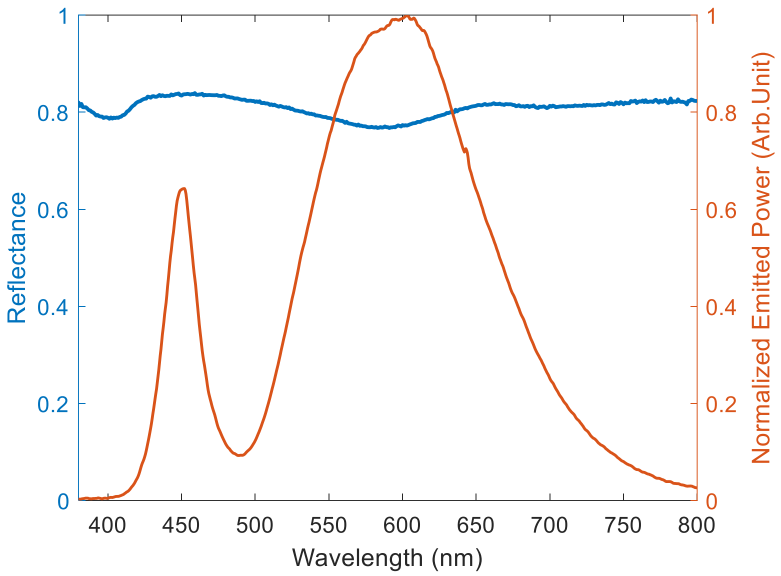

Figure 86: White paper spectral reflectance $\rho_{paper}(\lambda)$ (in blue) and source normalized PSD $S(\lambda)$ (in red).

Compared to LOS scenarios, broad-spectrum simulations demand significantly more processing time than single-wavelength simulations, as each wavelength requires an independent computation. For LOS+NLOS simulations, wavelengths ranging from 380 nm to 780 nm were considered, with a step size of 10 nm for discretization. Subsequently, a SISO simulation was conducted for two distinct configurations: the first scenario included both reflectors and was evaluated at five different positions, while the second scenario featured only the right-side reflector, also evaluated at five positions. The configurations for these scenarios are illustrated in Figure 87.

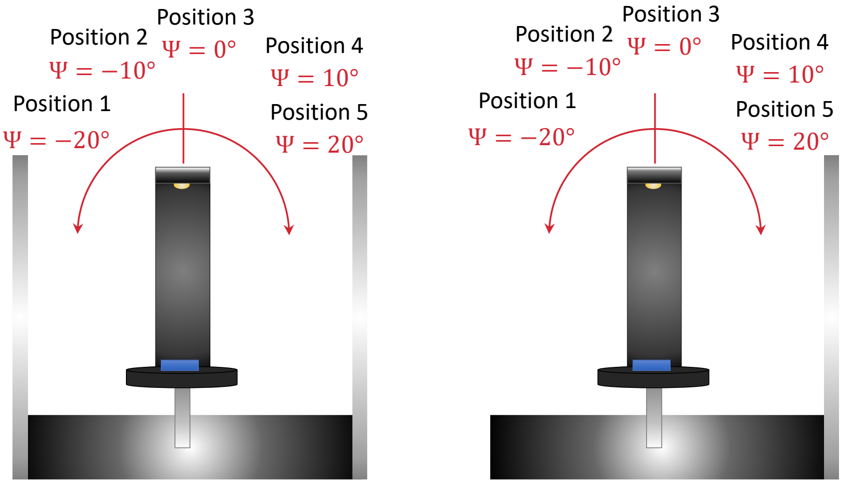

Scenario 1 Scenario 2

Figure 87: Employed scenarios for LOS+NLOS validation experiment.

Source: Reproduced with permission from reference [134].

In typical indoor environments, previous studies have shown that accounting for up to three reflections is sufficient for accurately estimating the channel impulse response in Monte Carlo-based simulations [240]. However, in the current scenario, where the transmitter-receiver distance and the separation between the reflectors and transceivers are on the order of centimetres, the number of reflections plays a significant role in the accuracy of the results. Following a detailed convergence analysis, it was determined that using one million rays with up to 10 reflections produced sufficiently converged results.

From the obtained $h(t;\lambda)$, RaPSor enables the extraction of the LOS link contribution, represented as $h^{(0)}(t)$ in Equation II-39. Consequently, the short-circuit current I_{sc} was also analysed under the condition of excluding reflections. The obtained results are shown in Figure 88.

In Scenario 1, where both reflectors are present, the inclusion of NLOS components increases the short-circuit current by 21%, emphasizing the importance of diffuse reflections in confined indoor environments. Conversely, in Scenario 2, with the left reflector removed, the short-circuit current gain reduces to 10%, as the influence of NLOS rays diminishes, approaching the values of a purely LOS link.

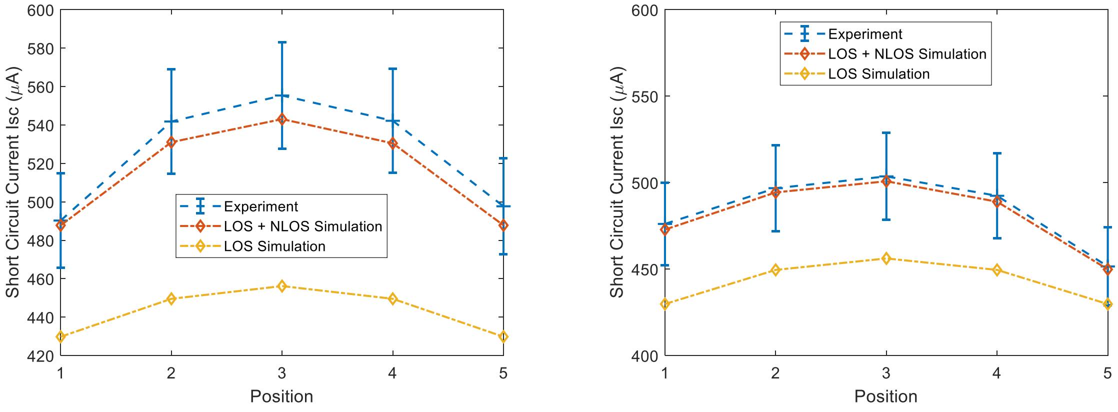

(a)

(b)

Figure 88: Obtained experimental short-circuit current with 5% error bar (in blue), expected short-circuit current obtained from the simulation results (in red) and expected short-circuit current obtained from the simulation results when no reflections are considered (in yellow) for: (a) Scenario 1; (b) Scenario 2.

Source: Reproduced with permission from reference [134].

Finally, the obtained results highlight the significant contribution of reflected rays in enhancing the short-circuit current generated by the OPV receiver. The simulations closely align with the experimental measurements for both scenarios, confirming the reliability of the OPV model implemented in the MCRT simulator.

The ability to predict I_{sc} with high accuracy further demonstrates the robustness of the methodology, offering potential for precise output power P_{out} estimations when combined with the OPV static characterization.

The validation of the OPV model was successfully conducted for both LOS and combined LOS+NLOS scenarios, as demonstrated by the close agreement between simulated and experimental results. This validation confirms the accuracy and reliability of the implemented model in capturing the behaviour of the OPV receiver under diverse optical link conditions. With this robust validation, the OPV model can now be confidently employed to perform indoor simulations, enabling the analysis of device performance in complex environments where both direct and diffuse light components heavily impact the optical channel impulse response. This capability is a strong basis for exploring and optimizing OPV-based systems in realistic indoor scenarios, while accounting for different IoT communication challenges, such as blockage or mobility.

Finally, we performed, for the first time ever, an indoor MCRT simulation employing an OPV as receiver, extending the results to energy harvesting performances.

IV.2.2. Wide spectrum indoor simulation

For wide spectrum simulation with an OPV, we adopted the classical scene, described by Barry *et al.* in [128]. The simulated environment is a 5 m × 5 m × 3 m empty room, composed of four plaster walls, a ceiling and a floor, each characterized by different spectral reflectances. The same surface geometries and spectral reflectances as in [128] were used, but the source PSD was updated as described in Section III.2. Four optical sources were evenly distributed around the centre of the ceiling, each with a normalized transmitted power $P_t = 1\ W$, half-power angle $\theta_{1/2} = 60°$ and a $1\ mm^2$ emitting surface, all facing downward.

The OPV receiver is located 10 cm above the ground facing upwards (typical case associated with an integration on a connected object or robot), and was considered across 400 different positions along the X and Y axes, uniformly divided, with its length aligned to the X axis. Here, thirty-seven wavelengths were employed, ranging from 380 nm to 740 nm with a 10 nm step. After performing a convergence analysis, it was determined that 5 million rays with up to three reflections were sufficient to achieve accurate results. Finally, Figure 89 shows the employed scenario while Table 11 resumes the employed simulation parameters.

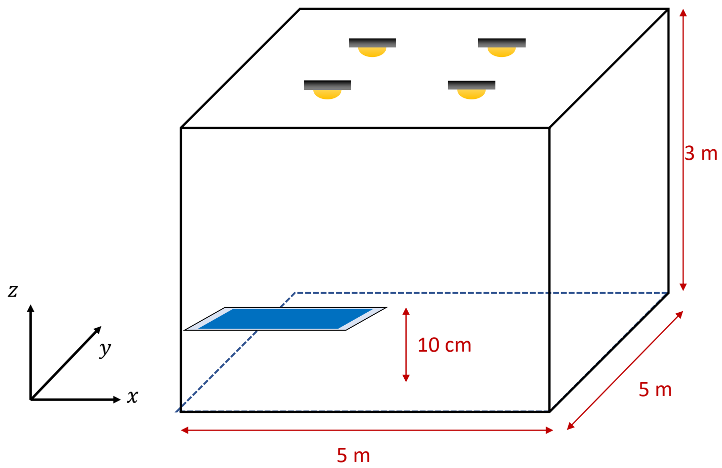

Figure 89: Employed indoor simulation scenario for flat OPV.

Table 11: Indoor flat OPV simulation parameters

Optical Sources	LED 1 position	(1.5, 1.5, 2.99)
	LED 2 position	(1.5, 3.5, 2.99)
	LED 3 position	(3.5, 1.5, 2.99)
	LED 4 position	(3.5, 3.5, 2.99)
	Optical power	4 × 1 W
	Half-power angle $\theta_{1/2}$	60°
OPV	Dimensions	4.7 cm × 0.66 cm
	Positions	400 positions at 10 cm height
	Half-current angle $\Psi_{1/2}$	60°

Simulation	Number of rays	5 million
	Maximum considered reflections	3
	Wavelength range	380 nm – 780 nm
	Wavelength step	10 nm
	Total time length	120 ns
	Time step Δt	0.15 ns

The spectral reflectances that compose the environment and the source normalized PSD $S(\lambda)$ are shown in Figure 90. These reflectance characteristics, combined with the source normalized PSD $S(\lambda)$, provide a comprehensive understanding of how light interacts with the surfaces. The plaster walls demonstrate higher reflectance over most wavelengths compared to the ceiling and floor. The source PSD concentrates its emission peak around 600 nm, matching with the regions of higher reflectance. This relation between surface reflectance and source emission significantly influences the propagation of light rays and the resulting channel impulse response in the simulated environment. Together, these curves underscore the importance of considering the channel impulse response weighted by the source normalized PSD, defined as $h_{\lambda}(t)$, to accurately obtain the system performance.

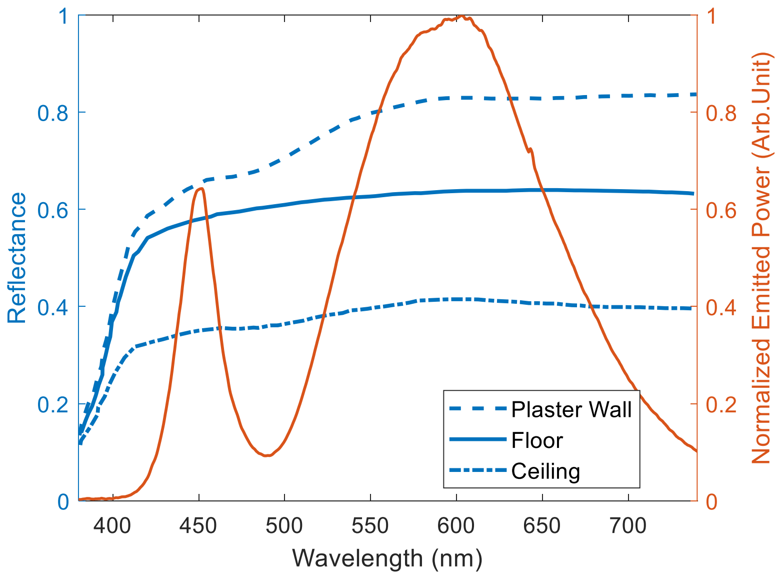

Figure 90: Spectral reflectance of the surfaces that compose the simulation environment (in blue) and source normalized PSD $S(\lambda)$ (in red).

Source: Modified with permission from reference [134].

For each position of the OPV receiver, $h(t;\lambda)$ can be obtained, which was then further extended to multiple different parameters. Initially, the focus was on $h_{\lambda}(t)$, where each position produced distinct curves with varying intensities. To simplify the analysis, two extreme positions were selected: one at the centre of the room and the other at a corner. The resulting curves for these positions are shown in Figure 91.

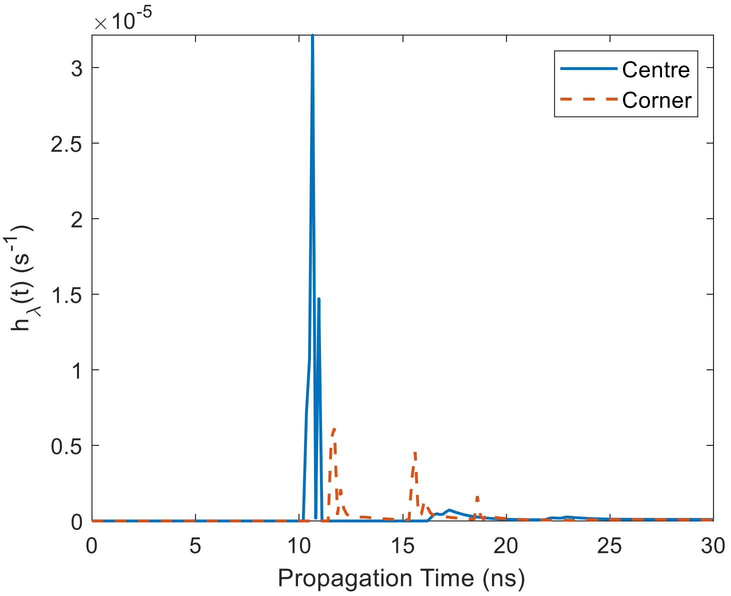

Figure 91: Obtained $h_{\lambda}(t)$ at the centre (in blue) and at the corner (in red) of the simulated environment.

Source: Reproduced with permission from reference [134].

At the centre of the room, a more important impulse response is observed, primarily due to the dominance of the LOS component, as this position is closer to the sources. Additionally, a small NLOS component is noticeable around 17 ns, resulting from surface reflections. In contrast, when moving toward the corner of the room, the LOS link weakens, while the NLOS contribution increases. Distinct LOS peaks are visible, reflecting multiple distances between the OPV and the different sources. Furthermore, in the corner position, a spreading of the impulse response is observed, attributed to the increased influence of the NLOS component and resulting in a dispersive signal.

The delay spread for the analysed positions was calculated using Equation II-48, achieving 1.13 ns at the centre and rising up to 3 ns at the corners. Furthermore, the maximum achievable data rates under these conditions, as determined by Equation II-38, are 89 Mbit/s at the centre and 33 Mbit/s at the corner. However, large-area photodetectors like the particular OPV used in this simulation exhibit reduced bandwidth, as demonstrated in Chapter III. Consequently, for single-carrier modulation schemes such as OOK or 2-PPM, the maximum achievable data rate is optimistically limited to approximately 20 kbit/s for this OPV. This suggests that, for this environment, the channel would not become the primary limiting factor for system performance.

From the received PSD $\Phi_r(\lambda)$ obtained at different positions, the spectral irradiance $E(\lambda)$ can be obtained by dividing the PSD by the OPV active surface A_r. Subsequently, the spectral illuminance $E_v(\lambda)$ (in lux) is determined by applying the photopic luminous function $V(\lambda)$, as described in Equation II-4. Finally, the illumination at different positions is obtained by integrating $E_v(\lambda)$ across all relevant wavelengths. Figure 92 shows the obtained illumination distribution across the simulation environment, at a height of 10 cm.

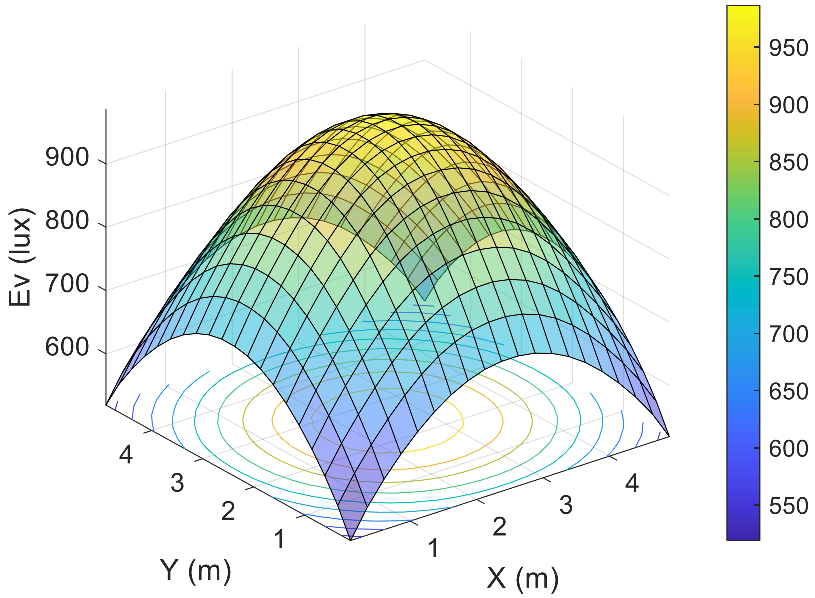

Figure 92: Spatial distribution of illuminance across the simulation environment.

Source: Reproduced with permission from reference [134].

The highest illuminance values, exceeding 990 lux, are observed at the centre of the room, where the distance to the light sources is minimal. As the receiver moves away from the centre toward the corners, the illuminance values gradually decrease, reaching approximately 550 lux. This behaviour reflects the natural attenuation of light with increasing distance and the importance of the LOS component. Furthermore, the obtained illumination values, ranging from 550 lux to 990 lux, align with the guidelines established by the International Organization for Standardization, which specifies that ideal workspace illumination levels should fall between 300 lux and 1500 lux [101].

From the channel impulse response $h(t;\lambda)$, the short-circuit current I_{sc} delivered by the OPV receiver can then be obtained through post-processing methods using Equation II-53, while considering that the OPV does not exhibit any specific angular behaviour. Figure 93 shows the obtained spatial distribution of the short-circuit current.

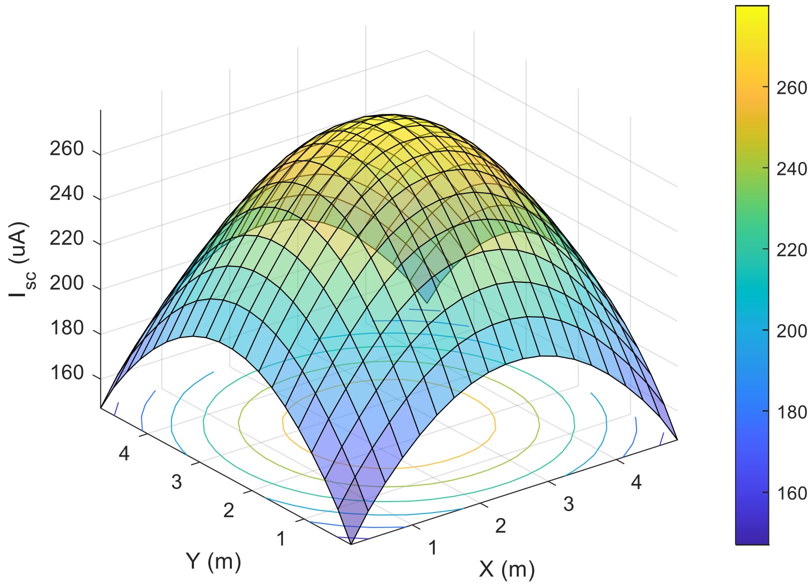

Figure 93: Spatial distribution of short-circuit current across the simulation environment.

The obtained short-circuit values range from approximately 150 µA in the corners of the room to 280 µA at the centre. Logically, the lowest current is associated with an illumination of 550 lx at the corners, while the highest value corresponds to 990 lx at the centre. This distribution closely follows the illuminance map depicted in Figure 92.

Using the illumination levels presented in Figure 92, the maximum output power P_{max} generated by the OPV at its MPP, can be estimated based on the P_{max} vs. illumination characterization, as shown in Figure 67. For simplicity, the analysis will focus solely on the diagonal axis of the environment. Additionally, the simulation results allow us to examine the impact of the LOS link alone on device performance. Figure 94 shows the simulated P_{max} along the diagonal axis, alongside the corresponding short-circuit current I_{sc}.

Across all simulated positions, an increase of approximately $95\ \mu A$ in the short-circuit current is noticeable when considering diffuse light. This represents a significant improvement of 172% at the corners and 51% at the centre of the current scenario, compared to the LOS-only case. Similarly, post-processing results reveal that the OPV device can deliver a minimum power output of $77\ \mu W$ at the corners, which increases up to $147\ \mu W$ at the centre of the room. In this case where the diffuse channel is ignored, an underestimation of approximately $50\ \mu W$ is observed at all simulated positions, representing an increase of 185% at the corners and 51% at the centre when diffuse light is incorporated. These findings highlight the significant contribution of NLOS links in systems performance, particularly in confined indoor IoT environments.

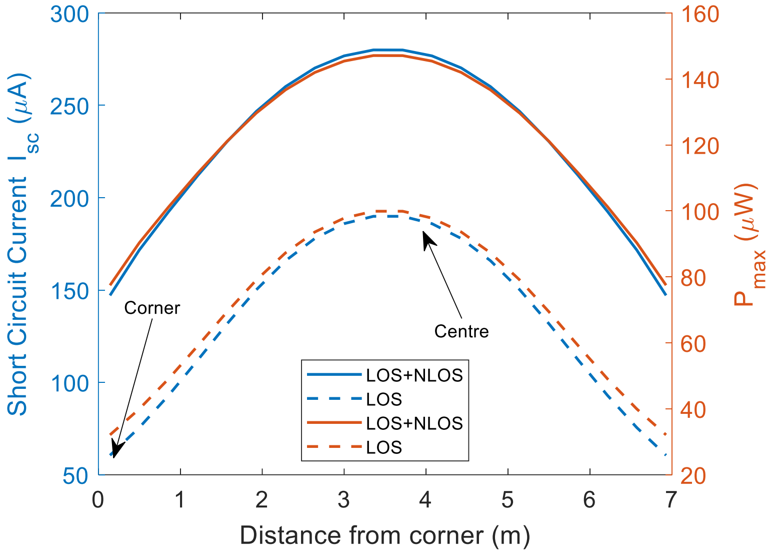

Figure 94: Simulated short-circuit current (blue) and maximum output power (red) along the diagonal axis of the simulated environment, comparing results for the LOS link only (dashed line) and the combined LOS+NLOS link (solid line).

Source: Reproduced with permission from reference [134].

Finally, the simulation results reveal the remarkable capability of OPVs to serve as viable energy harvesting devices in indoor environments, even when placed just 10 cm above ground level. These devices demonstrate the potential to generate adequate power levels to support various IoT wireless nodes employing diverse communication protocols. For instance, under low illumination conditions, OPVs can produce sufficient energy to operate devices such as LoRa Backscatter systems, which require $10–20\ \mu W$, or passive Wi-Fi nodes, demanding $50\text{-}70\ \mu W$. This highlights the practicality of integrating OPVs as a sustainable power source within the IoT ecosystem.

Additionally, conventional VLC systems typically uses a TIA to convert the output current from the photodetector into a corresponding voltage signal. When operating under zero bias mode, the generated current relates to the device short-circuit current. Evaluating the short-circuit current, while considering noise elements, allows the estimation of the SNR and supports theoretical evaluations of maximum data rates for different modulation schemes.

While communication and energy harvesting analyses have conventionally been approached independently, simulating the short-circuit current of OPVs in IoT contexts is a pioneer work for more sophisticated studies. These can eventually integrate receiver front-end designs aligned with SLIPT scenarios. By considering the intrinsic characteristics of the OPV, such as shunt and series resistances, it is possible to design specialized equivalent models and receiver circuits that meet specific communication and energy needs.

For the first time, an indoor MCRT simulation incorporating an OPV receiver has been successfully conducted, representing a significant advancement in the exploration of photovoltaic-based systems for communication and energy harvesting.

The analysis of the flat OPV model highlights its effectiveness in indoor energy harvesting and communication scenarios. However, the flexibility of OPVs enables curved configurations, which can influence their performance. The next section explores the curved OPV model, examining the impact of curvature on device behaviour in indoor environments.

IV.3. Curved OPV model

The flexibility of OPVs allows them to be bent and shaped to fit various surfaces, making them highly adaptable for different IoT applications [85], [241]. This raises important questions about the impact of curvature on energy harvesting and communication performance in indoor environments. In this section, we present, for the first time in the literature, a method to incorporate curved surfaces into MCRT optical channel simulations. Our approach uses the same OPV device as in previous analyses, supported by experimental validation.

Our methodology is based on the division of the flat OPV into M smaller sub cells, where each sub cell undergoes an independent ray tracing simulation to obtain its respective channel impulse response $h_k(t;\lambda)$. Here, the index k corresponds to a specific sub cell among the total M. The length and width of the OPV can be divided into non-zero natural numbers, and this division process is implemented using Matlab® for simplicity. An example schematic of this OPV division is shown in Figure 95, with both length and width divided by 14, resulting in a total of 196 smaller cells.

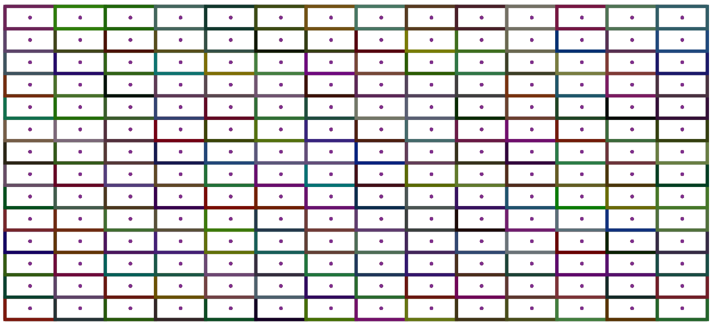

Figure 95: Schematic of OPV division into M smaller sub cells.

To model a curved OPV, the device is divided into smaller sub-cells, and their positions are determined using basic geometry. Figure 96 presents a schematic representation of the proposed curved OPV model.

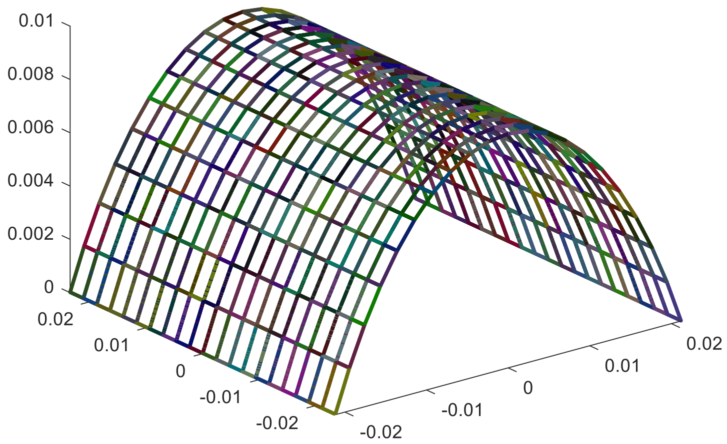

Figure 96: Schematic of curved OPV composed of M smaller sub cells.

Dividing the photodetector into multiple smaller sub cells significantly increases the processing time required for simulations, as it effectively transforms the system into a SIMO (or MIMO) scenario with multiple receivers. Consequently, wide-spectrum simulations involving a large number of emitted rays and numerous sub cells can become highly time-consuming, with simulation durations exceeding 48 hours, making them potentially impractical.

For the OPV used in this study, we arbitrarily divided both its length and width into ten smaller sections, resulting in $M = 100$ sub cells. The curvatures applied are the same as those previously described in Section III.3.5.

IV.3.1. Divided flat model validation

As an initial validation step, we verify that the impulse response $h(t;\lambda)$ of the original flat OPV is equivalent to the sum of the impulse responses $h_k(t;\lambda)$ of its individual sub-cells, as expressed in Equation IV-1. This verification is conducted using the flat OPV model results under the LOS scenario, as described in Section IV.2.1.1.

$$h(t;\lambda) = \sum_{k=1}^{M} h_k(t;\lambda) \qquad \text{IV-1}$$

To validate the divided flat OPV model, a SIMO simulation was conducted with $M = 100$ receivers. The overall impulse response of the full device was calculated using Equation IV-1 and subsequently converted into the expected short-circuit current using Equation II-53, with $N = 1$ (one optical source) and $R_\Psi = 1$ (no angular dependence). Figure 97 presents the results, including the measured short-circuit current with a 5% error margin (blue), the expected short-circuit current from the full OPV simulation (red), and the expected short-circuit current from the divided OPV simulation (yellow).

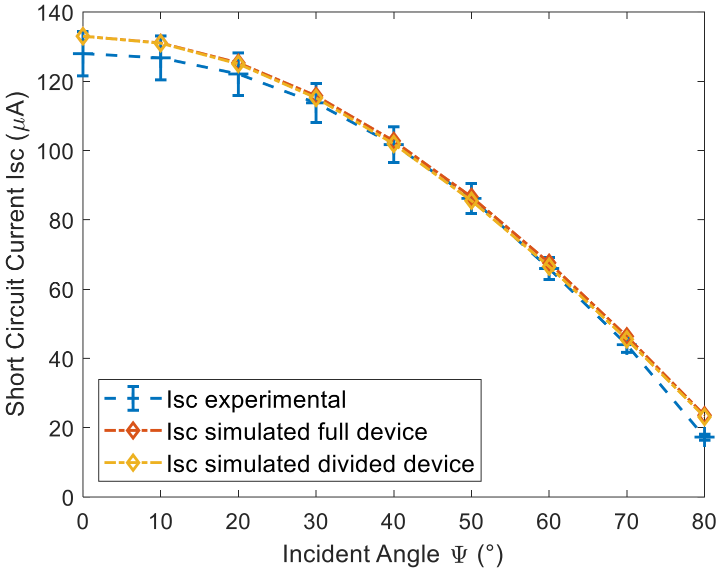

Figure 97: Obtained experimental short-circuit current with 5% error bar (in blue) and expected short-circuit current obtained from simulation results: with full OPV (in red); with divided OPV (in yellow).

The obtained results confirm the validity of dividing the OPV into smaller sub cells for simulation purposes. The comparison between the full OPV model and the divided OPV model shows excellent agreement, with both matching closely to the experimental results across all incident angles. The minor discrepancies remain within the acceptable error range, further validating that the sub cell division approach accurately reproduces the overall behaviour of the original device.

IV.3.2. Curved model validation

To validate the curved OPV model, we use two complementary approaches.

First, we analyse the LOS equation under perfect alignment for a curved device, investigating how curvature influences the solid angle subtended by the source and receiver and, consequently, its impact on the received optical power. RaPSor simulations in LOS link are then conducted at multiple distances to compare theoretical predictions with simulation results.

Second, the curved OPV model composed of smaller sub cells is validated by comparing simulated and measured short-circuit current results for all three curvature configurations (big, medium, and small) using our angular bench setup in both LOS and LOS+NLOS scenarios. For all scenarios, a convex curvature is analysed (refer to Figure 71).

IV.3.2.1. Theoretical received optical power P_r of curved surfaces

The complete derivation of the received optical power P_r for a curved surface involves extensive and detailed calculations. Therefore, only the key concepts and foundational definitions are presented here, while the full mathematical development is provided in

Appendix 3. The methodology relies on solving the transmitted optical power P_t equation as a function of radiant intensity, as described in Equation II-11. Based on the principle of energy conservation, the optical power transmitted within a given solid angle Ω_x is identical to the received optical power on any surface that subtends the same solid angle Ω_x relative to the source. Consequently, as stated in Equation II-28, larger surfaces are required at greater distances to maintain the same received optical power P_r. Here, we shall consider a Lambertian receiver with radiant intensity described by Equation II-9.

To introduce this concept, we assume a point source S, positioned at a distance d from the centre of a flat rectangular surface with dimensions $2l$ (length) and $2a$ (width). A perfect alignment scenario is considered, where $\theta = \Psi = 0°$. In this analysis, the source S is placed at the origin of the spherical coordinate system, while the centre of the flat rectangular surface lies along the z-axis. Here, the solid angle Ω_x is rectangular, as shown in Figure 98. The variables r, φ, θ correspond to the spherical coordinate parameters.

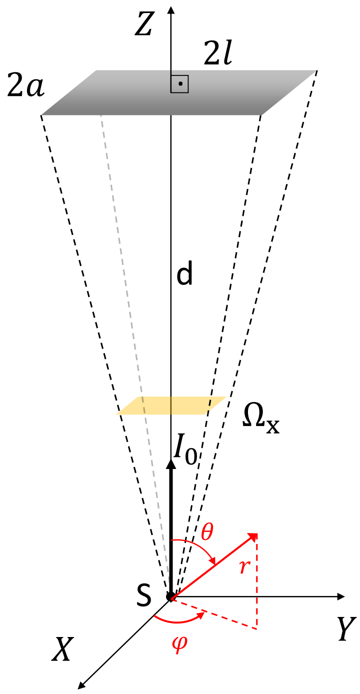

Figure 98: Schematic of a perfect alignment scenario between a source S and a rectangular surface with dimensions $2l$ (length) and $2a$ (width). In red, the spherical coordinate variables.

When the surface is curved along the y-axis, while keeping its corners fixed in the same plane, the centre of the surface shifts closer to the optical source (or further away for concave curvatures). Figure 99 presents a schematic representation of the curved surface, emphasizing key parameters as: the surface width $2l$, the curvature radius R, the height displacement h and the curvature angle θ_c. Here, h represents the vertical distance between the plane containing the corners and the virtual centre of the curvature. As a result of the curvature, the centre of the surface moves closer to the source by $R - h$, as depicted in the figure.

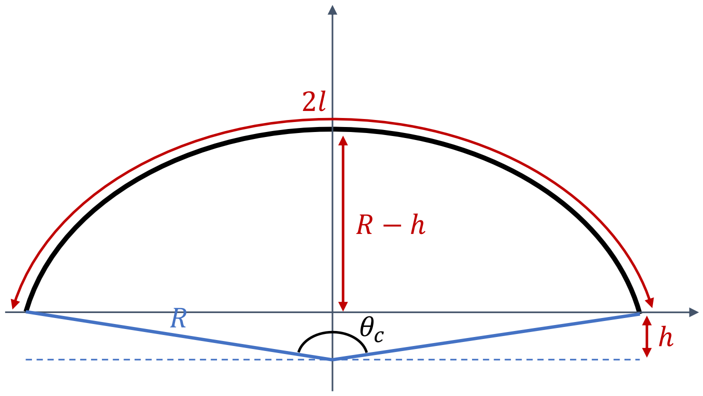

Figure 99: Schematic representation of the curvature variables for a bent surface.

Interestingly, bending the surface deforms the solid angle Ω_x into a different shape, which depends on many factors. Finally, by solving the radiant intensity integral for the deformed solid angle, the received optical power P_r is described by Equation IV-2.

$$P_r = \frac{2I_0}{m_1+1}\left\{\int_{-\varphi_0}^{\varphi_0}\left[1-\left(\frac{d|\sin(\varphi)|}{\sqrt{d^2\sin^2(\varphi)+y_\varphi^2}}\right)^{m_1+1}\right]d\varphi \right. \\ \left. +\int_{\varphi_0}^{\varphi_0+2\beta}\left[1-\left(\frac{dcos(\varphi-\varphi_0-\beta)}{\sqrt{d^2\cos^2(\varphi-\varphi_0-\beta)+l'^2}}\right)^{m_1+1}\right]d\varphi\right\} \tag{IV-2}$$

With the following variables:

$$l' = \frac{R}{2}\frac{\sin(\theta_c)}{\sin(\alpha)}$$

$$\alpha = \frac{180° - \theta_c}{2}$$

$$\varphi_0 = \arctan\left(\frac{l'}{a}\right)$$

$$\beta = \arctan\left(\frac{a}{l'}\right)$$

Also, y_φ is the solution of the Equation IV-3 for a given φ while solving for y.

$$y\left[d+h-\sqrt{R^2-y^2}\right] = \tan(\varphi)\times a\times d \tag{IV-3}$$

Here, the integral must be evaluated for multiple values of the azimuth angle φ. As a result, Equation IV-3 varies for each elementary point on the curved surface and lacks an analytical solution. However, by discretizing the problem, Equations IV-3 and IV-2 can be effectively solved using numerical methods. For a given distance d, the received optical power

P_r can be computed numerically with tools such as Matlab®. Similarly, a perfectly aligned LOS simulation can be conducted using RaPSor, which calculates the received optical power P_r based on Equation II-50 in a monochromatic scenario.

A RaPSor simulation was conducted using the previously introduced curved OPV model with dimensions of 4.7 cm × 0.66 cm. For this simulation, we arbitrarily selected a curvature angle $\theta_c = 50°$, corresponding to a curvature radius R of 5.39 cm and a height displacement h of 4.88 cm. As a result, the curved device approaches the optical source by $R - h = 0.51$ cm. We consider a hypothetical 60° Lambertian LED with a normalized transmitted optical power $P_t = 1\,W$. By varying the distance d from 1 cm to 15 cm in 1 cm increments, two curves were obtained: one from the RaPSor simulation and the other from the numerical solution of Equation IV-2. Figure 100 shows the obtained curves.

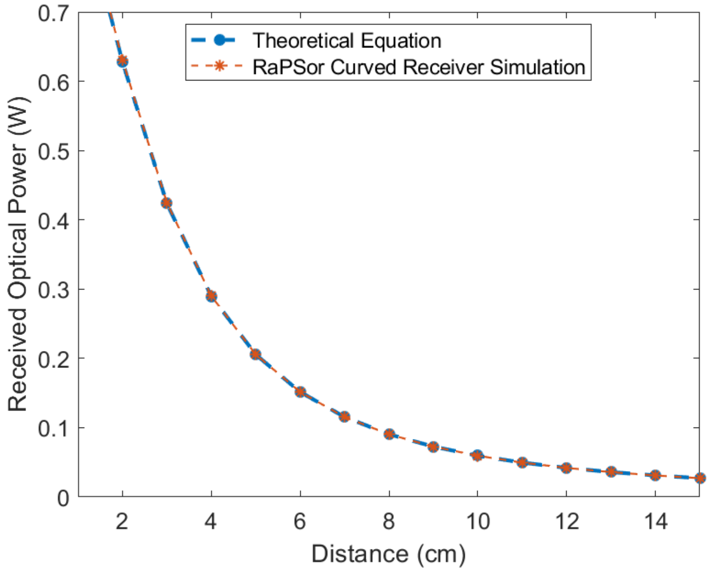

Figure 100: Comparison of received optical power P_r between the theoretical equation of curved devices (in blue) and RaPSor simulation results with curved OPV (in red) in function of the distance d under perfect alignment scenario.

The results presented in Figure 100 demonstrate an excellent agreement between the theoretical calculations and the RaPSor simulation for the curved OPV receiver. As the distance d from the optical source increases, the received optical power P_r decreases, which is consistent with the expected behaviour under LOS link. To emphasize the impact of curvature, a comparable simulation was conducted using a flat OPV model. The results of this analysis are presented in Figure 101.

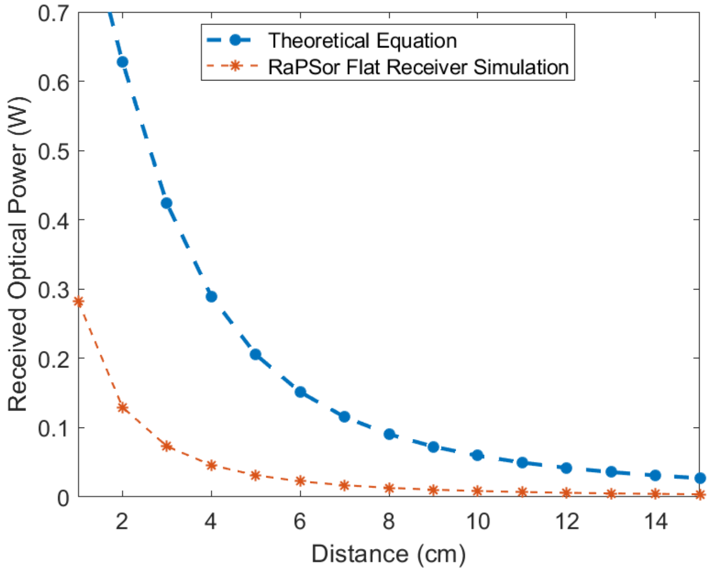

Figure 101: Comparison of received optical power P_r between the theoretical equation of curved devices (in blue) and RaPSor simulation results with flat OPV (in red) in function of the distance d under perfect alignment scenario.

Figure 101 highlights the difference between the received optical power P_r of a flat surface (simulated using RaPSor) and a curved surface (calculated using the theoretical equations). Thus, comparing the simplified direct LOS equation (Equation II-32) with the curved surface model is invalid because the simplified equation assumes small solid angles, which is not accurate for short distances. Notably, the curved surface captures more optical power than the flat one, a behaviour in contrast from the trends observed in Figure 73. This difference arises from the curved surface closer proximity to the optical source by $R - h$, which significantly enlarges the solid angle Ω_x at short distances. However, as the distance d increases, the solid angle of the curved surface becomes smaller than that of the flat surface.

This validation demonstrates the accuracy and reliability of the implemented curved OPV model in RaPSor for predicting received optical power P_r under direct LOS scenarios. Additionally, it confirms the validity of the proposed mathematical solution for calculating the received optical power of curved devices in LOS conditions.

In further sections, the curved OPV model is experimentally validated under LOS and LOS+NLOS scenarios.

IV.3.2.2. LOS

To experimentally validate the curved OPV model under the LOS scenario, we employed the same methodology used for the flat OPV model, as detailed in Section IV.2.1.1 and shown in Figure 84. The validation included all three previously defined curvatures. It is important to note that the curvature names correspond to the radius: the “big” configuration has a gentle curvature, while the “small” configuration represents a more pronounced curvature (refer to Figure 72). For comparison, we also simulated the flat OPV. Both experiments and simulations were conducted at varying incident angles Ψ using the angular characterization bench. The results are shown in Figure 102.

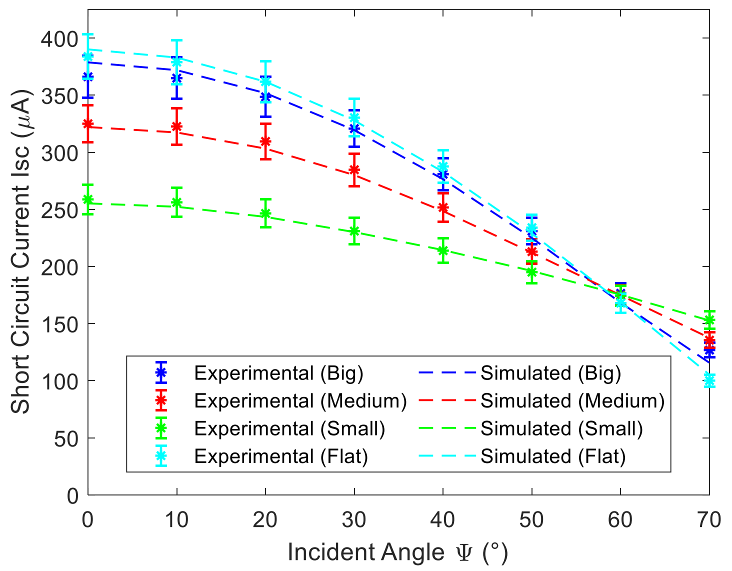

Figure 102: Obtained experimental short-circuit current with 5% error bar (markers) and expected short-circuit current obtained from simulation results (dashed lines) for different curvature topologies: big (in blue); medium (in red); small (in green); flat (in cyan).

The obtained results demonstrate a strong agreement between the experimental and simulated short-circuit currents for the different OPV curvatures under LOS conditions. As expected, the "small" topology exhibits the lowest short-circuit current values, owing to its pronounced curvature, which reduces the effective optical power received. In contrast, the "big" topology, with its smaller curvature, achieves the highest current values among the curved configurations, closely approaching the flat OPV performance. The flat OPV consistently shows the best performance due to its optimal alignment and maximized effective area for light capture. These results validate the curved OPV model reliability in accurately predicting performance across various curvatures and incident angles under LOS scenarios.

By applying the theoretical equations for curved surfaces under perfect alignment conditions ($\Psi = 0°$), the expected short-circuit current derived from the received optical power was evaluated on the characterization bench. The results demonstrate perfect agreement between the calculated values and the experimentally measured short-circuit current for each curvature configuration. This behaviour was in fact expected, as the theoretical equations also align with the curved OPV simulation results.

IV.3.2.3. LOS + NLOS

Similarly, the angular characterization bench was utilized for the experimental validation of the LOS+NLOS scenario, with adjustments to incorporate the Lambertian reflectors. Two configurations were analysed: one featuring both reflectors and another with only the right-side reflector, as illustrated in Figure 87. Since the curved model had already been validated under the LOS scenario, a strong correlation between the simulated and measured short-circuit current was anticipated. As a result, this experiment was conducted exclusively with the "medium" topology.

For this validation, a wide-spectrum simulation was required to account for the spectral reflectance of the white paper $\rho_{paper}(\lambda)$, which significantly increased the required simulation time. Again, the expected current when no reflections are considered can also be obtained from the simulation. Figure 103 shows the obtained results.

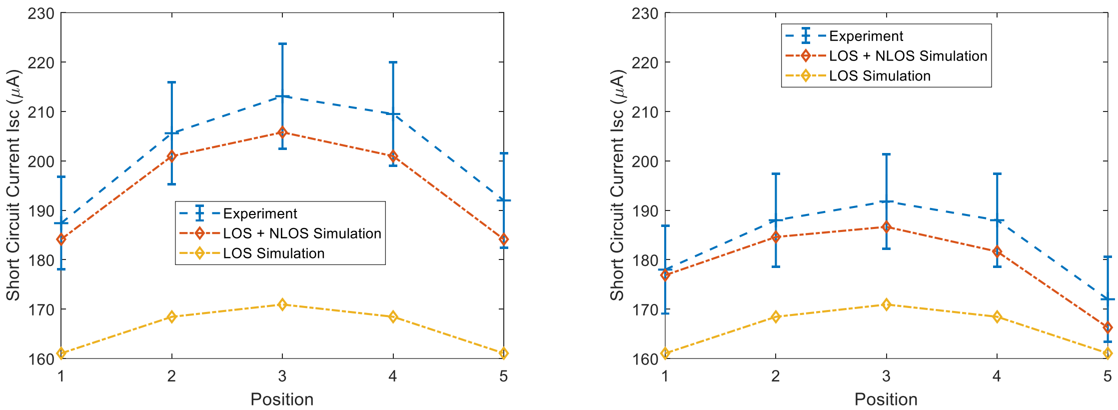

(a) (b)

Figure 103: Obtained experimental short-circuit current with 5% error bar (in blue), expected short-circuit current obtained from the simulation results (in red) and expected short-circuit current obtained from the simulation results when no reflections are considered (in yellow) for the medium curved topology in: (a) Scenario 1; (b) Scenario 2.

Source: Reproduced with permission from reference [238].

Finally, the results presented in Figure 103 validate the performance of the curved OPV model under LOS+NLOS conditions. A strong agreement is observed between the experimentally measured short-circuit current (blue) and the simulation results (red) across both scenarios. The influence of the reflectors is clearly evident, with higher short-circuit currents in scenario 1, where both reflectors contribute to the NLOS component. In scenario 2, the absence of the left reflector reduces the NLOS contribution, resulting in a decreased short-circuit current. Additionally, the comparison with the expected current obtained when no reflections are considered (yellow) emphasizes the significant role of the diffuse component in enhancing the performance of the curved OPV receiver in complex indoor environments. These results further demonstrate the validity of the curved OPV model for accurate simulations in real-world scenarios involving both LOS and NLOS links.

In the following section, we present the first-ever indoor MCRT simulation incorporating a curved OPV.

IV.3.3. Indoor simulation involving different curvatures

In these preliminary simulations with curved OPVs, the objective is to evaluate the impact of device curvature on system performance in comparison to a conventional flat device. Our study is a qualitative comparison between the performance of curvatures, consequently, a wide spectrum simulation is not required. Instead, single-wavelength simulations were conducted, and the performance comparison is based on the analysis of the received optical power P_r.

Additionally, the channel impulse response $h(t)$ is deliberately excluded from this analysis as it does not significantly contribute to the evaluation.

The simulated indoor environment is a 5 m × 5 m × 3 m room with Lambertian surfaces characterized by reflection coefficients of $\rho_{floor} = 0.3$ for the floor and $\rho_{general} = 0.8$ for the remaining surfaces. A single Lambertian optical source with $\theta_{1/2} = 60°$ is placed at the centre of the ceiling, facing downward, with a normalized transmitted optical power $P_t = 1$ W. Following previous simulations, 5 million rays were employed, with a maximum of three reflections on the surfaces. The simulation time window is 120 ns, with a resolution of 0.15 ns per step.

To emphasize the importance of curved topologies, two distinct simulations, relevant to different IoT applications, were performed: one involving the rotation of receivers around their centre and the other focusing on a movable receiver. Each simulation is described separately in the following sections.

IV.3.3.1. Rotating OPV

In this simulation, the real-life OPV device fabricated by Dracula Technologies (dimensions: 4.7 cm × 0.66 cm) was employed. Its length and width were divided into 10 smaller sections each, resulting in a total of $M = 100$ sub cells. The same experimental curvatures as those used in earlier studies, including the flat configuration, were employed. The OPV topologies were positioned at the centre of the room, 0.85 cm above the ground, and oriented towards the optical source, with the length l aligned along the x-axis (refer to Figure 104).

The received optical power P_r was analysed as the receiver rotates around the y-axis, with angles ranging from -180° to 180° in 10° increments (positive increments indicating clockwise rotation). A degradation of the LOS link is expected at higher rotation angles, as previously observed in angular characterization experiments. This simulation aims to investigate the influence of curvature on rotational scenarios often encountered in IoT applications, such as wearable devices or mobile IoT nodes, where consistent performance under varying orientations is critical.

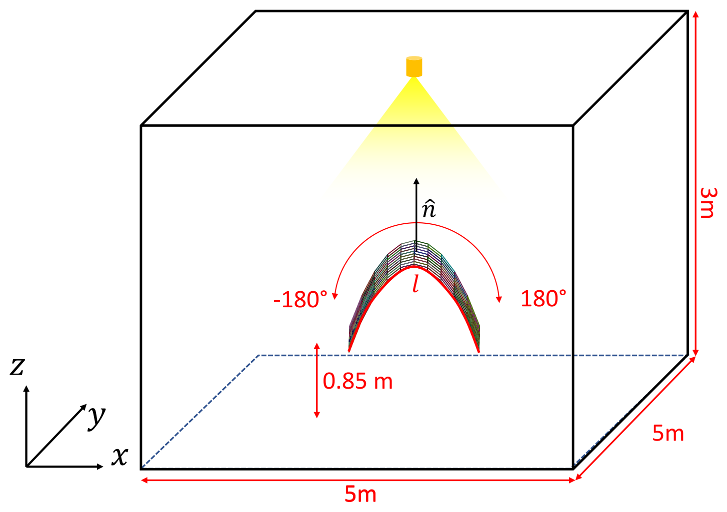

Figure 104: Employed indoor simulation scenario for curved OPV. Rotation analysis.

For clarity, the results were analysed using a dBm scale. The simulation demonstrated that rotation had minimal impact on the NLOS component of the received optical power, maintaining values around -24.5 dBm for all curvatures. This is expected, given the distance between the receiver and the reflective surfaces in the environment, where most of the contribution originates from the LOS link.

Finally, Figure 105 shows the simulated received optical power P_r across all rotations and curvatures, considering both LOS and NLOS components. Since the majority of the contribution arises from the LOS link, flatter configurations exhibit superior performance for rotation angles below 60°, fact that was demonstrated in previous experiments (refer to Figure 102). The maximum difference between the flat OPV and the “small” curvature topology reaches 0.81 dB under perfect alignment conditions. However, for rotation angles exceeding 60°, curvier devices outperform flatter ones, with the “small” topology surpassing the flat OPV by up to 3.81 dB at 90°.

A key advantage of curved devices is their naturally extended FOV. While flat devices have a maximum FOV of $\pm 90°$, curved configurations increase this range. For instance, the “small” curvature topology achieves an FOV of up to 140°. Beyond these angles, the LOS component diminishes entirely. This broader FOV makes curved OPVs particularly valuable for applications requiring performance under wide-angle rotations, such as wearable IoT devices.

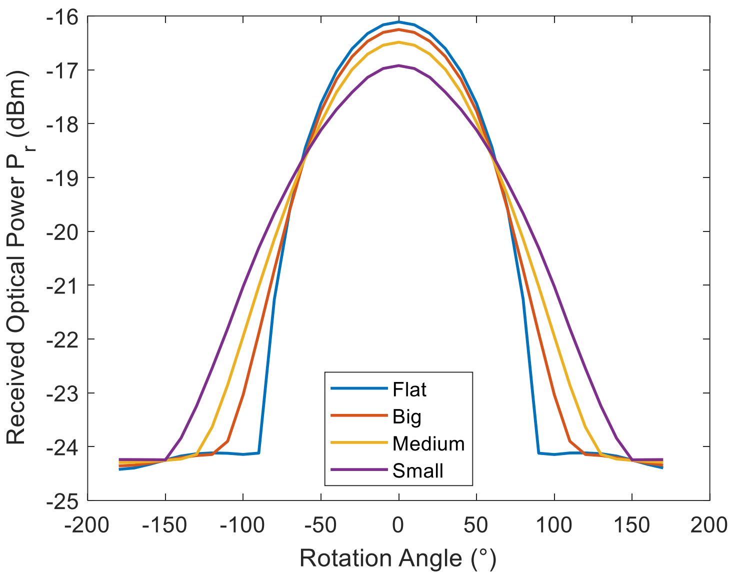

Figure 105: Simulated received optical power P_r in function of rotation while accounting for LOS+NLOS link for multiple curvatures.

Source: Reproduced with permission from reference [238].

Ultimately, Figure 105 illustrates that while curved devices may exhibit slightly reduced performance under perfect alignment, they are significantly less sensitive to variations in incident angles compared to their flat counterparts. This characteristic is particularly valuable in IoT applications involving dynamic orientations, such as wearable sensors or mobile IoT nodes, as it ensures reliable energy harvesting and communication performance even in suboptimal alignment scenarios.

IV.3.3.2. Moving OPV

In the second scenario, the objective is to assess the impact of the diffuse optical channel on the performance of curved OPVs. Initial analyses indicated that the curvature of the real-life OPV, developed by Dracula Technologies, had minimal influence on the NLOS link. This is primarily attributed to the relatively small size of the receiver compared to the overall dimensions of the environment. To further explore this, a hypothetical OPV surface with dimensions of 20 cm in length and 4 cm in width was employed, representing a feasible real-life inkjet-printed OPV. This larger area receiver was divided into $M = 100$ smaller sub-cells, and the performance of both flat and curved configurations was analysed.

In this scenario, the device is positioned at a height of 5 cm near the ground, located in one corner of the room with a fixed orientation pointing towards the centre. The received power for both the flat and curved OPVs was evaluated at seven distinct positions along the room diagonal, representing conditions where the device is either directly exposed to or obstructed from the source. The OPV length is maintained parallel to the floor (see Figure 106). The curved device is bent into a semi-circular shape ($\theta_c = 180°$ in Figure 99), corresponding to a curvature radius of 6.37 cm. This scenario simulates practical IoT applications, such as mobile robotic platforms, where incorporating a curved OPV is more advantageous due to spatial constraints or specific design requirements.

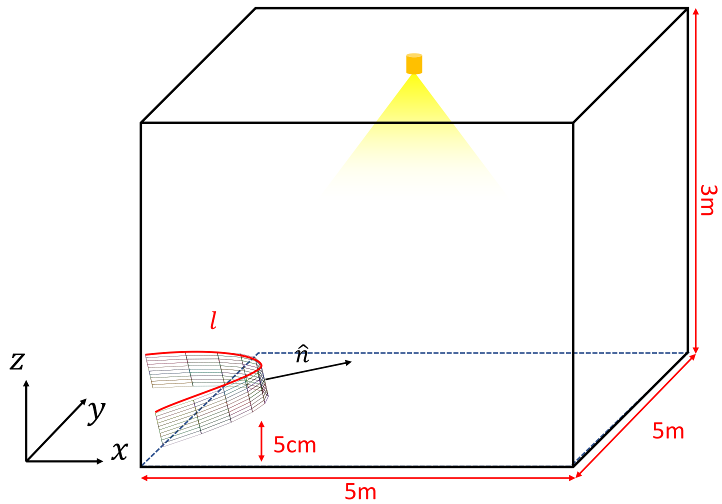

Figure 106: Employed indoor simulation scenario for curved OPV. Moving analysis.

The simulation results are presented in Figure 107, illustrating: (a) the received optical power P_r from LOS and NLOS links separately; and (b) the total P_r combining LOS+NLOS contributions.

From the LOS analysis, as depicted in Figure 107.a, both the flat and curved OPVs detect similar levels of optical power. This is primarily because the device curvature is oriented in the $x - y$ plane, which minimally impacts the solid angle subtended by the source and receiver. As the device move closer to the centre of the room (approximately 3.5 m from the corner), the LOS component diminishes due to an increase in the incident angle of the optical rays, eventually resulting in the complete loss of direct visibility.

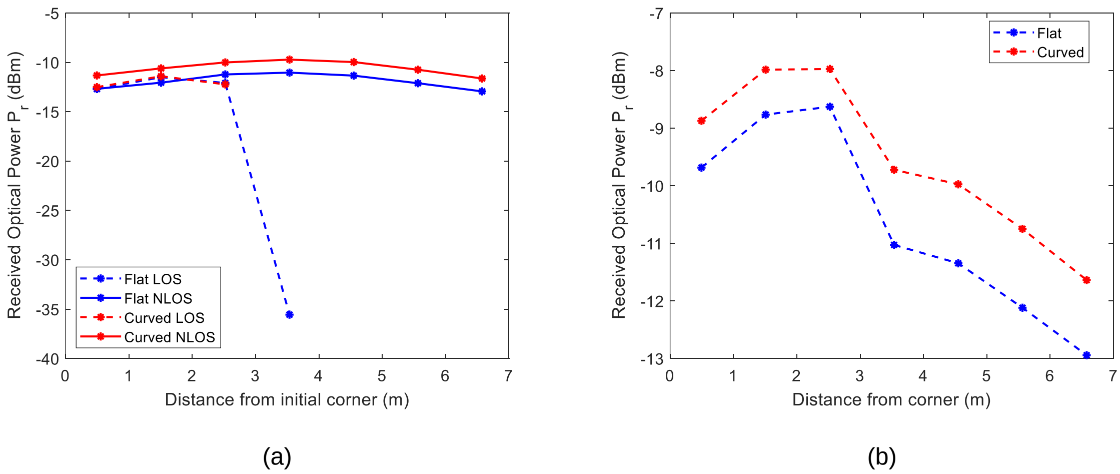

Figure 107: Simulated received optical power P_r in function of OPV position while accounting for two curvatures and: (a) LOS (in blue) and NLOS (in red) links separately; (b) LOS+NLOS link.

While the LOS link is highly dependent on the receiver position, the diffuse channel provides a relatively constant received optical power, with a maximum variation of only 1.6 dB between the corner and the centre of the room for both topologies. Notably, the curved OPV detects more optical power than its flat counterpart, showing an average improvement of 1.34 dB across all positions. Additionally, the LOS and NLOS components at initial positions are of comparable magnitude, underscoring the importance of the diffuse channel when direct visibility is unavailable.

Figure 107.b illustrates the total received optical power P_r, considering both LOS and NLOS contributions, for flat and curved OPVs. While approximately half of the received optical power comes from the LOS link at the initial positions, the diffuse channel plays a critical role in maintaining the link as the receiver moves to positions where LOS is obstructed. This demonstrates the robustness of the diffuse channel in sustaining system performance, regardless of receiver placement.

In summary, the simulation highlights the relevance of flexible OPVs in scenarios where maintaining a direct link between the source and receiver is challenging. For the real-life OPV developed by Dracula Technologies, the curvature had negligible impact on P_r, which suggests a compelling advantage: shaping the OPV to conform to curved IoT surfaces does not compromise system performance. Moreover, larger curved OPVs outperformed their flat counterparts, effectively meeting energy harvesting and communication requirements over greater distances by using the diffuse channel.

While the curved OPV simulations revealed promising insights into P_r, these findings can be extended to analyse the short-circuit current I_{sc}, and further assess energy harvesting and communication performance. Such analysis would require a wide-spectrum simulation, incorporating the optical source normalized PSD $S(\lambda)$, the spectral reflectance of reflective surfaces, and the OPV angular and spectral responsivities, R_Ψ and $R_\lambda(\lambda)$.

IV.4. Chapter conclusion

Chapter IV established the foundations of the role that indoor optical simulations can play in optimizing OPV-based systems for IoT applications. For the first time, we successfully implemented an OPV model into a MCRT simulator, enabling precise estimations of short-circuit currents and received optical power under complex indoor scenarios. This innovation marked a significant advancement in the field, as it extended the capability of simulations to incorporate not only flat but also curved OPV surfaces. The validation of these models through theoretical calculations and experimental measurements confirmed their reliability, making them important too for indoor light-based IoT networks.

The simulations emphasized the importance of diffuse light contributions in realistic environments, highlighting their role in maintaining link reliability, even under challenging conditions such as misalignments or obstructions. For the curved OPV model, novel equations were developed to mathematically describe the optical power received under LOS configurations. Curved OPVs demonstrated that their geometry enhances performance in IoT scenarios considering object rotation and mobility, which is crucial for dynamic applications.

The insights gained in this chapter establish the simulation as a powerful complementary tool for understanding OPV performance in complex indoor scenarios. While the simulations provide accurate estimations of short-circuit current and received optical power, the experiments detailed in Chapter V will extend this knowledge by exploring the communication and energy harvesting performance of OPVs under various operating points and front-end circuit configurations.

Chapter V

Bench for Simultaneous Energy and Data Transfer: An Experimental Approach

Summary

Chapter V. Bench for Simultaneous Energy and Data Transfer: An Experimental Approach

In this chapter, we present preliminary experiments conducted with the OPV developed by Dracula Technologies, focusing on its performance in both energy harvesting and communication. The evaluations consider various influencing factors, including operating point, front-end circuit and illumination conditions. The primary metrics analysed are the measured BER and output power P_{out}, with a particular emphasis on illustrating the trade-off between these two functionalities.

The chapter is structured as follows: first, we provide a detailed description of the experimental bench setup. Next, the bench is validated using a commercial amplified photodiode, comparing the measured BER with the theoretical error probability associated with the measured SNR. Following validation, the OPV is introduced into the experimental setup, using two distinct front-end configurations: parallel load and TIA. While this study does not employ a dedicated SLIPT front-end circuit capable of separating the DC and AC components, such as the one shown in Figure 44, both functionalities are independently analysed by assuming that the DC component is fully isolated from the AC one. This approach enables a focused evaluation of the optimal circuit strategy for specific applications.

The primary methodology involves varying the distance between the transmitter and receiver under perfect alignment conditions, thereby modifying the SNR and consequently affecting both the signal amplitude and its average value. For each distance, BER and P_{out} are measured, for different operating points. Additional analyses include the impact of data rate on communication performance. While initial experiments with curved OPVs were not feasible due to mechanical constraints, they remain an important consideration for future work and are highlighted as a key perspective of this study.

V.1. The experimental bench

Our experimental bench is based on a Software Defined Radio (SDR) strategy. Here, most of the signal processing is performed using software rather than traditional hardware components. In an SDR, functions like modulation, demodulation, filtering, encoding, and decoding of signals, which are traditionally implemented with fixed circuitry, are handled by software. This method provides a reliable and adaptable setup for communication testing, making it particularly suited for the experiments conducted in this study.

The experimental setup is realized with two Ettus USRPs X310 devices, each equipped with two channels, enabling multi-access approaches. The peripherals are equipped with the LFTX/LFRX daughterboards, allowing the transmission of real-mode signals up to 30 MHz. In the current study, we have employed a single channel transmission for a SISO link. The baseband electrical signal is converted into an optical signal with the same front-end circuit used for the dynamic characterization, shown in Figure 75. However, in this setup, both the V_{DC} and transistor voltage are fixed at 6 V, provided by the USRP DC output. Here, the DC component of the optical signal and its power cannot be changed and is fixed. Therefore, to adjust the system SNR, the distance between the transmitter and receiver is varied.

The same LED described in Section III.2 is used. Our whole setup is mounted onto a specialized mechanical structure, allowing precise alignment and distance measurement. To maintain simplicity and focus on the fundamental device characteristics, no optical lens nor filters are employed. The setup supports a maximum achievable distance of 2 m, providing a controlled environment to evaluate the system performance over a range of distances and conditions.

On the receiver side, two photosensitive devices are employed for different purposes. First, the PDA36A2 amplified detector, developed by Thorlabs, is used. The commercial photodiode has a built-in active amplification system with adjustable gain, and is directly connected to the USRP input. Second, the OPV is employed, and two different front-end circuits are used to transfer the desired output variable to the USRP. These configurations will be elaborated on in subsequent sections. Figure 108 shows a schematic of the experimental bench.

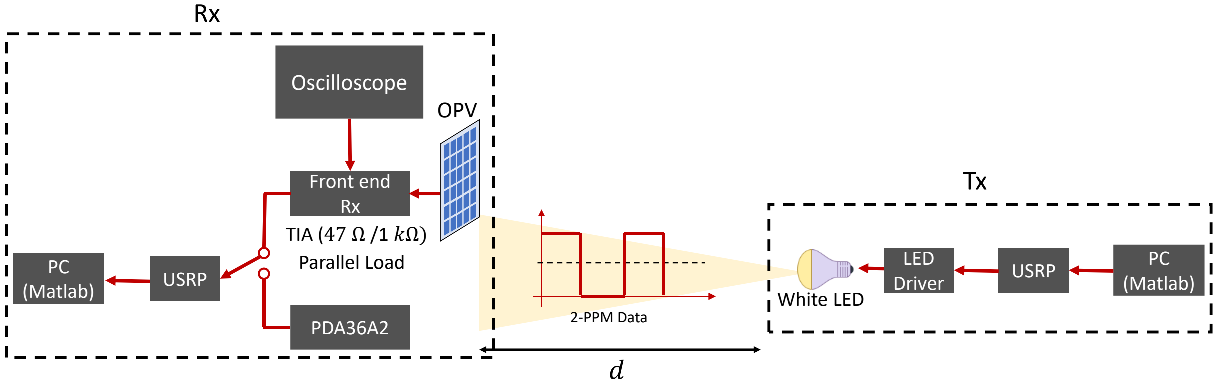

Figure 108: Schematic of the communication bench adapted to SLIPT scenario. The receiver features two different photodetectors: a commercial amplified PD (PDA36A2) and the OPV fabricated by Dracula Technologies.

Following previous works conducted within our team, we have opted to employ Matlab® as the signal processing software for this experimental bench [55]. For this study, the focus is on analysing the OPV performance at different conditions considering low data rates, so multi-carrier schemes were not included, although they remain an important consideration for future research. Among the available modulation schemes options, 2-PPM was chosen for its simplicity and suitability for the current setup. While OOK modulation offers lower bandwidth requirements than L-PPM and simpler implementation, it can face synchronization challenges when transmitting long sequences of “0” bits. Moreover, we do not consider higher-order L-PPM schemes as they demand more complex implementation and greater bandwidth for the same data rate, which may pose issues for low-bandwidth receivers like the OPV used here. Additionally, hard decoding for higher-order L-PPM schemes involves non-trivial threshold decisions.

Our SDR features a user-friendly Human-Machine Interface (HMI) that simplifies setup and configuration. Next, we outline key details about the USRPs and the coding implementation used in this experimental bench.

V.1.1. The USRPs

The LFTX/LFRX daughterboards feature an input impedance of 50 Ω and can handle a maximum input power of 10 dBm. Both the Digital-to-Analog Converter (DAC) and Analog-to-Digital Converter (ADC) are supplied with 3.3 V, limiting the maximum input voltage of the LFRX. For each USRP, the output and input signals can be transferred through coaxial cables. For the X310 model, the ADC supports a maximum sampling rate of 200 MS/s with 14-bit resolution, while the DAC offers a maximum sampling rate of 800 MS/s with 16-bit resolution. These specifications provide ample hardware capability for high-fidelity signal transmission within the daughterboard bandwidth of 30 MHz.

The AC output signal generated by the DAC is directly applied as the input voltage V_{in} to the circuit shown in Figure 75. The DC component is added through the DC voltage supplied by the USRP. On the receiver side, after the optical-to-electrical conversion performed by the photodetector, the resulting electrical signal is fed into the LFRX daughterboard. This component automatically removes the signal average value, isolating only the AC component. However, the LFRX is unable to process negative DC values, an important consideration for future experimental setups.

From a software perspective, several global variables need to be configured to enable the USRP hardware functions, such as the IP address, master clock frequency, and others. While the detailed description and explanation of these functions and variables fall outside the scope of this study, further insights can be found in the recommended reference [55]. In our implementation, we adopted a real-time communication approach, where the receiver continuously detects, processes, and decodes the signal with minimal time constraints.

V.1.2. Sent data and decoding

In our experiments, the transmitted data is oversampled by a factor of $N = 10$, simplifying the process of undersampling on the receiver side. Each transmission consists of a package containing 500 completely random bits (equivalent to 1000 2-PPM pulses), repeatedly sent for analysis. To ensure full synchronization between the transmitter and receiver, a dedicated header (Gold code of length 127 [149]) is added to each package.

The received electrical signal is captured using a dedicated Matlab® function, *RadioRx()*, and a convolution is performed between the noisy received signal and the header. This process generates a distinct peak at the position corresponding to the header location within the input signal, allowing precise identification of the package start and end points. Once identified, the header is removed from the signal for further processing. The remaining 2-PPM signal is then decoded using the two methods described in Chapter II.

In the hard decoding method, a decision on the received pulse is made using a threshold set at half of the amplitude and adjusted separately for a few packages after the header is removed. If the amplitude is greater than the threshold, the decision is “1” for the pulse, and “0” otherwise. In 2-PPM, a bit contains two slots. Due to noise, both slots may occasionally exceed the threshold, leading to an error as only one slot should contain a pulse. For all other cases, the position of the pulse determines the corresponding bit value. In contrast, the soft decoding method eliminates the possibility of both slots exceeding the threshold, as it relies on the relative levels between the slots to determine the bit value.

After receiving a predefined number of packages, specified within the reception code, the decoded information is compared to the transmitted data to calculate the experimental BER. To ensure reliable BER measurements, at least ten errors per transmission are required as a baseline. This imposes a limit on the minimum measurable BER for each experiment. To address this, the number of transmitted bits is adjusted according to the specific requirements of each experiment.

Finally, the bench validation through the use of the commercial and fast photodiode is described.

V.2. Bench validation – Photodiode

Our first experiments consist on validating the bench using the 13 mm² commercial Si-based photodiode (PDA36A2), featuring a built-in amplification system. This photodiode offers a broad responsivity spectrum, ranging from 350 nm to 1100 nm, making it suitable for various optical applications. It includes eight adjustable amplification levels, ranging from 0 dB to 70 dB in 10 dB increments. Notably, higher gain settings reduce the receiver bandwidth, which spans from 12 MHz at 0 dB to 3 kHz at 70 dB. Based on preliminary tests, the unitary gain configuration (0 dB) provided sufficiently clear and readable output signals for the distances proposed in our experiments.

Our approach involves measuring the SNR at various distances to determine the theoretical bit error probabilities for both decoding methods, as described in Equations II-82 and II-84. These theoretical probabilities are then compared with the experimentally measured BER for each method at each distance. The SNR measurement is conducted directly using the Matlab® software, which processes the noisy input signal from the USRP.

For the each measurement, we configured the receiver to process 1000 packets, each containing 500 bits, for a total of 500 kbits. To ensure reliable error measurement, a minimum of ten bit errors must be observed, establishing a minimum measurable BER of $10/500000 = 2 \times 10^{-5}$. This error rate is more than sufficient when forward error correction coding is applied to the communication system. Given the receiver bandwidth of approximately 12 MHz at unitary gain (0 dB), we selected a data rate of 5 kbit/s. For the 2-PPM modulation scheme, this corresponds to a signal bandwidth of 10 kHz, well within the receiver operational limits.

The following sections detail each aspect of the validation process.

V.2.1. SNR measurement

The SNR is mathematically defined as the ratio of the signal power P_{signal} to the noise power P_{noise}, as described by Equation II-69. Consequently, measuring the SNR involves determining both power components independently.

In our methodology, we assume — valid for most optical communication systems — that the primary noise source is induced by ambient lighting (shot noise). To measure the noise power, the modulated optical source is switched off, isolating the noise contribution. Using Matlab®, the noise signal from the photodiode electrical output, captured through the USRP, is analysed. The noise variance σ_{noise}^2 is then computed using Matlab® *std(.)* function, which provides the standard deviation of the discretized signal. Finally, the noise power P_{noise} is equivalent to its variance, as described by Equation V-1.

$$P_{noise} = \sigma_{noise}^2 \qquad \text{V-1}$$

Measuring the signal power is more complex than measuring noise power. With the modulated optical source turned on and the desired data transmitted, the photodiode output, containing both the 2-PPM signal $s(t)$ and noise $n(t)$, is captured. Following the removal of the header, the combined signal and noise power is determined by calculating the Root Mean Square (RMS) value using Matlab® function *rms(.)*. The power of $s(t) + n(t)$ is then obtained as the square of its RMS value, as described in Equation V-2.

$$P_{signal+noise} = \lim_{T\to\infty} \frac{1}{2T} \int_{-T}^{T} [s(t) + n(t)]^2 dt = RMS_{s(t)+n(t)}^2 \qquad \text{V-2}$$

The noise $n(t)$ is statistically independent of the signal $s(t)$. As a result, the RMS value of the combined signal and noise can be decomposed into the individual RMS values of $s(t)$ and $n(t)$, as shown in Equation V-3.

$$RMS_{s(t)+n(t)}^2 = RMS_{s(t)}^2 + RMS_{n(t)}^2 = RMS_{s(t)}^2 + \sigma_{noise}^2 \qquad \text{V-3}$$

Finally, the signal power can be obtained as described in Equation V-4.

$$P_{signal} = P_{signal+noise} - P_{noise} \qquad \text{V-4}$$

For each distance, the SNR is determined by independently measuring the signal and noise powers. However, the experimental environment is influenced by weather conditions, particularly ambient light from sunlight. As a result, experiments conducted on different days may yield varying outcomes for the same distances, as the SNR is highly sensitive to changes in ambient light levels.

To assess the fluctuations in SNR measurements, three readings were taken for each distance d. Figure 109 presents the results obtained for seven different positions.

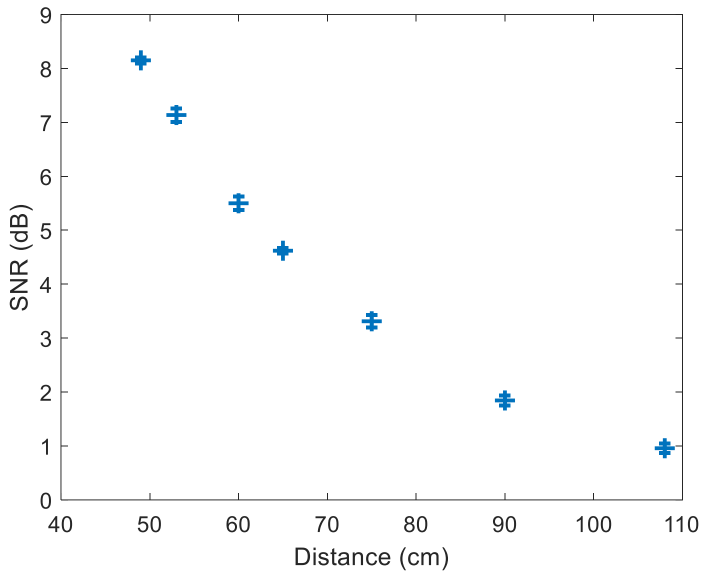

Figure 109: Measured SNR as a function of the distance between transmitter and photodiode.

The results follow an expected behaviour, decreasing proportionally to a factor of $1/d^2$. This aligns with the analysis of the LOS propagation equation (Equation II-33), which predicts that the received optical power diminishes with this factor. Consequently, this reduction in optical power leads to a decrease in the generated current and, ultimately, a reduction in the signal amplitude.

V.2.2. BER measurement

For each transmitter-receiver distance, the SNR was measured as outlined in the previous section, followed by a communication experiment to experimentally determine the BER for both decoding methods. To assess fluctuations and ensure repeatability, three transmissions were conducted for each position. The results are presented in Figure 110 with the minimum measurable BER (2×10^{-5}) indicated by a black line. Measurements below this threshold signify that an insufficient number of errors occurred to accurately determine the actual BER.

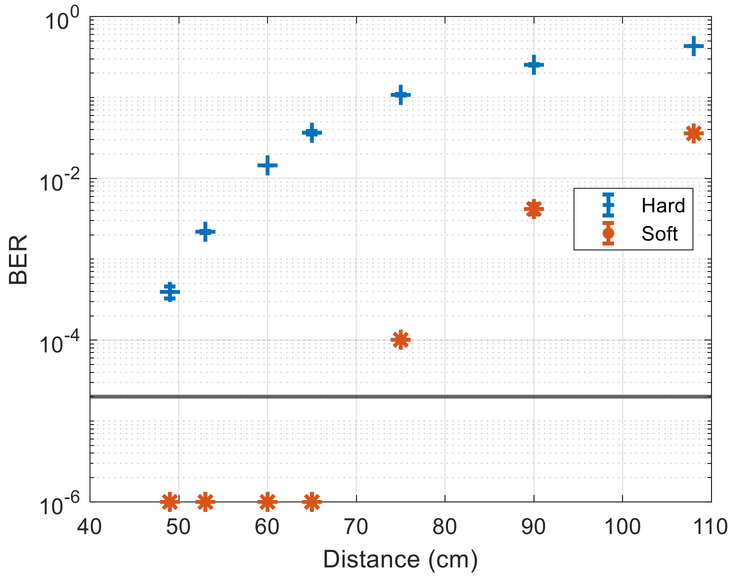

Figure 110: Measured BER as a function of the distance between transmitter and photodiode for hard decoding (in blue) and soft decoding (in red).

Similar to the SNR measurement results, the BER obtained at various distances follows an expected pattern. As the distance between the transmitter and receiver increases, the SNR decreases proportionally to $1/d^2$, leading to a corresponding rise in both hard and soft BERs. Notably, soft decoding consistently outperforms hard decoding, maintaining BER values below the measurable threshold (2×10^{-5}) for distances up to approximately 70 cm. In contrast, hard decoding exhibits a significant BER increase beyond this range, highlighting its susceptibility to noise and lower performance under reduced signal quality. At distances around 110 cm, the BER for hard decoding approaches the maximum value of 0.5, indicating that only half of the decoded information is correct.

For each distance, both SNR and BER were measured, enabling the analysis of the experimental SNR versus BER curve for the given scenario. Additionally, the theoretical error probabilities P_e as a function of SNR for both hard and soft decoding, as outlined in Equations II-82 and II-84, were calculated for comparison. The results of this analysis are presented in Figure 111.

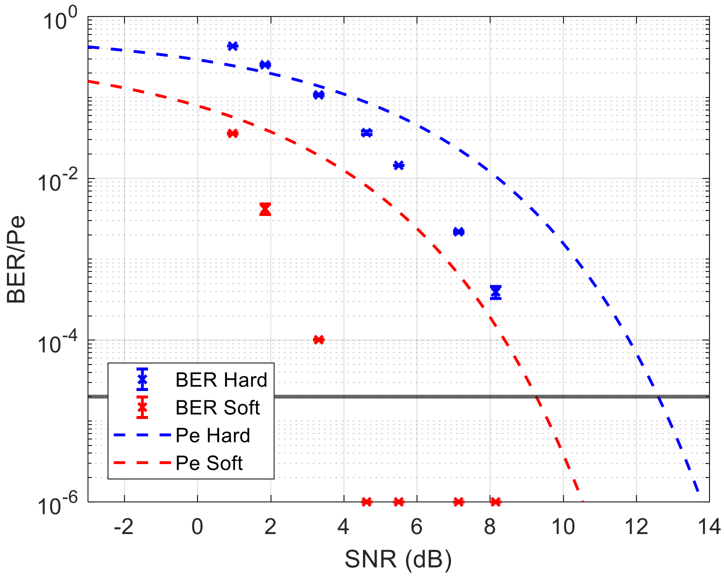

Figure 111: Comparison between the measured BER (solid markers) and the theoretical error probability P_e (dashed lines) for hard decoding (in blue) and soft decoding (in red) as a function of SNR (dB).

The experimentally measured BER values differ from the theoretical error probabilities P_e for both hard and soft decoding schemes. This discrepancy indicates the presence of unknown factors influencing the SNR measurement, such as signal processing within the USRP or inconsistencies in signal normalization across different inputs (signal or noise). This likely leads to an underestimation of the measured SNR. As a result, further investigation is necessary to identify and address these factors to ensure more accurate measurements and align the experimental data with theoretical expectations.

Nonetheless, recognizing the discrepancy in the SNR measurement, a normalization process can be applied to examine the BER behaviour as a function of the SNR if its measurement was properly realized. This involves selecting an arbitrary measured BER and linearly calibrating the experimentally obtained noise power P_{noise} so that the resulting SNR aligns with the theoretical SNR required for the BER to match the corresponding theoretical P_e. Subsequently, the same calibration value is applied to all measured P_{noise}, values, effectively recalibrating the SNR measurements across the dataset. An example of normalization is described in Appendix 4. The normalization is realized for both hard and soft decoding independently. The BER values below the threshold are ignored for the normalization.

The results shown in Figure 112 demonstrate that, after applying the normalization process to the SNR measurements, the experimentally obtained BER aligns closely with the theoretical error probabilities P_e for both hard and soft decoding methods. This alignment verifies that the normalization effectively compensates for the initial discrepancies in the SNR measurement. Furthermore, the analysis demonstrates that both hard and soft decoding exhibit the expected theoretical behaviours as a function of the SNR, confirming that the noise follows a Gaussian distribution, which aligns with the characteristics of shot noise.

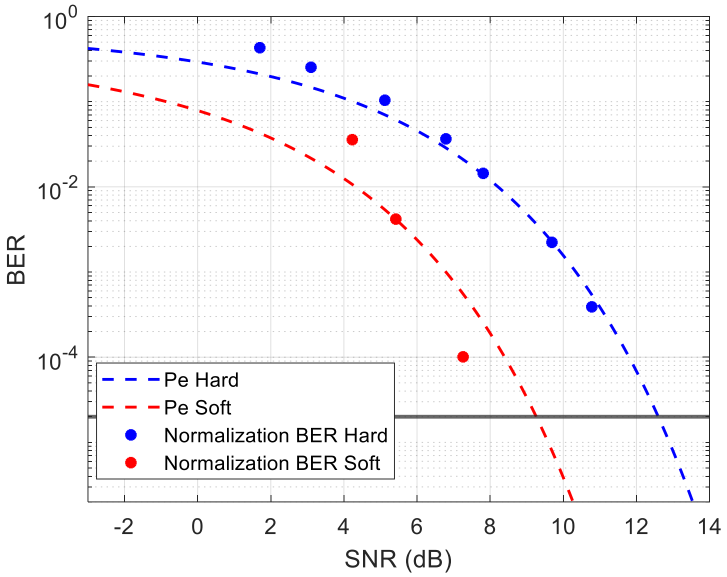

Figure 112: Comparison between the BER (solid markers) and the theoretical error probability (dashed lines) for hard decoding (in blue) and soft decoding (in red) as a function of the normalized SNR.

Although precise SNR measurements were not achievable with the commercial photodiode, the results indicate that, despite the unknown variables in our experimental setup, the BERs still follow the theoretical error probability trends. Consequently, the experimental bench has been validated for BER measurements. However, further efforts are required to accurately determine the system SNR.

V.3. OPV receiver

The commercial photodiode was subsequently replaced with the OPV to enable further SLIPT analysis. Based on the conclusions drawn in the previous section, we opted not to measure the signal SNR with the OPV, focusing instead on BER and output power P_{out} measurements. Additionally, for simplicity, the analysis was conducted exclusively using the hard decoding method. The primary objective of this investigation is to evaluate the impact of the output variable (current or voltage) and the operating point on communication and energy harvesting performance independently. Thus, the impact of the communication data rate on the communication performance is also analysed.

Given that the USRP has an input impedance of $50\,\Omega$ and does not accept negative DC components of the electrical signal, the originally proposed TIA and parallel load front-end circuits (refer to Figure 53) are not compatible with the current experimental setup. The TIA circuit outputs a negative voltage, while the parallel load method is constrained by the $50\,\Omega$ input impedance of the USRP. To address these limitations, both front-end circuits were adapted to ensure the effective extraction of the desired output variable.

In our methodology, energy harvesting parameters are derived from the DC values of the output current (I_{mean}) and voltage (V_{mean}), allowing the calculation of output power as $P_{out} = I_{mean}V_{mean}$. However, since the USRP entirely filters out the DC components of the input signal, it is impossible to determine the energy harvesting parameters directly through it.

Consequently, these static parameters are measured separately using the RTB2004 digital oscilloscope, by Rohde & Schwarz.

Given the measured OPV bandwidth values ranging from 1 kHz to 6 kHz under the analysed conditions, as described in Chapter III, a data rate of 2 kbit/s was selected for the 2-PPM modulation scheme. This corresponds to a required bandwidth of 4 kHz, which aligns well with the OPV capabilities. To accommodate the reduced data rate, the total transmitted bits were decreased to 100 kbits, thereby shortening the transmission time. Consequently, ensuring reliable BER measurement requires a minimum of ten errors per transmission, resulting in a minimum measurable BER of $10/100000 = 1 \times 10^{-4}$. This level is still sufficient when forward error correction coding is implemented in the system.

The subsequent sections provide detailed descriptions of each front-end circuit, along with the corresponding results obtained from the experiments.

V.3.1. TIA

As the TIA returns negative voltage values, which is not acceptable for the USRP, we propose to employ a unity gain inverting amplifier after the current to voltage conversion. We have arbitrarily chosen to use $1\ k\Omega$ as the feedback resistance of the inverter amplifier, which is equal to the negative input resistance for a unity gain. Figure 113 shows the proposed front-end circuit.

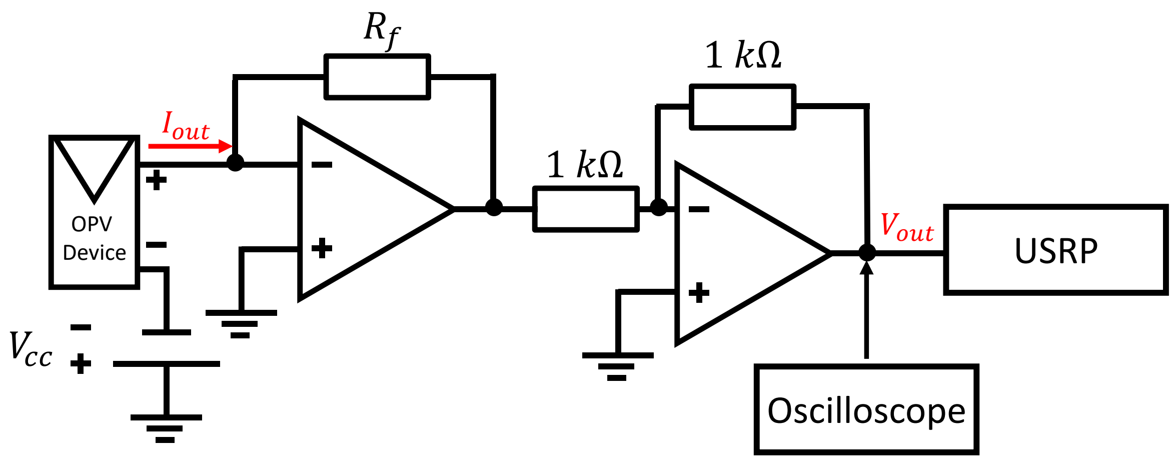

Figure 113: Modified TIA circuit with a unity-gain inverting amplifier to ensure compatibility with the USRP.

As in the dynamic characterization, the OPV operating point is determined by the V_{cc} voltage source. For the communication experiments using the TIA, the OPV was polarized at 0 V, 0.2 V, 0.3 V, 0.4 V, and 0.5 V. Polarization at 0.6 V was avoided as it could exceed the V_{oc}, potentially causing the system to inject current into the device. In our setup, both OP-AMPs were symmetrically polarized with $\pm$3 V.

To measure the output power P_{out} of the OPV at each distance and operating point, an oscilloscope was connected to the circuit while disconnecting the USRP to eliminate impedance interference. The variable V_{out}, comprising both AC and DC components (V_{AC} and V_{mean} respectively), was measured. Since the output voltage is directly proportional to the output current I_{out}, following the relationship $V_{out} = R_f I_{out}$, the output power P_{out} generated by the OPV in a SLIPT scenario is described by Equation V-5.

$$P_{out} = I_{mean}V_{cc} = \frac{V_{mean}V_{cc}}{R_f} \qquad \text{V-5}$$

As the feedback resistance R_f does not affect the output current I_{out} or the polarization point, it has no significant impact on the energy harvesting performance of the OPV. However, the amplitude of V_{AC} varies with the resistance value, thereby influencing the communication performance.

In a first approach, $R_f = 1\ k\Omega$ was selected to compare the results with the dynamic characterization performed in Chapter III. However, for the transmitter-receiver distances used in our experimental setup, no bit errors were observed across all operating voltages. This outcome is attributed to the large active area of the OPV, which generates a significant output current I_{out}, even at higher operating voltages, leading to a substantial amplification by the feedback resistor R_f. To obtain measurable BER values that contribute meaningfully to the analysis, the feedback resistance was subsequently reduced.

Following a thorough analysis, a feedback resistor R_f of $47\ \Omega$ was selected for the experiment. The measurements were conducted at distances of 50 cm, 56 cm, 66 cm, 80 cm, and 105 cm, providing sufficient data points to span multiple decades of the BER measurement. Finally, Figure 114 presents the BER results obtained using the hard decoding method.

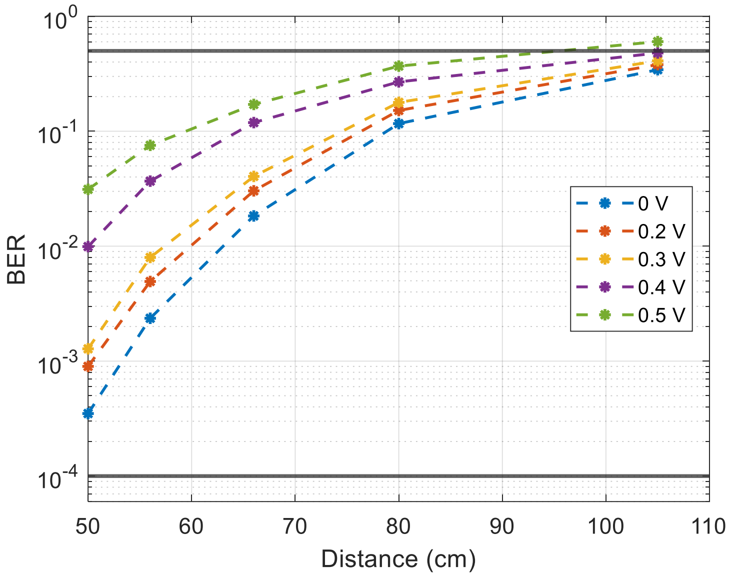

Figure 114: BER as a function of the distance between transmitter and receiver for various operating voltages (0 V, 0.2 V, 0.3 V, 0.4 V, and 0.5 V) using a TIA front-end with $R_f = 47\ \Omega$.

Black lines indicate the minimum measurable BER (1×10^{-4}) and the maximum theoretical BER (0.5). BER values exceeding the maximum signify a loss of synchronization between the receiver and transmitter, making decoding impossible.

As expected, a similar trend to that observed with the fast PD (refer to Figure 110) is evident here: the BER increases consistently with distance, regardless of the operating voltage. This behaviour aligns with the fact that the PD amplifier circuit also converts the output current to voltage, and I_{out} decreases proportionally to 1/d². Similarly, the received optical power P_r follows the same 1/d² relationship.

As shown in the dynamic characterizations and discussed in the literature, deeply described in Chapter II, higher operating voltages reduce both the output current and the OPV bandwidth. Consequently, this leads to a decrease in signal amplitude and, therefore, the system SNR. As a result, the BER rises with increasing operating voltage.

Concerning the output power P_{out}, the measured values for different operating points and distances are shown in Figure 115.

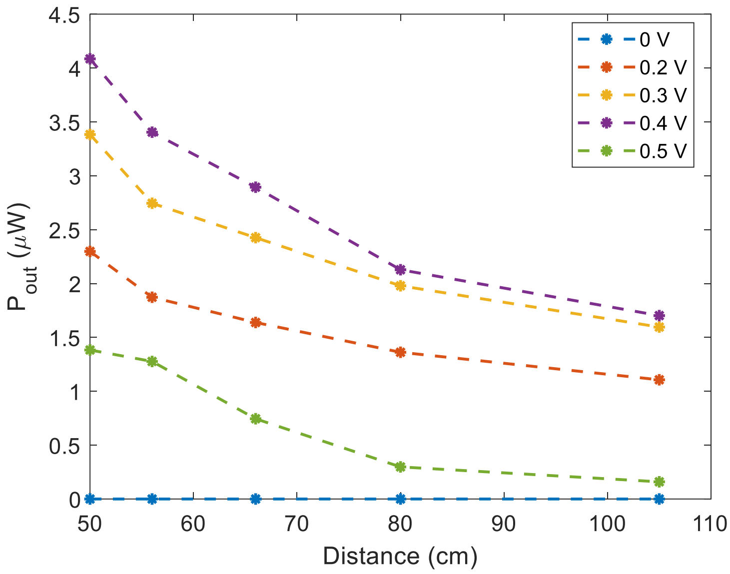

Figure 115: P_{out} as a function of the distance between transmitter and receiver for various operating voltages (0 V, 0.2 V, 0.3 V, 0.4 V, and 0.5 V) using a TIA front-end with $R_f = 47\ \Omega$.

As expected, the output power P_{out} decreases proportionally to 1/d², consistent with the behaviour of the received optical power P_r as described by the LOS link equation. Additionally, P_{out} does not exhibit a linear trend as a function of the operating point (see Figure 66). Under the low illumination conditions of our setup, the OPV generates approximately $4\ \mu W$ at an operating voltage of 0.4 V and a distance of 50 cm.

For a more detailed evaluation, both BER and output power P_{out} can be examined at a fixed distance while varying the operating point. We have selected $d = 50\ cm$ for this analysis, with additional distance analyses provided in Appendix 5. The result is illustrated in Figure 116.

This analysis highlights the trade-off between energy harvesting and communication performance. For a given signal amplitude and illumination condition, increasing the operating point improves the output power P_{out} until reaching the MPP (here, 0.4 V), while simultaneously degrading communication performance. Beyond the MPP, no further improvement in energy harvesting is observed. Consequently, the MPP represents the highest exploitable operating point under an output current configuration.

For instance, at a voltage level of 0.3 V where the output power is $3.5\ \mu W$, it ensures a BER close to 10^{-3}, which represents the threshold for error-free communication when using standard error correction codes. However, defining a single "best operating point" is a misconception. Since the operating point influences both communication and energy harvesting performance, it depends on the specific requirements of the wireless receiver, such as required power, bandwidth, and achievable data rate for an acceptable BER, all of which may vary depending on the application.

Under a fixed operating point, careful analysis is necessary to account for all factors impacting the receiver performance. However, more advanced topologies may offer dynamic approaches, allowing the OPV operating point to adapt to the receiver specific needs, such as battery state. This concept has been theoretically introduced in the literature [212].

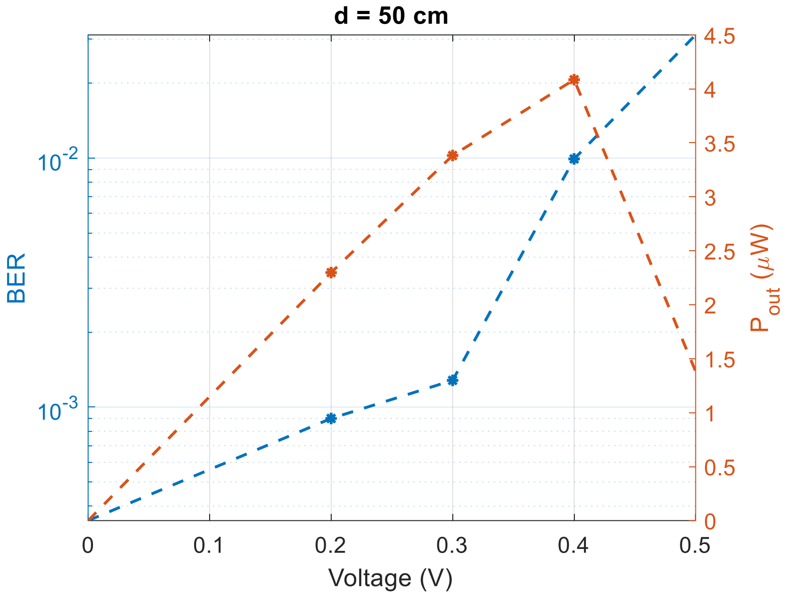

Figure 116: Measured BER (blue, left axis) and output power P_{out} (red, right axis) as functions of the operating voltage at a fixed distance of $d = 50\ cm$.

V.3.2. Parallel load

To operate in the parallel load configuration for voltage reading, an adaptation is required to prevent the USRP input impedance from interfering with the impedance observed by the OPV. For this purpose, a voltage buffer with an OP-AMP was implemented to transfer the output voltage to the USRP. Figure 117 shows the proposed front-end circuit.

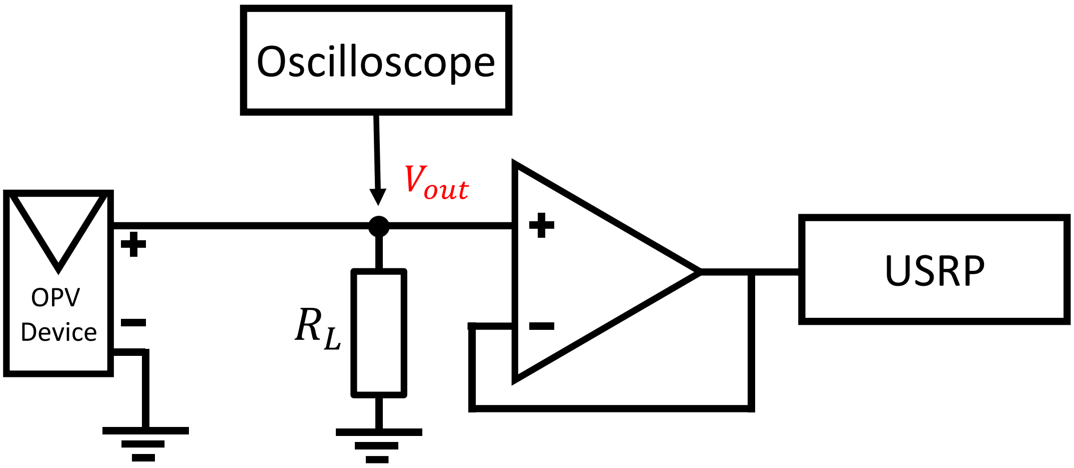

Figure 117: Modified parallel load circuit with a voltage buffer to ensure compatibility with the USRP.

As concluded from the dynamic characterizations, the OPV operating voltage, i.e. V_{mean}, is influenced not only by the load resistance but also by the illumination conditions (refer to Figure 69). In the current experiments, load resistances of $68\ \Omega, 560\ \Omega, 1\ k\Omega, 5.6\ k\Omega$ and $33\ k\Omega$ were employed. Additionally, the OP-AMP was symmetrically polarized with ± 3 V.

To determine the output power P_{out}, the oscilloscope was directly connected to the load R_L, with the USRP disconnected. The DC component of the output voltage, V_{mean}, was measured, and P_{out} was calculated using Equation V-6.

$$P_{out} = \frac{V_{mean}^2}{R_L} \qquad \text{V-6}$$

The distances employed for the parallel load front-end differs from the distances employed with the TIA. Trying to cover different BER decades, the following distances were used: 13 cm, 30 cm, 45 cm, 90 cm, 105 cm, 133 cm and 174 cm. Finally, the obtained BERs are shown in Figure 118. Again, measurements below the minimum measurable BER means that insufficient number of errors occurred to precisely estimate the system BER.

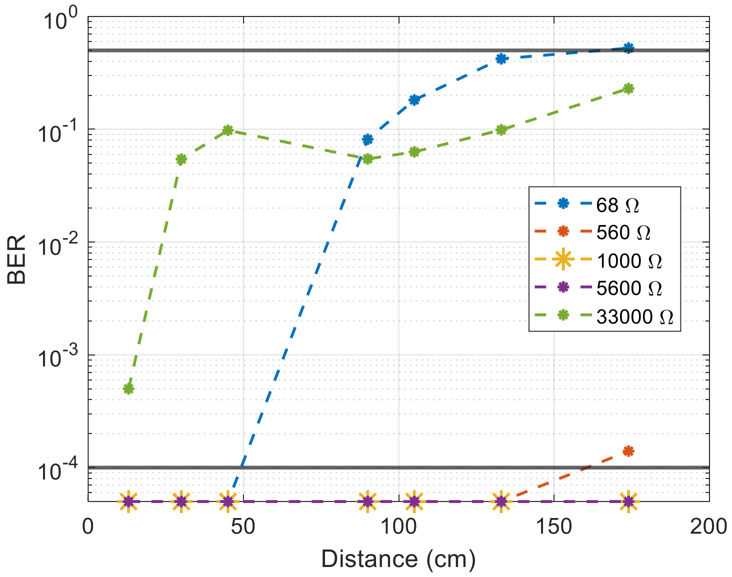

Figure 118: BER as a function of the distance between transmitter and receiver for various parallel load values.

Compared to the results obtained extracting the output current, the parallel load method yields significantly different outcomes. This divergence is expected, as this approach is highly influenced by the illumination conditions, as discussed in Chapter III. Notably, both $1\ k\Omega$ and $5.6\ k\Omega$ loads resulted in perfect transmissions with BER inferior to the threshold, while the $560\ \Omega$ load provided a measurable BER only at 174 cm. The $68\ \Omega$ load exhibited results comparable to those obtained with the TIA, whereas the $33\ k\Omega$ load demonstrated a significant distinct behaviour.

Interestingly, this trend aligns with the expectations based on the current setup. As detailed in Chapter III and explicitly shown in Figure 69, the OPV saturation point varies depending on the load and light intensity (defined by the DC component of the optical signal). Lower light intensities tend to shift the V-R curve to the right, toward higher resistance values, meaning the OPV will saturate only at high load values. Conversely, higher light intensities shift the V-R curve to the left, toward lower resistance values, causing the OPV to saturate quickly at low load values. In this setup, the transmitter-receiver distance affects not only the signal amplitude but also the OPV illumination condition.

For intermediate load values, such as $1\ k\Omega$ and $5.6\ k\Omega$, the OPV predominantly operates in its linear region, providing sufficient signal amplitude for reliable decoding even at greater distances.

For smaller load values, such as $560\ \Omega$, increasing the distance significantly reduces the signal amplitude and shifts the OPV operation out of the linear region toward the first flat part of the V-R curve, where the OPV sensitivity is lower. Consequently, the BER increases and becomes measurable.

At $68\ \Omega$, the OPV consistently operates in the initial flat region without ever reaching the linear region, regardless of the distance. As a result, the measurable BER is directly proportional to the signal amplitude and, consequently, inversely proportional to the distance.

Finally, for higher resistance values, such as $33\ k\Omega$, the OPV saturates quickly even under low illumination conditions. In this case, two factors significantly influence the OPV communication performance: the mean voltage value (defining its operating point) and the voltage amplitude. At short distances, the OPV is clearly saturated, but the optical signal is amplified sufficiently by the high resistance to achieve low BER values. As the distance increases, the OPV does not immediately leave saturation but detects lower optical signal amplitudes, resulting in a higher BER. However, at even greater distances, the OPV begins to leave saturation, and although the optical signal amplitude is reduced compared to closer distances, it is more effectively amplified in the linear region. As the distance increases further, the optical signal amplitude diminishes significantly, and even in the linear region, it is insufficiently amplified to reduce the BER, which subsequently increases again at greater distances.

Regarding the output power P_{out}, Figure 119 shows the measured values for different parallel loads and distance.

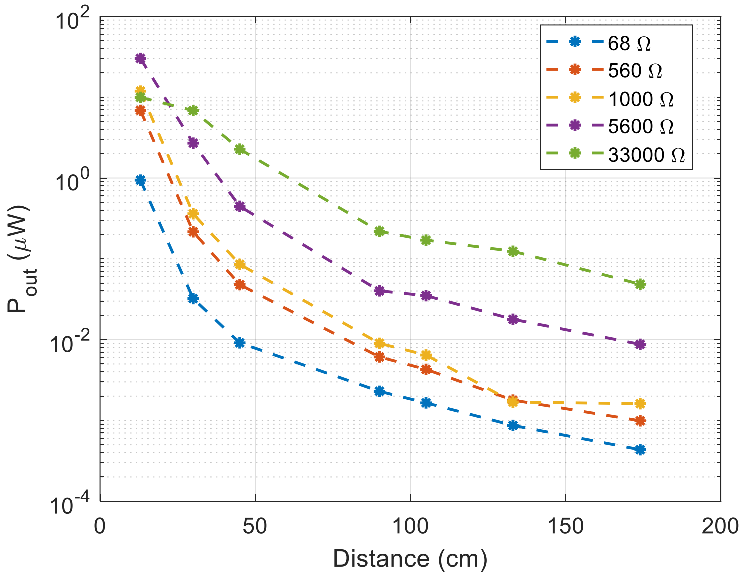

Figure 119: P_{out} as a function of the distance between transmitter and receiver for various parallel load values.

As anticipated, the output power decreases as the distance increases, a trend consistent with previous experiments. When compared to the results obtained with the TIA front end, the measured P_{out} remains similar for the same distances. Indeed, the power generated by the OPV is determined by both I_{out} and V_{out} and is independent of the specific front-end circuit used.

At a distance of 13 cm, P_{out} increases until it reaches the MPP at approximately $5.6\ k\Omega$ and then begins to decrease. However, as the distance from the optical source increases, the V-R curve shifts to the right, requiring higher load values to reach the MPP. Consequently, the highest P_{out} is achieved with the largest tested load, $33\ k\Omega$. For this setup, the MPP was not reached and remains undefined.

To highlight the influence of the illumination, represented here by the distance, on this topology, both BER and P_{out} were plotted for two strategically selected distances across multiple load resistances, as shown in Figure 120. Additional results for other distances are provided in the appendices.

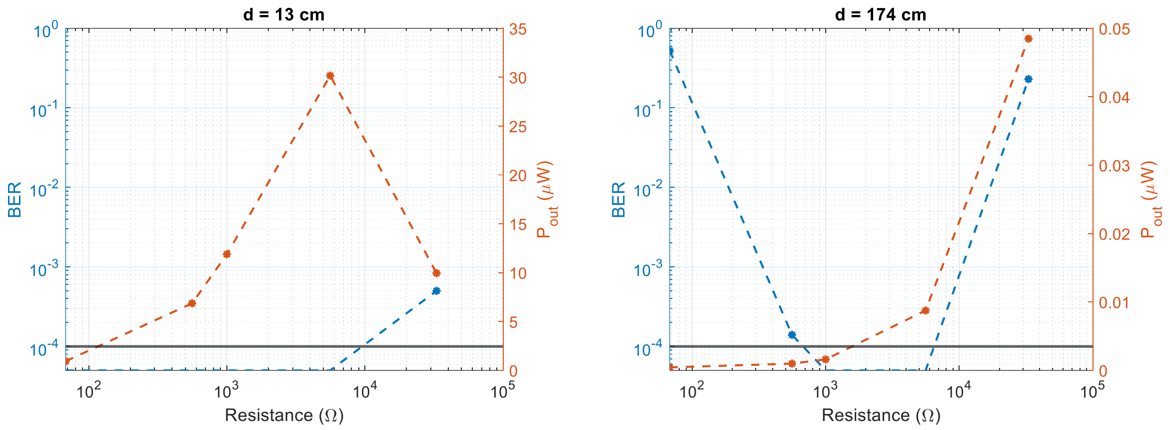

(a) (b)

Figure 120: Measured BER (blue, left axis) and output power P_{out} (red, right axis) as functions of the parallel load at fixed distances of: (a) $d = 13\ cm$; (b) $d = 174\ cm$.

In Figure 120.a, the approximate location of the MPP is evident at a distance of 13 cm. However, at 174 cm (Figure 120.b), the MPP remains undefined for the tested resistance values. Unlike the TIA topology, where the trade-off between energy harvesting and communication performance is consistent across all illumination levels (showing that operating points above the MPP provide no additional benefits and that the best communication performance is achieved under short-circuit conditions), the parallel load topology exhibits a more complex behaviour. The trade-off cannot be directly determined in this case. For instance, under this specific illumination scenario, the optimal results are obtained with a $5.6\ k\Omega$ resistance, as it yields error-free decoding while generating more power compared to smaller load values (30 μW at 13 cm and 0.01 μW at 174 cm).

To highlight the significant dependence of this topology on illumination conditions, an external high-power LED was added in parallel with the modulated optical source to enhance the OPV illumination. The external LED, identical to the modulated source, was driven at a higher power level compared to the modulated one. In this setup, the goal was not to precisely quantify the transmitted optical power P_t of the LED but rather to qualitatively evaluate the impact of the additional illumination on both energy harvesting and communication performance. The experiments were subsequently repeated under these modified conditions. Figure 121 shows the obtained BER as a function of the distance for multiple load values.

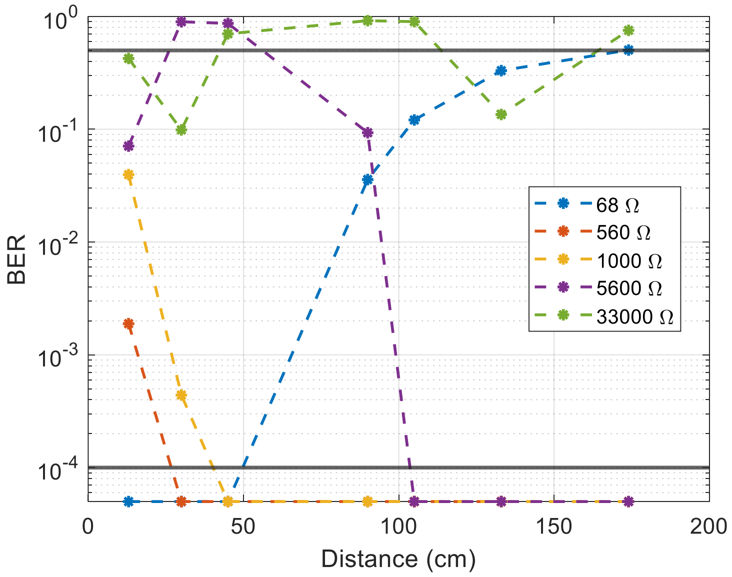

Figure 121: BER as a function of the distance between transmitter and receiver for various parallel load values with external high-power LED.

These results highlight the complexity of operating under the parallel load topology without a clear understanding of the OPV illumination conditions. The saturation effect is evident for higher resistance values ($5.6\ k\Omega$ and $33\ k\Omega$), while lower resistance values, such as $68\ \Omega$, show slight performance improvements compared to the previous scenario. This indicates that under high illumination levels, lower resistance values perform better, whereas at lower illumination levels, mid to high resistance values yield superior performance. Following the experiment analysis, Figure 122 presents the measured P_{out} as a function of distance for various load resistances.

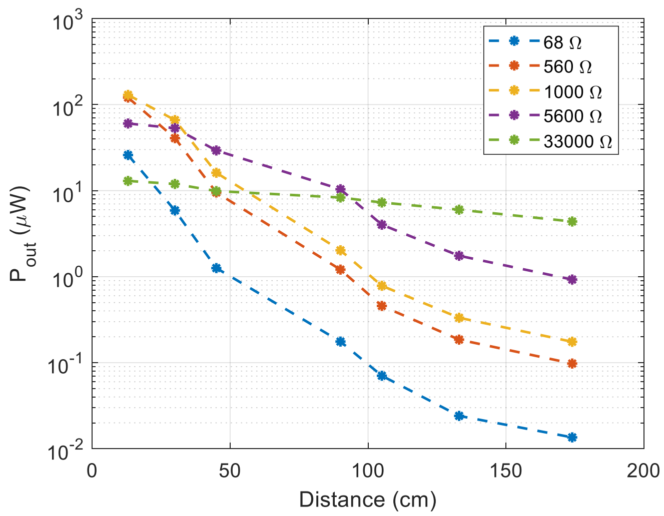

Figure 122: P_{out} as a function of the distance between transmitter and receiver for various parallel load values with external high-power LED.

As expected, the output power P_{out} increases significantly with the addition of external DC lighting. Moreover, the MPP shifts according to the illumination conditions, represented by the resistance at which the maximum output power is achieved. To visualize the evolution of the MPP, we have plotted the normalized P_{out} as a function of resistance for various distances, as illustrated in Figure 123. The results clearly show that as the distance from both LEDs increases, the illumination level decreases, requiring higher resistance values to reach the MPP.

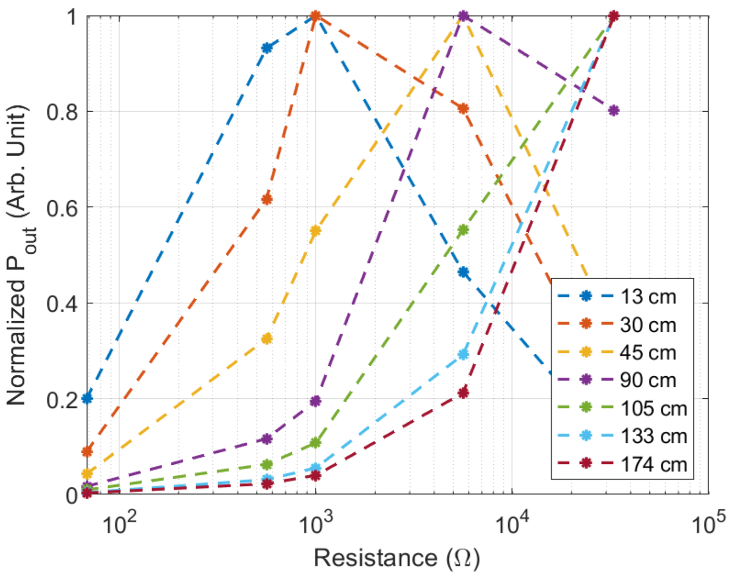

Figure 123: Normalized output power P_{out} as a function of the parallel load for multiple distances under external DC illumination.

Finally, the measured BER and P_{out} as functions of the parallel load for multiple distances are provided in Appendix 6. As observed earlier, the trade-off between BER and P_{out} is not straightforward, resulting from the complex interplay between the illumination conditions and the parallel load. This highlights the challenging nature of OPVs under varying illumination conditions in the parallel load topology, requiring refined circuits capable of actively tracking the optimal operating point to maximize overall performance, considering both energy harvesting and communication. Consequently, an alternative MPPT strategy is necessary.

Furthermore, direct comparisons between the performances of the TIA and the parallel load topologies are not feasible. The key difference lies in the intrinsic dependence of the parallel load topology on the illumination condition and the non-linear behaviour of the OPV under varying load resistances. While the TIA provides a controlled and consistent conversion of the output current to voltage, independent of the illumination intensity, the parallel load topology is highly sensitive to both illumination and load. The OPV operating point and the resulting signal amplitude vary significantly based on the resistance and illumination level, as highlighted in the analysis. Additionally, the saturation effect observed in the parallel load topology, particularly under high illumination and resistance values, further complicates direct comparisons with the TIA results, which are relatively unaffected by such conditions.

In essence, the differences in how the two topologies interact with the OPV characteristics under varying conditions make direct performance comparisons unfeasible. Each method has unique dependencies and applications, and their results must be interpreted within the context of their respective operating principles.

V.3.3. Data rate analysis

To assess the dynamic performance of the OPV and evaluate its communication capabilities, the data rate can be varied for a fixed distance. In this context, the BER is expected to increase if the required modulation bandwidth exceeds the OPV response time. Conversely, if the BER remains unchanged as the data rate increases, it indicates that the OPV bandwidth is sufficient to accommodate the transmitted signal. The experiments are conducted for both front-end circuits, with no intention of directly comparing their performance. Strategic operating points (or parallel loads) are selected to analyse the influence of bandwidth under different conditions. Additionally, the transmitter-receiver distance used in the experiments is adjusted according to the front-end circuit to ensure measurable BER values.

To evaluate the OPV performance, data rates of 1.5, 2, 3, 5 and 10 kbit/s were used, corresponding to required bandwidths of 3, 4, 6, 10 and 20 kHz respectively, for the 2-PPM modulation scheme. As the data rate itself does not change the average transmitted optical power, the output power P_{out} will not be evaluated in this scenario.

V.3.3.1. TIA

For the TIA configuration, we have employed $47\ \Omega$ as the feedback resistance, associated to a distance of 50 cm, providing sufficiently measurable BER for our analysis. Here, we have opted to use the extreme operating points, 0 V and 0.5 V. Based on the dynamic characterizations detailed in Chapter III (refer to Figure 77.a), the OPV bandwidth is estimated to be approximately 5.5 kHz at 0 V and 1 kHz at 0.5 V. Figure 124 shows the obtained results.

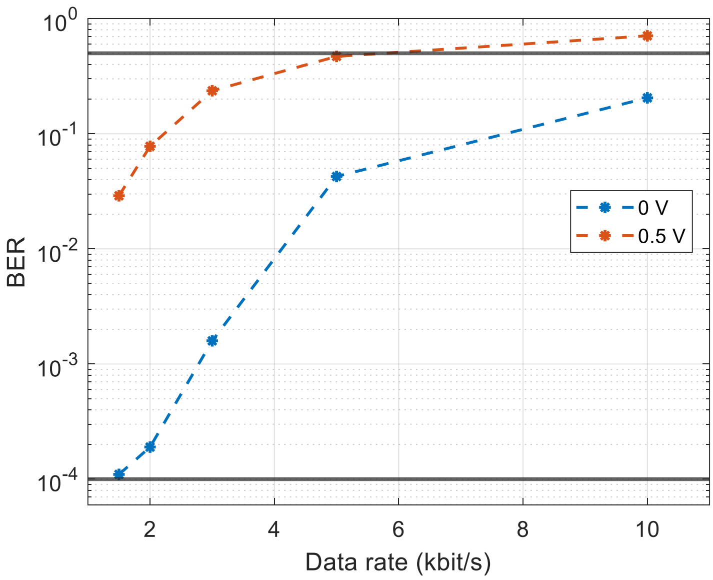

Figure 124: Measured BER as a function of data rate with TIA front-end at a distance of 50 cm for two operating points: 0 V (in blue) and 0.5 V (in red).

The results reaffirm the behaviour observed in previous experiments: increasing the operating point not only reduces the OPV dynamic response but also decreases the amplitude of the output current. These two factors together contribute to the increase in BER, driven by both the reduction in SNR and the OPV bandwidth limitation. However, it remains challenging to determine which factor has a more significant impact on communication performance.

Additionally, increasing the data rate results in a higher BER for both operating points, but with varying intensity. Notably, the highest operating point (0.5 V) experiences a more pronounced penalty when transitioning from 1.5 kbit/s to 2 kbit/s, as the BER rises from 3×10^{-2} to 8×10^{-2}, while the short-circuit condition (0 V) shows a weaker increase from 1×10^{-4} to 2×10^{-4}. This indicates that the OPV bandwidth at 0.5 V is indeed lower than its bandwidth at 0 V, a conclusion consistent with the findings from the dynamic characterization. Finally, as expected, the BER increases with higher data rates due to the modulation bandwidth exceeding the OPV bandwidth (which was estimated between $1\ kHz$ and $8\ kHz$ for any operating point, described in Chapter III).

V.3.3.2. Parallel load

For the parallel load front-end, we have employed $68\ \Omega$, $1\ k\Omega$ and $33\ k\Omega$ as resistances, with a distance of 90 cm (without an external DC lighting). The results are shown in Figure 125.

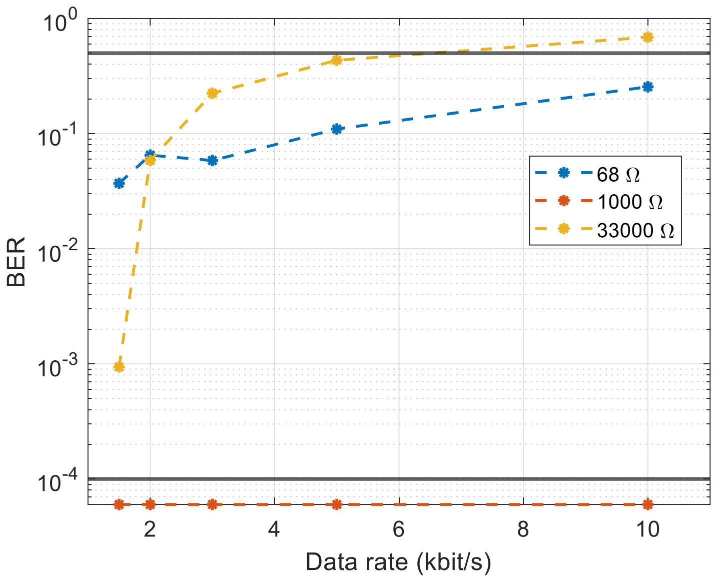

Figure 125: Measured BER as a function of data rate with parallel load front-end at a distance of 90 cm for three resistance values: $68\ \Omega$ (in blue), $1\ k\Omega$ (in red) and $33\ k\Omega$ (in yellow).

The $1\ k\Omega$ resistance demonstrated exceptional performance, achieving error-free transmission across all tested data rates, with a real BER below the threshold of 1×10^{-4}. Despite the measured bandwidth for $1\ k\Omega$ being between $1\ kHz$ and $3\ kHz$, the receiver maintained reliable performance even at a required bandwidth of $20\ kHz$. Typically, a signal exceeding the bandwidth would result in insufficient response time for the device to transition between low and high states, leading to reduced amplitude and signal distortion. However, the $1\ k\Omega$ resistance provided sufficient signal amplitude for perfect decoding, even when operating after the OPV cutoff frequency. Figure 126 shows the OPV output voltage measured directly with the oscilloscope at 1.5 kbit/s (top) and 10 kbit/s (bottom), where the signal distortion becomes evident. At 1.5 kbit/s, the signal maintains a relatively clean and undistorted waveform, whereas at 10 kbit/s, signal distortion becomes prominent, highlighting the limitations of the OPV bandwidth in handling higher data rates.

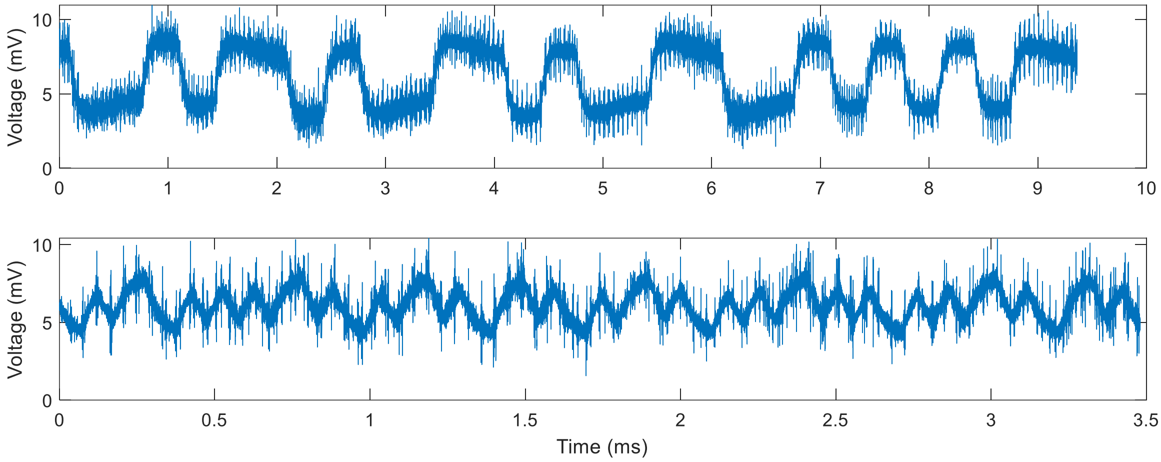

Figure 126: OPV output voltage measured with an oscilloscope at data rates of 1.5 kbit/s (top) and 10 kbit/s (bottom) at a parallel load of $1\ k\Omega$.

This observation underscores the dual importance of bandwidth and signal strength in communication scenarios, as previously analysed in Chapter III. Finally, determining the maximum achievable data rate for a parallel load of $1\ k\Omega$, while maintaining an acceptable BER, remains a topic for future investigation.

The influence of bandwidth is particularly evident when comparing the parallel load configuration to the TIA. At lower data rates, such as 1.5 kbit/s and 2 kbit/s, the $33\ k\Omega$ resistance performed better due to its ability to generate higher signal amplitudes under these conditions. However, lower operating points offer higher bandwidths. As the data rate increases, the OPV requires faster response times, which higher resistances cannot provide. Consequently, lower resistances, such as $68\ \Omega$, outperform higher resistances for data rates exceeding 3 kbit/s.

The performance disparity as a function of load resistances reinforces the importance of both bandwidth and signal strength in a communication scenario. At lower data rates, higher resistances such as $33\ k\Omega$ perform better due to their ability to generate stronger electrical signals, but as data rates increase beyond 3 kbit/s, the OPV bandwidth limitations become dominant, and lower resistances like $68\ \Omega$ achieve superior performance. This reinforces the inherent complexity of the parallel load topology for indoor communication scenarios, where the illumination level and resistance significantly influence the OPV operating point. Achieving optimal communication and energy harvesting performance under this topology requires a more sophisticated active circuit capable of dynamically adapting the load. Such concept would be a natural extension of MPPT commonly used in energy harvesting regimes adapted to the SLIPT context, such as the front-end circuits proposed in [214]. However, this adaptation is challenging, as the trade-off between these factors is non-trivial and context-dependent.

V.4. Chapter conclusion

The experimental findings presented in this chapter highlight the critical trade-off between energy harvesting and communication performance within the SLIPT concept, as analysed through OPV-based receivers. These results reaffirm and extend the observations from Chapter III, demonstrating how the dynamic behaviour of OPVs is intricately influenced by their operating conditions, illumination levels, and front-end configurations.

A key validation step involved the use of a commercial silicon photodiode to evaluate the experimental setup. This validation ensured the reliability of the measurement process and established the foundations for analysing the OPV performance. By comparing the measured SNR and BER with theoretical expectations, the experimental setup was shown to accurately reflect the system communication capabilities. This step was essential for verifying the robustness of the bench and for providing confidence in the subsequent OPV measurements.

The experiments confirmed the significant role of the OPV operating point in determining both the signal bandwidth and amplitude. As detailed in Chapter III, the bandwidth of the OPV is inversely correlated with its operating voltage, while higher voltages also diminish the output current amplitude for the TIA topology. This dual effect of reduced bandwidth and signal strength, observed again in Chapter V, compromises the SNR and consequently the BER. In contrast, the parallel load exhibited a more complex behaviour, where the output signal amplitude was simultaneously influenced by the illumination levels and the resistance, while the bandwidth showed an inverse relationship with the load.

Furthermore, the trade-off between communication and energy harvesting was explored, revealing differences based on the employed method. The TIA topology provides robustness against ambient lighting conditions and predictable communication and energy harvesting results. The findings emphasize that while operating close to the MPP can optimize energy harvesting, it imposes constraints on the communication performance. As also observed in Chapter III, operating at 0 V achieves the best communication performance but sacrifices energy harvesting potential. In contrast, the parallel load topology exhibits a highly complex behaviour where the trade-off between communication and energy harvesting is not readily apparent. Additionally, achieving the MPP is challenging and requires active tracking to optimize performance. The inherent complexity of the SLIPT concept requires further exploration of the intrinsic trade-offs between communication and energy harvesting. This underscores the need for developing a new set of metrics to evaluate performance, weighted to specific application requirements.

The data rate analysis reinforced the importance of bandwidth as a limiting factor for high-speed communication. For both front-end circuits, increasing the data rate led to measurable penalties in BER, with the OPV bandwidth acting as a bottleneck. Interestingly, as observed in Chapter III, the signal amplitude played a compensatory role in mitigating bandwidth constraints in certain scenarios, particularly under parallel load configurations. However, this topology introduced additional complexity, as the optimal resistance values shifted with illumination levels, underscoring the need for advanced circuits capable of active load adaptation.

Since both signal amplitude, and therefore SNR, and receiver bandwidth are essential for communication performance, the analysis performed in this chapter can be extended to the nature of the photosensitive device itself. Small-surface photodiodes are designed with minimal junction and geometric capacitances, enabling high bandwidth. However, their limited collection area significantly reduces the generated current, and thus the SNR, requiring the use of high-performance amplification circuits. In contrast, photovoltaic devices typically feature larger active areas, which substantially reduce receiver bandwidth but enable the detection and generation of higher current levels. This results in increased signal amplitude despite detecting more noise, ultimately improving the SNR due to the stronger signal. This also supports the use of the OPV developed by Dracula Technologies, which provides sufficient charge generation while maintaining a device bandwidth that is not constrained by its geometric capacitance.

Ultimately, while TIA topologies offer predictable performance, the ability to actively set the operating point of OPVs, and an inherent amplification gain, they require external electrical power to polarize the OP-AMPs. In contrast, the parallel load presents a simpler and more energy-efficient solution to address this limitation but introduces complex and less predictable behaviours for both energy harvesting and communication. Although advanced circuits such as MPPT systems can accurately track the MPP to optimize energy harvesting, this operating point does not inherently provide insights into communication performance. In the parallel load topology, the trade-off between energy harvesting and communication depends on factors beyond the point of maximum output power, adding further complexity. Additionally, MPPT systems are active components that also require external power. Therefore, the optimal utilization of OPVs in SLIPT scenarios should involve extracting the output current as the communication variable while actively maintaining a fixed operating point. By powering the front-end circuit using the OPV own output power, such a system can achieve complete autonomy. Autonomous systems of this nature have already been proposed in the literature, as referenced in [209], [213], [214].

In conclusion, the analyses conducted in this chapter demonstrate the potential of OPV-based receivers for SLIPT applications, while also highlighting the challenges posed by their complex dynamic behaviour. The trade-offs between communication and energy harvesting, coupled with the sensitivity to illumination and operating point, highlights the need for advanced circuit designs and control strategies. These insights, first seen in the characterizations of Chapter III, provide a guide for further optimization and practical implementation of OPV-based SLIPT systems.

Conclusion

This thesis explored the integration of OPVs and VLC within SLIPT context, providing a comprehensive analysis of their potential for energy-efficient communication and energy harvesting in IoT applications. Each chapter offered unique insights, contributing to a complete understanding of the challenges and opportunities in this emerging field, as detailed below.

Chapter I laid the foundation by establishing the context for this research. It highlighted the VLC advantages, such as spectrum availability and security, while emphasizing the increasing need for sustainable solutions to support IoT devices. The chapter also introduced OPVs, detailing their material properties and suitability for indoor environments, and positioned them as dual-function devices capable of both energy harvesting and optical communication.

Chapter II expanded on the fundamental concepts by exploring VLC, OPVs, and SLIPT in detail. It presented the principles and technical characteristics of these technologies, offering a theoretical basis for analysing their integration together. A detailed state-of-the-art review of the SLIPT context, extending beyond VLC and OPVs, was presented, offering valuable insights for future analyses. Furthermore, we highlighted the difficulty of comparing SLIPT work due to the lack of characterization standards. The chapter also identified the primary research areas within the SLIPT field and highlighted key gaps in the literature, such as the impact of different VLC link types, the role of OPV flexibility in communication and the optimization of receiver circuits. These insights provided a foundation for the practical investigations in subsequent chapters.

Chapter III described the static and dynamic characterizations of a particular OPV, fabricated by Dracula Technologies, focusing on its energy harvesting and communication performance. Static analyses revealed the effects of illumination, angular orientation, and mechanical deformation on the OPV performance. We demonstrated that the OPV maintain high efficiency under the measured low-light conditions (700 lux to 1800 lux), while its spectral responsivity measurement highlighted its ability to effectively absorb light in the visible range. Additionally, curvature experiments revealed that while curvier OPVs generate less current under perfect alignment conditions, they are less sensitive to variations in the incident angle of optical power.

The dynamic characterizations revealed that the OPV behaviour is strongly influenced by operating conditions, illumination levels, and device curvature. Measurements indicated that higher illumination levels slightly improve bandwidth, whereas increasing the operating voltage consistently reduces it. The role of the front-end circuit was also emphasized, with the output voltage topology demonstrating high susceptibility to illumination due to its non-linear behaviour. Curvature experiments revealed unexpected variations in bandwidth with increased curvature, likely due to changes in the internal properties of the device.

Overall, the OPV bandwidth was found to range between $1\,kHz$ and $8\,kHz$ for most conditions. These findings highlighted the trade-offs between energy harvesting and communication and proposed hybrid front-end circuit designs to address the limitations of current approaches.

Chapter IV transitioned to simulation-based analysis, integrating the OPV fabricated by Dracula Technologies into a MCRT simulator to study their performance in realistic indoor scenarios. For the first time, curved OPVs were modelled alongside flat configurations, with results validated through experimental measurements. The simulations highlighted the significance of diffuse light in maintaining link reliability and demonstrated the advantages of curved OPVs in dynamic IoT applications, such as those involving object rotation and mobility.

Chapter V focused on an experimental study, examining the SLIPT trade-offs through OPV-based receivers. It confirmed the influence of operating points, illumination, and front-end circuit configurations on both energy harvesting and communication performance independently. The experiments emphasized the challenges of achieving the MPP while maintaining acceptable communication performance for the TIA topology. Our findings highlighted the sensitivity of the parallel load based receiver on the illumination conditions, explicitly showing the saturation effects and validating the characterizations performed in Chapter III.

Furthermore, the main differences between the proposed front-ends were highlighted. As the parallel load is an attractive and passive approach, it can easily result in complex and unpredictable behaviour for both energy harvesting and communication under a scenario where the illumination can vary. The TIA, on the other hand, results in a predictable and simpler behaviour, while simultaneously amplifying the input signal, but requires external power. Therefore, we have proposed overall strategies of active front-ends, supplied by the OPV itself, that could address these challenges while considering a trade-off between communication and energy harvesting, which depends on the application. Thus, we have highlighted the lack of a figure of metrics to address SLIPT scenarios.

The last three chapters, while distinct in focus, are deeply interconnected and together provide a comprehensive evaluation of OPV performance across various aspects. Chapter III serves as the foundation for subsequent experimental approaches, addressing key challenges within the SLIPT context. The optical simulations developed and validated in Chapter IV build upon the characterizations from Chapter III to extend into real-life indoor scenarios. These simulations enable the estimation of illumination conditions, which in turn allow to evaluate the OPV non-linear V-R behaviour and its MPP, derived from the prior characterizations.

By incorporating a modulation scheme, such as 2-PPM, into the optical simulation, the communication performance of the OPV can be evaluated for specific operating points. These operating points also highlight the critical trade-off between communication and energy harvesting, a topic extensively analysed in Chapter V.

The methodology provided by this work opens new horizons and perspectives for the future development of sustainable, self-powered IoT networks, not previously seen in the current SLIPT state-of-the-art. The highly systematic characterizations allow a deep evaluation of the OPV performance under different IoT conditions, such as variable illumination and curvature. Additionally, the simulation-based approaches allow to evaluate complex and diverse IoT scenarios, extending the understanding of both energy harvesting and communication performance in dynamic and real-world environments.

While this thesis significantly contributed to the SLIPT context, employing OPVs within VLC, addressing several gaps in the current state of the art, it also paves the way for exciting new challenges that can be explored in future research. In short-term approaches, simpler and direct analysis can be derived from the current work. A key area for improvement is the optimization of the front-end circuit used in SLIPT experiments. While this work successfully analysed energy harvesting and communication performance independently, a more refined approach would involve designing a complete circuit capable of separating DC and AC components. This would not only enable more precise performance evaluations but also introduce new optimization challenges, as seen in existing literature [204]. Such circuit designs should incorporate the discoveries of this thesis, including the consideration of non-linear effects in output voltage topologies, and should ideally be powered by the OPV itself to enhance system autonomy.

Additionally, while the research in this thesis focused on a single OPV cell, future work should extend the analysis to OPV modules. The complexity of modules goes beyond the simple relationship between active surface area and bandwidth, as interconnection challenges introduce additional variables, such as shading effects and non-linear behaviour. Many of the methods used in this work, such as the measurement of short-circuit current I_{sc}, linked to spectral responsivity $R_{\lambda}(\lambda)$, are less applicable to modules due to variations in cell characteristics and the influence of interconnections. To address this limitation, a "global" characterization of the spectral responsivity of the device module, when all cells are illumination, could be proposed. Implementing modules in simulations would also significantly increase complexity, as the illumination of individual cells would result in non-straightforward behaviour. Additionally, modules as receivers could open the door to exploring new SLIPT techniques, such as spatial splitting, where different cells within the module serve distinct purposes (e.g., some for energy harvesting and others for communication). Despite the challenges, incorporating OPV modules into experimental and simulation setups would allow for a more realistic and comprehensive evaluation of SLIPT system performance.

Furthermore, building on the work developed in Chapter IV, simulations of complex indoor environments, such as dynamic setups with moving objects, varying light sources, and changing illumination conditions is an interesting short-term prospect. This approach would allow for the evaluation of OPV performance in realistic and complex IoT scenarios where environmental factors are constantly shifting, and by incorporating elements like object rotation, mobility, and partial shading would enable a deeper understanding of how these factors impact both energy harvesting and communication performance, offering valuable insights for optimizing OPV-based SLIPT systems in practical applications.

Moreover, building on the results of the 2-PPM-based experiments conducted in Chapter V, future research could focus on implementing and evaluating more advanced modulation schemes, such as OFDM combined with QAM. The use of OFDM would allow the simultaneous transmission of multiple data streams over different frequencies, improving data rates while potentially mitigating the effects of bandwidth limitations observed in OPVs.

Also, the contributions of this thesis create a basis for long-term perspectives. The development of the OPV autonomous receiver front-end could incorporate different active strategies to adapt the OPV operating point according to the environment. These systems would continuously monitor real-time variables, such as energy demands, communication requirements, and external environmental conditions, including light intensity variations and mobility of devices within the network. By employing intelligent control mechanisms, such systems could ensure optimal operation under fluctuating conditions, maximizing the efficiency of both energy and data transfer. Moreover, dynamic SLIPT systems could integrate multi-objective optimization, balancing energy harvesting and communication demands based on priority levels. For instance, during periods of high data traffic, the system could prioritize communication performance by adjusting the OPV operating point to enhance bandwidth and signal quality, while temporarily compromising energy harvesting efficiency. Conversely, during low data demand periods, the system could maximize energy harvesting to ensure sufficient power storage.

The insights and methodologies developed in this thesis play an important role in supporting the integration of OPVs into fully autonomous IoT systems. Indeed, such integration would enable IoT devices to operate efficiently in a wide range of environments, including indoor settings with low or variable illumination. The flexibility of OPVs makes them suitable for diverse IoT applications, such as smart building automation, industrial monitoring, and energy-efficient sensor networks. Future research could unlock their potential for wearable technologies, creating innovative solutions that combines energy harvesting and communication capabilities in compact, lightweight designs. These OPV-based wearables could revolutionize applications in health monitoring, fitness tracking, and portable IoT devices by providing a sustainable, self-powered alternative to conventional battery-reliant systems.

In conclusion, this thesis demonstrated the significant potential of OPVs for SLIPT applications, offering valuable insights into their dual functionality as energy harvesters and communication receivers. Through detailed characterizations, simulations, and experimental validations, this work revealed the trade-offs between energy harvesting and communication performance, emphasizing the importance of carefully balancing these factors to optimize system functionality. The findings not only highlight the versatility of OPVs but also establish their viability as a key component in sustainable IoT networks. While the research provides a robust foundation, it also underscores the complexity of the challenges that lie ahead.

Bibliography

[1] 'China Great Wall Beacon Towers: Chinese Oldest Telegram System'. Accessed: Jun. 04, 2024. [Online]. Available: https://www.travelchinaguide.com/china_great_wall/construction/tower/

[2] I. L. Idriess and J. Condon, *The Red Chief*, Unabridged edition. Bolinda Audio Books, 1998.

[3] C. H. Sterling, *Military Communications: From Ancient Times to the 21st Century*. Bloomsbury Academic, 2007.

[4] A. G. Bell, 'Upon the production and reproduction of sound by light', pp. 404–426, 1880.

[5] 'Evolution of Telecommunications from 1850 to 1900', in *The Worldwide History of Telecommunications*, John Wiley & Sons, Ltd, 2003, pp. 85–90. doi: 10.1002/0471722243.ch7.

[6] D. L. Sengupta and T. K. Sarkar, 'Maxwell, Hertz, the Maxwellians, and the early history of electromagnetic waves', *IEEE Antennas and Propagation Magazine*, vol. 45, no. 2, pp. 13–19, Apr. 2003, doi: 10.1109/MAP.2003.1203114.

[7] M. Alencar, T. T Alencar, and W. T. A Lopes, 'What Father Landell de Moura Used to Do in His Spare Time', in *Proceedings of the 2004 IEEE*, Bletchley Park: IEEE, 2014.

[8] P. K. Bondyopadhyay, 'Guglielmo Marconi - The father of long distance radio communication - An engineer's tribute', in *1995 25th European Microwave Conference*, Sep. 1995, pp. 879–885. doi: 10.1109/EUMA.1995.337090.

[9] P. Russer, 'Ferdinand Braun — A pioneer in wireless technology and electronics', in *2009 European Microwave Conference (EuMC)*, Sep. 2009, pp. 547–554. doi: 10.23919/EUMC.2009.5296324.

[10] M. A. Khalighi and M. Uysal, 'Survey on free space optical communication: A communication theory perspective', *IEEE Communications Surveys and Tutorials*, vol. 16, no. 4, pp. 2231–2258, 2014, doi: 10.1109/COMST.2014.2329501.

[11] R. J. Keyes and T. M. Quist, 'RESEARCH CONFERENCE', *Advances in Nursing Science*, vol. 12, no. 1, p. 84, Oct. 1962, doi: 10.1097/00012272-198910000-00013.

[12] R. H. Rediker, 'Semiconductor diode luminescence and lasers. A perspective', *IEEE Journal of Selected Topics in Quantum Electronics*, vol. 6, no. 6, pp. 1355–1362, Nov. 2000, doi: 10.1109/2944.902189.

[13] F. E. Goodwin, 'A Review of Operational Laser Communication Systems', *Proceedings of the IEEE*, vol. 58, no. 10, pp. 1746–1752, 1970, doi: 10.1109/PROC.1970.7998.

[14] G. Held, *Introduction to Light Emitting Diode Technology and Applications*, 1st edition. Boca Raton: Auerbach Publications, 2008.

[15] A. Al-kinani, C. Wang, L. Zhou, and W. Zhang, 'Optical Wireless Communication Channel Measurements and Models', vol. 20, no. 3, pp. 1939–1962, 2018.

[16] I. Akasaki, H. Amano, N. Koide, M. Kotaki, and K. Manabe, 'Conductivity control of GaN and fabrication of UV/blue GaN light emitting devices', *Physica B: Physics of Condensed Matter*, vol. 185, no. 1–4, pp. 428–432, 1993, doi: 10.1016/0921-4526(93)90274-A.

[17] S. Nakamura, 'High-power InGaN/AlGaN double-heterostructure blue-light-emitting diodes', in *Proceedings of 1994 IEEE International Electron Devices Meeting*, Dec. 1994, pp. 567–570. doi: 10.1109/IEDM.1994.383328.

[18] G. Zissis and P. Bertoldi, 'A Review of Advances in Lighting Systems' Technology—The Way Toward Lighting 4.0 Era', *IEEE Open Journal of Industry Applications*, vol. 4, pp. 111–120, 2023, doi: 10.1109/OJIA.2023.3263182.

[19] G. Pang, T. Kwan, C.-H. Chan, and H. Liu, 'LED traffic light as a communications device', in *Proceedings 199 IEEE/IEEJ/JSAI International Conference on Intelligent Transportation Systems (Cat. No.99TH8383)*, Oct. 1999, pp. 788–793. doi: 10.1109/ITSC.1999.821161.

[20] Y. Tanaka, S. Haruyama, and M. Nakagawa, 'Wireless optical transmissions with white colored LED for wireless home links', in *11th IEEE International Symposium on Personal Indoor and Mobile Radio Communications. PIMRC 2000. Proceedings (Cat. No.00TH8525)*, IEEE, 2000, pp. 1325–1329. doi: 10.1109/PIMRC.2000.881634.

[21] S. U. Rehman, S. Ullah, P. H. J. Chong, S. Yongchareon, and D. Komosny, 'Visible Light Communication: A System Perspective—Overview and Challenges', *Sensors*, vol. 19, no. 5, Art. no. 5, Jan. 2019, doi: 10.3390/s19051153.

[22] 'VLCA一般社団法人可視光通信協会'. Accessed: Jun. 14, 2024. [Online]. Available: https://j-photonics.org/vlca/en/

[23] 'JEITA Members | Japan Electronics and Information Technology Industries Association'. Accessed: Jun. 17, 2024. [Online]. Available: https://www.jeita.or.jp/cgi-bin/standard_e/list.cgi?cateid=1&subcateid=50

[24] S. Rajagopal, R. D. Roberts, and S.-K. Lim, 'IEEE 802.15.7 visible light communication: modulation schemes and dimming support', *IEEE Communications Magazine*, vol. 50, no. 3, pp. 72–82, Mar. 2012, doi: 10.1109/MCOM.2012.6163585.

[25] 'IEEE Standard for Local and metropolitan area networks–Part 15.7: Short-Range Optical Wireless Communications', *IEEE Std 802.15.7-2018 (Revision of IEEE Std 802.15.7-2011)*, pp. 1–407, Apr. 2019, doi: 10.1109/IEEESTD.2019.8697198.

[26] K. L. Bober, E. Ackermann, R. Freund, V. Jungnickel, T. Baykas, and S.-K. Lim, 'The IEEE 802.15.13 Standard for Optical Wireless Communications in Industry 4.0', in *IECON 2022 – 48th Annual Conference of the IEEE Industrial Electronics Society*, Oct. 2022, pp. 1–6. doi: 10.1109/IECON49645.2022.9968724.

[27] H. Haas, 'Harald Haas: Wireless data from every light bulb | TED Talk'. Accessed: Jun. 20, 2023. [Online]. Available: https://www.ted.com/talks/harald_haas_wireless_data_from_every_light_bulb

[28] H. Haas, L. Yin, Y. Wang, and C. Chen, 'What is LiFi?', *Journal of Lightwave Technology*, vol. 34, no. 6, pp. 1533–1544, 2016, doi: 10.1109/JLT.2015.2510021.

[29] 'IEEE Standards Association', IEEE Standards Association. Accessed: Jan. 13, 2025. [Online]. Available: https://standards.ieee.org/ieee/802.11bb/10823/

[30] D. M. Boroson, B. S. Robinson, D. A. Burianek, D. V. Murphy, and A. Biswas, 'Overview and status of the Lunar Laser Communications Demonstration', in *Free-Space Laser Communication Technologies XXIV*, SPIE, Feb. 2012, pp. 69–78. doi: 10.1117/12.914801.

[31] D. Karunatilaka, F. Zafar, V. Kalavally, and R. Parthiban, 'LED based indoor visible light communications: State of the art', *IEEE Communications Surveys and Tutorials*, vol. 17, no. 3, pp. 1649–1678, 2015, doi: 10.1109/COMST.2015.2417576.

[32] L. E. M. Matheus, A. B. Vieira, L. F. M. Vieira, M. A. M. Vieira, and O. Gnawali, 'Visible Light Communication: Concepts, Applications and Challenges', *IEEE Communications Surveys & Tutorials*, vol. 21, no. 4, pp. 3204–3237, 2019, doi: 10.1109/COMST.2019.2913348.

[33] H. Chun, A. Gomez, C. Quintana, W. Zhang, G. Faulkner, and D. O'Brien, 'A Wide-Area Coverage 35 Gb/s Visible Light Communications Link for Indoor Wireless Applications', *Sci Rep*, vol. 9, no. 1, p. 4952, Mar. 2019, doi: 10.1038/s41598-019-41397-6.

[34] P. A. Loureiro, V. N. H. Silva, M. C. R. Medeiros, F. P. Guiomar, and P. P. Monteiro, ‘Entropy loading for capacity maximization of RGB-based visible light communications’, *Opt. Express, OE*, vol. 30, no. 20, pp. 36025–36037, Sep. 2022, doi: 10.1364/OE.465195.

[35] P. A. Loureiro, F. P. Guiomar, and P. P. Monteiro, ‘25G+ Distance-Adaptive Visible Light Communications Enabled by Entropy Loading’, in *2023 Optical Fiber Communications Conference and Exhibition (OFC)*, Mar. 2023, pp. 1–3. doi: 10.1364/OFC.2023.M4F.1.

[36] ‘Cisco Annual Internet Report - Cisco Annual Internet Report (2018–2023) White Paper’, Cisco. Accessed: Jun. 20, 2023. [Online]. Available: https://www.cisco.com/c/en/us/solutions/collateral/executive-perspectives/annual-internet-report/white-paper-c11-741490.html

[37] Transforma Insights and Exploding Topics, ‘Number of Internet of Things (IoT) connections worldwide from 2022 to 2023, with forecasts from 2024 to 2033 (in billions) [Graph]’, Statista. Accessed: Jun. 19, 2024. [Online]. Available: https://www.statista.com/statistics/1183457/iot-connected-devices-worldwide/

[38] K. Chandra *et al.*, ‘mCRAN: A radio access network architecture for 5G indoor communications’, in *2015 IEEE International Conference on Communication Workshop (ICCW)*, Jun. 2015, pp. 300–305. doi: 10.1109/ICCW.2015.7247195.

[39] P. A. Loureiro, F. P. Guiomar, and P. P. Monteiro, ‘Visible Light Communications: A Survey on Recent High-Capacity Demonstrations and Digital Modulation Techniques’, *Photonics*, vol. 10, no. 9, Art. no. 9, Sep. 2023, doi: 10.3390/photonics10090993.

[40] O. Alamu, T. O. Olwal, and K. Djouani, ‘Cooperative visible light communications: An overview and outlook’, *Optical Switching and Networking*, vol. 52–53, p. 100772, May 2024, doi: 10.1016/j.osn.2024.100772.

[41] A. Petrosino, D. Striccoli, O. Romanov, G. Boggia, and L. A. Grieco, ‘Light Fidelity for Internet of Things: A survey’, *Optical Switching and Networking*, vol. 48, p. 100732, Mar. 2023, doi: 10.1016/j.osn.2023.100732.

[42] ‘IEEE Standard for Information Technology–Telecommunications and Information Exchange between Systems Local and Metropolitan Area Networks–Specific Requirements Part 11: Wireless LAN Medium Access Control (MAC) and Physical Layer (PHY) Specifications Amendment 1: Enhancements for High-Efficiency WLAN’, *IEEE Std 802.11ax-2021 (Amendment to IEEE Std 802.11-2020)*, pp. 1–767, May 2021, doi: 10.1109/IEEESTD.2021.9442429.

[43] ‘Wi-Fi Channels, Frequency Bands & Bandwidth » Electronics Notes’. Accessed: Jun. 19, 2024. [Online]. Available: https://www.electronics-notes.com/articles/connectivity/wifi-ieee-802-11/channels-frequencies-bands-bandwidth.php

[44] C.-W. Chow, ‘Recent Advances and Future Perspectives in Optical Wireless Communication, Free Space Optical Communication and Sensing for 6G’, *Journal of Lightwave Technology*, vol. 42, no. 11, pp. 3972–3980, Jun. 2024, doi: 10.1109/JLT.2024.3386630.

[45] C. L. Bas, ‘Système de télésurveillance médicale utilisant la technologie de transmission optique sans fil’, 2017.

[46] V. Guerra, J. Rabadan, and R. Perez-Jimenez, ‘Suitability of optical wireless communication receivers for virtual reality applications’, *ConTEL 2019 - 15th International Conference on Telecommunications, Proceedings*, Jul. 2019, doi: 10.1109/CONTEL.2019.8848557.

[47] E. Saavedra, L. Mascaraque, G. Calderon, G. del Campo, and A. Santamaria, ‘The Smart Meter Challenge: Feasibility of Autonomous Indoor IoT Devices Depending on Its Energy Harvesting Source and IoT Wireless Technology’, *Sensors*, vol. 21, no. 22, Art. no. 22, Jan. 2021, doi: 10.3390/s21227433.

[48] M. Dangana, S. Ansari, Q. H. Abbasi, S. Hussain, and M. A. Imran, 'Suitability of NB-IoT for Indoor Industrial Environment: A Survey and Insights', *Sensors*, vol. 21, no. 16, Art. no. 16, Jan. 2021, doi: 10.3390/s21165284.

[49] A. Boucouvalas, P. Chatzimisios, Z. Ghassemlooy, M. Uysal, and K. Yiannopoulos, 'Standards for indoor Optical Wireless Communications', *IEEE Communications Magazine*, vol. 53, no. 3, pp. 24–31, Mar. 2015, doi: 10.1109/MCOM.2015.7060515.

[50] M. Obeed, A. M. Salhab, M.-S. Alouini, and S. A. Zummo, 'Survey on Physical Layer Security in Optical Wireless Communication Systems', in *2018 Seventh International Conference on Communications and Networking (ComNet)*, Nov. 2018, pp. 1–5. doi: 10.1109/COMNET.2018.8622294.

[51] M. A. Khan, S. Ullah, T. Ahmad, K. Jawad, and A. Buriro, 'Enhancing Security and Privacy in Healthcare Systems Using a Lightweight RFID Protocol', *Sensors*, vol. 23, no. 12, Art. no. 12, Jan. 2023, doi: 10.3390/s23125518.

[52] 'What is an Eavesdropping Attack? How It Works & Examples | Twingate'. Accessed: Sep. 20, 2024. [Online]. Available: https://www.twingate.com/blog/glossary/eavesdropping%20attack

[53] S. Joumessi-Demeffo, 'Dispositif communicant par optique sans fil pour les transmissions audio à l'intérieur du cockpit d'un avion', PhD Thesis, Limoges, 2020.

[54] J. Schneider, L. Lucke, D. Wessels, and T. Schauer, 'Impacts of Wireless Power on Medical Device Design Safety', *Journal of Medical Devices*, vol. 3, no. 2, p. 27544, 2009, doi: 10.1115/1.3135198.

[55] A. Boussebt, 'Etude et mise en oeuvre de la technologie Li-Fi pour un lit de bébé connecté sans fil et sans radio', These de doctorat, Limoges, 2023. Accessed: Sep. 20, 2024. [Online]. Available: https://theses.fr/2023LIMO0091

[56] A. Chehbani, 'Etude et mise en œuvre d'un système communicant sans fil et sans radio pour la mesure de paramètres physiologiques des nouveau-nés', These de doctorat, Limoges, 2024. Accessed: Sep. 20, 2024. [Online]. Available: https://theses.fr/2024LIMO0009

[57] D. Ma, G. Lan, M. Hassan, W. Hu, and S. K. Das, 'Sensing, Computing, and Communications for Energy Harvesting IoTs: A Survey', *IEEE Communications Surveys & Tutorials*, vol. 22, no. 2, pp. 1222–1250, 2020, doi: 10.1109/COMST.2019.2962526.

[58] J. Hester and J. Sorber, 'The Future of Sensing is Batteryless, Intermittent, and Awesome', in *Proceedings of the 15th ACM Conference on Embedded Network Sensor Systems*, in SenSys '17. New York, NY, USA: Association for Computing Machinery, Nov. 2017, pp. 1–6. doi: 10.1145/3131672.3131699.

[59] S. Mohsen, 'A Solar Energy Harvester for a Wireless Sensor System toward Environmental Monitoring', *Proceedings of Engineering and Technology Innovation*, vol. 21, pp. 10–19, Apr. 2022, doi: 10.46604/peti.2022.9210.

[60] M. M. Ferreira, M. P. M. G. Miguel, Z. F. Da Silva Filho, C. P. De Souza, Y. An, and O. Baiocchi, 'Internet of Natural Things (IoNT): An Experimental Evaluation of Best Position to Harvest Thermal Energy from Trees', in *2023 IEEE International Conference on Smart Internet of Things (SmartIoT)*, Aug. 2023, pp. 196–202. doi: 10.1109/SmartIoT58732.2023.00035.

[61] V. Pecunia, L. G. Occhipinti, and R. L. Z. Hoye, 'Emerging Indoor Photovoltaic Technologies for Sustainable Internet of Things', *Advanced Energy Materials*, vol. 11, no. 29, 2021, doi: 10.1002/aenm.202100698.

[62] M. F. Müller, M. Freunek, and L. M. Reindl, 'Maximum efficiencies of indoor photovoltaic devices', *IEEE Journal of Photovoltaics*, vol. 3, no. 1, pp. 59–64, 2013, doi: 10.1109/JPHOTOV.2012.2225023.

[63] T. C. Wu, Y. S. Long, S. T. Hsu, and E. Y. Wang, 'Efficiency Rating of Various PV Technologies under Different Indoor Lighting Conditions', *Energy Procedia*, vol. 130, no. October, pp. 66–71, 2017, doi: 10.1016/j.egypro.2017.09.397.

[64] B. Li, B. Hou, and G. A. J. Amaratunga, 'Indoor photovoltaics, The Next Big Trend in solution-processed solar cells', *InfoMat*, vol. 3, no. 5, pp. 445–459, 2020, doi: 10.1002/inf2.12180.

[65] H. Zheng *et al.*, 'Emerging Organic/Hybrid Photovoltaic Cells for Indoor Applications: Recent Advances and Perspectives', *Solar RRL*, vol. 5, no. 7, pp. 1–17, 2021, doi: 10.1002/solr.202100042.

[66] L. K. Ma *et al.*, 'High-Efficiency Indoor Organic Photovoltaics with a Band-Aligned Interlayer', *Joule*, vol. 4, no. 7, pp. 1486–1500, 2020, doi: 10.1016/j.joule.2020.05.010.

[67] A. Venkateswararao, J. K. W. Ho, S. K. So, S.-W. Liu, and K.-T. Wong, 'Device characteristics and material developments of indoor photovoltaic devices', *Materials Science and Engineering: R: Reports*, vol. 139, p. 100517, Jan. 2020, doi: 10.1016/j.mser.2019.100517.

[68] M. L. Parisi, S. Maranghi, L. Vesce, A. Sinicropi, A. Di Carlo, and R. Basosi, 'Prospective life cycle assessment of third-generation photovoltaics at the pre-industrial scale: A long-term scenario approach', *Renewable and Sustainable Energy Reviews*, vol. 121, p. 109703, Apr. 2020, doi: 10.1016/j.rser.2020.109703.

[69] N. Shah *et al.*, 'A Review of Third Generation Solar Cells', *Processes*, vol. 11, no. 6, Art. no. 6, Jun. 2023, doi: 10.3390/pr11061852.

[70] S. Mori, T. Gotanda, Y. Nakano, M. Saito, K. Todori, and M. Hosoya, 'Investigation of the organic solar cell characteristics for indoor LED light applications', *Jpn. J. Appl. Phys.*, vol. 54, no. 7, p. 071602, Jun. 2015, doi: 10.7567/JJAP.54.071602.

[71] N. H. Reich, W. G. J. H. M. van Sark, and W. C. Turkenburg, 'Charge yield potential of indoor-operated solar cells incorporated into Product Integrated Photovoltaic (PIPV)', *Renewable Energy*, vol. 36, no. 2, pp. 642–647, Feb. 2011, doi: 10.1016/j.renene.2010.07.018.

[72] D. Müller *et al.*, 'Indoor Photovoltaics for the Internet-of-Things – A Comparison of State-of-the-Art Devices from Different Photovoltaic Technologies', *ACS Appl. Energy Mater.*, vol. 6, no. 20, pp. 10404–10414, Oct. 2023, doi: 10.1021/acsaem.3c01274.

[73] G. Kim, J. W. Lim, J. Kim, S. J. Yun, and M. A. Park, 'Transparent Thin-Film Silicon Solar Cells for Indoor Light Harvesting with Conversion Efficiencies of 36% without Photodegradation', *ACS Appl. Mater. Interfaces*, vol. 12, no. 24, pp. 27122–27130, Jun. 2020, doi: 10.1021/acsami.0c04517.

[74] B. H. Hamadani and M. B. Campanelli, 'Photovoltaic Characterization Under Artificial Low Irradiance Conditions Using Reference Solar Cells', *IEEE Journal of Photovoltaics*, vol. 10, no. 4, pp. 1119–1125, Jul. 2020, doi: 10.1109/JPHOTOV.2020.2996241.

[75] T. H. Kim *et al.*, 'Record indoor performance of organic photovoltaics with long-term stability enabled by self-assembled monolayer-based interface management', *Nano Energy*, vol. 112, p. 108429, Jul. 2023, doi: 10.1016/j.nanoen.2023.108429.

[76] B. Hou *et al.*, 'Multiphoton Absorption Stimulated Metal Chalcogenide Quantum Dot Solar Cells under Ambient and Concentrated Irradiance', *Advanced Functional Materials*, vol. 30, no. 39, p. 2004563, 2020, doi: 10.1002/adfm.202004563.

[77] S. M. Meethal *et al.*, 'Asymmetric dual species copper(II/I) electrolyte dye-sensitized solar cells with 35.6% efficiency under indoor light', *J. Mater. Chem. A*, vol. 12, no. 2, pp. 1081–1093, Jan. 2024, doi: 10.1039/D3TA06046B.

[78] Y. Wang *et al.*, 'Defect Passivation Refinement in Perovskite Photovoltaics: Achieving Efficiency over 45% under Low-Light and Low-Temperature Dual Extreme Conditions', *Advanced Materials*, vol. 36, no. 23, p. 2312014, 2024, doi: 10.1002/adma.202312014.

[79] L. Xie *et al.*, 'Recent progress of organic photovoltaics for indoor energy harvesting', *Nano Energy*, vol. 82, p. 105770, Apr. 2021, doi: 10.1016/j.nanoen.2021.105770.

[80] K. Sharma, V. Sharma, and S. S. Sharma, 'Dye-Sensitized Solar Cells: Fundamentals and Current Status', *Nanoscale Research Letters*, vol. 13, 2018, doi: 10.1186/s11671-018-2760-6.

[81] I. López-Fernández *et al.*, 'Lead-Free Halide Perovskite Materials and Optoelectronic Devices: Progress and Prospective', *Advanced Functional Materials*, vol. 34, no. 6, p. 2307896, 2024, doi: 10.1002/adfm.202307896.

[82] S. A. Abubaker and M. Z. Pakhuruddin, 'Progress and development of organic photovoltaic cells for indoor applications', *Renewable and Sustainable Energy Reviews*, vol. 203, p. 114738, Oct. 2024, doi: 10.1016/j.rser.2024.114738.

[83] M. K. H. Rabaia *et al.*, 'Environmental impacts of solar energy systems: A review', *Science of The Total Environment*, vol. 754, p. 141989, Feb. 2021, doi: 10.1016/j.scitotenv.2020.141989.

[84] I. Ibrahim Zamkoye, 'Réalisation et modélisation d'électrodes transparentes à base de nanofils d'argent appliquées aux cellules solaires organiques', These de doctorat, Limoges, 2023. Accessed: Sep. 25, 2024. [Online]. Available: https://theses.fr/2023LIMO0001

[85] J. Panidi, D. G. Georgiadou, T. Schoetz, and T. Prodromakis, 'Advances in Organic and Perovskite Photovoltaics Enabling a Greener Internet of Things', *Advanced Functional Materials*, vol. 32, no. 23, p. 2200694, 2022, doi: 10.1002/adfm.202200694.

[86] M. B. Schubert and J. H. Werner, 'Flexible solar cells for clothing', *Materials Today*, vol. 9, no. 6, pp. 42–50, Jun. 2006, doi: 10.1016/S1369-7021(06)71542-5.

[87] I. Mathews, S. N. Kantareddy, T. Buonassisi, and I. M. Peters, 'Technology and Market Perspective for Indoor Photovoltaic Cells', *Joule*, vol. 3, no. 6, pp. 1415–1426, Jun. 2019, doi: 10.1016/j.joule.2019.03.026.

[88] S. Hwang and T. Yasuda, 'Indoor photovoltaic energy harvesting based on semiconducting π-conjugated polymers and oligomeric materials toward future IoT applications', *Polymer Journal 2022*, pp. 1–20, Nov. 2022, doi: 10.1038/s41428-022-00727-8.

[89] C. L. Cutting, M. Bag, and D. Venkataraman, 'Indoor light recycling: A new home for organic photovoltaics', *Journal of Materials Chemistry C*, vol. 4, no. 43, pp. 10367–10370, 2016, doi: 10.1039/c6tc03344j.

[90] M. T. Todaro *et al.*, 'Biocompatible, Flexible, and Compliant Energy Harvesters Based on Piezoelectric Thin Films', *IEEE Transactions on Nanotechnology*, vol. 17, no. 2, pp. 220–230, Mar. 2018, doi: 10.1109/TNANO.2017.2789300.

[91] Z. Ghassemlooy, W. Popoola, and S. Rajbhandari, *Optical Wireless Communications System and Channel Modelling with Matlab*. Boca Raton: Taylor & Francis, 2013.

[92] S. Fuada, A. P. Putra, Y. Aska, and T. Adiono, 'Trans-impedance amplifier (HA) design for Visible Light Communication (VLC) using commercially available OP-AMP', in *2016 3rd International Conference on Information Technology, Computer, and Electrical Engineering (ICITACEE)*, IEEE, 2016, pp. 31–36. doi: 10.1109/ICITACEE.2016.7892405.

[93] A. Ramli, S. Mahdaliza Idrus, A. Sahmah Mohd Supa'at, M. Al-Farabi, and M. Iqbal, 'Optical Front-End Receiver Design for Optical Wireless Communication System', *Recent Patents on Electrical Engineeringe*, vol. 5, no. 1, pp. 11–19, Apr. 2012, doi: 10.2174/1874476111205010011.

[94] A. Kay, 'Introduction to Op-Amp Noise', in *Operational Amplifier Noise*, Elsevier, 2012, pp. 13–27. doi: 10.1016/B978-0-7506-8525-2.00002-2.

[95] M. J. Hayes, 'A nonlinear optical preamplifier for sensing applications', *IEEE Transactions on Circuits and Systems I: Fundamental Theory and Applications*, vol. 49, no. 1, pp. 1–9, 2002, doi: 10.1109/81.974869.

[96] A. Bhat, 'Stabilize Your Transimpedance Amplifier Wild Oscillations : Why Do They Happen ?', 2012.

[97] D. RIBEIRO DOS SANTOS, A. JULIEN-VERGONJANNE, and J. BOUCLÉ, 'Cellules Solaires pour les Télécommunications et la Récupération d'Énergie', Limoges, Dec. 2022, pp. 1–12. doi: 10.25965/lji.661.

[98] A. Kaba, 'Incitation à l'activité physique des personnes âgées par réseaux de capteurs sans fil', phdthesis, Université de Limoges, 2022. Accessed: Oct. 24, 2024. [Online]. Available: https://theses.hal.science/tel-03631391

[99] B. Hussain, X. Li, F. Che, C. Patrick Yue, and L. Wu, 'Visible Light Communication System Design and Link Budget Analysis', *Journal of Lightwave Technology*, vol. 33, no. 24, pp. 5201–5209, Dec. 2015, doi: 10.1109/JLT.2015.2499204.

[100] 'EN_12464-1.pdf'. Accessed: Oct. 29, 2024. [Online]. Available: https://www.ageta.lt/app/webroot/files/uploads/filemanager/File/info/EN_12464-1.pdf

[101] *ISO 8995 CIE S 008/E, International Standard for Lighting of indoor work places.*, 2002.

[102] S. Long and M. Ali Khalighi, 'Advantage of CAP Signaling for VLC Systems Under Non-Linear LED Characteristics', in *2019 2nd West Asian Colloquium on Optical Wireless Communications (WACOWC)*, Apr. 2019, pp. 21–25. doi: 10.1109/WACOWC.2019.8770002.

[103] N. S. Nise, *Control Systems Engineering*, 8th EMEA edition. Hoboken, NJ: John Wiley & Sons, 2019.

[104] H. Zhao, C.-H. Su, J.-N. Xu, and J.-W. Zhu, 'An OLED Efficiency Enhancement Strategy to Accelerate the Application of Flexible Optoelectronic Devices in the Biomedical Field', in *2022 16th ICME International Conference on Complex Medical Engineering (CME)*, Nov. 2022, pp. 95–98. doi: 10.1109/CME55444.2022.10063272.

[105] Q.-H. Do, 'Fabrication and characterization of green light-emitting diodes based on halide perovskites', phdthesis, Université de Limoges, 2023. Accessed: Oct. 29, 2024. [Online]. Available: https://theses.hal.science/tel-04473330

[106] J. Jayabharathi, S. Sivaraj, V. Thanikachalam, S. Panimozhi, and J. Anudeebhana, 'Red, green and blue phosphorescent organic light-emitting diodes with ITO-free anode material', *Journal of Photochemistry and Photobiology A: Chemistry*, vol. 389, p. 112229, Feb. 2020, doi: 10.1016/j.jphotochem.2019.112229.

[107] J. M. Kahn and J. R. Barry, 'Wireless infrared communications', *Proceedings of the IEEE*, vol. 85, no. 2, pp. 265–298, 1997, doi: 10.1109/5.554222.

[108] H. T. Bang, 'INFRARED AND VISIBLE WIRELESS OPTICAL TECHNOLOGY FOR BODY SENSOR CONNECTIVITY', 2019.

[109] A. M. Street, P. N. Stavrinou, D. C. O'brien, and D. J. Edwards, 'Indoor optical wireless systems–a review', *Optical and Quantum Electronics*, vol. 29, no. 3, pp. 349–378, Mar. 1997, doi: 10.1023/A:1018530828084.

[110] S. Bastiaens, W. Raes, N. Stevens, W. Joseph, and D. Plets, ‘New Photodiode Responsivity Model for RSS-based VLP’, *2019 Global LIFI Congress, GLC 2019*, pp. 0–5, 2019, doi: 10.1109/GLC.2019.8864136.

[111] S. Bastiaens, W. Raes, N. Stevens, L. Martens, W. Joseph, and D. Plets, ‘Impact of a photodiode’s angular characteristics on RSS-Based VLP accuracy’, *IEEE Access*, vol. 8, pp. 83116–83130, 2020, doi: 10.1109/ACCESS.2020.2991298.

[112] J. L. Gardner and F. J. Wilkinson, ‘Angular effects in silicon photodiode responsivity comparisons’, *Metrologia*, vol. 34, no. 2, pp. 111–114, 1997, doi: 10.1088/0026-1394/34/2/1.

[113] S. M. Sze and K. K. Ng, *Physics of Semiconductor Devices*, 3rd edition. Hoboken, N.J: Wiley-Interscience, 2006.

[114] J. Nelson, *The Physics of Solar Cells*. PUBLISHED BY IMPERIAL COLLEGE PRESS AND DISTRIBUTED BY WORLD SCIENTIFIC PUBLISHING CO., 2003. doi: 10.1142/p276.

[115] Quantum Devices, ‘Silicon Photodiodes - Modes of Operation and Characteristics’. Quantym Devices, Inc., 1998. Accessed: Jan. 13, 2025. [Online]. Available: https://www.quantumdev.com/wp-content/uploads/2016/09/qf1-01.pdf?utm_source=chatgpt.com

[116] R. M. Gagliardi, *Optical Communications*, 1st edition. New York: 1976, 1976.

[117] C. Hoyle and A. Peyton, ‘Bootstrapping techniques to improve the bandwidth of transimpedance amplifiers’, in *IEE Colloquium Analog Signal Processing*, IEE, 1998, pp. 7–7. doi: 10.1049/ic:19980849.

[118] C. Ciofi, F. Crupi, C. Pace, and G. Scandurra, ‘How to enlarge the bandwidth without increasing the noise in OP-AMP-Based transimpedance amplifier’, *IEEE Transactions on Instrumentation and Measurement*, vol. 55, no. 3, pp. 814–819, 2006, doi: 10.1109/TIM.2006.873782.

[119] M. De Murcia, H. Boeglen, and A. Julien-Vergonjanne, ‘ZEROES: Robust Derivative-Based Demodulation Method for Optical Camera Communication’, *Photonics*, vol. 11, no. 10, Art. no. 10, Oct. 2024, doi: 10.3390/photonics11100949.

[120] D. B. Baker, ‘Design Transimpedance Amplifiers for Precision Opto-Sensing’, DigiKey. Accessed: Nov. 04, 2024. [Online]. Available: https://www.digikey.be/nl/articles/design-transimpedance-amplifiers-for-precision-opto-sensing

[121] D. Ribeiro Dos Santos, ‘Implementation of a Visible Light Communication System: Motivation and Challenges’, Final course dissertation, Federal University of Paraíba, João Pessoa, Brazil, 2021. [Online]. Available: https://drive.google.com/file/d/1x8xrbDK2eiwGpThlbJmLDoTxYn-_hhKP/view?usp=sharing

[122] R. Green, M. Higgins, H. Joshi, and M. Leeson, ‘Bandwidth extension for optical wireless receiver-amplifiers’, *Proceedings of 2008 10th Anniversary International Conference on Transparent Optical Networks, ICTON*, vol. 4, pp. 201–204, 2008, doi: 10.1109/ICTON.2008.4598768.

[123] R. J. Green and M. G. McNeill, ‘Bootstrap transimpedance amplifier: A new configuration’, *IEE proceedings. Part G. Electronic circuits and systems*, vol. 136, no. 2, pp. 57–61, 1989, doi: 10.1049/ip-g-2.1989.0009.

[124] S. M. Idrus, S. S. Rais, and A. Ramli, ‘Bandwidth Analysis of Bootstrap Transimpedance Amplifier for Optical Free Space Receiver’, *Elektrika*, vol. 10, no. 1, pp. 13–19, 2008.

[125] M. Joharifar, ‘IM/DD Techniques in Mid-Infrared for Free Space Optical Communications’, KTH Royal Institute of Technology, 2024. Accessed: Nov. 04, 2024. [Online]. Available: https://urn.kb.se/resolve?urn=urn:nbn:se:kth:diva-355454

[126] K. Fan, T. Komine, Y. Tanaka, and M. Nakagawa, ‘The effect of reflection on indoor visible-light communication system utilizing white LEDs’, in *The 5th International Symposium on Wireless Personal Multimedia Communications*, Oct. 2002, pp. 611–615 vol.2. doi: 10.1109/WPMC.2002.1088247.

[127] A. Julien-Vergonjanne, S. Sahuguède, and L. Chevalier, ‘Optical Wireless Body Area Networks for Healthcare Applications’, pp. 569–587, 2016, doi: 10.1007/978-3-319-30201-0_26.

[128] K. Lee, H. Park, and J. R. Barry, ‘Indoor Channel Characteristics for Visible Light Communications’, *IEEE Communications Letters*, vol. 15, no. 2, pp. 217–219, Feb. 2011, doi: 10.1109/LCOMM.2011.010411.101945.

[129] R. W. R. W. Preisendorfer, ‘Hydrologic Optics: V. II Foundations’, p. 410, 1976.

[130] P. Combeau, L. Aveneau, P. T. L. Gac, and R. Xiao, ‘Characterization of Materials for Optical Wireless Channel Simulation’, *2022 13th International Symposium on Communication Systems, Networks and Digital Signal Processing, CSNDSP 2022*, no. July, pp. 156–161, 2022, doi: 10.1109/CSNDSP54353.2022.9908050.

[131] M. Pharr and G. Humphreys, *Physically Based Rendering: From Theory To Implementation*, vol. 2. 2004.

[132] B. T. Phong, ‘Illumination for computer generated pictures’, *Commun. ACM*, vol. 18, no. 6, pp. 311–317, juin 1975, doi: 10.1145/360825.360839.

[133] S. Dimitrov and H. Haas, ‘Information Rate of OFDM-Based Optical Wireless Communication Systems With Nonlinear Distortion’, *Journal of Lightwave Technology*, vol. 31, no. 6, pp. 918–929, Mar. 2013, doi: 10.1109/JLT.2012.2236642.

[134] D. R. D. Santos *et al.*, ‘Toward Indoor Simulations of OPV Cells for Visible Light Communication and Energy Harvesting’, *IEEE Access*, vol. 12, pp. 41027–41041, 2024, doi: 10.1109/ACCESS.2024.3378056.

[135] F. R. Gfeller and U. Bapst, ‘Wireless In-House Data Communication via Diffuse Infrared Radiation’, *Proceedings of the IEEE*, vol. 67, no. 11, pp. 1474–1486, 1979, doi: 10.1109/PROC.1979.11508.

[136] J. R. Barry, J. M. Kahn, W. J. Krause, E. A. Lee, and D. G. Messerschmitt, ‘Simulation of multipath impulse response for indoor wireless optical channels’, *IEEE Journal on Selected Areas in Communications*, vol. 11, no. 3, pp. 367–379, Apr. 1993, doi: 10.1109/49.219552.

[137] A. Appel, ‘Some techniques for shading machine renderings of solids’, in *Proceedings of the April 30--May 2, 1968, spring joint computer conference*, in AFIPS ’68 (Spring). New York, NY, USA: Association for Computing Machinery, avril 1968, pp. 37–45. doi: 10.1145/1468075.1468082.

[138] J. P. Rossi, J. C. Bic, A. J. Levy, Y. Gabillett, and M. Rosen, ‘A ray launching method for radio-mobile propagation in urban area’, in *Antennas and Propagation Society Symposium 1991 Digest*, Jun. 1991, pp. 1540–1543 vol.3. doi: 10.1109/APS.1991.175146.

[139] A. Behlouli, P. Combeau, L. Aveneau, S. Sahuguede, and A. Julien-Vergonjanne, ‘Efficient Simulation of Optical Wireless Channel Application to WBANs with MISO Link’, *Procedia Computer Science*, vol. 40, no. C, pp. 190–197, Jan. 2014, doi: 10.1016/J.PROCS.2014.12.027.

[140] A. Behlouli, P. Combeau, and L. Aveneau, ‘MCMC Methods for Realistic Indoor Wireless Optical Channels Simulation’, *Journal of Lightwave Technology*, vol. 35, no. 9, pp. 1575–1587, May 2017, doi: 10.1109/JLT.2017.2662939.

[141] P. Combeau *et al.*, ‘Optical Wireless Channel Simulation for Communications Inside Aircraft Cockpits’, *Journal of Lightwave Technology*, vol. 38, no. 20, pp. 5635–5648, Oct. 2020, doi: 10.1109/JLT.2020.3003989.

[142] A. Chehbani, S. Sahuguede, A. Julien-Vergonjanne, and O. Bernard, ‘Quality Indexes of the ECG Signal Transmitted Using Optical Wireless Link’, *Sensors*, vol. 23, no. 9, Art. no. 9, Jan. 2023, doi: 10.3390/s23094522.

[143] B. Sklar and F. Harris, *Digital Communications: Fundamentals and Applications*, 3rd edition. Hoboken: Pearson, 2020.

[144] A. J. C. Moreira, R. T. Valadas, and A. M. De Oliveira Duarte, ‘Optical interference produced by artificial light’, *Wireless Networks*, vol. 3, no. 2, pp. 131–140, 1997, doi: 10.1023/A:1019140814049/METRICS.

[145] Y. Rahmatallah and S. Mohan, ‘Peak-To-Average Power Ratio Reduction in OFDM Systems: A Survey And Taxonomy’, *IEEE Communications Surveys & Tutorials*, vol. 15, no. 4, pp. 1567–1592, 2013, doi: 10.1109/SURV.2013.021313.00164.

[146] X. Li, R. Mardling, and J. Armstrong, ‘Channel Capacity of IM/DD Optical Communication Systems and of ACO-OFDM’, in *2007 IEEE International Conference on Communications*, Jun. 2007, pp. 2128–2133. doi: 10.1109/ICC.2007.358.

[147] J. B. Carruthers and J. M. Kahn, ‘Multiple-subcarrier modulation for nondirected wireless infrared communication’, *IEEE Journal on Selected Areas in Communications*, vol. 14, no. 3, pp. 538–546, Apr. 1996, doi: 10.1109/49.490239.

[148] J. Armstrong and A. J. Lowery, ‘Power efficient optical OFDM’, *Electron. Lett.*, vol. 42, no. 6, pp. 370–372, Mar. 2006, doi: 10.1049/el:20063636.

[149] J. Proakis and M. Salehi, *Digital Communications, 5th Edition*, 5th edition. Boston: McGraw-Hill Education, 2007.

[150] J. R. Barry, *Wireless Infrared Communications*, 1994th edition. Boston London: Springer, 1994.

[151] G. Kumar and F.-C. Chen, ‘A review on recent progress in organic photovoltaic devices for indoor applications’, *J. Phys. D: Appl. Phys.*, vol. 56, no. 35, p. 353001, Jun. 2023, doi: 10.1088/1361-6463/acd2e5.

[152] Y. Li, X. Huang, H. K. M. Sheriff, and S. R. Forrest, ‘Semitransparent organic photovoltaics for building-integrated photovoltaic applications’, *Nat Rev Mater*, vol. 8, no. 3, pp. 186–201, Mar. 2023, doi: 10.1038/s41578-022-00514-0.

[153] E. Kondolot Solak and E. Irmak, ‘Advances in organic photovoltaic cells: a comprehensive review of materials, technologies, and performance’, *RSC Advances*, vol. 13, no. 18, pp. 12244–12269, 2023, doi: 10.1039/D3RA01454A.

[154] M. Hiramoto, *Organic solar cells : energetic and nanostructural design*. 2021.

[155] T. Liu *et al.*, ‘A Polymeric Two-in-One Electron Transport Layer and Transparent Electrode for Efficient Indoor All-Organic Solar Cells’, *Advanced Science*, vol. 11, no. 40, p. 2405676, 2024, doi: 10.1002/advs.202405676.

[156] S. Lattante, ‘Electron and Hole Transport Layers: Their Use in Inverted Bulk Heterojunction Polymer Solar Cells’, *Electronics*, vol. 3, no. 1, Art. no. 1, Mar. 2014, doi: 10.3390/electronics3010132.

[157] A. S. Mahdi, L. M. Shaker, and A. Alamiery, ‘Recent advances in organic solar cells: materials, design, and performance’, *J Opt*, vol. 53, no. 2, pp. 1403–1419, Apr. 2024, doi: 10.1007/s12596-023-01262-2.

[158] V. Petrova-Koch, ‘Milestones of Solar Conversion and Photovoltaics’, in *High-Efficient Low-Cost Photovoltaics: Recent Developments*, V. Petrova-Koch, R. Hezel, and A. Goetzberger, Eds., Berlin, Heidelberg: Springer, 2009, pp. 1–5. doi: 10.1007/978-3-540-79359-5_1.

[159] A. Einstein, ‘Über einen die Erzeugung und Verwandlung des Lichtes betreffenden heuristischen Gesichtspunkt’, *Annalen der Physik*, vol. 322, no. 6, pp. 132–148, 1905, doi: 10.1002/andp.19053220607.

[160] ‘The Nobel Prize in Chemistry 2000’, NobelPrize.org. Accessed: Nov. 21, 2024. [Online]. Available: https://www.nobelprize.org/prizes/chemistry/2000/summary/

[161] C. W. Tang, ‘Two-layer organic photovoltaic cell’, *Applied Physics Letters*, vol. 48, no. 2, pp. 183–185, Jan. 1986, doi: 10.1063/1.96937.

[162] G. Yu, J. Gao, J. C. Hummelen, F. Wudl, and A. J. Heeger, ‘Polymer Photovoltaic Cells: Enhanced Efficiencies via a Network of Internal Donor-Acceptor Heterojunctions’, *Science*, vol. 270, no. 5243, pp. 1789–1791, Dec. 1995, doi: 10.1126/science.270.5243.1789.

[163] M. T. Dang, L. Hirsch, and G. Wantz, ‘P3HT:PCBM, Best Seller in Polymer Photovoltaic Research’, *Advanced Materials*, vol. 23, no. 31, pp. 3597–3602, 2011, doi: 10.1002/adma.201100792.

[164] M. A. Ali, H. H. Kim, C. Y. Lee, H. S. Soh, and J. G. Lee, ‘Effects of the FeCl3 concentration on the polymerization of conductive poly(3,4-ethylenedioxythiophene) thin films on (3-aminopropyl) trimethoxysilane monolayer-coated SiO2 surfaces’, *Met. Mater. Int.*, vol. 15, no. 6, pp. 977–981, Dec. 2009, doi: 10.1007/s12540-009-0977-8.

[165] Y. Liang *et al.*, ‘For the Bright Future—Bulk Heterojunction Polymer Solar Cells with Power Conversion Efficiency of 7.4%’, *Advanced Materials*, vol. 22, no. 20, pp. E135–E138, May 2010, doi: 10.1002/ADMA.200903528.

[166] J.-D. Chen *et al.*, ‘Single-Junction Polymer Solar Cells Exceeding 10% Power Conversion Efficiency’, *Advanced Materials*, vol. 27, no. 6, pp. 1035–1041, 2015, doi: 10.1002/adma.201404535.

[167] Z. He *et al.*, ‘Single-junction polymer solar cells with high efficiency and photovoltage’, *Nature Photon*, vol. 9, no. 3, pp. 174–179, Mar. 2015, doi: 10.1038/nphoton.2015.6.

[168] W. Zhao *et al.*, ‘Fullerene-Free Polymer Solar Cells with over 11% Efficiency and Excellent Thermal Stability’, *Adv Mater*, vol. 28, no. 23, pp. 4734–4739, Jun. 2016, doi: 10.1002/adma.201600281.

[169] V. V. Sharma, A. Landep, S.-Y. Lee, S.-J. Park, Y.-H. Kim, and G.-H. Kim, ‘Recent advances in polymeric and small molecule donor materials for Y6 based organic solar cells’, *Next Energy*, vol. 2, p. 100086, Jan. 2024, doi: 10.1016/j.nxener.2023.100086.

[170] Y. Lin *et al.*, ‘An Electron Acceptor Challenging Fullerenes for Efficient Polymer Solar Cells’, *Advanced Materials*, vol. 27, no. 7, pp. 1170–1174, 2015, doi: 10.1002/adma.201404317.

[171] J.-L. Wang, K.-K. Liu, L. Hong, G.-Y. Ge, C. Zhang, and J. Hou, ‘Selenopheno[3,2-b]thiophene-Based Narrow-Bandgap Nonfullerene Acceptor Enabling 13.3% Efficiency for Organic Solar Cells with Thickness-Insensitive Feature’, *ACS Energy Lett.*, vol. 3, no. 12, pp. 2967–2976, Dec. 2018, doi: 10.1021/acsenergylett.8b01808.

[172] J. Yuan *et al.*, ‘Single-Junction Organic Solar Cell with over 15% Efficiency Using Fused-Ring Acceptor with Electron-Deficient Core’, *Joule*, vol. 3, no. 4, pp. 1140–1151, Apr. 2019, doi: 10.1016/j.joule.2019.01.004.

[173] Q. Liu *et al.*, ‘18% Efficiency organic solar cells’, *Sci Bull (Beijing)*, vol. 65, no. 4, pp. 272–275, Feb. 2020, doi: 10.1016/j.scib.2020.01.001.

[174] A. Sperlich, M. Auth, and V. Dyakonov, ‘Charge Transfer in Ternary Solar Cells Employing Two Fullerene Derivatives: Where do Electrons Go?’, *Israel Journal of Chemistry*, vol. 62, no. 7–8, p. e202100064, 2022, doi: 10.1002/ijch.202100064.

[175] L. Zhu *et al.*, ‘Single-junction organic solar cells with over 19% efficiency enabled by a refined double-fibril network morphology’, *Nat. Mater.*, vol. 21, no. 6, Art. no. 6, Jun. 2022, doi: 10.1038/s41563-022-01244-y.

[176] H. Chen *et al.*, ‘Organic solar cells with 20.82% efficiency and high tolerance of active layer thickness through crystallization sequence manipulation’, *Nat. Mater.*, pp. 1–10, Jan. 2025, doi: 10.1038/s41563-024-02062-0.

[177] M. Jahandar, S. Kim, and D. C. Lim, ‘Indoor Organic Photovoltaics for Self-Sustaining IoT Devices: Progress, Challenges and Practicalization’, *ChemSusChem*, vol. 14, no. 17, pp. 3449–3474, 2021, doi: 10.1002/cssc.202100981.

[178] B. H. S. Miranda *et al.*, ‘Efficient fully roll-to-roll coated encapsulated organic solar module for indoor applications’, *Solar Energy*, vol. 220, pp. 343–353, May 2021, doi: 10.1016/j.solener.2021.03.025.

[179] ‘IEC TS 62607-7-2:2023’. Accessed: Apr. 04, 2025. [Online]. Available: https://webstore.iec.ch/en/publication/61819

[180] S. Hegedus, *Handbook of Photovoltaic Science and Engineering*. 2003.

[181] M. Plakhotnyuk, ‘Nanostructured Heterojunction Crystalline Silicon Solar Cells with Transition Metal Oxide Carrier Selective Contacts’, 2018. doi: 10.13140/RG.2.2.15200.17929.

[182] S. B. Prakash, G. Singh, and S. Singh, ‘Modeling and Performance Analysis of Simplified Two-Diode Model of Photovoltaic Cells’, *Front. Phys.*, vol. 9, Oct. 2021, doi: 10.3389/fphy.2021.690588.

[183] S. R. Fahim, H. M. Hasanien, R. A. Turky, S. H. E. A. Aleem, and M. Ćalasan, ‘A Comprehensive Review of Photovoltaic Modules Models and Algorithms Used in Parameter Extraction’, *Energies*, vol. 15, no. 23, Art. no. 23, Jan. 2022, doi: 10.3390/en15238941.

[184] A. A. Amelenan Torimtubun, J. Pallarès, and L. F. Marsal, ‘Analysing the Efficiency Enhancement of Indoor Organic Photovoltaic using Impedance Spectroscopy Technique’, in *2021 IEEE Latin America Electron Devices Conference (LAEDC)*, Apr. 2021, pp. 1–4. doi: 10.1109/LAEDC51812.2021.9437965.

[185] A. Pockett, H. K. Hin Lee, B. L. Coles, W. C. Tsoi, and M. J. Carnie, ‘A combined transient photovoltage and impedance spectroscopy approach for a comprehensive study of interlayer degradation in non-fullerene acceptor organic solar cells’, *Nanoscale*, vol. 11, no. 22, pp. 10872–10883, 2019, doi: 10.1039/C9NR02337B.

[186] C.-H. Kim *et al.*, ‘Equivalent Circuit Modeling for a High-Performance Large-Area Organic Photovoltaic Module’, *IEEE Journal of Photovoltaics*, vol. 5, no. 4, pp. 1100–1105, Jul. 2015, doi: 10.1109/JPHOTOV.2015.2419136.

[187] H. Hawashin, ‘Etude des propriétés dynamiques de cellules solaires pérovskites pour la réception de données par voie optique dans le visible’, Thèse de doctorat, Université de Limoges, 1968-...., France, 2021. Accessed: Nov. 24, 2024. [Online]. Available: http://www.theses.fr/2021LIMO0111/document

[188] E. von Hauff, ‘Impedance Spectroscopy for Emerging Photovoltaics’, *J. Phys. Chem. C*, vol. 123, no. 18, pp. 11329–11346, May 2019, doi: 10.1021/acs.jpcc.9b00892.

[189] Z. He, K. Asare-Yeboah, and S. Bi, 'Advances in Charge Carrier Mobility of Diketopyrrolopyrrole-Based Organic Semiconductors', *Coatings*, vol. 14, no. 9, Art. no. 9, Sep. 2024, doi: 10.3390/coatings14091080.

[190] J. Brebels, J. V. Manca, L. Lutsen, D. Vanderzande, and W. Maes, 'High dielectric constant conjugated materials for organic photovoltaics', *J. Mater. Chem. A*, vol. 5, no. 46, pp. 24037–24050, Nov. 2017, doi: 10.1039/C7TA06808E.

[191] N. Zhou and A. Facchetti, 'Charge Transport and Recombination in Organic Solar Cells (OSCs)', in *Organic and Hybrid Solar Cells*, H. Huang and J. Huang, Eds., Cham: Springer International Publishing, 2014, pp. 19–52. doi: 10.1007/978-3-319-10855-1_2.

[192] S. Zhang *et al.*, 'Organic solar cells as high-speed data detectors for visible light communication', *Optica*, vol. 2, no. 7, p. 607, 2015, doi: 10.1364/optica.2.000607.

[193] N. A. Mica *et al.*, 'Triple-cation perovskite solar cells for visible light communications', *Photonics Research*, vol. 8, no. 8, p. A16, 2020, doi: 10.1364/prj.393647.

[194] N. Lorriere *et al.*, 'LiFi Reception from Organic Photovoltaic Modules Subject to Additional DC Illuminations and Shading Effects', in *2019 Global LIFI Congress (GLC)*, IEEE, Jun. 2019, pp. 1–5. doi: 10.1109/GLC.2019.8864115.

[195] A. J. Heeger, 'Semiconducting polymers: the Third Generation', *Chem. Soc. Rev.*, vol. 39, no. 7, pp. 2354–2371, Jun. 2010, doi: 10.1039/B914956M.

[196] C. X. Zhao, A. Y. Mao, and G. Xu, 'Junction capacitance and donor-acceptor interface of organic photovoltaics', *Applied Physics Letters*, vol. 105, no. 6, p. 063302, Aug. 2014, doi: 10.1063/1.4892963.

[197] C. Deibel and V. Dyakonov, 'Polymer–fullerene bulk heterojunction solar cells', *Rep. Prog. Phys.*, vol. 73, no. 9, p. 096401, Aug. 2010, doi: 10.1088/0034-4885/73/9/096401.

[198] J. Bisquert and G. Garcia-Belmonte, 'On Voltage, Photovoltage, and Photocurrent in Bulk Heterojunction Organic Solar Cells', *J. Phys. Chem. Lett.*, vol. 2, no. 15, pp. 1950–1964, Aug. 2011, doi: 10.1021/jz2004864.

[199] G. Garcia-Belmonte, A. Munar, E. M. Barea, J. Bisquert, I. Ugarte, and R. Pacios, 'Charge carrier mobility and lifetime of organic bulk heterojunctions analyzed by impedance spectroscopy', *Organic Electronics*, vol. 9, no. 5, pp. 847–851, Oct. 2008, doi: 10.1016/j.orgel.2008.06.007.

[200] D. C. Tripathi and Y. N. Mohapatra, 'Diffusive capacitance in space charge limited organic diodes: Analysis of peak in capacitance-voltage characteristics', *Applied Physics Letters*, vol. 102, no. 25, p. 253303, Jun. 2013, doi: 10.1063/1.4812487.

[201] L. Mallette, 'Modeling the Silicon Solar Cell as an Optical Detector', *Retrospective Theses and Dissertations*, Jan. 1977, [Online]. Available: https://stars.library.ucf.edu/rtd/355

[202] S.-M. Kim and J.-S. Won, 'Simultaneous reception of visible light communication and optical energy using a solar cell receiver', in *2013 International Conference on ICT Convergence (ICTC)*, Oct. 2013, pp. 896–897. doi: 10.1109/ICTC.2013.6675511.

[203] Z. Wang, D. Tsonev, S. Videv, and H. Haas, 'Towards self-powered solar panel receiver for optical wireless communication', *2014 IEEE International Conference on Communications, ICC 2014*, pp. 3348–3353, 2014, doi: 10.1109/ICC.2014.6883838.

[204] Z. Wang, D. Tsonev, S. Videv, and H. Haas, 'On the Design of a Solar-Panel Receiver for Optical Wireless Communications with Simultaneous Energy Harvesting', *IEEE Journal on Selected Areas in Communications*, vol. 33, no. 8, pp. 1612–1623, 2015, doi: 10.1109/JSAC.2015.2391811.

[205] P. D. Diamantoulakis and G. K. Karagiannidis, ‘Simultaneous Lightwave Information and Power Transfer (SLIPT) for Indoor IoT Applications’, in *GLOBECOM 2017 - 2017 IEEE Global Communications Conference*, Dec. 2017, pp. 1–6. doi: 10.1109/GLOCOM.2017.8254781.

[206] P. D. Diamantoulakis, G. K. Karagiannidis, and Z. Ding, ‘Simultaneous Lightwave Information and Power Transfer (SLIPT)’, *IEEE Transactions on Green Communications and Networking*, vol. 2, no. 3, pp. 764–773, Sep. 2018, doi: 10.1109/TGCN.2018.2818325.

[207] B. Arredondo *et al.*, ‘Visible Light Communication System Using an Organic Bulk Heterojunction Photodetector’, *Sensors 2013, Vol. 13, Pages 12266-12276*, vol. 13, no. 9, pp. 12266–12276, Sep. 2013, doi: 10.3390/S130912266.

[208] C. Vega-Colado *et al.*, ‘An All-Organic Flexible Visible Light Communication System’, *Sensors 2018, Vol. 18, Page 3045*, vol. 18, no. 9, p. 3045, Sep. 2018, doi: 10.3390/S18093045.

[209] W.-H. Shin, S.-H. Yang, D.-H. Kwon, and S.-K. Han, ‘Self-reverse-biased solar panel optical receiver for simultaneous visible light communication and energy harvesting’, *Optics Express*, vol. 24, no. 22, p. A1300, 2016, doi: 10.1364/oe.24.0a1300.

[210] B. Malik and X. Zhang, ‘Solar panel receiver system implementation for visible light communication’, *Proceedings of the IEEE International Conference on Electronics, Circuits, and Systems*, vol. 2015, pp. 502–503, 2015, doi: 10.1109/ICECS.2015.7440361.

[211] W. Lei, Z. Chen, Y. Xu, C. Jiang, J. Lin, and J. Fang, ‘Negatively Biased Solar Cell Optical Receiver for Underwater Wireless Optical Communication System With Low Peak Average Power Ratio’, *IEEE Photonics Journal*, vol. 14, no. 4, Aug. 2022, doi: 10.1109/JPHOT.2022.3186702.

[212] S. Sepehrvand, L. N. Theagarajan, and S. Hranilovic, ‘Rate-power trade-off in simultaneous lightwave information and power transfer systems’, *IEEE Communications Letters*, vol. 25, no. 4, pp. 1249–1253, 2021, doi: 10.1109/LCOMM.2020.3047379.

[213] S. Kadirvelu *et al.*, ‘A Circuit for Simultaneous Reception of Data and Power Using a Solar Cell’, *IEEE Transactions on Green Communications and Networking*, vol. 5, no. 4, pp. 2065–2075, Dec. 2021, doi: 10.1109/TGCN.2021.3087008.

[214] J. I. De Oliveira Filho, O. Alkhazragi, A. Trichili, B. S. Ooi, M. S. Alouini, and K. N. Salama, ‘Simultaneous Lightwave and Power Transfer for Internet of Things Devices’, *Energies 2022, Vol. 15, Page 2814*, vol. 15, no. 8, p. 2814, Apr. 2022, doi: 10.3390/EN15082814.

[215] S. Das, A. Sparks, E. Poves, S. Videv, J. Fakidis, and H. Haas, ‘Effect of Sunlight on Photovoltaics as Optical Wireless Communication Receivers’, *Journal of Lightwave Technology*, vol. 39, no. 19, pp. 6182–6190, Oct. 2021, doi: 10.1109/JLT.2021.3096734.

[216] E. Bialic, L. Maret, and D. Kténas, ‘Specific innovative semi-transparent solar cell for indoor and outdoor LiFi applications’, *Applied Optics*, vol. 54, no. 27, p. 8062, Sep. 2015, doi: 10.1364/AO.54.008062.

[217] N. Lorriere *et al.*, ‘An OFDM testbed for LiFi performance characterization of photovoltaic modules’, *2018 Global LIFI Congress, GLC 2018*, vol. 2018-Janua, pp. 1–5, 2018, doi: 10.23919/GLC.2018.8319116.

[218] N. Lorriere *et al.*, ‘Photovoltaic solar cells for outdoor lifi communications’, *Journal of Lightwave Technology*, vol. 38, no. 15, pp. 3822–3831, 2020, doi: 10.1109/JLT.2020.2981554.

[219] S. Chen, L. Liu, and L.-K. Chen, ‘On the Nonlinear Distortion Characterization in Photovoltaic Modules for Visible Light Communication’, *IEEE Photonics Technology Letters*, vol. 33, no. 24, pp. 1467–1470, Dec. 2021, doi: 10.1109/LPT.2021.3128680.

[220] C. I. del V. Morales, J. C. T. Zafra, M. M. Céspedes, I. Martinez-Sarriegui, and J. M. Sánchez-Pena, ‘Exploring Bandwidth Capabilities of Solar Cells for VLC Applications’, *IEEE Transactions on Industrial Informatics*, pp. 1–8, 2024, doi: 10.1109/TII.2024.3468449.

[221] Y. Zhou, A. Ibrahim, M. Muttillo, H. Ziar, O. Isabella, and P. Manganiello, ‘Investigation on simultaneous energy harvesting and visible light communication using commercial c-Si PV cells: Bandwidth characterization under colored LEDs’, *Energy*, p. 133387, Oct. 2024, doi: 10.1016/j.energy.2024.133387.

[222] J. Fakidis, S. Videv, H. Helmers, and H. Haas, ‘0.5-Gb/s OFDM-Based Laser Data and PowerTransfer Using a GaAs Photovoltaic Cell’, vol. 30, no. 9, pp. 841–844, 2018.

[223] J. Fakidis, H. Helmers, and H. Haas, ‘Simultaneous Wireless Data and Power Transfer for a 1-Gb/s GaAs VCSEL and Photovoltaic Link’, *IEEE Photonics Technology Letters*, vol. 32, no. 19, pp. 1277–1280, 2020, doi: 10.1109/LPT.2020.3018960.

[224] S. Das, J. Fakidis, A. Sparks, E. Poves, S. Videv, and H. Haas, ‘Towards 100 Mb / s Optical Wireless Communications Using a Silicon Photovoltaic Receiver’, *GLOBECOM 2020 - 2020 IEEE Global Communications Conference*, pp. 9–14, 2020, doi: 10.1109/GLOBECOM42002.2020.9322495.

[225] S. Das, E. Poves, J. Fakidis, A. Sparks, S. Videv, and H. Haas, ‘Towards Energy Neutral Wireless Communications: Photovoltaic Cells to Connect Remote Areas’, *Energies 2019, Vol. 12, Page 3772*, vol. 12, no. 19, p. 3772, Oct. 2019, doi: 10.3390/EN12193772.

[226] M. Saliba *et al.*, ‘Cesium-containing triple cation perovskite solar cells: improved stability, reproducibility and high efficiency’, *Energy Environ. Sci.*, vol. 9, no. 6, pp. 1989–1997, Jun. 2016, doi: 10.1039/C5EE03874J.

[227] I. Tavakkolnia *et al.*, ‘Organic photovoltaics for simultaneous energy harvesting and high-speed MIMO optical wireless communications’, *Light: Science and Applications*, vol. 10, no. 1, 2021, doi: 10.1038/s41377-021-00487-9.

[228] J. Zhang, H. S. Tan, X. Guo, A. Facchetti, and H. Yan, ‘Material insights and challenges for non-fullerene organic solar cells based on small molecular acceptors’, *Nat Energy*, vol. 3, no. 9, pp. 720–731, Sep. 2018, doi: 10.1038/s41560-018-0181-5.

[229] J. Bouclé, D. Ribeiro Dos Santos, and A. Julien-Vergonjanne, ‘Doing More with Ambient Light: Harvesting Indoor Energy and Data Using Emerging Solar Cells’, *Solar 2023, Vol. 3, Pages 161-183*, vol. 3, no. 1, pp. 161–183, Mar. 2023, doi: 10.3390/SOLAR3010011.

[230] T. M. Cover and J. A. Thomas, *Elements of Information Theory*. John Wiley & Sons, 2012.

[231] S. H. Lee, ‘A Passive Transponder for Visible Light Identification Using a Solar Cell’, *IEEE Sensors Journal*, vol. 15, no. 10, pp. 5398–5403, 2015, doi: 10.1109/JSEN.2015.2440754.

[232] H. Y. Wang *et al.*, ‘Using pre-distorted PAM-4 signal and parallel resistance circuit to enhance the passive solar cell based visible light communication’, *Optics Communications*, vol. 407, no. September 2017, pp. 245–249, 2018, doi: 10.1016/j.optcom.2017.09.010.

[233] M. Kong *et al.*, ‘Toward self-powered and reliable visible light communication using amorphous silicon thin-film solar cells’, *Optics Express*, vol. 27, no. 24, p. 34542, 2019, doi: 10.1364/oe.27.034542.

[234] E. López-Fraguas *et al.*, ‘Visible Light Communication system using an organic emitter and a perovskite photodetector’, *Organic Electronics*, vol. 73, pp. 292–298, Oct. 2019, doi: 10.1016/J.ORGEL.2019.06.028.

[235] ‘Our LAYER® Technology | Dracula Technologies’. Accessed: Feb. 05, 2024. [Online]. Available: https://dracula-technologies.com/technology-layer/

[236] D.-P. Tran, H.-I. Lu, and C.-K. Lin, ‘Conductive Characteristics of Indium Tin Oxide Thin Film on Polymeric Substrate under Long-Term Static Deformation’, *Coatings*, vol. 8, no. 6, Art. no. 6, Jun. 2018, doi: 10.3390/coatings8060212.

[237] S.-K. Lu, J.-T. Huang, T.-H. Lee, J.-J. Wang, and D.-S. Liu, ‘Flexibility of the Indium Tin Oxide Transparent Conductive Film Deposited Onto the Plastic Substrate’, *Smart Science*, vol. 2, no. 1, pp. 7–12, Jan. 2014, doi: 10.1080/23080477.2014.11665597.

[238] D. R. dos Santos *et al.*, ‘Indoor Performance Simulation of Flexible OPV Cells Towards Visible Light Communication and Energy Harvesting’, in *2024 14th International Symposium on Communication Systems, Networks and Digital Signal Processing (CSNDSP)*, Jul. 2024, pp. 581–586. doi: 10.1109/CSNDSP60683.2024.10636500.

[239] A. Behlouli, ‘Simulation du canal optique sans fil. Application aux télécommunications optique sans fil’, These de doctorat, Poitiers, 2016. Accessed: Jan. 17, 2025. [Online]. Available: https://theses.fr/2016POIT2308

[240] F. J. López-Hernández, R. Pérez-Jiménez, and A. Santamaría, ‘Monte Carlo calculation of impulse response on diffuse IR wireless indoor channels’, *Electronics Letters*, vol. 34, no. 12, pp. 1260–1262, Jun. 1998.

[241] L. Sun, K. Fukuda, and T. Someya, ‘Recent progress in solution-processed flexible organic photovoltaics’, *npj Flex Electron*, vol. 6, no. 1, pp. 1–14, Oct. 2022, doi: 10.1038/s41528-022-00222-3.

List of Figures

List of Tables

Appendices

Appendix 1. Full extension of LOS equation

As described in Chapter II, Section II.1.5.1.1, when the solid angle is sufficiently small, such that $A_r \ll d^2$, the solid angle Ω_{rx} subtended by a real area A_r with incident angle Ψ subtended by its normal $\hat{n}$ and the distance vector $\hat{d}$ to the centre of an optical source, is described as:

$$\Omega_{rx} = \frac{A_r}{d^2}\cos(\Psi)$$

This is only valid for sufficiently small solid angles. In cases where this condition does not hold, the computations described in the section are no longer applicable. For a real area A_r that is large enough to invalidate the small solid angle assumption, the area can be divided into multiple elementary surfaces dA_r. Each of these surfaces has a specific distance d from the source to its centre, and an incident angle Ψ. Here, the solid angle $d\Omega_{rx}$ subtended by each elementary surface dA_r is given by:

$$d\Omega_{rx} = \frac{dA_r}{d^2}\cos(\Psi)$$

The elementary area has a received optical power dP_r, which can be defined as follows, while considering a constant radiant intensity I for an elementary solid angle $d\Omega_{rx}$:

$$dP_r = I(\Omega_{rx})d\Omega_{rx}$$

Therefore, the receiver optical power P_r of the total area A_r is the sum of the optical power contributions from each elementary surface dP_r, expressed mathematically as an integral. For a Lambertian optical source, the radiant intensity depends on the polar angle θ (refer to Equation II-14). Therefore, the received optical power of a real area A_r subtended by a solid angle Ω_{rx} is given by:

$$P_r = \int I(\Omega_{rx})d\Omega_{rx}{}'$$

$$P_r = P_t\left[\frac{m_1+1}{2\pi}\int_{\Omega_{rx}} \cos^{m_1}(\theta)\, d\Omega_{rx}{}'\right]$$

Where the index $'$ is used to distinguish the integral variable from the solid angle Ω_{rx} subtended by the real area A_r. Ultimately, determining the received optical power P_r involves understanding the solid angle for various area sizes and shapes while considering the polar behaviour of the radiant intensity, expressed in this case as $\cos^{m_1}(\theta)$.

Appendix 2. Dynamic characterization - transient method

For the transient method, a square wave was applied at the LED emitter front-end circuit from the arbitrary wave generator integrated into the oscilloscope. The signal has a 660 mV peak-to-peak amplitude, ranging from -330 mV up to 330 mV. As in the frequency method, the DC component determined the average illumination level. The receiver output is directly connected to the oscilloscope, and the following variables can be measured: rise time τ_r, fall time τ_f, mean voltage V_{mean} and peak-to-peak voltage V_{pp}.

The mean voltage is proportional to the OPV illumination and depends on the operating point, while the peak-to-peak voltage represents the signal strength, analogous to the DC gain of the Bode measurement. Therefore, to compare the results obtained with both methods, some V_{pp} values are plotted on a logarithmic scale when required. The -3 dB bandwidth was derived from the maximum of the rise and fall times (the time required to transition between states) using Equation II-95.

Illumination influence

For both receiver front-end circuits (TIA and parallel load), an increase in V_{mean} is expected when the illumination level rises. In the TIA configuration, V_{mean} is expected to decrease at higher operating points, consistent with the trends observed in the I-V characterizations. This behaviour is logical since the TIA output variable is directly related to the current. In the parallel load configuration, V_{mean} is expected to follow a logarithmic trend as the load increases, similar to previous measured behaviours (refer to Figure 69). Regarding V_{pp}, the expected behaviour is similar to the ones observed with the DC gain (Figure 77.b and Figure 78.b), while the bandwidths are expected to behave as obtained before (Figure 77.a and Figure 78.a).

TIA – Output current

The necessary measured dynamic parameters are shown in Figure 127.

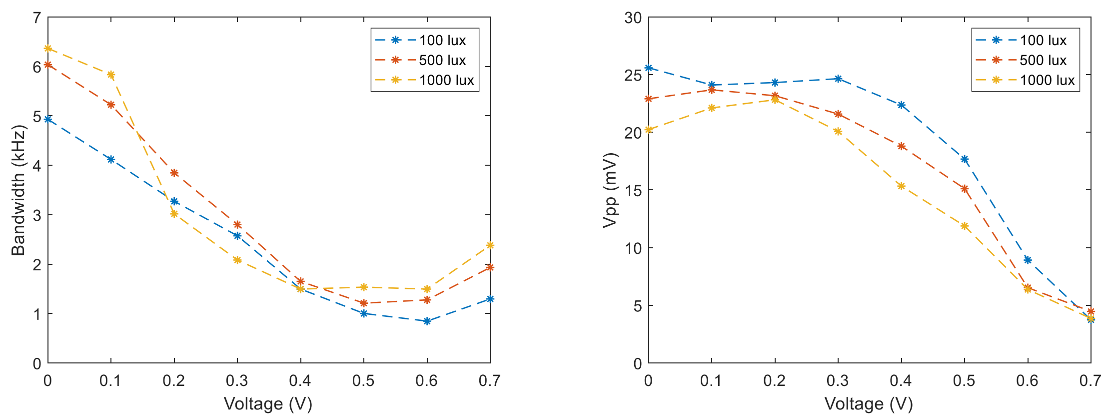

(a) (b)

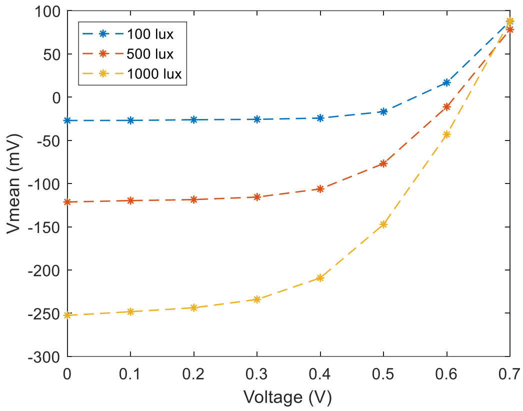

(c)

Figure 127: OPV measured dynamic parameters in function of operating point for multiple illuminations, transient method and output current: (a) Bandwidth; (b) V_{pp}; (c) V_{mean}.

A review of the measured data reveals notable inaccuracies associated with this specific measurement. Using the TIA in combination with the transient method results in significant variability and oscillation, particularly under higher illumination levels. The root cause of this increased noise remains unclear, though it is evident that greater illumination amplifies the noise power. One hypothesis suggests that the TIA circuit contributes additional noise to the system, which the oscilloscope may have filtered out during the Bode measurement.

In Figure 127.a, the overall trend is still observed: the operating point increases, the device bandwidth decreases. However, the results in this case are less straightforward to interpret compared to the frequency method, primarily due to noise interference that affects the precision of the measurements. Quantifying this noise influence is complex and was not analysed in this work. Despite this, the increase in bandwidth with rising illumination levels is still evident, demonstrating the enhanced dynamic performance of the device under brighter conditions. Interestingly, a slight increase in bandwidth is observed for voltages exceeding the open-circuit voltage (0.7 V), a phenomenon not previously noted.

In Figure 127.b, the same behaviour seen in Figure 77.b is noticed: higher illumination levels lead to a reduction in output signal amplitude, attributed to increased ambient light noise. Similar to the bandwidth analysis, the noisier nature of the measurements makes the results less clear than those obtained with the frequency method.

Finally, in Figure 127.c, the results associated with V_{mean} confirm the expected behaviour of a solar cell under rising illumination, closely aligning with the I-V curve measurements previously obtained for illumination levels of 100 lux, 500 lux, and 1000 lux. It is important to highlight that the obtained results are negative since the TIA provides an inverse response, as described in Equation II-22.

Parallel load – Output voltage

Figure 128 shows the following parameters for the parallel load front-end under variable illumination: bandwidth, V_{pp} and V_{mean}.

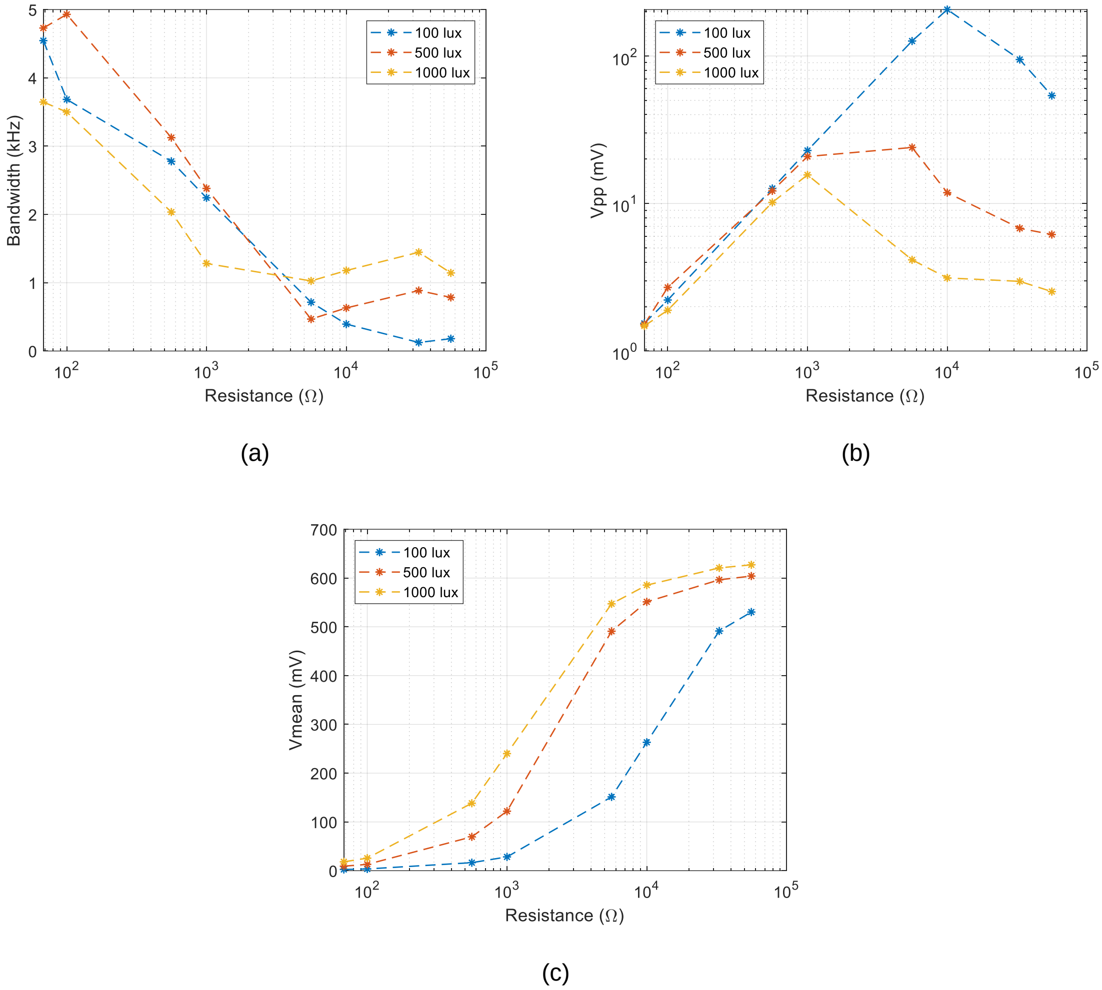

Figure 128: OPV measured dynamic parameters in function of operating point for multiple illuminations, transient method and output voltage: (a) Bandwidth; (b) V_{pp}; (c) V_{mean}.

Compared to the TIA front-end, using the parallel load with the transient method yielded more accurate and reliable results. However, at low resistance values, such as $68\ \Omega$ and $100\ \Omega$, the measurements exhibit higher noise due to the reduced voltage signal amplitude. This effect is also observed at higher illumination levels, where the device reaches saturation at lower load resistances, further decreasing the signal amplitude and consequently reducing the SNR. This explains why results at higher illumination levels are less precise, a trend that was also observed with the frequency method.

In Figure 128.a, the bandwidth decreases with increasing load resistance, a trend consistently observed across all experiments. However, the influence of illumination on bandwidth does not align with the behaviour noticed in previous experiments. Higher illumination levels increase shot noise, interfering with the precise determination of bandwidth. Despite this, it remains evident that for all illumination levels, the bandwidth converges to approximately $1\,kHz$ as the operating point approaches the open-circuit condition.

In Figure 128.b, the behaviour observed with the frequency method is similarly illustrated. Under low illumination conditions, saturation occurs at higher load resistances, whereas in strong illumination scenarios, saturation is reached at lower resistances. Again, this was previously seen in Figure 69.

Finally, in Figure 128.c, the expected behaviour, as described before, is observed: the average voltage increases logarithmically with the resistance value. At higher illumination levels, the OPV output voltage saturates at lower resistance values, while at lower illumination, it requires higher load resistances to reach saturation. Once again, this highlights the significant dependence of dynamic performance on illumination conditions when using the parallel load front-end configuration.

Overall, the obtained results are in accordance with the employed frequency method, confirming that higher operating points lead to reduced bandwidths. Similarly, higher illumination levels increase the noise level and decreases the signal amplitude for both TIA and parallel load front-end configurations. The saturation effect of output voltage reading is also observed through the analysis of the peak-to-peak voltage V_{pp} values.

Despite these challenges, the transient method provides valuable insights into the mean output voltage V_{mean}, highlighting the static behaviour of the OPV across different operating points. Also, V_{mean} helps determine whether the OPV is operating within the linear region in the parallel load configuration.

Curvature influence

The procedure detailed Section III.4.2.2 was performed here, while obtaining the following variables for both front-end circuits: bandwidth, V_{mean} and V_{pp}.

- **TIA – Output current**

  Across all curvature configurations, the operating points at 0.7 V and 0.5 V produced weak signals, while the “small” curvature exhibited unexpected behaviour at the 0.4 V operating point. As a result, these values were excluded from the bandwidth and V_{pp} measurements but were still included in the V_{mean} analysis, as they do not impact the average voltage. The resulting dynamic parameters are presented in Figure 129.

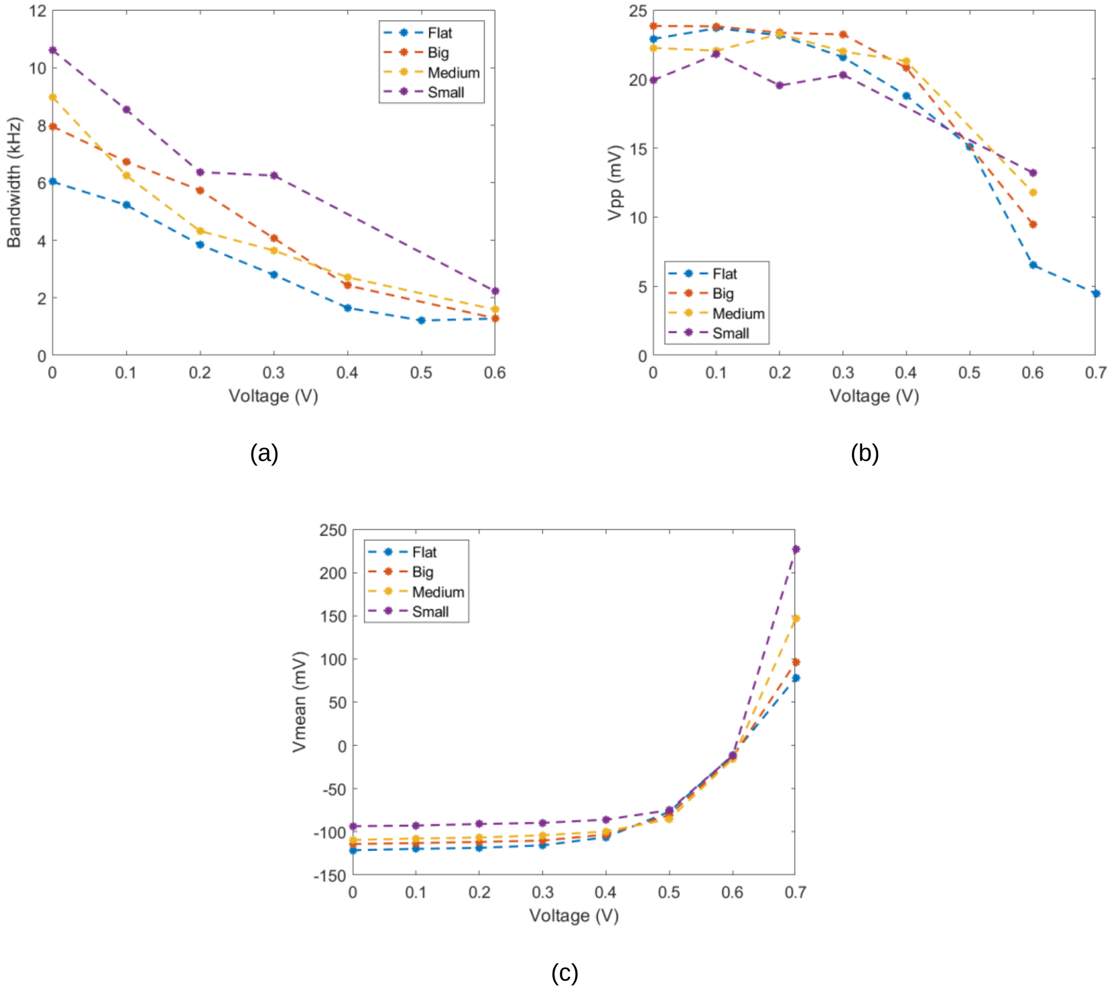

Figure 129: OPV measured dynamic parameters in function of operating point for multiple curvatures, transient method and output current: (a) Bandwidth; (b) V_{pp}; (c) V_{mean}.

As observed in previous experiments, using the TIA with the transient method introduces significant noise and oscillation. In Figure 129.a, the bandwidth follows the expected trend of decreasing with increasing operating voltage. Once again, the “small” curvature topology exhibits higher bandwidth values compared to other configurations (for the values that could be extracted). The bandwidths for the “big” and “medium” configurations are similar and closely match the performance of the flat device.

The measurement inaccuracies also affect the extraction of V_{pp} as shown in Figure 129.b. The trend observed with the frequency method is consistent here, with higher operating points resulting in reduced signal amplitude.

Finally, Figure 129.c shows the V_{mean} curves for various curvatures. As expected, configurations with smaller radii detect less optical power, leading to lower V_{mean} values. These results confirm the influence of curvature on the device ability to capture optical signals, with smaller radii showing diminished performance under perfect alignment scenario. The main reason is linked to a decrease in the received optical power P_r for curvier devices, as detailed in Chapter IV.

Parallel load – Output voltage

For the parallel load front-end, the extracted parameters are shown in Figure 130.

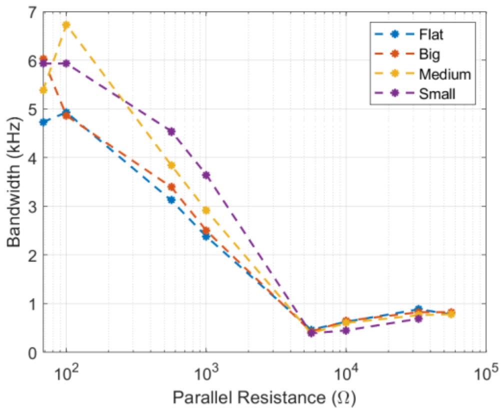

(a)

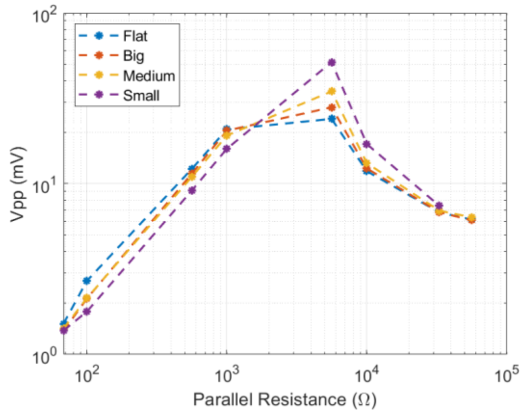

(b)

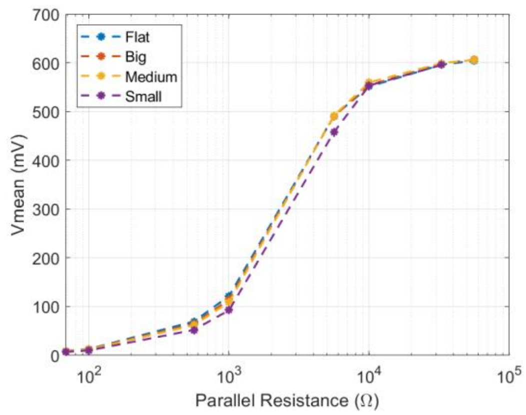

(c)

Figure 130: OPV measured dynamic parameters in function of operating point for multiple curvatures, transient method and output voltage: (a) Bandwidth; (b) V_{pp}; (c) V_{mean}.

Here, the results obtained for the first two resistances are reliable. Starting from a resistance of $560\ \Omega$ and above, the bandwidth analysis results shown in Figure 130.a, align with those obtained using the frequency method. Curvier devices exhibit a slightly increased bandwidth, with all configurations converging to approximately $1\ kHz$ near the open-circuit condition.

The V_{pp} analysis, displayed in Figure 130.b, also corresponds to the trends observed in the frequency method. Curvier devices, due to their lower detection of the DC component of the optical power, require higher load resistances to reach saturation.

Finally, the reduced optical power detection for curvier devices is further supported by Figure 130.c. The "small" configuration shows a slight shift to higher resistance regions, consistent with the behaviour seen in Figure 128.c for low illumination level.

The results obtained using the transient method exhibit the same trends observed with the frequency measurement one. Curvier devices consistently detect less optical power, a behaviour evident across multiple results.

Appendix 3. Curved surface received optical power P_r

When a square-shaped device is bent towards an optical source S, the solid angle Ω_x subtended between the device and the source is deformed, which in turn affects the received optical power P_r (refer to Figure 98 and Section IV.3.2.1). As an initial step, it is essential to understand how the solid angle is altered by the curvature. To achieve this, the curved device is projected onto a plane perpendicular to the source, located at a distance d from the optical source S, as shown below.

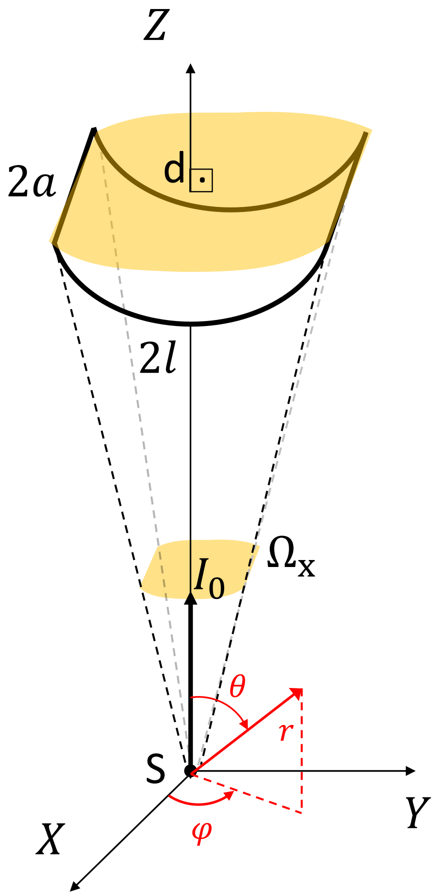

In this scenario, two deformations are observed. Firstly, the length of the projected surface decreases compared to the original length of the curved device, $2l$. Secondly, the width of the projected surface increases and exhibits a curved shape. To begin the analysis, let us focus on the length of the projected surface. In a 2D representation, viewed by the YZ plane, the projected surface length is defined as $2l'$, as shown below, where R is the curvature radius and h is the height displacement. Note the following:

$$h = Rcos\left(\frac{\theta_c}{2}\right)$$

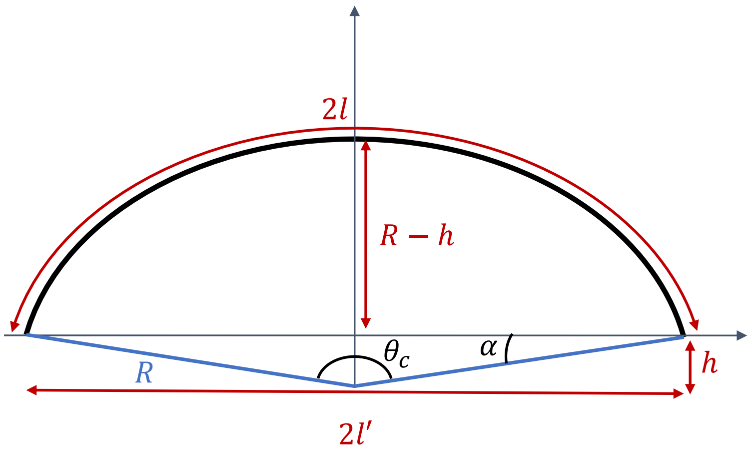

In this scenario, using basic trigonometry, we find that $2\alpha + \theta_c = 180°$, which simplifies to $\alpha = \frac{180° - \theta_c}{2}$. Applying the law of sines, we obtain:

$$\frac{2l'}{\sin(\theta_c)} = \frac{R}{\sin(\alpha)}$$

$$2l' = R\frac{\sin(\theta_c)}{\sin(\alpha)}$$

The width distortion, however, is more complex to analyse. Observing the XZ plane, an increase in width becomes evident, with the maximum expansion occurring at the point where the receiver is closest to the optical source. This maximum value is represented as $2a'$. The schematic below illustrates the concept, where h is the height displacement, defined in Chapter IV.

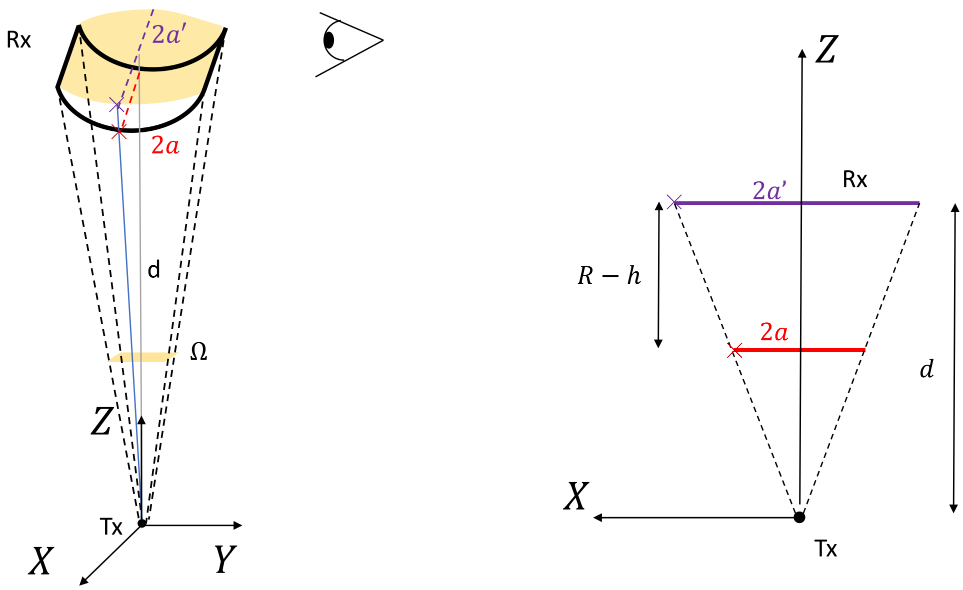

By the similar triangles theory, we have:

$$\frac{a'}{d} = \frac{a}{d-(R-h)}$$

$$a' = a\left(\frac{d}{d-(R-h)}\right)$$

In fact, the width gradually increases from $2a$ until it reaches $2a'$,and this increase depends on the Y variable, as shown below by analysing the projection of the curved surface. For values between the centre $(y = 0)$ and the corner $(y = l')$, the width is denoted as $2a^*(y)$, shown below.

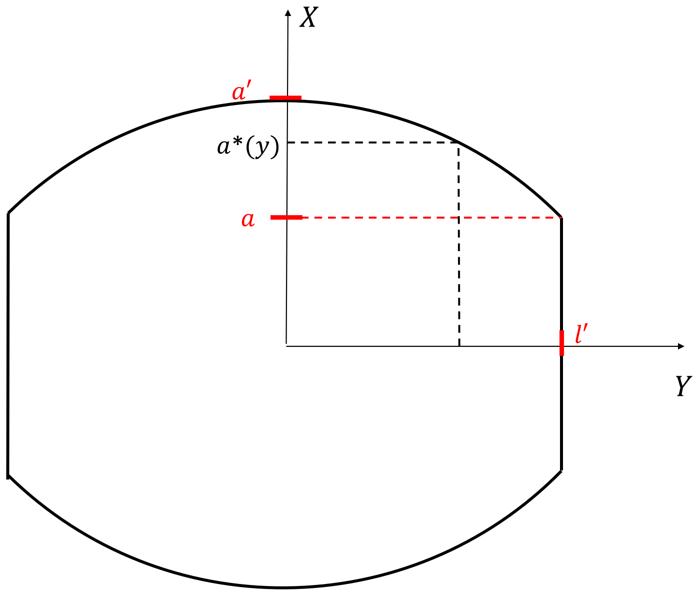

The height of each point is now defined as the variation in the Z-coordinate, corresponding to how close the point is to the optical source. The maximum height variation occurs at the centre of the surface, denoted as $R - h$. The width increase between the centre of the device and its edge is influenced by the height of each analysed point as it approaches the source. For every point on the curved surface, a similar triangle analysis can be applied, where the height variation ranges from 0 (at the edges) to $R - h$ (at the centre). The schematic below depicts the height variation, represented as z^*, for a specific point on the surface.

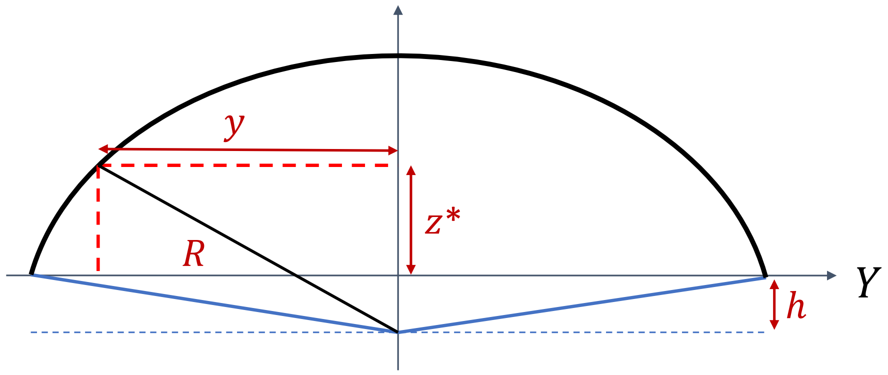

With Pythagorean theorem, we have that:

$$z^* = \sqrt{R^2 - y^2} - h$$

Applying the similar triangles theorem for each point of the surface, each with different height, we obtain the function for the width of the values between the centre and the corners:

$$a^*(y) = a\left(\frac{d}{d - \left(\sqrt{R^2 - y^2} - h\right)}\right)$$

Finally, the projected surface is shown below:

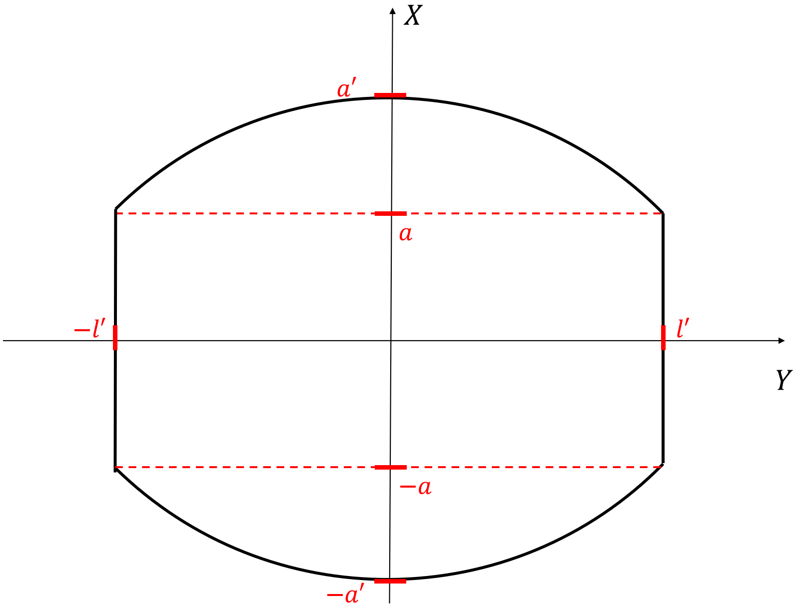

With the distorted curves defined as shown below, for $y \in [-l, l]$.

$$x(y) = \pm a\left(\frac{d}{d - \left(\sqrt{R^2 - y^2} - h\right)}\right)$$

The challenge of determining the received optical power now involves solving the radiant intensity equation for the solid angle Ω_x subtended by the projected surface, as shown above, and the optical source S. To address this, the projected surface is divided into four equal sections, as shown below, with each section corresponding to a portion of the received optical power, denoted as P_I, P_{II}, P_{III} and P_{IV}.

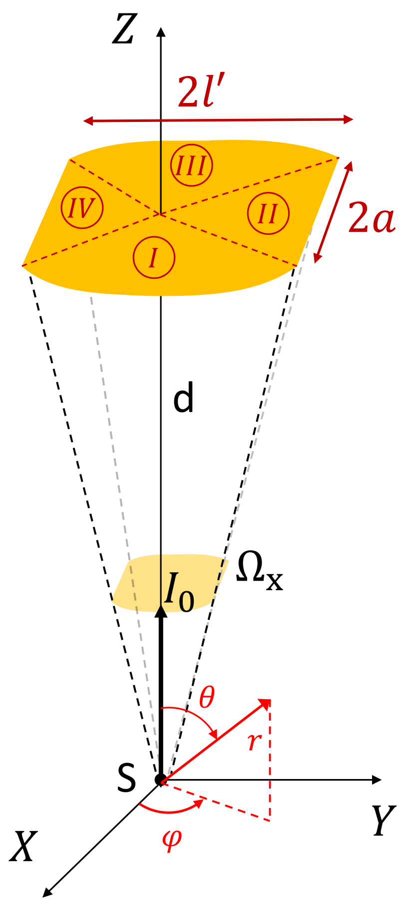

Due to the Lambertian source symmetry at the azimuth angle φ, we have that:

$$P_I = P_{III}$$

$$P_{II} = P_{IV}$$

Finally, the received optical power P_r is then:

$$P_r = 2P_I + 2P_{II}$$

Further analysis involves converting all variables into azimuthal φ and polar θ coordinates within the spherical coordinate system. As the radiant intensity equation for Lambertian receivers depends on the cosine of the polar angle θ, our methodology is based on obtaining the expression of $\cos(\theta)$ as a function of the azimuthal angle, as described below for each region of the projected surface.

- **Obtaining P_{II}**

The image below shows the second region of the projected surface, including important variables for our analysis.

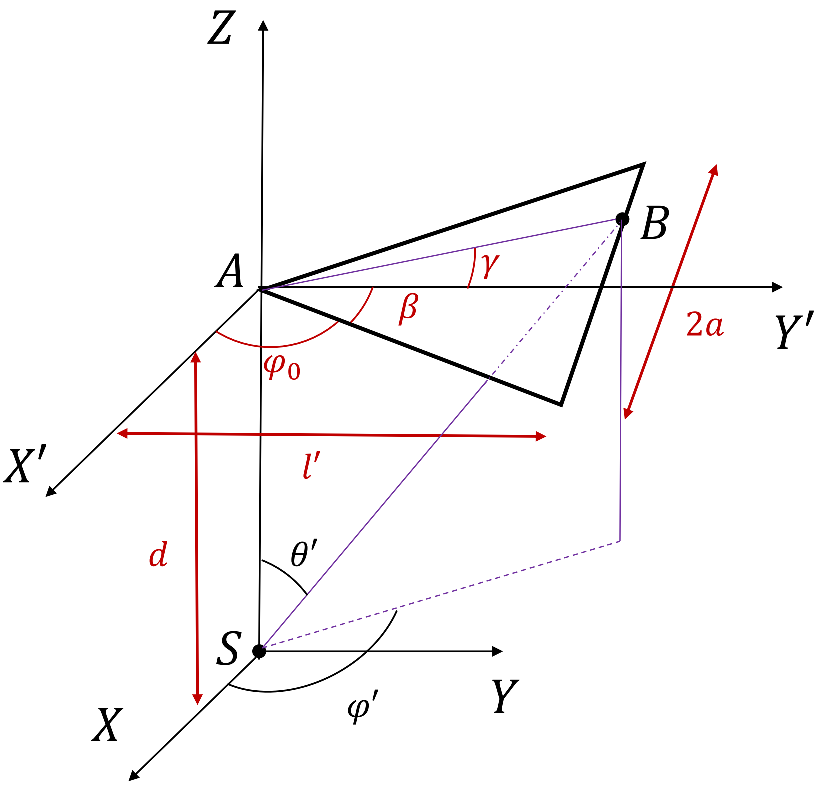

For a given point B at the limits of the projected surface, we have that:

$$\cos(\theta') = \frac{d}{\overline{SB}} = \frac{d}{\sqrt{d^2 + \overline{AB}^2}}$$

With $\overline{AB}$ defined as:

$$\overline{AB} = l' / \cos\gamma$$

Also, we have that $\gamma = \varphi' - \varphi_0 - \beta$, with:

$$\varphi_0 = \operatorname{atan}\left(\frac{l'}{a}\right)$$

$$\beta = \operatorname{atan}\left(\frac{a}{l'}\right)$$

Finally, the $\cos(\theta')$ is defined as:

$$\cos(\theta') = \frac{d}{\sqrt{d^2 + l'^2 \sec^2(\varphi' - \varphi_0 - \beta)}}$$

The received optical power by the second part of the projected surface is described below, were Ω_{II} is solid angle subtended by the second section and the optical source S.

$$P_{II} = \int_{\Omega_{II}} I(\Omega) d\Omega$$

Therefore, it can be written as:

$$P_{II} = \int\int I_0 \cos^{m_1}(\theta) \sin(\theta)\, d\theta d\varphi = I_0 \int\int \cos^{m_1}(\theta) \sin(\theta)\, d\theta d\varphi$$

Solving the internal integral involves varying the polar angle θ from 0 to θ', depending on the specific point under analysis, and applying the substitution method:

$$\int_0^{\theta'} \cos^{m_1}(\theta) \sin(\theta)\, d\theta = \frac{1}{m_1 + 1}[1 - \cos^{m_1+1}(\theta')]$$

We have then the following equation, with φ varying from φ_0 to $\varphi_0 + 2\beta$:

$$P_{II} = \frac{I_0}{m_1 + 1} \int_{\varphi_0}^{\varphi_0+2\beta} [1 - \cos^{m_1+1}(\theta')] d\varphi$$

As detailed before, $\cos(\theta')$ can be described as a function of the azimuth angle. Please note that, here, the integration variable φ equals φ'. Therefore:

$$\cos(\theta') = \frac{d}{\sqrt{d^2 + l'^2 \sec^2(\varphi - \varphi_0 - \beta)}} = \frac{d cos(\varphi - \varphi_0 - \beta)}{\sqrt{d^2 \cos^2(\varphi - \varphi_0 - \beta) + l^2}}$$

$$P_{II} = \frac{I_0}{m_1 + 1} \int_{\varphi_0}^{\varphi_0+2\beta} \left[1 - \left(\frac{d cos(\varphi - \varphi_0 - \beta)}{\sqrt{d^2 \cos^2(\varphi - \varphi_0 - \beta) + l^2}}\right)^{m_1+1}\right] d\varphi$$

This received optical power can be numerically obtained.

- **Obtaining P_I**

The first segment is illustrated below, highlighting key variables relevant to our analysis. In this scenario, we observe:

$$\cos(\theta') = \frac{d}{\overline{SB}} = \frac{d}{\sqrt{d^2 + \overline{AB}}}$$

In comparison to the scenario previously analysed, $\overline{AB}$ is more complex and depends on the previously determined width distortion. In this case, we have:

$$\overline{AB} = \frac{x'}{\cos(\varphi')} = \frac{y'}{\sin(\varphi')}$$

$$y' = \tan(\varphi') x'$$

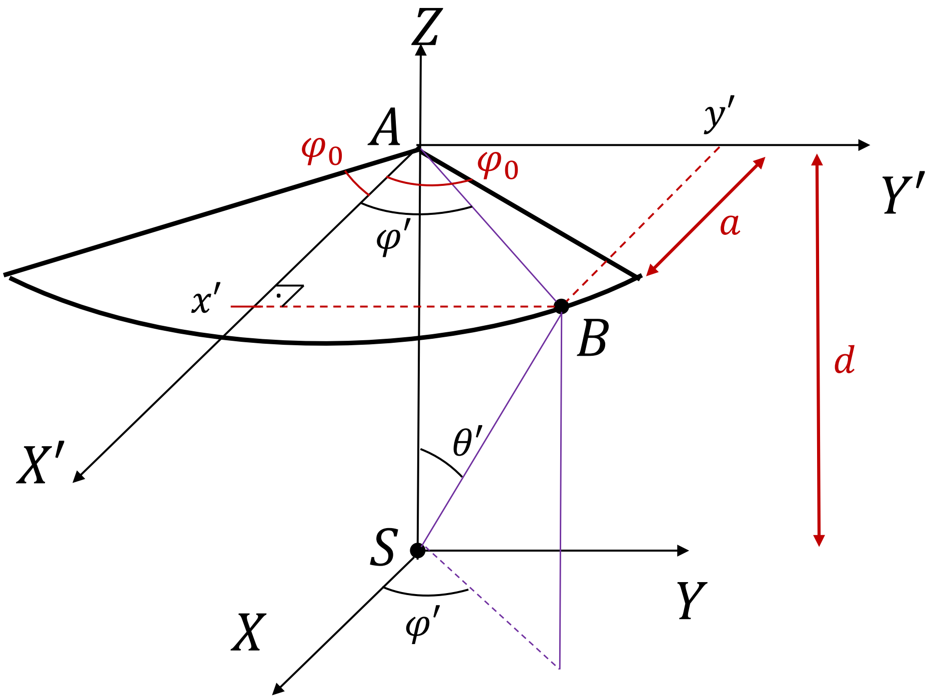

As obtained before, the x component is a function of the y one. Therefore:

$$y'\left[d-\left(\sqrt{R^2-y'^2}-h\right)\right]=\tan(\varphi')\,a\times d$$

The solution of this equation depends on φ' and is not trivial. We introduce then the variable y_φ, which are the real solutions of the equations above. Finally, $\overline{AB}$ can be described as:

$$\overline{AB}=\frac{y_\varphi}{\sin(\varphi')}$$

Then, $\cos(\theta')$ is written as:

$$\cos(\theta')=\frac{d|\sin(\varphi')|}{\sqrt{y_\varphi^2+d^2\sin^2(\varphi')}}$$

Similarly, the received optical power P_I of the first region is:

$$P_I=\int\int I_0\cos^{m_1}(\theta)\sin(\theta)\,d\theta d\varphi=I_0\int\int\cos^{m_1}(\theta)\sin(\theta)\,d\theta d\varphi$$

The solution of the inner integral is similar to the one applied for the region II. Therefore, P_I can be obtained as follow (please notice that φ varies between $-\varphi_0$ to φ_0):

$$P_I = \frac{I_0}{m_1+1}\int_{-\varphi_0}^{\varphi_0}[1-\cos(\theta')^{m_1+1}]d\varphi$$

Finally:

$$P_I = \frac{I_0}{m_1+1}\int_{-\varphi_0}^{\varphi_0}\left[1-\left(\frac{d|\sin(\varphi)|}{\sqrt{y_\varphi^2+d^2\sin^2(\varphi)}}\right)^{m_1+1}\right]d\varphi$$

- **Total received optical power P_r**

Now, by including the contribution of each region, the received optical power of curved surfaces that approach the Lambertian optical source is:

$$P_r = \frac{2I_0}{m_1+1}\left\{\int_{-\varphi_0}^{\varphi_0}\left[1-\left(\frac{d|\sin(\varphi)|}{\sqrt{d^2\sin^2(\varphi)+y_\varphi^2}}\right)^{m_1+1}\right]d\varphi \right.$$
$$\left. + \int_{\varphi_0}^{\varphi_0+2\beta}\left[1-\left(\frac{d\cos(\varphi-\varphi_0-\beta)}{\sqrt{d^2\cos^2(\varphi-\varphi_0-\beta)+l'^2}}\right)^{m_1+1}\right]d\varphi\right\}$$

Finally, the same analysis can be applied to curvatures that position the surface farther from the optical source.

Appendix 4. SNR normalization example

For the normalization, an arbitrary point was chosen to calibrate the SNR. In this example, the hard-decoding method is used. The chosen SNR and BER pair was (7.136 dB, 2.183$\times 10^{-3}$), and the corresponding measured power values were:

$$P_{noise} = 1.78 \times 10^{-9}\, W$$

$$P_{signal} = 9.18 \times 10^{-9}\, W$$

However, the required SNR to theoretically obtain a BER of 2.183×10^{-3} is 9.69 dB. To account for potential errors in noise measurement, a calibration is applied by multiplying the noise value by a coefficient K ensuring that the adjusted SNR matches 9.69 dB. Thus:

$$\frac{P_{signal}}{KP_{noise}} = 10^{\frac{9.69}{10}}$$

$$K = 0.55$$

This correction factor is then applied to all other measured P_{noise} values. For example, to adjust the SNR and BER pair ($5.5\, dB, 1.445 \times 10^{-2}$), where the measured power levels were as follows:

$$P_{noise} = 1.81 \times 10^{-9}\, W$$

$$P_{signal} = 6.42 \times 10^{-9}\, W$$

The calibrated P_{noise} is then $KP_{noise} = 9.95 \times 10^{-10}$, which results in a calibrated SNR of:

$$SNR = 10 \log_{10} \frac{6.42 \times 10^{-9}}{9.95 \times 10^{-10}} = 8.10\, dB$$

Which approximates to the required theoretical SNR of 7.8 dB to obtain the measured BER of 1.445×10^{-2}.

Appendix 5. BER and P_{out} with a TIA for fixed distances

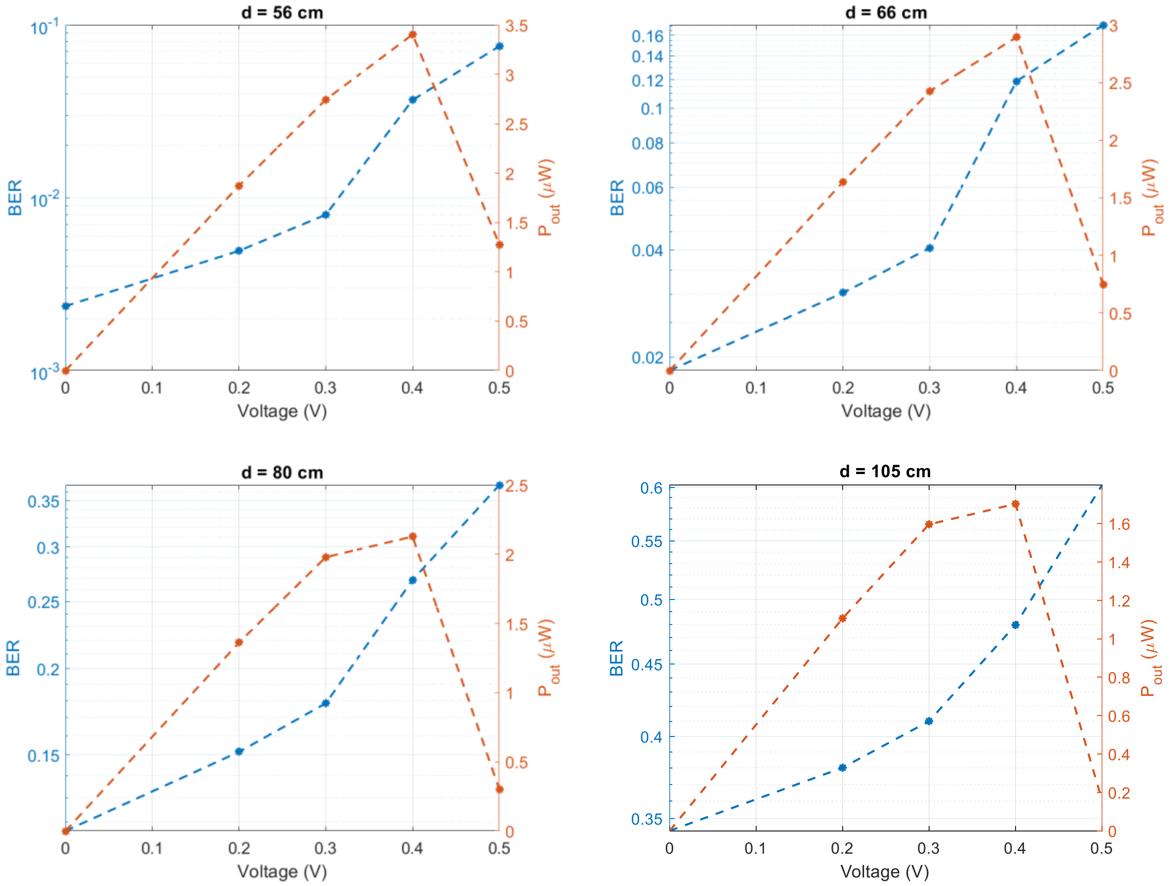

Appendix 6. BER and P_{out} with parallel load for fixed distances

- Without external DC lighting

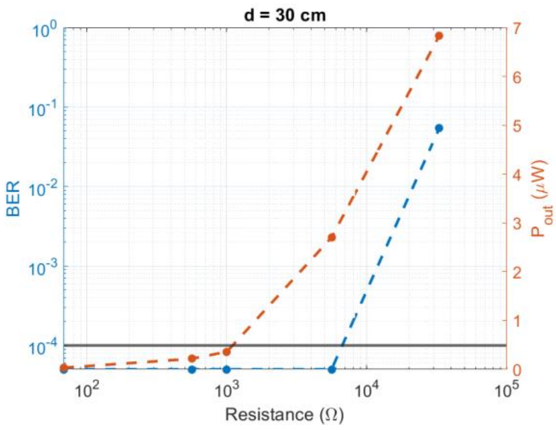

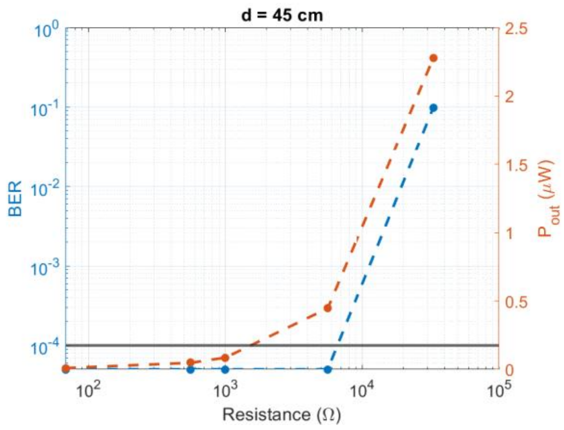

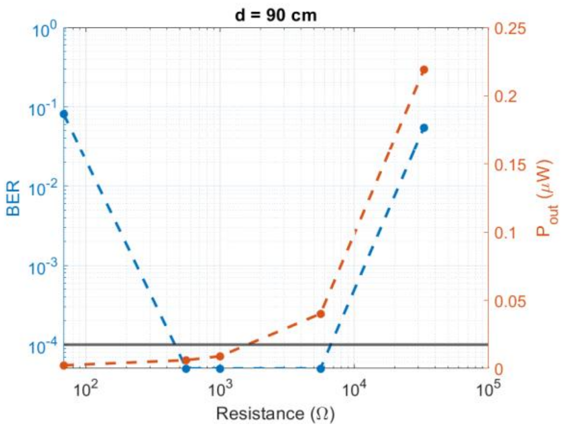

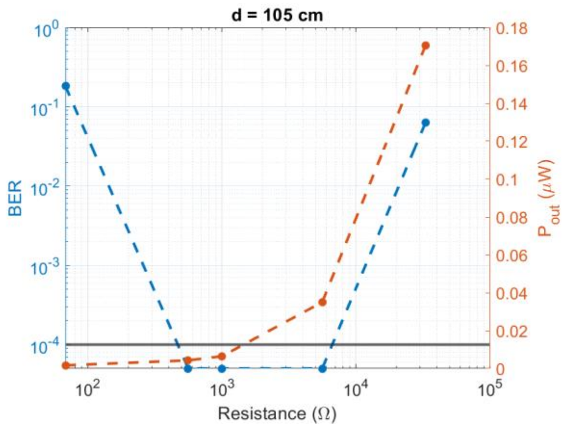

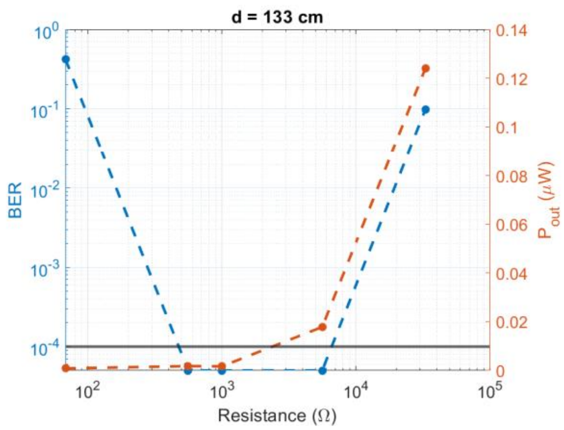

- With external DC lighting

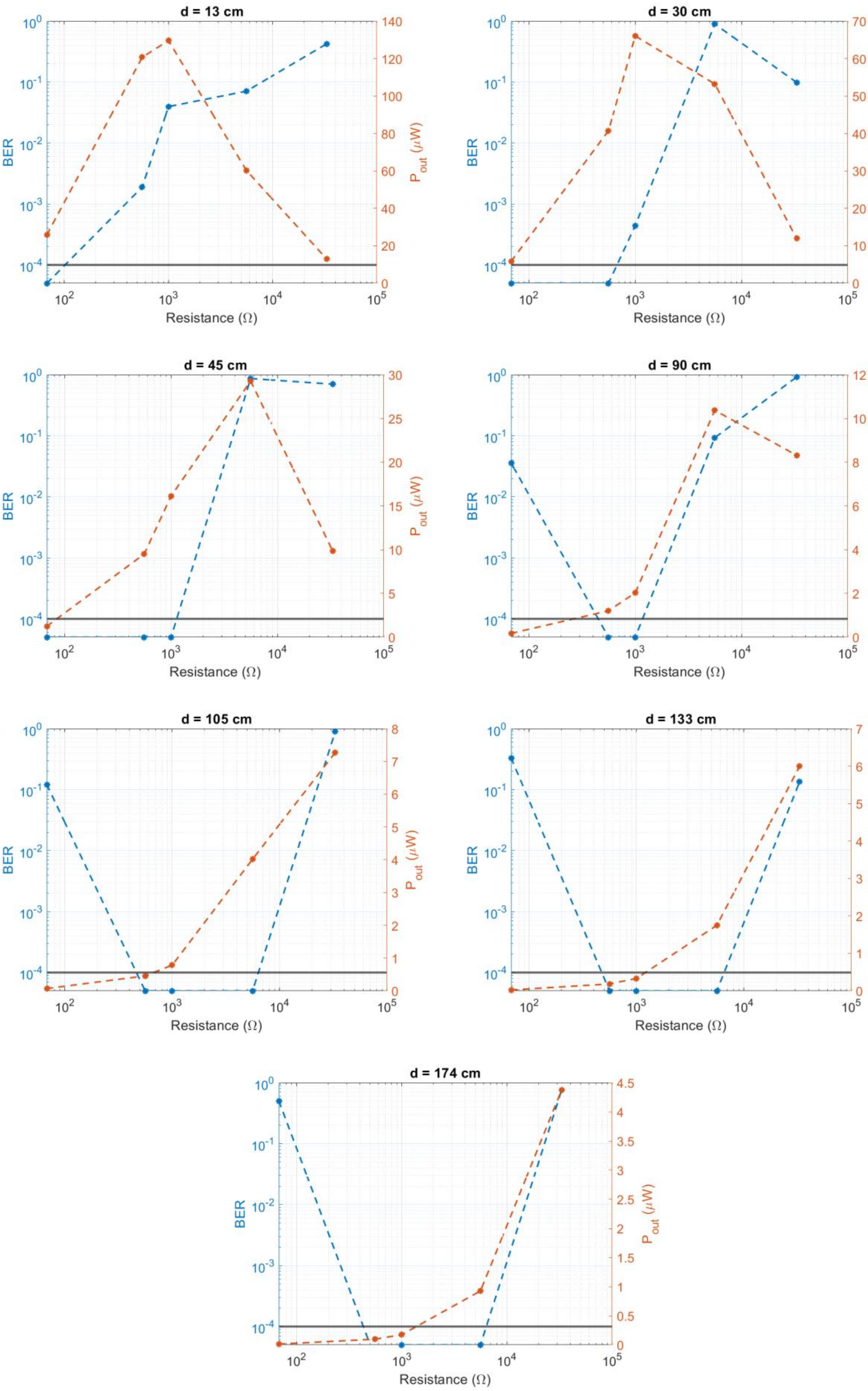
d = 13 cm
d = 30 cm
d = 45 cm
d = 90 cm
d = 105 cm
d = 133 cm
d = 174 cm
BER
P_{out} (μW)
Resistance (Ω)

Articles

RIBEIRO DOS SANTOS, D., JULIEN-VERGONJANNE, A., & BOUCLÉ, J. (2022). Cellules Solaires pour les Télécommunications et la Récupération d'Énergie. 1–12. https://doi.org/10.25965/lji.661

Bouclé, J., Ribeiro Dos Santos, D., & Julien-Vergonjanne, A. (2023). Doing More with Ambient Light: Harvesting Indoor Energy and Data Using Emerging Solar Cells. Solar 2023, Vol. 3, Pages 161-183, 3(1), 161–183. https://doi.org/10.3390/SOLAR3010011

Santos, D. R. Dos, Julien-Vergonjanne, A., Dkhil, S. Ben, Parmentier, M., Combeau, P., Sahuguede, S., & Boucle, J. (2024). Toward Indoor Simulations of OPV Cells for Visible Light Communication and Energy Harvesting. IEEE Access, 12, 41027–41041. https://doi.org/10.1109/ACCESS.2024.3378056

Dos Santos, D. R., Bouclé, J., Julien-Vergonjanne, A., Dkhil, S. Ben, Parmentier, M., Combeau, P., & Sahuguede, S. (2024). Indoor Performance Simulation of Flexible OPV Cells Towards Visible Light Communication and Energy Harvesting. 2024 14th International Symposium on Communication Systems, Networks and Digital Signal Processing, CSNDSP 2024, 581–586. https://doi.org/10.1109/CSNDSP60683.2024.10636500

Conferences

Dos Santos, D. R., Bouclé, J., Julien-Vergonjanne, A., Dkhil, S. Ben, Parmentier, M., Combeau, P., & Sahuguede, S. (2024). Indoor Performance Simulation of Flexible OPV Cells Towards Visible Light Communication and Energy Harvesting. 2024 14th International Symposium on Communication Systems, Networks and Digital Signal Processing, CSNDSP 2024, 581–586. https://doi.org/10.1109/CSNDSP60683.2024.10636500

RIBEIRO DOS SANTOS, D., JULIEN-VERGONJANNE, A., & BOUCLÉ, J. (2022). Cellules Solaires pour les Télécommunications et la Récupération d'Énergie. 1–12. https://doi.org/10.25965/lji.661

Daniel Ribeiro dos Santos, Johann Bouclé, Anne Julien-Vergonjanne. Bringing photovoltaics to a new era: Organic solar cells for telecommunication and energy harvesting. 11ème Workshop des Doctorants XLIM, Mar 2023, Limoges, France. ⟨hal-04060946⟩

Daniel Ribeiro dos Santos, Anne Julien-Vergonjanne, Johann Bouclé. OPV for Energy Harvesting and Data Reception. 5ème Journées Annuelles du GDR OERA, Oct 2023, Marseille, France. ⟨hal-04586266⟩

Printable photovoltaic photoreceptors for the factory of the future and the Internet of Things: toward energy harvesting and wireless optical communications

Visible Light Communication (VLC) and Organic Photovoltaics (OPVs) cells offer promising solutions for the increasing energy and communication demands of the Internet of Things (IoT). VLC uses the visible light spectrum for secure and efficient data transmission, while OPVs provide flexible, low-cost, and sustainable energy harvesting, particularly under indoor lighting conditions. Together, they form the basis of Simultaneous Lightwave Information and Power Transfer (SLIPT), enabling devices to harvest energy and communicate through light. Despite their potential, integrating OPVs into SLIPT systems presents challenges such as managing the trade-offs between energy harvesting and communication, handling nonlinear behaviors, and optimizing performance under real-world indoor conditions. This thesis explores these challenges by investigating the performance of OPVs in SLIPT systems. Static and dynamic characterizations revealed their effectiveness in energy harvesting and communication, even under low-light and curved configurations. Systematic studies examined the impact of illumination levels, device curvature, and front-end circuitry on OPV performance, demonstrating their robustness and adaptability. Advanced simulations were also developed and validated experimentally, offering insights into OPV behavior in indoor scenarios, including mobility and diffuse light conditions. An experimental bench was developed to analyze SLIPT trade-offs, comparing an active front-end, which offered predictable performance but required external power, with a passive alternative that was more energy-efficient but exhibited less consistent behavior. By combining experimental and simulation approaches, this work advances the understanding of OPV-based SLIPT systems and addresses critical gaps in the field. It establishes a foundation for integrating OPVs into autonomous IoT networks, opening new pathways for sustainable, self-powered, and efficient technologies tailored to meet the demands IoT needs.

Keywords: Internet of Things (IoT), Organic Photovoltaics (OPVs), Simultaneous Lightwave Information and Power Transfer (SLIPT), Visible Light Communication (VLC)

Photorécepteurs photovoltaïques imprimables pour l’usine du futur et l’Internet des Objets : vers la récupération d’énergie et les communications optiques sans fils

La Communication par Lumière Visible (VLC) et les cellules Photovoltaïques Organiques (OPVs) offrent des solutions prometteuses face aux besoins croissants en énergie et en communication pour l’Internet des Objets (IoT). La VLC exploite le spectre de la lumière visible pour une transmission de données sécurisée et efficace, tandis que les OPVs permettent la récupération d’énergie flexible, peu coûteuse et durable, particulièrement sous éclairage intérieur. Ensemble, ces technologies forment la base du Transfert Simultané d’Information et d’Énergie par Onde Lumineuse (SLIPT), permettant aux dispositifs de récupérer de l’énergie et de communiquer via la lumière. Cependant, l’intégration des OPVs dans les systèmes SLIPT présente des défis, tels que la gestion des compromis entre la récupération d’énergie et la communication, l’analyse des comportements non linéaires, et l’optimisation des performances dans des conditions réelles en intérieur. Cette thèse explore ces défis en étudiant les performances des OPVs dans des systèmes SLIPT. Les caractérisations statiques et dynamiques ont démontré leur efficacité dans la récupération d’énergie et la communication, même sous faible éclairage et dans des configurations courbées. Des études systématiques ont analysé l'impact des niveaux d’éclairement, de la courbure des dispositifs, et des circuits de réception sur les performances des OPVs, montrant leur robustesse et leur adaptabilité. Des simulations avancées, validées expérimentalement, ont permis de mieux comprendre le comportement des OPVs dans des scénarios intérieurs complexes, incluant la mobilité et les conditions de lumière diffuse. Un banc expérimental a été développé pour analyser les compromis dans les systèmes SLIPT, en comparant un circuit actif offrant des performances prévisibles mais nécessitant une alimentation externe, et une alternative passive plus économe en énergie mais moins prévisible. En combinant des approches expérimentales et de simulation, ce travail approfondit la compréhension des systèmes SLIPT basés sur les OPVs et traite des lacunes majeures dans ce domaine. Il établit une base solide pour l'intégration des OPVs dans des réseaux IoT autonomes, ouvrant la voie à des technologies durables, autoalimentées et efficaces, adaptées aux besoins modernes de l'IoT.

Mots-Clés : Internet des Objets (IoT), Photovoltaïques Organiques (OPVs), Transfert Simultané d'Information et d'Énergie par Onde Lumineuse (SLIPT), Communication par Lumière Visible (VLC)